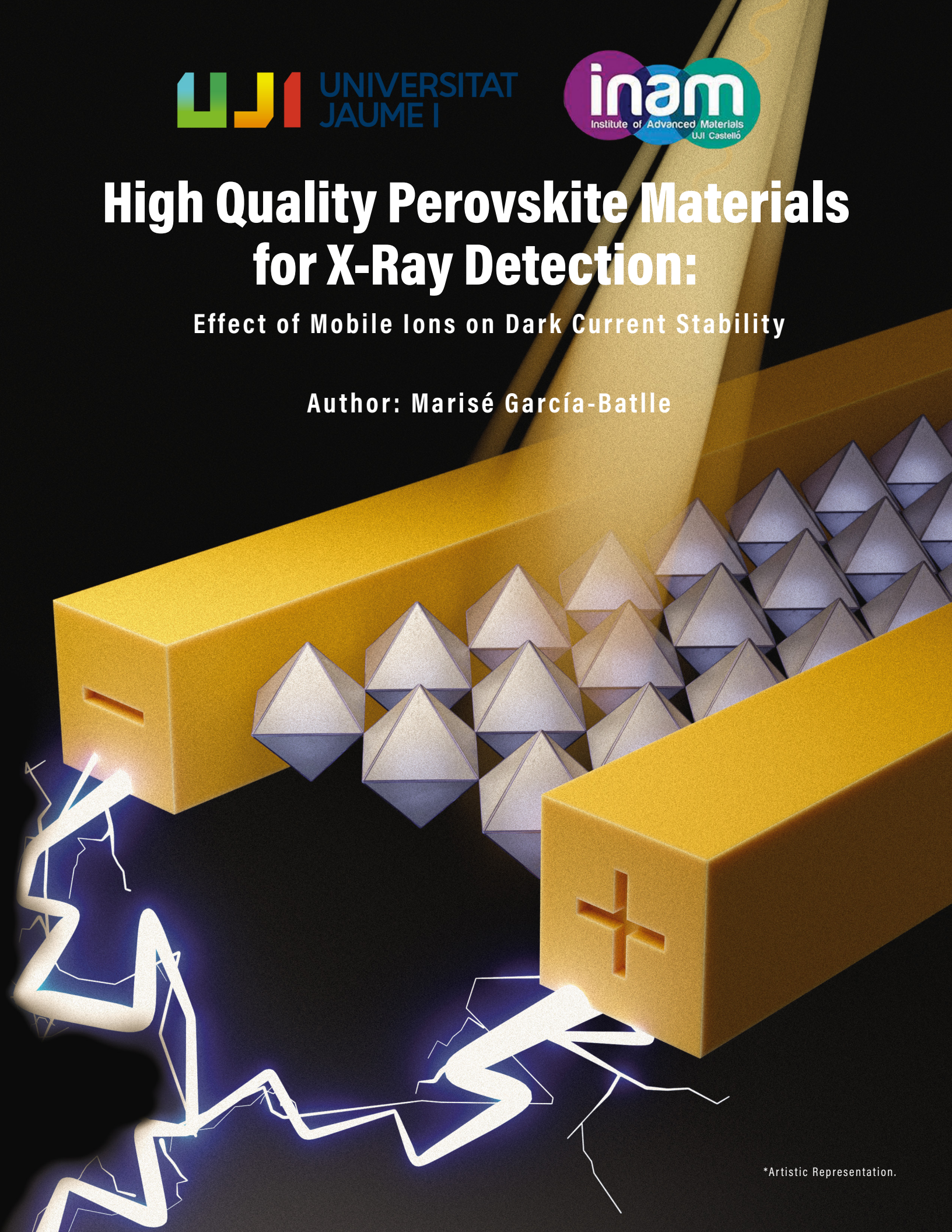


High Quality Perovskite Materials for X-Ray Detection:

Effect of Mobile Ions on Dark Current Stability

Author: Marisé García-Batlle





Programa de Doctorado en Ciencias

Escuela de Doctorado de la Universitat Jaume I

High Quality Perovskite Materials for X-Ray Detection: Effect of Mobile Ions on Dark Current Stability

Memoria presentada por Marisé García Batlle para optar al grado de doctora por la Universitat Jaume I

Doctoranda

Marisé García Batlle

Directores:

Prof. Dr. Germà Garcia-Belmonte

Dr. Antonio Guerrero

Castellón de la Plana, noviembre de 2022

*A mis abus Rafa y Luis, que, desde arriba,
me miran sonriendo ...*

*“I was taught that the way of progress was neither
swift nor easy.”*

Marie Skłodowska Curie

Fundings

The following sources were responsible for funding the research conducted in this thesis.

- ✓ Santiago Grisolia Grant for foreign researchers provided by Generalitat Valenciana BEFPI2020, under the grant number (GRISOLIAP/2018/073)
- ✓ Project- “Transformación de Energía Solar en Combustibles solares a partir de Perovskitas” TREScope, under the entity code UJI-B2017-32.
- ✓ Project – “European Union's Horizon 2020 research and innovation program under the Photonics Public Private Partnership (www.photonics21.org) with the project PEROXIS under the grant agreement N° 871336.



Licencia CC Reconocimiento - No comercial - Sin obra derivada (BY-NC-ND).

Acknowledgements

It was a privilege to be part of the Institute of Advanced Materials during my doctoral studies in Spain, I am very grateful to many people I have learned from and worked with in the last four years. First of all, I would like to thank my thesis supervisor Prof. Dr. Germà Garcia-Belmonte for offering me the opportunity to be part of the project of Hybrid Halide Perovskites as X-ray detectors. His expertise and deep knowledge of the topic was crucial in my learning-through process and my research abilities progress. I feel really humbled and mostly grateful for the opportunity to work under his supervision. I'm also thankful to Dr. Antonio Guerrero and Dr. Osbel Almora both have been an important part of this project assessing my progress with attention and concern always providing theoretical and experimental advice in the fabrication and characterization of perovskite materials.

I am very thankful to Dr. Clara Aranda who was the first researcher I had the chance to work with at INAM. I am grateful to her for getting me started with perovskite synthesis and crystal growth in the laboratory. Many thanks to Prof. Dr. Francisco Fabregat, Prof. Dr. Ivan Mora-Seró and Dr. Pablo Boix for their support. I highly appreciate their critical feedback and valuable input. I express my gratitude to Prof. Dr. Juan Bisquert who contributed to my professional growth with the improvement of my writing skills and encouragement to participate in many scientific conferences and international events. I would like to thank all the research members of the groups GAME and GAS for their support and sharing day-to-day experiences. I would like to generally thank the researchers at SCIC who have helped me with many of the experimental characterization techniques.

I had the opportunity of joining Prof Michael Saliba's group during 3 months of research at the Institute für Photovoltaik in Stuttgart, Germany. I really like to thank colleagues, and staff for making my time at the *ipv* a great experience.

I cannot thank enough to Loles Merchan Mundina and the administrative staff for all their support with efficiency and professionalism. Loles, you have become part of my family. Many thanks for everything.

I express my most sincere gratitude to my friends, those I met here and those I had met before. My dear friend Drialys for helping me from my first day in Castellón, she has always been there for me, I have been there for her. To my fellows from Centralita. Thanks to Marti, Roser, Nuri, Ramonet and Agus for all the laughs, tears, and fun. It has

been wonderful to spend those year with all of you. Thanks to my friend Clau who has always been caring and enduring with me and thanks to Sandra, Eva, Sofia, Irene, and Bou for always motivating me at coffee time. Thanks to Cam and Ernest for their critical feedback and for helping me to improve the writing in this thesis. Lastly, I'd like to thank to my new colleagues Laura, Ana, Sijo and Christian for their continued support.

My special and heartfelt feelings are to my family members who probably will not be here in my thesis defense, but they are always in my heart and in my thoughts. My grandmom Magda, mi little brother, "mis Batlle", my dear cousins, aunts and uncles. Mostly, my gratitude is to my parents, their hard work and dedication over the past 30 years have been the mainstay of my goals. Special thanks to my brother-in-law Dani who designed the beautiful cover for my thesis.

Finally, I would like to thank my husband, Fabricio Mulet Martinez, any of my achievements would not have been possible without your encouragement, self-sacrifice, patience, and love.

Declaration

I hereby declare that this thesis contains no material that has been used to obtain any other degree or certification. The co-authors of the publications arising from this work have waived their right to present them as part of another PhD thesis.

The research work for this thesis was carried out at the Institute of Advanced Materials (INAM), Department of Physics, Universitat Jaume I in Castellon de la Plana, Spain, under the direction of Prof. Dr Germà Garcia Belmonte who served as both supervisor - tutor and co-direction of Dr Antonio Guerrero.

Publications included in the thesis

1. **García-Batlle, M.**; Baussens, O.; Amari, S.; Zaccaro, J.; Gros-Daillon, E.; Verilhac, J.-M.; Guerrero, A.; Garcia-Belmonte, G. Moving Ions Vary Electronic Conductivity in Lead Bromide Perovskite Single Crystals through Dynamic Doping. *Advanced Electronic Materials*, **2020**, 6, 2000485.
<https://onlinelibrary.wiley.com/doi/10.1002/aelm.202000485>.
2. **García-Batlle, M.**; Deumel, S.; Huerdler, J.E.; Tedde, S.F.; Guerrero, A.; Almora, O.; Garcia-Belmonte, G. Mobile Ion-Driven Modulation of Electronic Conductivity Explains Long-Timescale Electrical Response in Lead Iodide Perovskite Thick Pellets. *ACS Applied Materials and Interfaces*, **2021**, 13, 35617–35624.
<https://pubs.acs.org/doi/abs/10.1021/acsami.1c06046>
3. **García-Batlle, M.**; Guillén, Jayen; Chapran, M.; Baussens, O.; Zaccaro, J.; Verilhac, J.M.; Gros-Daillon, E.; Guerrero, A.; Almora, O.; Garcia-Belmonte, G. Coupling between Ion Drift and Kinetics of Electronic Current Transients in MAPbBr₃ Single Crystals. *ACS Energy Letters*, **2022**, 7, 946–951.
<https://pubs.acs.org/doi/10.1021/acsenergylett.1c02578>
4. **García-Batlle, M.**; Zia, W.; Aranda, C.; Saliba, M.; Almora, O.; Guerrero, A.; Garcia-Belmonte, G., Observation of Long-Term Stable Response in MAPbBr₃ Single Crystals Monitored through Displacement Currents under Varying Illumination. *Solar RRL*, **2022**, 6, 2200173.
<https://onlinelibrary.wiley.com/doi/abs/10.1002/solr.202200173>
5. **García-Batlle, M.** Marisé García-Batlle, Sarah Deumel, Judith E. Huerdler, Sandro F. Tedde, Osbel Almora, and Germà Garcia-Belmonte, Effective Ion Mobility and Long-Term Dark Current of Metal-Halide Perovskites of Different Crystallinities and Compositions, *Adv. Photonics Res.* **2022**, 2200136.
<https://doi.org/10.1002/adpr.202200136>

This thesis has been accepted by the co-authors of the publications listed above that have waived the right to present them as part of another PhD thesis.

Publications not included in this thesis

1. Almora, O.; **García-Battle, M.**; Garcia-Belmonte, G. Utilization of Temperature-Sweeping Capacitive Techniques to Evaluate Band-Gap Defect Densities in Photovoltaic Perovskites. *The Journal of Physical Chemistry Letters*, 2019, 10, 3661–3669.
<https://pubs.acs.org/doi/10.1021/acs.jpcllett.9b00601>.
2. Ravishankar, S.; Riquelme, A.; Sarkar, S.S.; **García-Battle, M.**; Garcia-Belmonte, G.; Bisquert, J. Intensity Modulated Photocurrent Spectroscopy (IMPS) and its Application to Perovskite Solar Cells. *The Journal of Physical Chemistry C*, 2019, 123,41, 2499525014.
<https://pubs.acs.org/doi/10.1021/acs.jpcc.9b07434>
3. Caram, J.; **García-Battle, M.**; Almora, O.; Arce, R.D.; Guerrero, A.; Garcia-Belmonte, G. Direct observation of surface polarization at hybrid perovskite/Au interfaces by dark transient experiments. *Applied Physics Letters*, 2020, 116, 183503. <https://aip.scitation.org/doi/full/10.1063/5.0006409>
4. Ravishankar, S.; **García-Battle, M.**; Bisquert, J.; Garcia-Belmonte, G.; Odrobina, J.; Schiller, C.A. Removing Instability-Caused Low-Frequency Features in Small Perturbation Spectra of Perovskite Solar Cells. *The Journal of Physical Chemistry C*, 2020, 124, 15793–15799.
<https://pubs.acs.org/doi/10.1021/acs.jpcc.0c04050>
5. Deumel, S.; van Breemen, A.; Gelinck, G.; Peeters, B.; Maas, J.; Verbeek, R.; Shanmugam, S.; Akkerman, H.; Meulenkamp, E.; Huedler, J.E.; Acharya, M.; **García-Battle, M.**; Almora, O.; Guerrero, A.; Garcia-Belmonte, G.; Heiss, W.; Schmidt, O.; Tedde, S.F. High-sensitivity high-resolution X-ray imaging with soft-sintered metal halide perovskites. *Nature Electronics*, 2021, 4, 681–688.
<https://www.nature.com/articles/s41928-021-00644-3>
6. Almora, O.; Miravet, D.; **García-Battle, M.**; Garcia-Belmonte, G. Ballistic-like space-charge-limited currents in halide perovskites at room temperature. *Applied Physics Letters*, 2021, 119, 242107-1-6.
<https://aip.scitation.org/doi/10.1063/5.0076239>

**Abbreviations, acronyms, and chemical formulas
in alphabetical order**

AC	Alternating Current
AE	Activation Energy
AFM	Atomic Force Microscopy
Ag	Silver
Au	Gold
AVC	Antisolvent Vapor-Assisted Crystallization
BVM	Ballistic-like Voltage-Dependent Mobility
C_0	Reference linear capacitor
CB	Conduction Band
CC	Cooling Crystallization
$\text{CH}(\text{NH}_2)_2^+$	Formamidinium Cation
CH_3NH_3^+	Methylammonium Cation
Cs^+	Cesium Cation
D	Diffusion Coefficient
DC	Direct Current
DMF	<i>N,N</i> -Dimethylformamide
DMSO	Dimethylsulfoxide
DSVD	Dual-Source Vapor Deposition
E	Electric Field

ETL	Electron Transport Layer
eV	Electron Volt
ϵ_0	Permittivity Of Free Space
ϵ_r	Dielectric Constant
σ	Electronic Conductivity
FTO	Fluorine-doped Tin Oxide
FPD	Flat Panel Detectors
FWHM	Full Width at Half Maximum
GBL	Butyrolactone
$^1\text{H-NMR}$	Proton Nuclear Magnetic Resonance
HPGe	High-Purity Germanium
HTL	Hole Transport Layer
IDD	Ionic Dynamic Doping
I_{dark}	Leakage Current
IS	Impedance Spectroscopy
ITC	Inverse Temperature Crystallization
ITO	Indium Tin Oxide
J_{sc}	Short-circuit Density Current
j - V	Current-voltage measurement
L	Device Thickness
L_D	Diffusion Length
LEDs	Light Emitting Diodes

LSCM	Laser Scanning Confocal Microcopy
MAPbBr ₃	Methylammonium Lead Bromide
MAPbI ₃	Methylammonium Lead Iodide
MCs	Micro-Crystal
MTF	Modulation Transfer Function
<i>n</i>	Charge-Carrier Concentration
NIR	Near-Infrared
NORM	Naturally Occurring Radioactive Materials
μ	Carrier Mobility
μ_f	Octahedral Factor
OSPD	One-Step Precursor Deposition
PCE	Power Conversion Efficiency
PL	Photoluminescence spectroscopy
PSC	Perovskite Solar Cell
<i>q</i>	Electronic Charge
QDs	Quantum Dots
<i>Q</i>	Charge storage
SCLC	Space-Charge Limited-Current
SCs	Single Crystal
SDM	Sequential Deposition Method
SeC	Semiconductors
SEM	Scanning Electron Microcopy

SSG	Seeded Solution Growth
t_G	Goldschmidt Factor
τ	Carrier Lifetime
TENORM	Technologically Enhanced Naturally Occurring Radioactive Materials
TFT	Thin-Film Transistor
THz	Thera Hertz Spectroscopy
TID	Transient Ion Drift
TOF	Time Of Flight
UV-vis	Absorption spectroscopy
V	Voltage
VASP	Vapor-Assisted Solution Process
V_0	Voltage at the Reference Capacitor.
V_{App}	Voltage Pulse
V_X	Vacancies
XRD	X-ray diffraction
2D-XRD	Two-dimensional X-ray diffraction
ϕ	Work Function
Z	Atomic Number
Z'	Real part of impedance
Z''	Imaginary part of impedance

Abstract

Long-term stability of perovskite-based X ray detectors under working condition remains as the bottle-neck for technological purpose. Several effects are attributed to the presence of mobile ions in these materials such as shielding of the internal electrical field upon biasing and chemical interaction between intrinsic moving defects and electrode materials. As a matter of fact, high and instable dark current levels found in these devices are considered to be connected to ion migration upon polarization. However, it is still unknown how ion displacement alters the electronic current level, and which ionic transport parameters or ionic species determine the time-scale of the current evolution. Therefore, new insights for carrier transport mechanisms, including contact effects in addition to bulk conduction, is still needed due to the complex ionic-electronic nature of this material. In this work, different compositions of methylammonium lead bromide (MAPbBr₃) and methylammonium lead iodine (MAPbI₃) perovskites and structures (single- and micro-crystalline) are synthesized and tested by the analysis of the resistance evolution by impedance spectroscopy (IS) measurements and the investigation of current transient responses upon biasing. In addition to electronic features, our analysis of ion diffusion mechanism (short-circuit condition) and ion drift under an increasing electric field extracts values for the ion diffusivity in the range of $\sim 10^{-8} \text{ cm}^2 \text{ s}^{-1}$ and effective ionic mobilities in the order of $\sim 10^{-6} \text{ V}^{-1} \text{ cm}^2 \text{ s}^{-1}$, respectively. Additionally, dissimilar current responses are encountered for the bromide-based perovskite samples and the iodine ones presumably connected to the chemistry of the defect formation. Our findings corroborate the existence of a coupling between electronic transport and ion kinetics that ultimately establishes the time scale of electronic current. Since ion-originated modulations of electronic properties constitute an essential piece of knowledge to progress into the halide perovskite device physics, this thesis sheds light on the dark current issue by helping to clarify the ongoing debate about potential processes governing detector operation concerning long timescale functioning and current stabilization upon polarization.

Resumen

La estabilidad a largo plazo de los detectores de rayos X basados en materiales de perovskita de haluro en condiciones de operación, sigue siendo el cuello de botella para fines tecnológicos. Varios efectos son atribuidos a la presencia de iones móviles en estos materiales, entre ellos, el blindaje del campo eléctrico interno como resultado de la polarización y la interacción química entre los defectos internos en movimiento y el material de los electrodos. En efecto, los altos niveles de corriente en oscuridad de estos dispositivos se considera que están relacionados con la migración de iones bajo el efecto del campo eléctrico. Sin embargo, aún se desconoce como el desplazamiento de iones altera el nivel de la corriente electrónica, así como los parámetros de transporte iónico. Por lo tanto, aún se necesita un análisis apropiado para los mecanismos de transporte que tengan en cuenta los mecanismos de contacto además de la conducción interna debido a la compleja interacción iónico-electrónica. En este trabajo, se estudian diferentes composiciones de perovskitas y estructuras (monocristalinas y microcristalinas) de yoduro de plomo y metilamonio (MAPbI₃) y bromuro de plomo y metilamonio (MAPbBr₃). El análisis de la evolución de la resistencias extraídas en estas muestras, se realiza por espectroscopia de impedancia (IS) y la evaluación de los transitorios de corriente a tiempos largos se estudia bajo el efecto de un campo eléctrico creciente en oscuridad. Además de estudiar las características electrónicas de estos dispositivos, se profundiza en el mecanismo de difusión y deriva de iones, el primero bajo condición de cortocircuito (0 V-bias) y el segundo bajo un campo eléctrico variable. Estos experimentos de difusión y deriva de iones, permiten extraer valores para la difusividad de iones en el rango de $\sim 10^{-8} \text{ cm}^2 \text{ s}^{-1}$ y para las movilidades iónicas efectivas en el orden de $\sim 10^{-6} \text{ V}^{-1} \text{ cm}^2 \text{ s}^{-1}$, respectivamente. Asimismo, en el análisis de los transitorios de corriente se encuentran tendencias diferentes para las muestras de perovskita a base de bromuro en comparación con las de yoduro, lo que presumiblemente puede estar relacionado con la química de la formación del defecto. Es así como nuestros hallazgos corroboran la existencia de un acoplamiento entre el transporte electrónico y la cinética iónica que finalmente establece la escala de tiempo de la corriente electrónica. Una mejor comprensión del mecanismo de modulación de las propiedades electrónicas promovida por iones móviles constituye un paso esencial para avanzar hacia una mejor comprensión de la física de los dispositivos de perovskita de haluro. Por lo tanto, esta

tesis arroja luz sobre el problema de los altos niveles de corriente en oscuridad e intenta aclarar el debate en curso sobre los procesos que rigen el funcionamiento del detector en lo que respecta al funcionamiento a largo plazo y la estabilización de la corriente bajo polarización externa.

Table of Content

Chapter 1. Introduction	1
1.1 Style and motivation	1
1.2 Objectives	2
1.3 Radiation detection	2
1.3.1 Radiation sources and interaction with matter	3
1.3.2 General properties of radiation detectors	5
1.3.3 Technologies for X-ray detection.....	7
1.3.3.1 Current technologies for fast and efficiency X-ray detection: indirect conversion vs direct conversion	8
1.3.3.2 Scintillation detectors	9
1.3.3.3 Semiconductor detectors.....	10
1.3.3.3.1 Electrical contacts and leakage currents.....	12
1.3.3.3.2 Reverse biasing.....	13
1.3.4 Emerging Technologies for radiation detection	14
1.3.4.1 Perovskite materials for radiation detection	15
1.3.4.1.1 Chemical properties of Pb-halide perovskite compounds.....	16
1.3.4.1.2 Structural and defect features of metal halide perovskite	17
1.3.4.1.2.1 MAPbI ₃ vs MAPbBr ₃	18
1.3.4.1.3 Optoelectronic properties of Pb-halide perovskites	20
1.3.4.2 Metal Halide Perovskites Single Crystals (SCs).....	21
1.3.4.2.1 Growth procedures: Inverse Temperature Crystallization (ITC)	22
1.3.4.2.2 Properties of Metal Halide perovskite SCs	24
1.3.4.3 Metal Halide perovskite Micro-Crystals (MCs)	26
1.3.4.3.1 Mechanochemical synthesis of halide perovskite MCs	27
References	30
Chapter 2. Critical Overview	39
2.1 Chemical stability: structural issues in Metal Halide Perovskites Materials...	40
2.1.1 Device composition and architecture	40
2.1.2 Effects of Oxygen and Moisture	43
2.1.3 Effects of the Temperature and UV-light.....	47
2.2 Effect of the electrical bias	48
2.2.1 Dark current.....	51
2.2.2 Ion Migration.....	53
References	62
Chapter 3. Materials and Methods	71
3.1 Perovskite synthesis	71
3.1.1 Single crystal (SCs) growth.....	71
3.1.2 Soft-sintering procedure of Microcrystals (MCs).....	74
3.2 Device preparation	75
3.3 Structural characterization techniques	76

3.3.1 X ray diffraction (XRD).....	76
3.3.2 Scanning Electron Microcopy (SEM) imaging and Laser Scanning Microscopy.....	77
3.4 Optical characterization techniques.....	78
3.4.1 Photoluminescence spectroscopy.....	78
3.4.2 UV-vis absorption spectroscopy.....	79
3.5 Electrical measurements.....	80
3.5.1 Dark current-voltage characteristics.....	80
3.5.2 Impedance Spectroscopy.....	81
3.5.3 Long-term current transient experiments.....	84
3.5.4 Charging transient experiments.....	85
References.....	87
Chapter 4: Publication 1.....	89
4.1 Candidate's contribution.....	89
4.2 Brief summary.....	89
4.3 Published manuscript.....	90
4.4 Supplemental Information.....	109
Chapter 5: Publication 2.....	111
5.1 Candidate's contribution.....	111
5.2 Brief summary.....	111
5.3 Published manuscript.....	112
5.4 Supplemental Information.....	131
Chapter 6: Publication 3.....	139
6.1 Candidate's contribution.....	139
6.2 Brief summary.....	139
6.3 Published manuscript.....	140
6.4 Supplemental Information.....	157
Chapter 7: Publication 4.....	172
7.1 Candidate's contribution.....	172
7.2 Brief summary.....	172
7.3 Published manuscript.....	173
7.4 Supplemental Information.....	188
Chapter 8: Publication 5.....	196
8.1 Candidate's contribution.....	196
8.2 Brief summary.....	196
8.3 Published manuscript.....	197

8.4 Supplemental Information	218
General Conclusions.....	227
Conclusiones Generales.....	229
Future Outlooks.....	231
References	234

Chapter 1. Introduction

1.1 Style and motivation

The structure of this thesis is based on a journal article compilation style. This format implies that the thesis must be divided into several chapters. These chapters are based on a collection of published articles addressing the main aspects of the work carried out. The methodological framework is developed in *Chapter 1* reviewing the general properties of radiation detectors. In addition, the main objectives of the thesis are proposed addressing the structural features and optoelectronic properties of perovskite-based X-ray detectors. At the end of the chapter, the main advantages and disadvantages of these devices are presented and compared to the current conventional technologies. Next, *Chapter 2* describes a critical overview of the existing literature related to the field of perovskite based-X ray detectors, more specifically, the origin of the dark current and the processes that affect the long-term current operation stability. *Chapter 3* summarizes the experimental conditions, measurement protocols and the instrumentation setup used during the course of the research. *Chapter 4 to 8* show the achieved results with partial conclusions in the structure of the final version of the manuscript prior to publication (pre-print version) and the corresponding statement of contribution. Finally, in a general conclusion's chapter all findings are reviewed, and future outlooks are addressed.

Radiation detection is of great interest for broad applications such as: therapeutic, diagnostic healthcare, industrial inspection, and scientific research.¹⁻³ The last decade of intense research activity on lead-halide perovskites materials, firstly, in solar cells and light emitters devices, and recently as promising candidate for high-performance X-ray detectors have levered the outstanding optoelectronic properties of these materials.⁴⁻⁶ Although many efforts have been made to discern the origin of the chemical and electrical instability related to moisture and oxygen exposure on the one hand,⁷⁻⁸ and defect-induced ion migration,⁹⁻¹¹ which results in large instable dark current.¹²⁻¹⁵ There is still some debate on how ion migration governs the electronic current for the long-term operational stability of the radiation detector. Consequently, it is essential to further develop our understanding of fundamentals physics and device

structuring. This research work studies the influence of mobile ions in the dark current level in perovskite materials of different structure and crystallinity. The results in this thesis extend our understanding of the defect chemistry and prove a framework for the development of perovskite detectors with high dark resistivity and with long-term operational stability.

1.2 Objectives

The following points are the primary objectives of this project:

- i. Developing a well-controlled growth method and determining growth rates to obtain high quality single crystals of MAPbBr₃ perovskite.*
- ii. Design, fabrication, structural and optical characterization of micro and single crystalline perovskite devices based on MAPbI₃ and MAPbBr₃ for X-ray detection.*
- iii. Exploring the electrical performance and dark current stability of single-crystalline and micro-crystalline perovskites devices of MAPbI₃ and MAPbBr₃ perovskite.*
- iv. Investigating the ion migration in perovskite devices of MAPbI₃ and MAPbBr₃ and its role in the long-term dark current stability.*

1.3 Radiation detection

In general terms, radiation is the emission or transmission of energy in the form of waves or particles through a material medium. The traditional unit of radiation energy is the electron volt (eV), and relates the kinetic energy gained by an electron by its acceleration through a potential difference of 1 V.¹⁶ One of the many approaches used to classify different types of radiation is in terms of ionizing and nonionizing radiation. Nonionizing radiation is electromagnetic radiation with wavelength of about 10 nm or longer. This group includes radiowaves, microwaves, visible light, and ultraviolet light (See **Figure 1.1**). On the other hand, ionizing radiation has the ability to ionize an atom or a molecule (a process by which an atom acquires a negative or positive charge by gaining or losing electrons) of the medium and includes the rest of the electromagnetic spectrum (X and γ rays) with wavelength between $\lambda \sim 0.01$ -10 nm.

Ionizing radiation is generated in nuclear reactors, energy accelerators, in medical research and nuclear medicine.^{3, 16-17} However, naturally occurring radioactive materials (NORM) are also observed in the environment with very low activity concentrations of the radionuclides in rocks and soil.¹⁸ Moreover, technologically enhanced naturally occurring radioactive materials (TENORM) which are those natural radioactive material, in which the radionuclide concentration increases to levels above natural sources as a result of human activity have been studied in biochemical, geological, and environmental sciences for decades.¹⁹

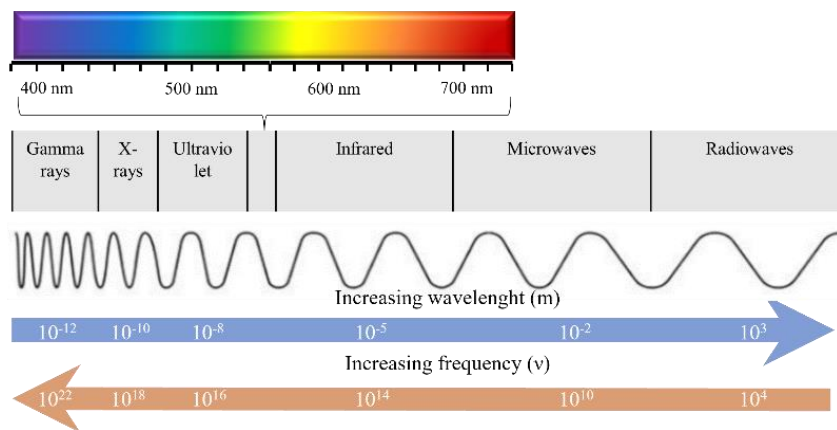


Figure 1.1. Electromagnetic spectrums in the range of the electromagnetic radiation frequencies with their respective wavelengths. Ionizing radiation possess the shorter wavelength and the higher energies to ionize atoms.

Ionizing radiation includes subatomic particles and electromagnetic waves: alpha (α), beta (β) and neutron particles and X and gamma (γ) rays. The mechanistic understanding behind the interaction of radiation (energy losses) as it moves through matter will depend on the radiation nature, energy, and material composition.³

1.3.1 Radiation sources and interaction with matter

One of the main properties of radioactive sources is their ability to penetrate through material's bulk. Each type of radiation interacts with matter in varying ways and each interaction holds a certain probability of occurring. Starting from α particles (large subatomic fragments consisting of ${}^4_2\text{He}$) that lose energy rapidly and interact with the

electrons or nucleus of the atoms in a material.²⁰ Monoenergetic α particles are highly ionizing and have low penetration depth, therefore can be shielded with a piece of paper (**Figure 1.2**). On the other hand, β particles (equivalents to electrons) are subatomic particles ejected from the nucleus of some radioactive atoms. The two forms of beta decay are the β^- and β^+ decay producing electrons and positrons respectively with a continuous spectrum of energy. Depending on the particle energy, they may travel up to about ~ 1 m in air and ~ 1 mm in tissue, thus they need to be shielded with aluminum, steel or plastic (**Figure 1.2**), which reduce the intensity of the radiation exponentially.^{16, 21} Remarkably when fast electrons interact with matter, part of their energy is converted into electromagnetic radiation in the form of *bremsstrahlung* (braking radiation). This last process is important in the production of X-rays from conventional X-ray tubes.^{18, 20}

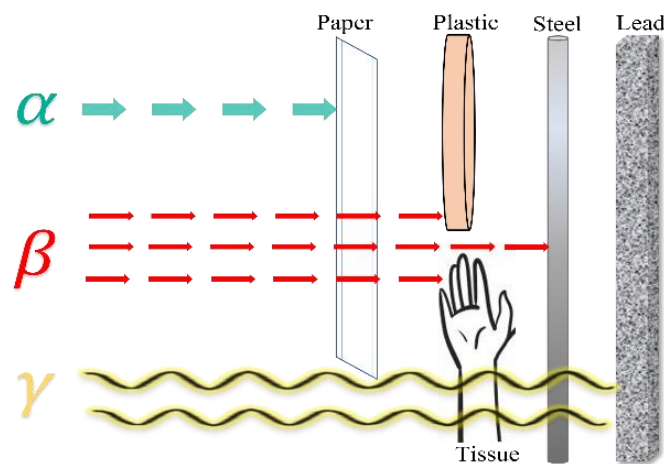


Figure 1.2. Interaction of ionizing radiation with matter. Penetration and ionization ability depends on the particle energy.

Finally, gamma radiation is characterized by not having mass nor charge and it is emitted by excited nuclei in their transition to lower-lying nuclear levels. γ -photons can travel longer distances in air and are often shielded by using materials with a high electron density, like Pb. γ -photons can be stopped in living tissue causing ionizations in the stopping tissue. Depending on the energy range, three different processes may occur when photons interact with matter: photoelectric effect ($E_\gamma < 0.1$ MeV), Compton effect or Compton scattering ($0.1 < E_\gamma < 1$ MeV) and creation of a pair of

electron and positron ($E_\gamma > 1.022 \text{ MeV}$), this process is represented in **Figure 1.3**. In the *photoelectric effect*, photons are absorbed in the material while in the *Compton effect* part of the energy of the photon is absorbed and the scattered photon moves on with lower energy. The *pair formation* happens when high energy photons interact with the nucleus and produces a pair of particles, an electron and positron. These two particles have the same mass, each equivalent to a rest mass energy of 0.51 MeV .^{16, 20} Today's modern radiation detectors have been designed based on those principles between interaction radiation-matter and ionization mechanisms. For the purpose of this thesis, in the next section, the general properties of radiation sensors specifically design for X-ray detection, are presented. Other types of radiation-matter interactions are not discussed because they are not part of the main objectives of the dissertation.

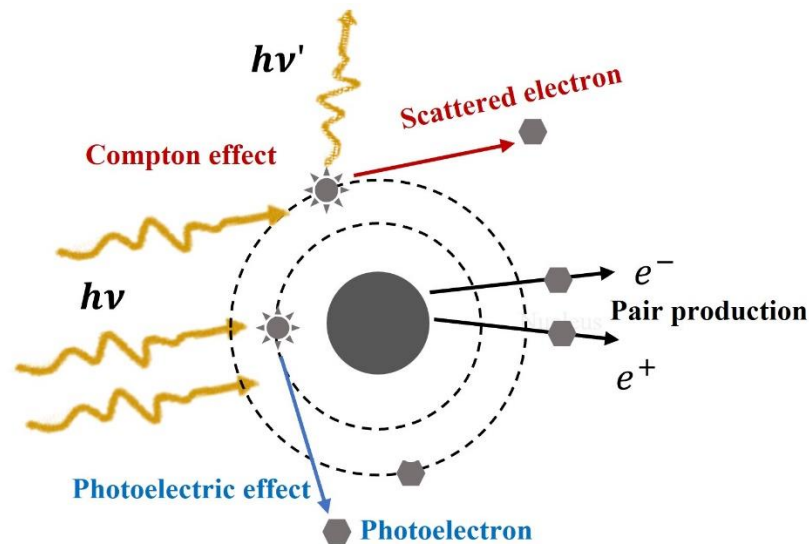


Figure 1.3. Representation of the main process of the interaction of γ -photons with matter.

1.3.2 General properties of radiation detectors

Radiation detectors rely on the measurement of the interaction of radiation with matter, because the probability of a charged particle going through a material without any interaction is zero.¹⁶ The main function of a detector is to produce a signal for every particle entering across the compound and most of the signal at the output of detectors is a current pulse. Overall, from the interaction of a single particle/radiation quantum with the detector, a charge may appear within the detector at initial time and

this charge must be collected to form the basic electrical signal. By imposing an electric field, the charge can be collected, and the positive and negative pair created flow in opposite directions.¹⁸ The time required to fully collect the charge varies from one detector to another. Therefore, for efficient detection, sensors used in radiation spectroscopy must have certain properties including:

- *Energy resolution*: is the parameter related to the detector response function to the energy of the detected particle or photon. In spectroscopy terms, it is conventionally defined as the full width at half maximum (FWHM) divided by the location of the peak centroid. The energy resolution R is expressed as a percentage (%).
- *Spatial resolution*: is the term referred to the number of pixels that are used to construct a digital image. For imaging application, a high spatial resolution is important in helping to discriminate between structures that are located within a small proximity to each other. The spatial resolution on a Flat Panel X-ray Detectors (FPD) is measure by the Modulation Transfer Function (MTF).
- *Detection efficiency*: is the factor related to the number of pulses counted per number of neutrons or photons incident on the detector N_C/N_E . The detection efficiency ϵ is a measure of the percentage (%) of radiation that a given detector detects from the overall yield emitted from the source.
- *Detective Quantum Efficiency (DQE)* is the parameter used to describe the combined effects of the signal (related to image contrast) and noise performance of an imaging system. The ideal detector would have a DQE of 1 (DQE 100% at all spatial frequencies), meaning that all the radiation energy is absorbed and converted into image information.
- *Sensitivity*: is the factor based on how efficiently radiation is converted into a useable signal. A highly sensitive detectors should improve the signal to noise ratio, resulting in superior measurement performance. Sensitivity is usually expressed as $\mu\text{C Gy}_{\text{air}}^{-1}\text{cm}^{-2}$ (1 Gy is the absorbed dose and is equal to 1 J/kg in the international System of Units (SI)).
- *Counting Speed*: is the time separation between two separate pulses. This parameter can be an issue when many pulses hit the detector per unit time and

for accurate counting measurements, sometimes, correction for these losses must be included.^{16, 22}

Today's standard commercial X-ray systems consist of either amorphous silicon backplane, photodiodes stacked with CsI scintillators and Flat Panel X-ray Detectors (FPD) or in solid-state conductors such as α -Se on Si backplane and CdTe. However, some limitations are reported in terms of sensitivity-resolution trade-off.²³⁻²⁴ The next section briefly describes different approaches used to convert X-ray radiation into an electrical signal presenting a new material for the radiation detection to overcome today's limitations in terms of detector efficiency, spatial resolution, scalability and cost effectiveness.

1.3.3 Technologies for X-ray detection

Detectors are classified according to how X-ray radiation is converted into electrical pulses. In most operating X-ray detector systems, the X-ray photons are first converted into visible light by means of a scintillator material (**Figure 1.4**, left panel), which in turn requires a photodetector to convert the visible light to an electric charge.^{22, 25-26} This process is called indirect conversion and the X-ray to light conversion in the scintillation layer will present a trade-off between the detector efficiency, which needs thick layers to efficiently absorb X-rays, and the spatial resolution for which thin layers are necessary to reduce optical cross talk. Alternatively, a simpler approach is to convert X-ray radiation directly into an electrical signal, as this requires a simpler system configuration providing higher spatial resolution (**Figure 1.4**, right panel), these detectors use direct readout by means of a thin-film transistor array. The process of direct conversion enables a high spatial resolution but some of the available materials as amorphous selenium (α -Se), suffers from poor detector efficiency due to its low atomic number and low absorption for high X-ray energy ranges. The next section addresses some of the advantages and disadvantages of the two different modalities for X-ray detection.

1.3.3.1 Current technologies for fast and efficiency X-ray detection: indirect conversion vs direct conversion

Indirect conversion using scintillation crystals as Cesium Iodide (CsI), converts X-rays into visible light at a first stage system.²⁷ The use of a two-stage techniques for conversion may entail that light is converted at a second stage into an electric charge by means of an amorphous silicon photodiode array. On the other hand, the conversion process of the X-ray beam by *direct conversion* come up in one step and using an X-ray photoconductor. One example of an X-ray photoconductor can be α -Se, this material directly converts in one stage X-ray photons into electric charges.²⁸⁻²⁹ Discerning between the most reliable configuration is not easy although the indirect conversion technology developed in the 80's is now well established, and no significant further technological improvement is expected to occur any longer.

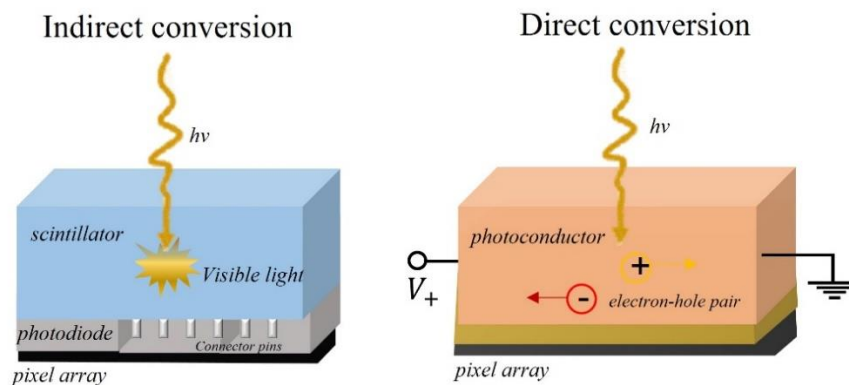


Figure 1.4. Schematic draw of the process of conversion of X-rays into light in a scintillator-based detector (indirect conversion) and into electrical signal in a semiconductor detector (direct conversion).

Therefore, direct conversion has been developed as a suitable alternative in comparison with the conventional indirect ones. The advantages of modern direct converters are numerous: a high effective atomic number that leads to excellent photo-absorption efficiency, high resistivity $>10 \text{ M}\Omega \text{ cm}$ of the material, being a suitable choice when employed for room temperature applications.¹³ Furthermore, they are compatible with compact size and high spatial resolution. Moreover, the low leakage

current (dark current) found on these devices is associated to an excellent energy resolution.^{12,30} As far as disadvantages is concerned, charge trapping²⁹ has been found to promote undesirable effects when the material is employed in high X-ray applications. Therefore, continuous improvement is required in the optimization of all the technical factors for X-ray detection and imaging acquisition. The improvement of both the detector efficiency and the spatial resolution is a crucial point through the increment in the signal-to-noise ratio (SNR). In X-ray imaging and detection of small-low-contrast structures those positive features enable a precise and early diagnosis with an accurate management of the patient's dose.³¹

1.3.3.2 Scintillation detectors

The “ideal” material used as scintillator (indirect convertors) should possess a high scintillation efficiency to convert the kinetic energy of charged particles into detectable light and a linear conversion (light yield must be proportional to the energy deposited). In terms of light collection, the material must be transparent to the wavelength of its own emission to collect fast signal pulses and the decay time of the induced luminescence should be as short as possible. The material should also have a good optical quality and must be compatible with processes for large size with the purpose of designing a practical detector. Lastly, the index of refraction should be ~ 1.5 (like glass) to permit efficient coupling of the scintillation light to a photomultiplier tube or other light sensor.

Figure 1.5 shows the bandgap energy of some iodide-based commercialized scintillators that have been popular for many years thanks to their small bandgaps and high light yields. The light yield is defined as the number of photons (N_p) in scintillation per 1 MeV energy radiation absorbed by scintillator.^{4,32}

Despite many years of improvements, nonproportionality of scintillators is one of the important limiting factors for improving energy resolution. Therefore, the use of direct semiconductor materials has emerged as a suitable alternative for increasing the energy resolution.

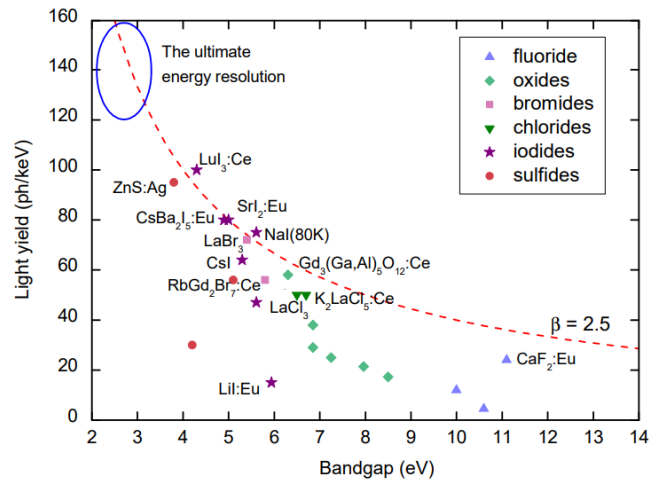


Figure 1.5. Light yield versus the bandgap energy E_g of different scintillators detectors with theoretical limit (dashed line). Reprinted with permission.³² Copyright 2022, Springer International Publishing

1.3.3.3 Semiconductor detectors

Semiconductor (SeC) detectors (direct convertors) offer a great energy resolution, good absorption, and high sensitivity. As a result of the interaction of X-rays with the semiconductor material, electrons are excited from valence bands to high energy states. Those high energy electrons are rapidly thermalized to conduction band minimum generating pairs of electrons and holes for a given incident radiation event. The motion of the electron-hole pairs (EHP) as a result of the bias voltage, generates the basic electrical signal from the detector.¹⁶ The energy needed to produce an EHP in a SeC is typically about 2–10 eV, which is considerably less than that required to produce ionizations in air, therefore, a relatively large number of charge carriers is produced for each photon absorbed. Many SeC detectors are operated under high electrical field values, producing saturated velocities on the order of 10^7 cm/s. Then, for a typical SeC detector of ~ 0.1 cm thickness, the charge collection times will be close to 10 ns, so this kind of detector is considered one of the fastest responding of all radiation detector types.^{31, 33} SeC X-ray detectors have two types of work modes: current mode and voltage mode. The first configuration is commonly used for dose rate measurement or imaging contrast applications. In contrast the voltage mode is applied to photon counters or energy spectroscopy of X-ray. The analysis of the

electrical response for a radiation detector is a complicated process; one of the central parameters to study transport and collection of carriers is the product of carrier mobility and carrier lifetime ($\mu\tau$), which represents the mean distance drifted by the carrier per unit electric field before the carrier disappears by recombination or trapped by defects.³⁴

Conventional technologies of direct conversion of X-rays, are based on silicon³⁵ and germanium elements.³⁶ The resolution energy of these detectors is better than the scintillation ones but deep impurities acting as recombination center can be found. Additionally, structural defects such as vacancies or interstitials defects tend to behave as acceptors or donors leading to charge carrier losses within the crystal lattice. For hard X-rays experiments, SeC materials of high atomic number are required and today's most common materials used are Gallium arsenide (GaAs), Cadmium Telluride (CdTe) and Cadmium Zinc Telluride (CZT).³⁷ **Table 1.1** summarizes some of the benefits and drawbacks of the conventional technologies for X-ray detection. In the case of the carrier lifetime product, it has been reported a values of $\mu\tau \sim 1 \text{ cm}^2 \text{ V}^{-1}$ for Si detectors³⁸⁻³⁹ while for CZT⁴⁰⁻⁴¹ and α -Se sensors,^{24, 42} values oscillate between 10^{-5} to $10^{-2} \text{ cm}^2 \text{ V}^{-1}$ and 10^{-7} to $10^{-6} \text{ cm}^2 \text{ V}^{-1}$ respectively.

Table 1.1 Summary of the advantages/disadvantages of the state-of-the-art materials involved in X-ray detection

Scintillation counters (indirect conversion)		Semiconductors detectors (direct conversion)	
Advantages	Disadvantages	Advantages	Disadvantages
High sensitivity capacity ²⁵	Hygroscopicity ²⁷	High atomic numbers ^{31, 43}	Usually needs to be cooled (thermal noise) ³⁶
Possible high precision and counting rates ¹⁸	Poor low-energy gamma response.	Very good energy resolution and fast response ⁴⁴	Usually requires very high purity materials ^{36, 44}
Spectroscopy (intensity of the flashes are proportional to the energy of the radiation) ³²	Liquid scintillators are relatively cumbersome	Large Crystals (total absorption detector)	Higher prices

Major challenges for the development progress of these materials are therefore linked to the crystal uniformity and the defect dynamics affecting the sensor performance. At the end, some requirements must be fulfilled to efficiently collect electric charges in a practical SeC-based radiation detector. The next two sections focus on some of this critical means that needs to be considered in order to obtain reliable data.

1.3.3.3.1 Electrical contacts and leakage currents

Electrical contacts allow electrical current to be collected from the detector. Depending on the final application, different electrodes can be selected such as nonrectifying (ohmic contacts) or blocking electrodes. The work functions of the contacts will control the open-circuit potential, establishing the fundamental operating mechanisms within the device.^{26, 34, 45} To collect charge at the outer electrodes, an applied voltage of typically hundreds or thousands of volts is imposed across the device¹⁶ and if non-injecting electrodes are used, then, the steady state leakage current can be reduced.⁴⁴ In an X-ray measurement the configuration of the radioactive source and shielding elements are also crucial. The linear attenuation coefficient (μ_a) is the magnitude that describes the fraction of attenuated incident photons in a monoenergetic beam per unit thickness of a material.⁴⁶

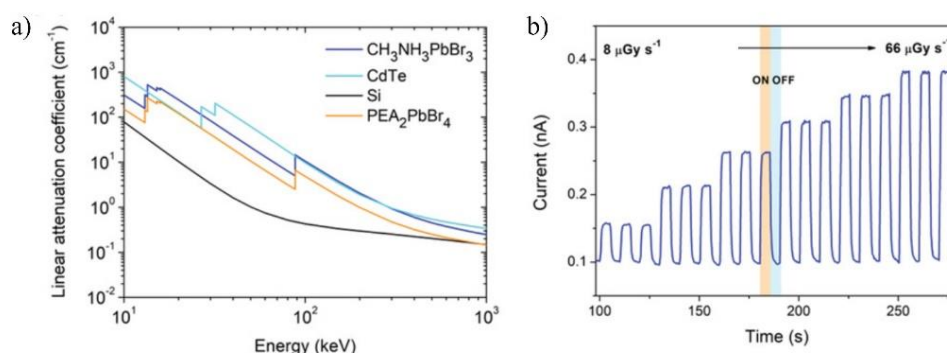


Figure 1.6. Example of the electrical response to X-rays. a) Comparison between the different linear attenuation coefficient of some benchmark materials as a function of photon energy. b) Dynamic X-rays response under X-rays with 150 kVp accelerating voltage (80 V bias). Noted the current exhibits a fast box-like response to X-rays Reprinted with permission.⁴⁷ Copyright 2021, Wiley Online Library.

Figure 1.6 shows the (μ_a) of different materials used for ionizing radiation detection together with the dynamic response of the measured photocurrent in a conventional microcrystalline perovskite sample under X-rays at 150 kVp with dose rates ranging from 8 to 66 $\mu\text{Gy s}^{-1}$ and 80 V applied bias.⁴⁷

In an X-ray detector, the dark current under bias should be negligibly small. This parameter can be related to both the bulk or surface of the detector and should preferably not exceed the 10-pA mm^{-2} , depending on the application it can affect the resolution and reliability of the device. In fact, for medical applications, the leakage current must not go over ~ 10 nA to prevent resolution losses.³¹ A small dark current implies that the contacts to the SeC should be non-injecting, and the rate of thermal generation of carriers from various defects or states in the bandgap should be negligibly small. However, if any hysteretic behavior is observed during the characteristic j - V measurements a more detail inspection has to be performed.⁴⁸⁻⁴⁹ In a radiation detector based on metal halide perovskites (**Section 1.3.4**) this hysteretic behavior will depend on the scan rate, and the sweep direction of the applied bias.

1.3.3.3.2 Reverse biasing

In SeC-based radiation detectors achieving a low dark current may be challenging. In pulse mode radiation detectors are connected to external voltages sources to make a successful charge carries collection process.¹⁶ Common procedures of measurement are based in p-n junction using rectifying elements. In that configuration the flow of current will present a large resistance in one direction compared to the opposite one. By applying a reverse direction pulse, the device will conduct less dark current showing an improved temporal stability of the material and a lower detection noise.^{15, 17, 50} Previous reports shown how by using a combination of low work function metals as Ga ($\phi = -4.1$ eV) and a large work function as Au ($\phi = -5.1$ eV) the final device configuration Ga/CsPbBr₃/Au presents a low reverse leakage current density (**Figure 1.7**), of only 10 nAcm⁻² under reverse bias at a high electric field (-200 V, corresponding to 2000 V cm⁻¹).⁴³⁻⁴⁴ Other options of low-work function materials can be Al, Ga, Cr and In, but also organic polymeric layers, fullerenes or inorganic electron extraction layers such as ZnO, TiO₂, and MoO₃ and metal salts (LiF).⁵¹

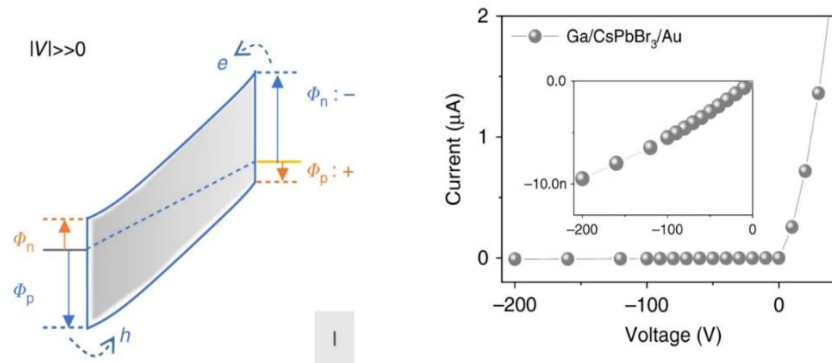


Figure 1.7. Band diagrams a Ga/CsPbBr₃/Au detector under large reversed electric fields. Note that the +, - and ϕ_n and ϕ_p represent the forward and reversed bias and Schottky barrier for electron and hole at the semiconductor–metal interface, respectively. Reproduced with permission.⁴³ Copyright 2020, Springer Nature.

1.3.4 Emerging Technologies for radiation detection

Future applications of an improved X-ray detection systems may be extended to other emerging family of semiconductors. Indeed, for effective absorption of X-rays, materials with heavy elements and high average atomic numbers must provide absorbing layers with high dark resistivity, low defect density and high carrier mobility–lifetime ($\mu\tau$) product to maximize the collection efficiency of the ionized charges. In the field of SeC devices for X-ray detection, high-purity germanium (HPGe) constitute the gold standard in terms of high-spectral-resolution applications. However, its superior semiconductor properties are affected if low temperatures of liquid nitrogen (-196°C) are not used to minimize leakage current due to its small bandgap energy.³⁶ Amongst single-crystalline semiconductors CdZnTe, is well-known. This material is grown around 800°C increasing the possibility of thermal stress cracking in the SCs and raising the cost of the crystal growth.²⁷ Fortunately, a next generation of solid-state semiconductors devices based on metal halide perovskites materials has been develop presenting high crystalline, reasonable defect tolerance and excellent long carrier lifetime.²⁷ As perovskite compounds present outstanding optoelectronic properties they have revolutionized almost all fields of material science and industry (**Figure 1.8**). The unprecedented progress from fundamental properties to device engineering is still driving extensive research and

development efforts, from solar cells,⁵²⁻⁵³ light emitters devices,⁵⁴ to key materials in fuel cells⁵⁵ and electrodes for water electrolyzers.^{6, 56} In the next section we will introduce metal halide perovskites materials as a new class of raw material for X-ray imaging and ionizing radiation detectors.

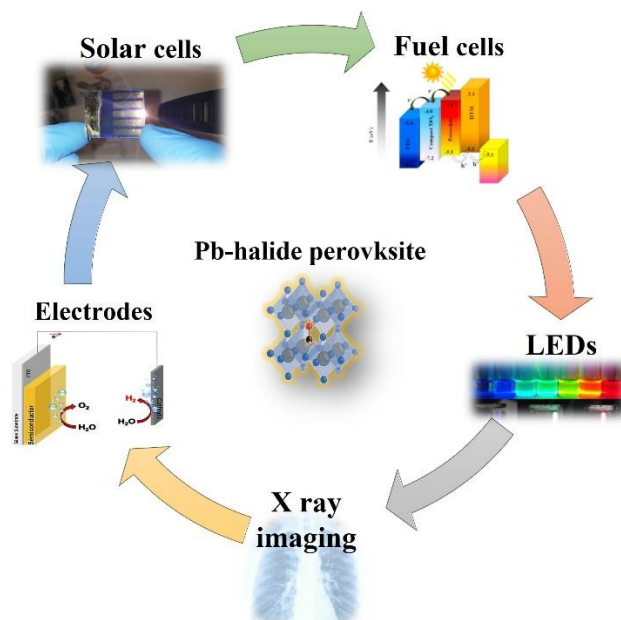


Figure 1.8. Example of the versatility and numerous applications of perovskite materials in different fields. From light emitting devices to sensor and X-ray detectors Adapted with permission.²⁷ Copyright 2022, Springer Nature.

1.3.4.1 Perovskite materials for radiation detection

Perovskite-structured materials were discovered in the 1830s but only in the last decades their rich physical properties have been deeply explored.⁵⁷⁻⁵⁸ Recent reports have evidenced the outstanding performance of metal halide perovskites, specifically, the Pb-based ones, in the field of radiation detection. They present a strong stopping power (high Z number, $Z(\text{Pb}) = 82$) and radiation hardness. In addition, their long charge carrier diffusion lengths ($>10 \mu\text{m}$) and low trap densities ($10^9 - 10^{10} \text{ cm}^{-3}$) allows to maximize the product of the charge mobility and carrier lifetime by minimizing the bulk/surface defect density and promoting a good charge collection efficiency.^{2, 59-60} Additionally, Pb-perovskites-based X-rays detectors can be prepared with low-cost raw materials using non sophisticated preparation methods from solution.^{33, 61-62} In the next section we elucidate the relationship among the chemical

structure, device composition, device architecture, charge-carrier transport properties, and long-term operation mechanism. In the last section, we discuss the state-of-art for preparing single and micro crystals samples of Pb-halide perovskites with different compositions.

1.3.4.1.1 Chemical properties of Pb-halide perovskite compounds.

As shown in **Figure 1.9** the chemical formula of perovskites compounds is ABX_3 in which A is a cation (it can be inorganic or organic), B is a metal ion and X is an anion that bonds to both A and B cations. The A cations are usually larger than B atoms, forming the “ideal” cubic structure in which A is surrounded by a BX_6 octahedra.⁶³ Numerous distortions can happen in the structure because of the cation size and the flexibility of the bonding angles.^{52, 64} Nonetheless, very stable structure can be formed by controlling the composition and via phase transition engineering. The versatility of the chemical composition offers countless possibilities, tuning the chemistry of the constituents will dictate the ionic radii of the atoms in the structure.

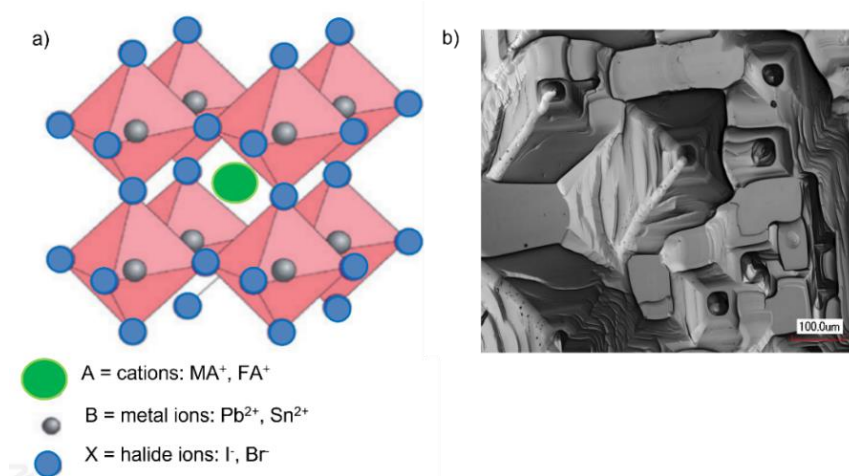


Figure 1.9. a) General ideal crystal structure of a generic perovskite materials. Adapted with permission.⁶⁴ Copyright 2014, Nature Publishing Group b) Image of the top view of a perovskite compound by Laser Scanning Microcopy showing a nonhomogeneous morphology of the surface.

The tolerance factor, also known as the Goldschmidt factor, t_G specifies the atoms that can fit in the perovskite structure without compromising the lattice stability. t_G can be calculated from the ratio of the ionic radii as:⁶⁵

$$t_G = \frac{(r_A + r_X)}{\sqrt{2}(r_B + r_X)} \quad (1.1)$$

Where r_A , r_B and r_X are the ionic radii of the A cation, B-site metal, and X anion, respectively.

The acceptable tolerance factor range for Pb-halide perovskite compounds goes from 0.8 to 1, in fact, below 0.8 and above 1, perovskite structure will lose symmetry and will get distorted. In **Figure 1.10** one can observe the tolerance factor value calculated for different perovskite compositions.

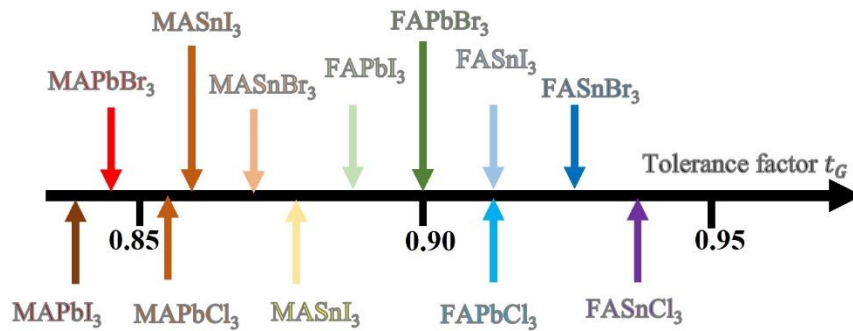


Figure 1.10. Tolerance factors values (t_G) of various halide perovskites. Adapted with permission.⁶⁵ Copyright 2016, The Royal Society of Chemistry.

As can be noted all lead-free perovskite presented a distortion factor $0.92 < t_G < 0.95$ which is still acceptable for the lattice stability. Also of importance is the geometrical elements known as the octahedral factor $\mu_f = r_B/r_X$, when $\mu > 0.42$, the structure is stable, and a balanced close packed cubic perovskite can be designed.

1.3.4.1.2 Structural and defect features of metal halide perovskite

The family of halide perovskites ($X = \text{Cl}^-$, Br^- , I^-) presents remarkable semiconducting properties which make them suitable for a wide range of optoelectronic applications. The cation B in the structure is typically a bivalent metal from the carbon group (group 14) of the periodic table usually: Pb^{2+} , Ge^{2+} and Sn^{2+} . Amongst these three metals, lead (Pb^{2+}) offers the better performance in optoelectronic devices, being relatively stable in air against oxidation.^{53, 66-67} We next present the intrinsic properties of Pb-halide perovskites, specifically the atomic interactions, creation of defects and its role for device performance.

A series of stability issues have been found in these devices. Most studied perovskites are microcrystalline and during the synthesis process, defects and grain boundaries are formed which cause significant carrier losses, due to the formation of recombination sites.⁶⁸ Other example of its peculiar properties is the hysteresis. The hysteresis is observed when measuring the current of the solar cell under a voltage sweep at a constant velocity and the forward and reverse scans do not match. This phenomenon has been connected, among other reasons, to ion migration and the modification of electronic barriers at the interface.⁶⁹⁻⁷¹ Hysteretic currents have been related to typical capacitive charging and discharging effects,⁷² electrode polarization⁶⁷ or can be connected to the nature of contact materials, degradation reactivity effects at the electrodes or excess ions as interstitial defects in the case of the non-capacitive currents.⁷³⁻⁷⁵ Another remarkable feature is the ferroelectric behavior observed in these compounds, the existence of dipole-like structure has been found to affect the material symmetry and the charge carrier extraction.⁷⁶⁻⁷⁷ The large dielectric constants⁷⁸ has also been also explored in halide perovskites, many reports found these features to be a result of the microstructural networks⁷⁹ or even induced by structural fluctuations of the perovskite cell, and the rotation of the polar CH_3NH_3^+ cation.⁸⁰ Moreover, their ambipolar characteristic and high charge carrier mobilities has been also examined for halide perovskite transistor applications.⁸¹ It has been stated that crystallographic defects in MHPs do not form deep level traps,^{10, 82-83} and dominant intrinsic defects create only shallow level trap.⁸⁴ Certainly, they exhibited superior defect tolerance which make them ideal for optical and electrical measurements.⁵⁷ On the other hand, semiconductors based on lead-halide do not require high-temperature and high vacuum processing compared to traditional inorganic semiconductor devices.³⁵ The next section discusses how the optoelectronic properties of MHPs can be altered by halide substitution in the structure.

1.3.4.1.2.1 MAPbI_3 vs MAPbBr_3

Methylammonium lead iodide (MAPbI_3) has been the benchmark system for many years and several reports showed its versatility as light absorber together with its

exceptional charge transport properties.^{33, 85-87} However, its poor environmental stability has brought the development of alternative compositions.^{11, 88-89} Because the stability of metal halide perovskites is composition-dependent, methylammonium lead bromide (MAPbBr₃) has been extensively studied.^{11, 60, 90-91} Theoretical calculations predict a stronger Pb–Br bond for MAPbBr₃ that might increase the halide ion defect formation energy.¹¹ There are numerous structural distinctions between both compounds: (i) at room temperature, the tetragonal I4/mcm phase is described for MAPbI₃ while a cubic perovskite structure phase Pm $\bar{3}$ m is registered for MAPbBr₃ (see **Figure 1.11a**) (ii) using the Goldsmith factor and the ionic radius of 2.2 Å and 1.96 Å, for I⁻ and Br⁻ respectively, a more favorable cubic structure is predicted for Br-based⁶⁵ (iii) the long-term environmental stability for MAPbBr₃ under higher electric fields has shown great potential for perovskite radiation detectors^{60, 92} (iv) the different band gap energies 1.5 and 2.3 eV for MAPbI₃ and MAPbBr₃, respectively.

Figure 1.11b shows the higher bandgap of MAPbBr₃ compared to MAPbI₃ perovskite, hence Br-based devices showed a lower power conversion efficiency when the compound is used in a solar cells and light emitting devices.⁹³⁻⁹⁴ In terms of optical properties the light emission peaks in a photoluminescence measurements (PL experiments) appears around 550-580 nm and 780-800 nm for bromide and iodide-base material, respectively..

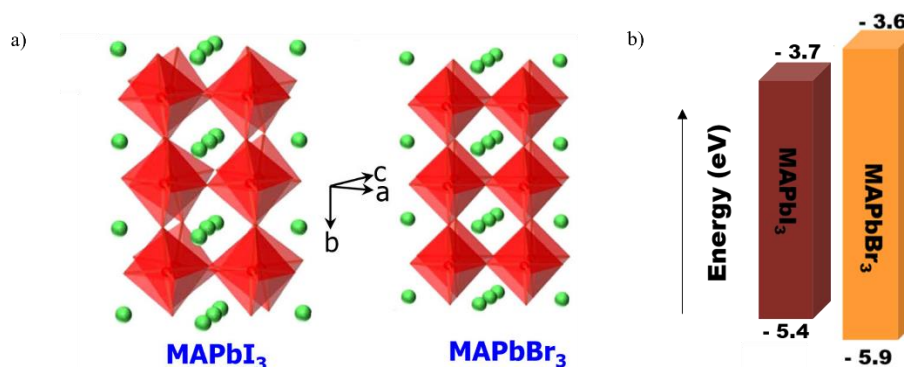


Figure 1.11. a) Distorted tetragonal perovskite structure of MAPbI₃ at room temperature and cubic perovskite structure of MAPbBr₃ at room temperature. Red: polyhedron [PbX₆²⁻] (X = I, Br); green sphere: CH₃NH₃ = MA. Adapted with permission⁹⁵ Copyright 2013, American Chemical Society (b) The conduction band (CB) and valence band (VB) of MAPbI₃ and MAPbBr₃.

Moreover, it is important to mention that some degradation mechanisms have been reported for MAPbI₃ caused by ion migration of the iodine vacancies (lower activation energy and reduced diffusion coefficient).^{11,83} Realizing this difference in halide migration is a crucial step in understanding the enhanced stability of MAPbBr₃ versus MAPbI₃.

1.3.4.1.3 Optoelectronic properties of Pb-halide perovskites

So far, we have shown how the chemical composition dictates the crystal structure and stability of Pb-halide perovskites. However, some of the most attractive properties of these materials rely on tuning its bandgap. The color of halide perovskites can be tuned from the visible to the near-infrared (NIR) region.⁹⁵⁻⁹⁶ Depending on the perovskite composition a stronger light emission is observed in PL measurements. Chloride perovskites show a violet-blue emission, bromide samples exhibit a well-known green emission and iodide samples display deep-red close to NIR emission.⁵³ Pb-halide perovskites, as direct bandgap semiconductors⁹⁷ are efficient charge-transport layers for multifunctional optoelectronic devices. In a radiation detector, the charge carrier transport properties are commonly evaluated by the mobility-lifetime ($\mu\tau$) product. Enhancing the carrier mobility and charge transport properties by suppressing the formation of deep-level defects plays a vital role on these devices.⁹⁸ Therefore, charge carrier dynamics has been extensively studied. The diffusion coefficient (D) and carrier mobility (μ) (See equation 1.2), which are related through the Einstein relation, are the main parameters extracted in free carrier dynamics reports^{87, 99-101}

$$\mu = \frac{qD}{k_B T} \quad (1.2)$$

where q is the electronic charge, k_B is the Boltzmann constant and T is the temperature. Another important parameter is diffusion length L_D which is related to the carrier mobilities as $L_D = \frac{k_B T \mu \tau}{q} = (D\tau)^{1/2}$ where τ is the carrier lifetime.¹⁰² As predicted from the last relation a high mobility and long lifetime of charge carriers

implies a long L_D , which is an important requirement for perovskites to be an efficient charge transport layer.⁵³ Diffusion length can be quantified (on the order of 1–100 μm) by time transient methods¹⁰³ and carrier mobilities can be determined by a range of techniques such as: Hall effect,¹⁰⁴⁻¹⁰⁵ space-charge limited-current (SCLC),¹⁰⁶⁻¹⁰⁸ THz frequency measurements,¹⁰⁰ etc.

As it has been demonstrated,^{27, 45, 47, 109} unlike traditional semiconductors, perovskite possesses a superior defect tolerance, most crystallographic defects in halide perovskites do not form deep levels due to its unique band structure and ionic lattice. Moreover, halide perovskites benefit from low-cost wet chemistry techniques at relatively low temperatures without affecting their remarkable optoelectronic properties. The next section focuses on how halide perovskites can be prepared from solution process in a variety of structures such as: single crystal and microcrystalline films. Moreover, crystallization process, fundamental properties and applications are presented.

1.3.4.2 Metal Halide Perovskites Single Crystals (SCs)

A single crystal (SCs) is a material in which the crystal lattice is continuous and unbroken (**Figure 1.12a**). In this crystal network, the absence of grain boundaries allows to have a long-range atomic order with low defect densities ($\sim 10^{10} \text{ cm}^{-3}$).^{82, 110} For a SCs all symmetry operations are equal for the whole single crystalline body. This means that when performing an operation on the body of the SCs, if the body becomes indistinguishable from its initial configuration it is said to possess a symmetry element.¹¹¹ This unique chemical structure distinguishes SCs from microcrystalline samples. A SCs often consists in repeated patterns or regions with a slightly misoriented distribution. On the other hand, a microcrystalline (MCs) material consist on a small regions of the order of micrometers but randomly distributed without a preferred orientation (**Figure 1.12b**).¹¹² Grain boundaries (GBs) which are the interface between two individual homophase crystal grains of the same material that are generally oriented in different crystallographic directions, will determine many of the properties of the material.

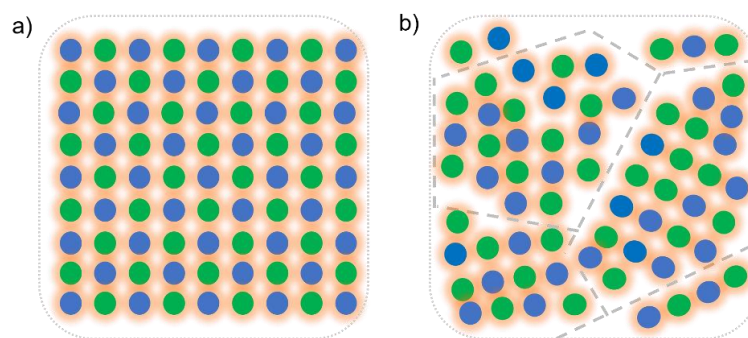


Figure 1.12. a) Example of the periodic pattern a) across the whole volume for a generic Single-crystal b) across each grain or grain boundary for a micro-crystal

Several methods have been used to grow single crystals from the microcrystalline substance^{59, 113} and X-ray diffraction measurements (XRD) has been used to prove the signature of a single crystalline structure with the existence of Bragg spots in the 2D diffraction pattern of the pure phase perovskite. Other methods such as Scanning Electron Microscopy (SEM) and Atomic Force Microscopy (AFM) reveal information about the surface morphologies, chemical composition, and crystalline shape and orientation (See **Chapter 3: Materials and Methods** for more information about the structural characterization methods).

1.3.4.2.1 Growth procedures: Inverse Temperature Crystallization (ITC)

Crystallization is a process which typically involves two consecutive steps: first, the formation of the nucleus of a small particle (nucleation process) and second, the successive growth of this nucleus into a larger crystal. In **Figure 1.13** the time scale of the different crystallization methods is shown. In the case of the synthesis of metal halide perovskite SCs, various solution-based crystallization methods have been developed such as: Seeded Solution Growth (SSG),^{99, 114} Antisolvent Vapor-assisted Crystallization (AVC),^{59, 115} the Cooling Crystallization (CC),¹¹⁶⁻¹¹⁷ and retrograde solubility or Inverse Temperature Crystallization (ITC).^{62, 112} A *classical cooling crystallization* uses low temperatures, and the crystalline phase is formed upon cooling of the solution. One crucial parameter is the cooling rate, after weeks or months, large crystals of MAPbI₃ has been grown using the CC procedure.¹¹⁷

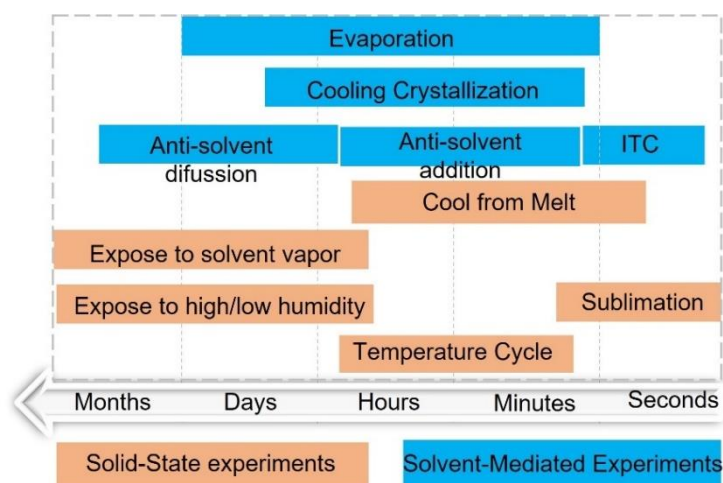


Figure 1.13. State-of-art growth protocols for the preparation of halide perovskite SCs. Adapted with permission¹¹⁸ Copyright 2008, Elsevier.

The *seeded solution growth* is similar to the CC methodology, but in this case, the use of seed crystals placed at the top of the solution enables a mass transfer and subsequent growth into larger crystals. In *antisolvent vapor-assisted methods*, an antisolvent vapor is immersed into the perovskite solution to create a supersaturated state and to promote the crystallization. Despite the high quality observed in crystals grown by this procedure, the process is usually very slow, it can take days to months.¹¹⁵ Despite the fact that all these growth methods allow the synthesis of single crystals with almost the same optical and electronic properties, some of them, require days and or spend even weeks.⁵⁹

One alternative to these conventional methodologies is the *Inverse Temperature Crystallization (ITC) method*. With this procedure, sizable single crystals have been grown within a few hours (See **Figure 1.14a**).

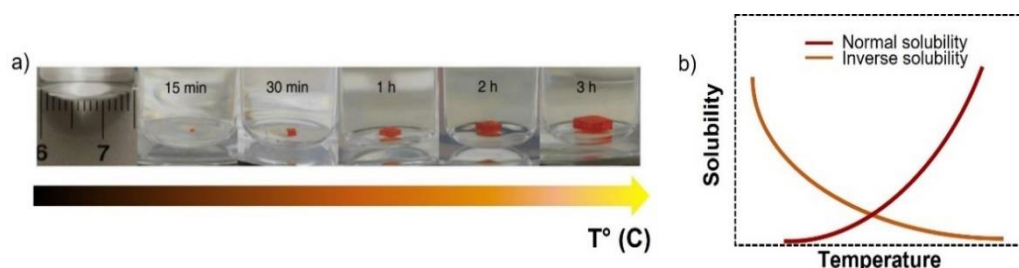


Figure 1.14. a) Growth steps by ITC method of a MAPbBr₃ perovskite SCs. b) Solubility behavior of 1M solution of MAPbBr₃ in DMF (dark-red line) and in HBr_(ac) (orange line) as a function of the temperature. Adapted with permission,⁶² Copyright 2015, Springer Nature.

ITC is based on the retro-solubility property of halide perovskites in certain organic solvents. This implies selecting a proper organic solvent in which the solute may dissolve less when increasing the temperature.^{61, 119} Several reports used the ITC methodology for high repeatability experiments.^{62, 120} Amari et al., showed a high quality SCs of bromide based-Pb-halide perovskite grown by this methodology.¹¹¹ In a typical procedure MAPbI₃ SCs are grown in 1 M solutions of precursors using butyrolactone (GBL) at 90-100° C,^{59, 112} while Br- and Cl based perovskites are grown at lower temperatures in *N,N*-dimethylformamide (DMF) or dimethylsulfoxide (DMSO).^{61-62, 111} In **Chapter 3**, Materials and Methods we briefly discuss further mechanistic insights into the ITC procedure.

1.3.4.2.2 Properties of Metal Halide perovskite SCs

Over the last five years, perovskite SCs have attracted great attention. As described in the previous section, the crystal growth methodologies have been optimized to the point that, nowadays, it is very easy and cheap to grow a high quality SCs in just a few hours which is essential for designing a low-cost radiation detector. One can expect that SCs perovskites will present superior optoelectronic properties than its thin-film counterpart, due to the absence of grain boundaries. In fact, as shown in **Figure 1.15** the applications reported for this material are quite extensive. From photodetectors (a device that responds to the change of light), LEDs and solar cells based on SCs (typically displaying higher Power Conversion Efficiency (PCE)) to X and γ ray detectors with high resistivity ($\leq 10^{10} \Omega \text{ cm}$) and high average atomic numbers ($Z_{\text{Pb}} = 82$). Additionally, SCs remain stable for thousands of hours under humidity conditions and illumination exposure.¹¹³ As one can note, SCs are a unique class of materials with unprecedented properties. In particular, carrier concentration, carrier mobility, carrier lifetime and densities of carrier of SCs-based ionizing detector (See section 1.3.3), are crucial parameters to consider for accurate detection.

Therefore, further advanced investigations of perovskite single crystals and their integration into efficient optoelectronic devices is still a mandatory task.¹¹² **Table 1.2** shows the most important optoelectronic parameters estimated by different techniques considering various SC and MCs perovskite compositions used as the sensitive

materials in X-ray detectors and we also compared those values with those reported for the state-of-art α -Se detectors .

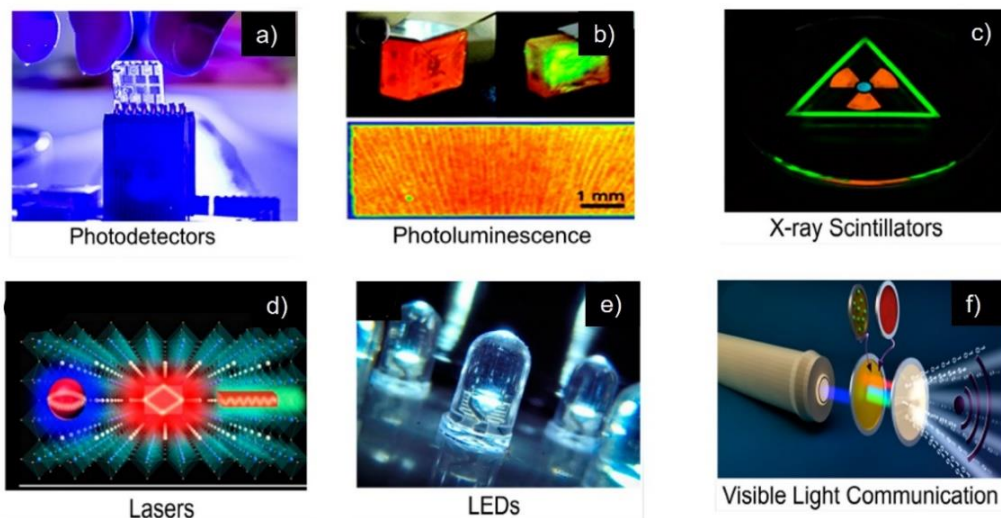


Figure 1.15. Different optoelectronic application of perovskite SCs a) photodetectors, adapted with permission.¹²¹ Copyright 2018, Wiley b) photoluminescence. Adapted with permission.¹²² Copyright 2017, Royal Society of Chemistry c) X-ray scintillation (X-ray illumination at a voltage of 50 kV) Adapted with permission.²⁵ Copyright 2018, Nature Publishing Group d) small perovskite-based lasers. Adapted with permission.¹²³ Copyright 2016, Nature Publishing Group e) LEDs. Adapted with permission.⁵⁴ Copyright 2014, Nature Publishing Group and f) visible-light communication, adapted with permission.⁹⁶ Copyright 2016, American Chemical Society.

The SCs perovskite field is growing in terms of various optoelectronic applications. However, a clearer understanding of critical parameters such as the ion migration pathways in the device and main transport mechanism at the interfaces is needed. The critical overview of **Chapter 2** describes some of the limitations, stability issues and challenges encountered when SCs of metal halide perovskite are used to design efficient X-ray sensor devices.

Table 1.2 Charge transport properties of halide perovskite SCs and MCs used for X-ray detection compared to the state-of-art α -Se sensors.

MAPbX ₃ (X = Br, I)	Single-Crystals (SCs)	Micro-Crystals (MCs)	State-of-art α -Se
Mobility [cm ² V ⁻¹ s ⁻¹]	20-115 (TOF, Hall) 38(SCLC) ^{62, 102, 115}	8 to 35 (THz spectroscopy) ¹⁰¹	$\mu_h = 0.125$ $\mu_e = 0.0034$
$\mu\tau$ (cm ² V ⁻¹)	1.2×10^{-2} (60) to 10^{-3}	2×10^{-4} (33)	10^{-7} to 10^{-5} (24)
Carrier concentration [cm ⁻³]	10^9 to 10^{10}	10^{15} to 10^{17} (THz, PL) ^{87, 102}	$\sim 10^{13}$ (124)
Diffusion length	2-17 μ m	<1 μ m	-
Trap density [cm ⁻³]	10^{10} to 10^{12}	10^{15} to 10^{17}	10^{13} to 10^{14} (125)
Stability in air	months-years	days	Crystallize easily at room temperature ¹²⁶

1.3.4.3 Metal Halide perovskite Micro-Crystals (MCs)

So far, we had presented the versatility of metal halide perovskite devices. Something peculiar about these compounds is that even MCs perovskite materials exhibit outstanding optoelectronic properties enabling several chemical combinations for improving device performance.^{31, 33, 121, 127} As a matter of fact, for various applications, high quality crystalline thin films are desired and usually prepared by different standard methodologies (See below **Figure 1.16**). The MCs compound contrary to the SCs one show Debye rings in a 2D-XRD pattern rather than Bragg spots due to the grains and grain boundaries (GBs). Microcrystalline perovskite films can be produced by spin coating the perovskite solution on top of ETL layer or HTL layers. This is a standard and very well-known methodology to prepare methylammonium lead iodide (MAPbI₃) perovskite films used as the absorbing photo-active layer in a solar cell.^{52, 128-129} Therefore, MCs samples can be prepared from

solution, by using either spin coating or dip-coating or from gas phase by evaporating the two precursor salts.¹²⁸

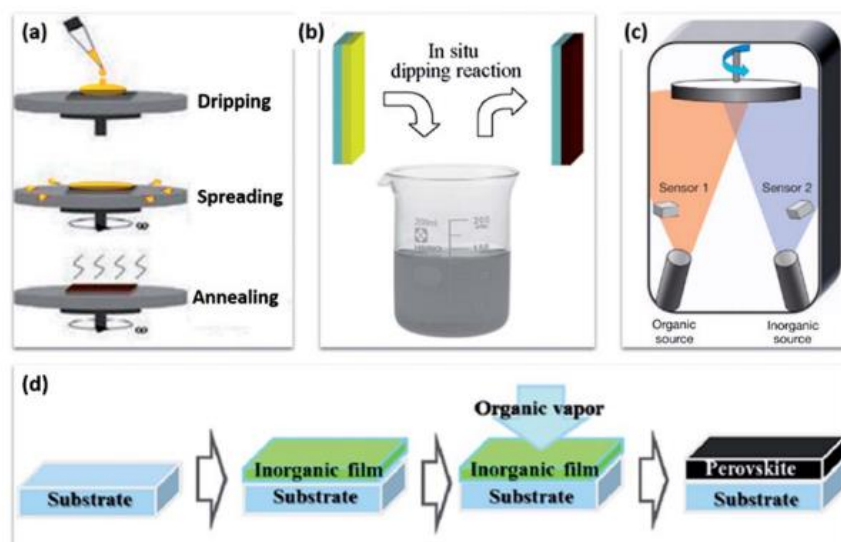


Figure 1.16. General methods to prepare perovskite active layers. (a) One-Step Precursor Deposition (OSPD). (b) Sequential Deposition Method (SDM) (c) Dual-Source Vapor Deposition (DSVD) (d) Vapor-Assisted Solution Process (VASP). Reprinted with permission.¹²⁸ Copyright 2014, Royal Society of Chemistry.

Several approaches have been developed with the purpose of improving all the mentioned synthetical procedures. In order to avoid the disadvantage of getting a non-pure material, a number of strategies have been used. For example, high quality MCs films has been obtained by enhancement the long-term stability and preventing the interfacial degradation in perovskite solar cells.^{94, 130} Some of the strategies developed are the atomistic surface passivation to heal the surface defects,¹³¹ the used of charge transport layers at the outer interfaces,^{99, 132} ionic doping/loading techniques, etc.^{68, 133}

1.3.4.3.1 Mechanochemical synthesis of halide perovskite MCs

The so-called powder sintered method (also known as soft-sintered method) is commonly used in the field of ceramics. In this method the powders of raw materials are mixed in an appropriate amount that after pressurization solidify into a certain shape to obtain the desired compound. Usually, an inert atmosphere is required to promote the agglomeration of crystal grains by the action of pressing and warming.¹³⁴ In the field of metal halide perovskites this protocol has demonstrated promising

results in the last few years.^{31, 33} In **Figure 1.17** the reported methodologies based on employing perovskite powder as the starting point for film or device fabrication are shown.¹²⁷

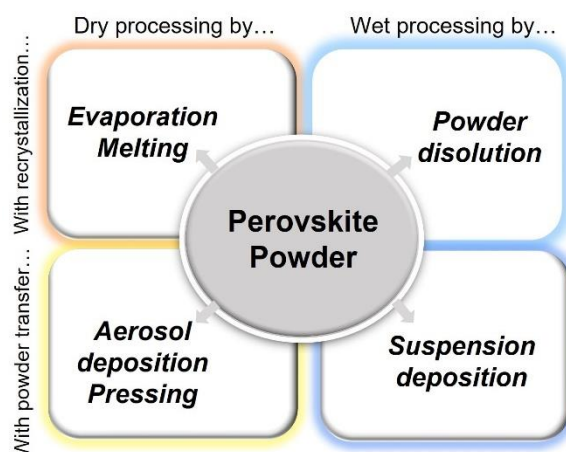


Figure 1.17. Overview of the different approaches and procedures for preparing perovskite MCs films from perovskite powders. Adapted with permission.¹³⁴ Copyright 2003, Elsevier.

These conventional methods can be grouped into procedures where the powder is completely dissolved during the process and procedures where the powder essentially endures during processing and is just transferred into a layer.

For example, MAPbI_3 microcrystals presented here in **Figure 1.18** were synthesized by the simplest mechanochemical approach. The individual precursor powder salts, MAI and PbI_2 , are grounded together with a pestle and mortar at room temperature with the desired stoichiometry.^{31, 33}

The advantages of this kind of procedure are numerous: it is an ease low-cost technique, with a high versatility in terms of achievable compositions, from a technological point of view, ball mills are often used in industrial facilities, thus facilitating the upscale of the synthesis to several kilograms or even tons per day. One more important aspect is their ability to combine other compounds as in traditional synthesis approaches, such as: passivating layers, interlayers, binders' molecules, etc. Lastly, the high stability of mechanochemically synthesized perovskite powders has been repeatedly reported in literature.^{127, 135-137}

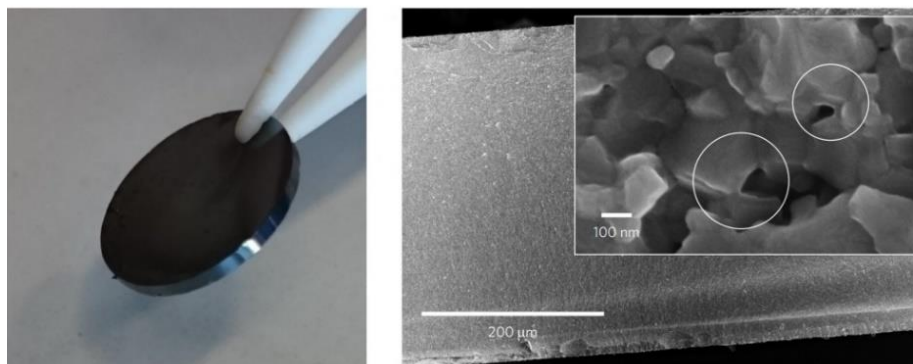


Figure 1.18. a) MAPbI₃ wafer of 1/2 inch × 1 mm. b) Cross-section image obtained by SEM of a sintered MAPbI₃ wafer. Inset: higher-magnification image. Circles indicate two interconnected microcrystals. Reprinted with permission,³³ Copyright 2017, Springer Nature.

As extensively described in this chapter, metal halide perovskites, specifically those devices based on Pb-halide structures, have emerged as a low-cost solution for X-ray detection due to their impressive optoelectronic properties and sensing performance. Additionally, switching from micro crystalline to single crystalline morphologies, not only allows to maintain the outstanding properties that characterize perovskite materials, but also enhances them for accurate detection of ionizing radiation. Nevertheless, the poor control over the thickness and size during growing methods has been reported¹¹³ leading to considerable differences between surface and bulk responses. A deep understanding into the kinetics governing the device response and performance is still needed. A proper model describing how ion migration may influence the electronic current for the long-term operational stability of a perovskite-based X-ray detectors is needed. This model should account for the electronic-ionic nature of this semiconductor material together with the structural stability issues commonly observed in Pb-halide perovskite devices.

References

1. Pan, Z.; Wu, L.; Jiang, J.; Shen, L.; Yao, K., Searching for High-Quality Halide Perovskite Single Crystals toward X-Ray Detection. *J. Phys. Chem. Lett.* **2022**, *13*, 2851-2861.
2. Heiss, W.; Brabec, C., Perovskites Target X-Ray Detection. *Nat. Photon.* **2016**, *10*, 288-289.
3. Tsoulfanidis, N.; Landsberger, S., *Measurement and Detection of Radiation*; CRC Press, 2021.
4. Liu, F.; Wu, R.; Wei, J.; Nie, W.; Mohite, A. D.; Brovelli, S.; Manna, L.; Li, H., Recent Progress in Halide Perovskite Radiation Detectors for Gamma-Ray Spectroscopy. *ACS Energy Lett.* **2022**, *7*, 1066-1085.
5. Trivedi, S.; Prochowicz, D.; Parikh, N.; Mahapatra, A.; Pandey, M. K.; Kalam, A.; Tavakoli, M. M.; Yadav, P., Recent Progress in Growth of Single-Crystal Perovskites for Photovoltaic Applications. *ACS omega* **2021**, *6*, 1030-1042.
6. Zhu, L.; Ran, R.; Tadé, M.; Wang, W.; Shao, Z., Perovskite Materials in Energy Storage and Conversion. *Asia-Pac. J. Chem. Eng.* **2016**, *11*, 338-369.
7. Roose, B.; Wang, Q.; Abate, A., The Role of Charge Selective Contacts in Perovskite Solar Cell Stability. *Adv. Energy Mater.* **2019**, *9*, 1803140.
8. Aranda, C.; Bisquert, J.; Guerrero, A., Impedance Spectroscopy of Perovskite/Contact Interface: Beneficial Chemical Reactivity Effect. *J. Chem. Phys.* **2019**, *151*, 124201.
9. Futscher, M. H.; Gangishetty, M. K.; Congreve, D. N.; Ehrler, B., Quantifying Mobile Ions and Electronic Defects in Perovskite-Based Devices with Temperature-Dependent Capacitance Measurements: Frequency Vs Time Domain. *J. Chem. Phys.* **2020**, *152*, 044202.
10. Futscher, M. H.; Deibel, C., Defect Spectroscopy in Halide Perovskites Is Dominated by Ionic Rather Than Electronic Defects. *ACS Energy Lett.* **2022**, *7*, 140-144.
11. McGovern, L.; Futscher, M. H.; Muscarella, L. A.; Ehrler, B., Understanding the Stability of MAPbBr_3 Versus MAPbI_3 : Suppression of Methylammonium Migration and Reduction of Halide Migration. *J. Phys. Chem. Lett.* **2020**, *11*, 7127-7132.
12. Liu, Y., et al., Inch-Size 0d-Structured Lead-Free Perovskite Single Crystals for Highly Sensitive Stable X-Ray Imaging. *Matter* **2020**, *3*, 180-196.
13. Zhuang, R., et al., Highly Sensitive X-Ray Detector Made of Layered Perovskite-Like $(\text{NH}_4)_3\text{Bi}_2\text{I}_9$ Single Crystal with Anisotropic Response. *Nat. Photon.* **2019**, *13*, 602-608.
14. Zheng, X.; Zhao, W.; Wang, P.; Tan, H.; Saidaminov, M. I.; Tie, S.; Chen, L.; Peng, Y.; Long, J.; Zhang, W.-H., Ultrasensitive and Stable X-Ray Detection Using Zero-Dimensional Lead-Free Perovskites. *J. Energy Chem.* **2020**, *49*, 299-306.
15. Song, Y., et al., Elimination of Interfacial-Electrochemical-Reaction-Induced Polarization in Perovskite Single Crystals for Ultrasensitive and Stable X-Ray Detector Arrays. *Adv. Mater.* **2021**, *33*, 2103078.
16. Knoll, G. F., *Radiation Detection and Measurement*; Wiley, 2010.
17. Kasap, S. O., X-Ray Sensitivity of Photoconductors: Application to Stabilized a-Se. *J. Phys. D: Appl. Phys.* **2000**, *33*, 2853-2865.

18. M., G. S., *Radiation Protection and Dosimetry. An Introduction to Health Physics*; Springer New York, NY, 2008, p XVI, 384.
19. Brookhaven National Laboratory, N. N. D. C. w. <http://www.nndc.bnl.gov/> (accessed Agost 15th 2022).
20. Spencer Jones, H., Nuclear Radiation Part I. In *Techniques for Radioactivity Measurements.*, Jones, H. S., Ed. Pergamon: Pergamon Press, 2013; p vii.
21. (IAEA), I. A. E. A. Training Course Series No. 18 (Rev. 1). <https://www.iaea.org/topics/health> (accessed Agost 16th, 2022).
22. Prekas, G.; Sabet, H.; Bhandari, H.; Derderian, G.; Robertson, F.; Kudrolli, H.; Stapels, C.; Christian, J.; Kleinfelder, S.; Cool, S. In *Direct and Indirect Detectors for X-Ray Photon Counting Systems*, Nuclear Science Symposium and Medical Imaging Conference (NSS/MIC), 2011 IEEE, IEEE: 2011; pp 1487-1493.
23. Leijtens, T.; Bush, K.; Checharoen, R.; Beal, R.; Bowring, A.; McGehee, M. D., Towards Enabling Stable Lead Halide Perovskite Solar Cells; Interplay between Structural, Environmental, and Thermal Stability. *J. Mater. Chem. A* **2017**, *5*, 11483-11500.
24. Kasap, S., et al., Amorphous and Polycrystalline Photoconductors for Direct Conversion Flat Panel X-Ray Image Sensors. *Sensors (Basel, Switzerland)* **2011**, *11*, 5112-57.
25. Chen, Q., et al., All-Inorganic Perovskite Nanocrystal Scintillators. *Nature* **2018**, *561*, 88-93.
26. Wang, J.-X., et al., Nearly 100% Energy Transfer at the Interface of Metal-Organic Frameworks for X-Ray Imaging Scintillators. *Matter* **2022**, *5*, 253-265.
27. Tsai, H.; Tisdale, J.; Shrestha, S.; Liu, F.; Nie, W., Emerging Lead-Halide Perovskite Semiconductor for Solid-State Detectors. In *Advanced X-Ray Detector Technologies: Design and Applications*, Iniewski, K., Ed. Springer International Publishing: Cham, 2022; pp 35-58.
28. Rowlands, J. A.; Hunter, D. M.; Araj, N., X-Ray Imaging Using Amorphous Selenium: A Photoinduced Discharge Readout Method for Digital Mammography. *Med. Phys.* **1991**, *18*, 421-431.
29. Martin, C.; Henri, R.; Jean-Pierre, M.; Luc, L.; Ziad, S.; Brad, T. P. In *Direct Selenium X-Ray Detector for Fluoroscopy, R&F, and Radiography*, Proc.SPIE, 2000.
30. Xu, Y.; Jiao, B.; Song, T.-B.; Stoumpos, C. C.; He, Y.; Hadar, I.; Lin, W.; Jie, W.; Kanatzidis, M. G., Zero-Dimensional Cs₂TeI₆ Perovskite: Solution-Processed Thick Films with High X-Ray Sensitivity. *ACS Photon.* **2019**, *6*, 196-203.
31. Deumel, S., et al., High-Sensitivity High-Resolution X-Ray Imaging with Soft-Sintered Metal Halide Perovskites. *Nat. Electron.* **2021**, *4*, 681-688.
32. Wolszczak, W. W.; Carroll, D. L.; Williams, R. T., Toward Perovskite-Related Scintillators with Necessary Stokes Shift and Thickness for Hard X-Ray Radiography and Gamma Spectroscopy. In *Advanced X-Ray Detector Technologies: Design and Applications*, Iniewski, K., Ed. Springer International Publishing: Cham, 2022; pp 1-34.
33. Shrestha, S., et al., High-Performance Direct Conversion X-Ray Detectors Based on Sintered Hybrid Lead Triiodide Perovskite Wafers. *Nat. Photon.* **2017**, *11*, 436-440.
34. Su, Y.; Ma, W.; Yang, Y., Perovskite Semiconductors for Direct X-Ray Detection and Imaging. *Journal of Semiconductors* **2020**, *41*, 051204.

35. Schlosser, D. M., et al., Expanding the Detection Efficiency of Silicon Drift Detectors. *Nuclear Instruments and Methods in Physics Research Section A: Accelerators, Spectrometers, Detectors and Associated Equipment* **2010**, 624, 270-276.
36. Dos Santos, J. M.; Monteiro, C. M., The Response of High-Purity Germanium Detectors to X-Rays with Energy in the Region of the Ge K-Absorption Edge. *Applied radiation and isotopes : including data, instrumentation and methods for use in agriculture, industry and medicine* **2001**, 55, 331-4.
37. Tsigaridas, S.; Ponchut, C., High-Z Pixel Sensors for Synchrotron Applications. In *Advanced X-Ray Detector Technologies: Design and Applications*, Iniewski, K., Ed. Springer International Publishing: Cham, 2022; pp 87-107.
38. Owens, A.; Peacock, A., Compound Semiconductor Radiation Detectors. *Nuclear Instruments and Methods in Physics Research Section A: Accelerators, Spectrometers, Detectors and Associated Equipment* **2004**, 531, 18-37.
39. Guerra, M.; Manso, M.; Longelin, S.; Pessanha, S.; Carvalho, M. L., Performance of Three Different Si X-Ray Detectors for Portable Xrf Spectrometers in Cultural Heritage Applications. *Journal of Instrumentation* **2012**, 7, C10004-C10004.
40. Del Sordo, S. A. L. C. E. M. A. M. Z. A. U. P. P. i. t. D. o. C.; CdZnTe Semiconductor Radiation Detectors for, A.; Medical, A. *Sensors* **2009**, DOI: 10.3390/s90503491.
41. Szeles, C., CdZnTe and CdTe Materials for X-Ray and Gamma Ray Radiation Detector Applications. *physica status solidi (b)* **2004**, 241, 783-790.
42. Kim, Y. C.; Kim, K. H.; Son, D.-Y.; Jeong, D.-N.; Seo, J.-Y.; Choi, Y. S.; Han, I. T.; Lee, S. Y.; Park, N.-G., Printable Organometallic Perovskite Enables Large-Area, Low-Dose X-Ray Imaging. *Nature* **2017**, 550, 87-91.
43. He, Y., et al., CsPbBr₃ Perovskite Detectors with 1.4% Energy Resolution for High-Energy Γ -Rays. *Nat. Photon.* **2021**, 15, 36-42.
44. He, Y., et al., High Spectral Resolution of Gamma-Rays at Room Temperature by Perovskite CsPbBr₃ Single Crystals. *Nat. Commun.* **2018**, 9, 1609.
45. Wei, H.; Huang, J., Halide Lead Perovskites for Ionizing Radiation Detection. *Nat. Commun.* **2019**, 10, 1066.
46. Paris, R., Chapter 17 - X-Ray Tomography Applied to Tsunami Deposits. In *Geological Records of Tsunamis and Other Extreme Waves*, Engel, M.; Pilarczyk, J.; May, S. M.; Brill, D.; Garrett, E., Eds. Elsevier: 2020; pp 365-380.
47. Lédée, F.; Ciavatti, A.; Verdi, M.; Basiricò, L.; Fraboni, B., Ultra-Stable and Robust Response to X-Rays in 2d Layered Perovskite Micro-Crystalline Films Directly Deposited on Flexible Substrate. *Advanced Optical Materials* **2022**, 10, 2101145.
48. Weber, S. A. L.; Hermes, I. M.; Turren-Cruz, S.-H.; Gort, C.; Bergmann, V. W.; Gilson, L.; Hagfeldt, A.; Graetzel, M.; Tress, W.; Berger, R., How the Formation of Interfacial Charge Causes Hysteresis in Perovskite Solar Cells. *Energy Environ. Sci.* **2018**, 11, 2404-2413.
49. Wei, J.; Zhao, Y.; Li, H.; Li, G.; Pan, J.; Xu, D.; Zhao, Q.; Yu, D., Hysteresis Analysis Based on the Ferroelectric Effect in Hybrid Perovskite Solar Cells. *J. Phys. Chem. Lett.* **2014**, 5, 3937-3945.
50. Shaikh, P. A.; Shi, D.; Retamal, J. R. D.; Sheikh, A. D.; Haque, M. A.; Kang, C.-F.; He, J.-H.; Bakr, O. M.; Wu, T., Schottky Junctions on Perovskite Single Crystals:

Light-Modulated Dielectric Constant and Self-Biased Photodetection. *J. Mater. Chem. C* **2016**, *4*, 8304-8312.

51. Wu, Y.; Liu, Y.; Emrick, T.; Russell, T. P., Polymer Design to Promote Low Work Function Surfaces in Organic Electronics. *Progress in Polymer Science* **2020**, *103*, 101222.

52. Almora, O.; Vaillant-Roca, L.; Garcia-Belmonte, G., Perovskite Solar Cells: A Brief Introduction and Some Remarks. *Rev. Cubana Fis.* **2017**, *34*, 58-68.

53. Chouhan, L.; Ghimire, S.; Subrahmanyam, C.; Miyasaka, T.; Biju, V., Synthesis, Optoelectronic Properties and Applications of Halide Perovskites. *Chemical Society Reviews* **2020**, *49*, 2869-2885.

54. Tan, Z. K., et al., Bright Light-Emitting Diodes Based on Organometal Halide Perovskite. *Nat. Nanotechnol.* **2014**, *9*, 687-92.

55. Dong, H.; Yu, H.; Wang, X.; Zhou, Q.; Sun, J., Carbon-Supported Perovskite Oxides as Oxygen Reduction Reaction Catalyst in Single Chambered Microbial Fuel Cells. *J. Chem. Technol. Biotechnol.* **2013**, *88*, 774-778.

56. Monama, G. R.; Ramohlola, K. E.; Iwuoha, E. I.; Modibane, K. D., Progress on Perovskite Materials for Energy Application. *Results Chem.* **2022**, *4*, 100321.

57. Miyasaka, T., A Decade of Perovskite Photovoltaics. *Nat. Energy* **2019**, *4*, 1-1.

58. Thankappan, A., Perovskite Photovoltaics: Basic to Advanced Concepts and Implementation. In *Perovskite Photovoltaics*, Thomas, S.; Thankappan, A., Eds. Academic Press: 2018; pp xv-xvii.

59. Basiricò, L.; Ciavatti, A.; Fraboni, B., Solution-Grown Organic and Perovskite X-Ray Detectors: A New Paradigm for the Direct Detection of Ionizing Radiation. *Adv. Mater. Technol.* **2021**, *6*, 2000475.

60. Wei, H., et al., Sensitive X-Ray Detectors Made of Methylammonium Lead Tribromide Perovskite Single Crystals. *Nat. Photonics* **2016**, *10*, 333.

61. Maculan, G.; Sheikh, A. D.; Abdelhady, A. L.; Saidaminov, M. I.; Haque, M. A.; Murali, B.; Alarousu, E.; Mohammed, O. F.; Wu, T.; Bakr, O. M., $\text{CH}_3\text{NH}_3\text{PbCl}_3$ Single Crystals: Inverse Temperature Crystallization and Visible-Blind UV-Photodetector. *J. Phys. Chem. Lett.* **2015**, *6*, 3781-3786.

62. Saidaminov, M. I., et al., High-Quality Bulk Hybrid Perovskite Single Crystals within Minutes by Inverse Temperature Crystallization. *Nat. Commun.* **2015**, *6*, 7586.

63. Akkerman, Q. A.; Manna, L., What Defines a Halide Perovskite? *ACS Energy Lett.* **2020**, *5*, 604-610.

64. Green, M. A.; Ho-Baillie, A.; Snaith, H. J., The Emergence of Perovskite Solar Cells. *Nat. Photon.* **2014**, *8*, 506-514.

65. Travis, W.; Glover, E. N. K.; Bronstein, H.; Scanlon, D. O.; Palgrave, R. G., On the Application of the Tolerance Factor to Inorganic and Hybrid Halide Perovskites: A Revised System. *Chemical Science* **2016**, *7*, 4548-4556.

66. Wang, K.-H.; Li, L.-C.; Shellaiah, M.; Wen Sun, K., Structural and Photophysical Properties of Methylammonium Lead Tribromide (MAPbBr_3) Single Crystals. *Sci. Rep.* **2017**, *7*, 13643.

67. Tisdale, J. T.; Muckley, E.; Ahmadi, M.; Smith, T.; Seal, C.; Lukosi, E.; Ivanov, I. N.; Hu, B., Dynamic Impact of Electrode Materials on Interface of Single-Crystalline Methylammonium Lead Bromide Perovskite. *Adv. Mater. Interfaces* **2018**, *5*, 1800476.

68. Yang, Y.; Yang, M.; Moore, David T.; Yan, Y.; Miller, Elisa M.; Zhu, K.; Beard, Matthew C., Top and Bottom Surfaces Limit Carrier Lifetime in Lead Iodide Perovskite Films. *Nat. Energy* **2017**, *2*, 16207.
69. Snaith, H. J.; Abate, A.; Ball, J. M.; Eperon, G. E.; Leijtens, T.; Noel, N. K.; Stranks, S. D.; Wang, J. T.-W.; Wojciechowski, K.; Zhang, W., Anomalous Hysteresis in Perovskite Solar Cells. *J. Phys. Chem. Lett.* **2014**, *5*, 1511-1515.
70. Bisquert, J.; Guerrero, A.; Gonzales, C., Theory of Hysteresis in Halide Perovskites by Integration of the Equivalent Circuit. *ACS Phys. Chem. Au* **2021**, *1*, 25-44.
71. Ravishankar, S.; Almora, O.; Echeverría-Arrondo, C.; Ghahremanirad, E.; Aranda, C.; Guerrero, A.; Fabregat-Santiago, F.; Zaban, A.; Garcia-Belmonte, G.; Bisquert, J., Surface Polarization Model for the Dynamic Hysteresis of Perovskite Solar Cells. *J. Phys. Chem. Lett.* **2017**, *8*, 915–921.
72. Almora, O.; Aranda, C.; Zarazua, I.; Guerrero, A.; Garcia-Belmonte, G., Noncapacitive Hysteresis in Perovskite Solar Cells at Room Temperature. *ACS Energy Lett.* **2016**, *1*, 209–215.
73. Almora, O.; Guerrero, A.; Garcia-Belmonte, G., Ionic Charging by Local Imbalance at Interfaces in Hybrid Lead Halide Perovskites. *Appl. Phys. Lett.* **2016**, *108*, 043903.
74. Caram, J.; García-Batlle, M.; Almora, O.; Arce, R. D.; Guerrero, A.; Garcia-Belmonte, G., Direct Observation of Surface Polarization at Hybrid Perovskite/Au Interfaces by Dark Transient Experiments. *Appl. Phys. Lett.* **2020**, *116*, 183503.
75. Carrillo, J.; Guerrero, A.; Rahimnejad, S.; Almora, O.; Zarazua, I.; Mas-Marza, E.; Bisquert, J.; Garcia-Belmonte, G., Ionic Reactivity at Contacts and Aging of Methylammonium Lead Triiodide Perovskite Solar Cells. *Adv. Energy Mater.* **2016**, *6*, 1502246
76. Singh, R.; Parashar, M., Origin of Hysteresis in Perovskite Solar Cells. In *Soft-Matter Thin Film Solar Cells*, AIP Publishing LLC: 2020; pp 1-1-1-42.
77. Pospisil, J.; Guerrero, A.; Zmeskal, O.; Weiter, M.; Gallardo, J. J.; Navas, J.; Garcia-Belmonte, G., Reversible Formation of Gold Halides in Single-Crystal Hybrid-Perovskite/Au Interface Upon Biasing and Effect on Electronic Carrier Injection. *Adv. Funct. Mater.* **2019**, *29*, 1900881.
78. Wilson, J. N.; Frost, J. M.; Wallace, S. K.; Walsh, A., Dielectric and Ferroic Properties of Metal Halide Perovskites. *APL Materials* **2019**, *7*, 010901.
79. Onoda-Yamamuro, N.; Matsuo, T.; Suga, H., Dielectric Study of $\text{Ch}_3\text{nh}_3\text{pbx}_3$ (X = Cl, Br, I). *J. Phys. Chem. Solids* **1992**, *53*, 935-939.
80. Juarez-Perez, E. J.; Sanchez, R. S.; Badia, L.; Garcia-Belmonte, G.; Kang, Y. S.; Mora-Sero, I.; Bisquert, J., Photoinduced Giant Dielectric Constant in Lead Halide Perovskite Solar Cells. *J. Phys. Chem. Lett.* **2014**, *5*, 2390-2394.
81. Li, F.; Zheng, R., Halide Perovskites with Ambipolar Transport Properties for Transistor Applications. Chapter 4 In *Ambipolar Materials and Devices*, The Royal Society of Chemistry: 2021; pp 41-82.
82. Liu, Y.; Yang, Z.; Liu, S., Recent Progress in Single-Crystalline Perovskite Research Including Crystal Preparation, Property Evaluation, and Applications. *Adv. Sci.* **2018**, *5*, 1700471.

83. Azpiroz, J. M.; Mosconi, E.; Bisquert, J.; De Angelis, F., Defect Migration in Methylammonium Lead Iodide and Its Role in Perovskite Solar Cell Operation. *Energy Environ. Sci.* **2015**, *8*, 2118-2127.
84. Yin, W.-J.; Shi, T.; Yan, Y., Unusual Defect Physics in $\text{CH}_3\text{NH}_3\text{PbI}_3$ Perovskite Solar Cell Absorber. *Appl. Phys. Lett.* **2014**, *104*, 063903.
85. Meggiolaro, D.; Mosconi, E.; De Angelis, F., Modeling the Interaction of Molecular Iodine with MAPbI_3 : A Probe of Lead-Halide Perovskites Defect Chemistry. *ACS Energy Lett.* **2018**, *3*, 447-451.
86. Xu, Y., et al., Solution-Processed Epitaxial Growth of MAPbI_3 Single-Crystal Films for Highly Stable Photodetectors. *Front. Mater.* **2021**, *8*.
87. Wehrenfennig, C.; Eperon, G. E.; Johnston, M. B.; Snaith, H. J.; Herz, L. M., High Charge Carrier Mobilities and Lifetimes in Organolead Trihalide Perovskites. *Adv. Mater.* **2014**, *26*, 1584-1589.
88. Lin, Y., et al., Excess Charge-Carrier Induced Instability of Hybrid Perovskites. *Nat. Commun.* **2018**, *9*, 4981.
89. Choi, J. I. J.; Khan, M. E.; Hawash, Z.; Kim, K. J.; Lee, H.; Ono, L. K.; Qi, Y.; Kim, Y.-H.; Park, J. Y., Atomic-Scale View of Stability and Degradation of Single-Crystal MAPbBr_3 Surfaces. *J. Mater. Chem. A* **2019**, *7*, 20760-20766.
90. Wang, C.; Ecker, B. R.; Wei, H.; Huang, J.; Gao, Y., Environmental Surface Stability of the MAPbBr_3 Single Crystal. *J. Phys. Chem. C* **2018**, *122*, 3513-3522.
91. Tan, R.; Dryzhakov, B.; Charest, J.; Hu, B.; Ahmadi, M.; Lukosi, E., Improved Radiation Sensing with Methylammonium Lead Tribromide Perovskite Semiconductors. *Nucl. Instrum. Methods Phys. Res., Sect. A* **2021**, *986*, 164710.
92. Bag, M.; Renna, L. A.; Adhikari, R. Y.; Karak, S.; Liu, F.; Lahti, P. M.; Russell, T. P.; Tuominen, M. T.; Venkataraman, D., Kinetics of Ion Transport in Perovskite Active Layers and Its Implications for Active Layer Stability. *J. Am. Chem. Soc.* **2015**, *137*, 13130-13137.
93. Aranda, C.; Cristobal, C.; Shooshtari, L.; Li, C.; Huettner, S.; Guerrero, A., Formation Criteria of High Efficiency Perovskite Solar Cells under Ambient Conditions. *Sustainable Energy Fuels* **2017**, *1*, 540-547.
94. Aranda, C.; Guerrero, A.; Bisquert, J., Ionic Effect Enhances Light Emission and the Photovoltage of Methylammonium Lead Bromide Perovskite Solar Cells by Reduced Surface Recombination. *ACS Energy Lett.* **2019**, *4*, 741-746.
95. Noh, J. H.; Im, S. H.; Heo, J. H.; Mandal, T. N.; Seok, S. I., Chemical Management for Colorful, Efficient, and Stable Inorganic–Organic Hybrid Nanostructured Solar Cells. *Nano Lett.* **2013**, *13*, 1764-1769.
96. Dursun, I., et al., Perovskite Nanocrystals as a Color Converter for Visible Light Communication. *ACS Photonics* **2016**, *3*, 1150-1156.
97. Sarritzu, V., et al., Direct or Indirect Bandgap in Hybrid Lead Halide Perovskites? *Adv. Opt. Mater.* **2018**, *6*, 1701254.
98. Zhang, Z.; Saporov, B., Charge Carrier Mobility of Halide Perovskite Single Crystals for Ionizing Radiation Detection. *Applied Physics Letters* **2021**, *119*, 030502.
99. Dong, Q.; Fang, Y.; Shao, Y.; Mulligan, P.; Qiu, J.; Cao, L.; Huang, J., Electron-Hole Diffusion Lengths > 175 nm in Solution-Grown $\text{CH}_3\text{NH}_3\text{PbI}_3$ Single Crystals. **2015**, *347*, 967-970.

100. Oga, H.; Saeki, A.; Ogomi, Y.; Hayase, S.; Seki, S., Improved Understanding of the Electronic and Energetic Landscapes of Perovskite Solar Cells: High Local Charge Carrier Mobility, Reduced Recombination, and Extremely Shallow Traps. *J. Am. Chem. Soc.* **2014**, *136*, 13818-13825.
101. Xia, C. Q., et al., Limits to Electrical Mobility in Lead-Halide Perovskite Semiconductors. *J. Phys. Chem. Lett.* **2021**, *12*, 3607-3617.
102. Herz, L. M., Charge-Carrier Mobilities in Metal Halide Perovskites: Fundamental Mechanisms and Limits. *ACS Energy Lett.* **2017**, *2*, 1539-1548.
103. Stranks, S. D.; Eperon, G. E.; Grancini, G.; Menelaou, C.; Alcocer, M. J. P.; Leijtens, T.; Herz, L. M.; Petrozza, A.; Snaith, H. J., Electron-Hole Diffusion Lengths Exceeding 1 Micrometer in an Organometal Trihalide Perovskite Absorber. *Science* **2013**, *342*, 341-344.
104. Chen, Y.; Yi, H. T.; Wu, X.; Haroldson, R.; Gartstein, Y. N.; Rodionov, Y. I.; Tikhonov, K. S.; Zakhidov, A.; Zhu, X. Y.; Podzorov, V., Extended Carrier Lifetimes and Diffusion in Hybrid Perovskites Revealed by Hall Effect and Photoconductivity Measurements. *Nat. Commun.* **2016**, *7*, 12253.
105. Wang, J., et al., Investigation of Electrode Electrochemical Reactions in $\text{CH}_3\text{NH}_3\text{PbBr}_3$ Perovskite Single-Crystal Field-Effect Transistors. *Adv. Mater.* **2019**, *31*, 1902618.
106. Almora, O.; Miravet, D.; García-Batlle, M.; Garcia-Belmonte, G., Ballistic-Like Space-Charge-Limited Currents in Halide Perovskites at Room Temperature. *Appl. Phys. Lett.* **2021**, *119*, 242107.
107. Tress, W.; Marinova, N.; Moehl, T.; Zakeeruddin, S. M.; Nazeeruddin, M. K.; Grätzel, M., Understanding the Rate-Dependent J–V Hysteresis, Slow Time Component, and Aging in $\text{CH}_3\text{NH}_3\text{PbI}_3$ Perovskite Solar Cells: The Role of a Compensated Electric Field. *Energy Environ. Sci.* **2015**, *8*, 995-1004.
108. Almora, O.; Matt, G. J.; These, A.; Kanak, A.; Levchuk, I.; Shrestha, S.; Osvet, A.; Brabec, C. J.; Garcia-Belmonte, G., Surface Versus Bulk Currents and Ionic Space-Charge Effects in CsPbBr_3 Single Crystals. *J. Phys. Chem. Lett.* **2022**, *13*, 3824-3830.
109. Wang, F.; Bai, S.; Tress, W.; Hagfeldt, A.; Gao, F., Defects Engineering for High-Performance Perovskite Solar Cells. *npj Flexible Electron.* **2018**, *2*, 22.
110. Liu, Y.; Zheng, X.; Fang, Y.; Zhou, Y.; Ni, Z.; Xiao, X.; Chen, S.; Huang, J., Ligand Assisted Growth of Perovskite Single Crystals with Low Defect Density. *Nature communications* **2021**, *12*, 1686.
111. Amari, S.; Verilhac, J.-M.; Gros D'Aillon, E.; Ibanez, A.; Zaccaro, J., Optimization of the Growth Conditions for High Quality $\text{CH}_3\text{NH}_3\text{PbBr}_3$ Hybrid Perovskite Single Crystals. *Cryst. Growth Des.* **2020**, *20*, 1665-1672.
112. Murali, B.; Kolli, H. K.; Yin, J.; Ketavath, R.; Bakr, O. M.; Mohammed, O. F., Single Crystals: The Next Big Wave of Perovskite Optoelectronics. *ACS Mater. Lett.* **2020**, *2*, 184-214.
113. Afroz, M. A.; Aranda, C. A.; Tailor, N. K.; Yukta; Yadav, P.; Tavakoli, M. M.; Saliba, M.; Satapathi, S., Impedance Spectroscopy for Metal Halide Perovskite Single Crystals: Recent Advances, Challenges, and Solutions. *ACS Energy Lett.* **2021**, 3275-3286.

114. Dang, Y.; Zhou, Y.; Liu, X.; Ju, D.; Xia, S.; Xia, H.; Tao, X. J. A. C., Formation of Hybrid Perovskite Tin Iodide Single Crystals by Top-Seeded Solution Growth. **2016**, *55 10*, 3447-50.
115. Shi, D., et al., Low Trap-State Density and Long Carrier Diffusion in Organolead Trihalide Perovskite Single Crystals. *Science* **2015**, *347*, 519-522.
116. Steele, J. A., et al., Photophysical Pathways in Highly Sensitive Cs₂AgBiBr₆ Double-Perovskite Single-Crystal X-Ray Detectors. *Adv. Mater.* **2018**, *30*, 1804450.
117. Dang, Y.; Liu, Y.; Sun, Y.; Yuan, D.; Liu, X.; Lu, W.; Liu, G.; Xia, H.; Tao, X. J. C., Bulk Crystal Growth of Hybrid Perovskite Material Ch₃NH₃PbI₃. **2015**, *17*, 665-670.
118. Llinàs, A.; Goodman, J. M., Polymorph Control: Past, Present and Future. *Drug Discovery Today* **2008**, *13*, 198-210.
119. Yuan, Z.; Zhou, J.; Zhang, Y.; Ma, X.; Wang, J.; Dong, J.; Lu, F.; Han, D.; Kuang, B.; Wang, N., Growing Masni₃ Perovskite Single-Crystal Films by Inverse Temperature Crystallization. *J. Phys.: Condens. Matter* **2022**, *34*, 144009.
120. Cheng, X.; Yang, S.; Cao, B.; Tao, X.; Chen, Z., Single Crystal Perovskite Solar Cells: Development and Perspectives. *Adv. Funct. Mater.* **2020**, *30*, 1905021.
121. Bao, C.; Yang, J.; Bai, S.; Xu, W.; Yan, Z.; Xu, Q.; Liu, J.; Zhang, W.; Gao, F., High Performance and Stable All-Inorganic Metal Halide Perovskite-Based Photodetectors for Optical Communication Applications. *Adv. Mater.* **2018**, *30*, 1803422.
122. Kanemitsu, Y., Luminescence Spectroscopy of Lead-Halide Perovskites: Materials Properties and Application as Photovoltaic Devices. *J. Mater. Chem. C* **2017**, *5*, 3427-3437.
123. Zhang, Q.; Su, R.; Liu, X.; Xing, J.; Sum, T. C.; Xiong, Q., High-Quality Whispering-Gallery-Mode Lasing from Cesium Lead Halide Perovskite Nanoplatelets. *Adv. Funct. Mater.* **2016**, *26*, 6238-6245.
124. Yunus, M.; Kabir, M. Z.; Kasap, S. O., Sensitivity Reduction Mechanisms in Amorphous Selenium Photoconductive X-Ray Image Detectors. *Applied Physics Letters* **2004**, *85*, 6430-6432.
125. Kasap, S. O.; Yang, J.; Simonson, B.; Adeagbo, E.; Walornyj, M.; Belev, G.; Bradley, M. P.; Johanson, R. E., Effects of X-Ray Irradiation on Charge Transport and Charge Collection Efficiency in Stabilized a-Se Photoconductors. *Journal of Applied Physics* **2020**, *127*, 084502.
126. Chen, Z.; Dong, M.; Li, C.; Shao, S.; Hu, T.; Kang, D., Improved Thermal Stability of Antimony-Doped Amorphous Selenium Film for X-Ray Flat-Panel Detectors. *physica status solidi (a)* **2013**, *210*, 580-584.
127. Leupold, N.; Panzer, F., Recent Advances and Perspectives on Powder-Based Halide Perovskite Film Processing. *Adv. Funct. Mater.* **2021**, *31*, 2007350.
128. Gao, P.; Grätzel, M.; Nazeeruddin, M. K., Organohalide Lead Perovskites for Photovoltaic Applications. *Energy Environ. Sci.* **2014**, *7*, 2448-2463.
129. Lee, M. M.; Teuscher, J.; Miyasaka, T.; Murakami, T. N.; Snaith, H. J., Efficient Hybrid Solar Cells Based on Meso-Superstructured Organometal Halide Perovskites. *Science* **2012**, *338*, 643-647.
130. Guerrero, A.; You, J.; Aranda, C.; Kang, Y. S.; Garcia-Belmonte, G.; Zhou, H.; Bisquert, J.; Yang, Y., Interfacial Degradation of Planar Lead Halide Perovskite Solar Cells. *ACS Nano* **2016**, *10*, 218-224.

131. Song, Y., et al., Atomistic Surface Passivation of $\text{CH}_3\text{NH}_3\text{PbI}_3$ Perovskite Single Crystals for Highly Sensitive Coplanar-Structure X-Ray Detectors. *Research* **2020**, 2020, 5958243.
132. Sanhira, E. M.; Tremolet de Villers, B. J.; Schulz, P.; Reese, M. O.; Ferrere, S.; Zhu, K.; Lin, L. Y.; Berry, J. J.; Luther, J. M., Influence of Electrode Interfaces on the Stability of Perovskite Solar Cells: Reduced Degradation Using MoO₃/Al for Hole Collection. *ACS Energy Lett.* **2016**, 1, 38-45.
133. Kiermasch, D.; Rieder, P.; Tvingstedt, K.; Baumann, A.; Dyakonov, V., Improved Charge Carrier Lifetime in Planar Perovskite Solar Cells by Bromine Doping. *Sci. Rep.* **2016**, 6, 39333.
134. Stojanovic, B. D., Mechanochemical Synthesis of Ceramic Powders with Perovskite Structure. *J. Mater. Process. Technol.* **2003**, 143-144, 78-81.
135. Dou, B.; Wheeler, L. M.; Christians, J. A.; Moore, D. T.; Harvey, S. P.; Berry, J. J.; Barnes, F. S.; Shaheen, S. E.; van Hest, M. F. A. M., Degradation of Highly Alloyed Metal Halide Perovskite Precursor Inks: Mechanism and Storage Solutions. *ACS Energy Lett.* **2018**, 3, 979-985.
136. Hong, Z.; Tan, D.; John, R. A.; Tay, Y. K. E.; Ho, Y. K. T.; Zhao, X.; Sum, T. C.; Mathews, N.; García, F.; Soo, H. S., Completely Solvent-Free Protocols to Access Phase-Pure, Metastable Metal Halide Perovskites and Functional Photodetectors from the Precursor Salts. *iScience* **2019**, 16, 312-325.
137. Leupold, N., et al., High Versatility and Stability of Mechanochemically Synthesized Halide Perovskite Powders for Optoelectronic Devices. *ACS Appl. Mater. Interfaces* **2019**, 11, 30259-30268.

Chapter 2. Critical Overview

Regardless the outstanding optoelectronics properties of metal halide perovskites (MHPs), there are still fundamental issues keeping perovskites materials apart from industrial implementation. In reality, MHPs are, sometimes, intrinsically unstable under certain conditions. Several irreversible degradation pathways have been reported including the exposure to high temperatures,¹⁻² light,³⁻⁴ moisture⁵⁻⁶ and various chemicals including oxygen.⁶⁻⁹ In this thesis, the effect of humidity and temperature has been considered because they may induce chemical and structural changes.¹⁰ However, a number of reports have showed that water can be an ally to avoid degradation caused by atmospheric exposure of perovskite materials during fabrication of solar cells.¹¹⁻¹² Therefore, *chemical stability* of perovskite compounds is then one of the critical issues to be considered.

Along with the chemical factors affecting the stability, the electrical performance has been evaluated in perovskite-based devices potentially used for X-ray detection. Therefore, in this thesis, *ion migration* has been the major concern in terms of long-term electrical performance of the device.¹³ Redistribution of mobile species affects the chemical properties and transport dynamic within the device by generating recombination centers, modifying the electronic conductivity or by inducing degradation paths.¹⁴⁻¹⁶ The persist drawback of ions migrating is, often, unavoidable and intrinsic in MHPs.^{13, 17-19}

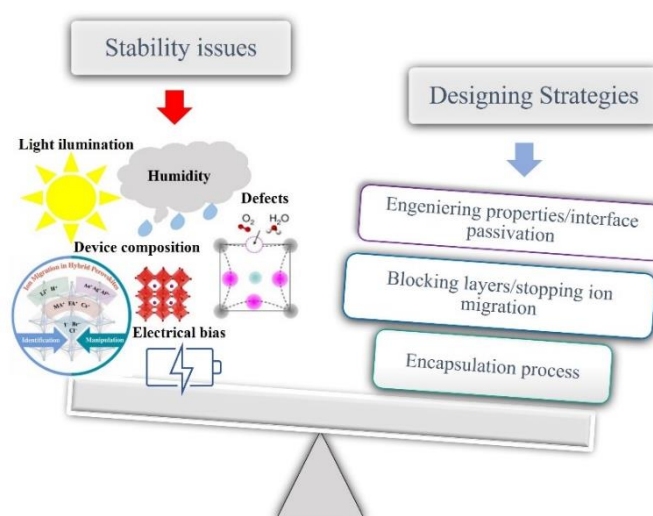


Figure 2.1. Schematic overview of some of the critical degradation pathways reported for Pb-halide perovskite materials together with emerging strategies used to solve them.

Consequently, it is important to understand the mechanism behind ion migration and how these species may alter the electrical response of the device to engineer its properties and modeling novel strategies to increase device performance. In this chapter a brief outline on the nature of ion migration is described by integrating experimental findings and current understanding on the topic. Stability challenges are presented in **Figure 2.1** together with the key strategies used to solve them.

2.1 Chemical stability: structural issues in Metal Halide Perovskites Materials

2.1.1 Device composition and architecture

The crystalline arrangement of the perovskites depends on their chemical composition and may vary from three-dimensional (3D) perovskite crystals, two-dimensional (2D) perovskite nanosheets to one-dimensional (1D) and zero-dimensional (0D) perovskite quantum dots (QDs)²⁰ (see **Figure 2.2**). Please refer to **section 1.34.1** in **Chapter 1** for a thorough revision on structural features and chemical properties of MHPs. Considerable processing versatility and engineering composition has been developed using this metal halide compounds.²¹⁻²² However, ambiguous results are reported due to material inhomogeneities and local lattice mismatches that result in lattice distortion of the microscopic crystal structure.^{19, 22} Importantly, for X-ray detectors device composition and architecture should be linked to the crystal uniformity and the defect dynamic affecting the sensor performance.²³ As a result, in solid-state X-ray detectors the elemental composition of the detector material, its crystallinity, its absorption coefficient, the photon energy, and the direction with respect to the orientation of the detector material need to be controlled.²⁴⁻²⁵

Recent reports on the field of X-ray detectors used diverse photoactive materials based on 3D halide perovskites with controlled morphologies.²⁶⁻²⁹ From polycrystalline thin films to nanoparticles/wires/sheets, and bulk single crystals, these materials have showed higher responsivity and detectivity.³⁰⁻³² In **Figure 2.2** one can observe a summary with different configurations and various perovskite composition covering the sensing region from ultraviolet-visible-near infrared (UV-Vis-NIR) to gamma photons based on two- or three-terminal device architecture.

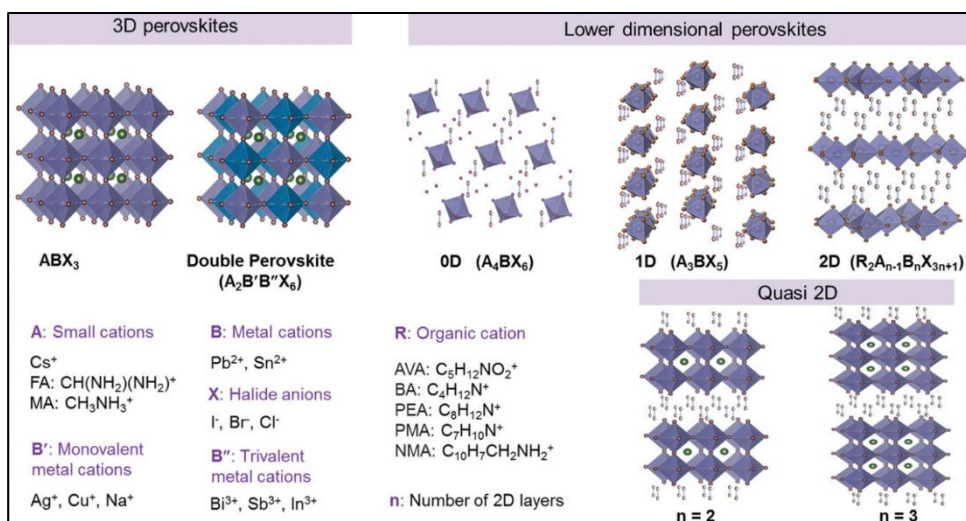


Figure 2.2. Representation of different possible structures for perovskite: 3D (simple and double), 0D, 1D, 2D, and quasi-2D perovskites together with some examples of commonly used metal and organic cations in the structures. Reproduced with permission.²⁰ Copyright 2020. Wiley Online Library.

Accordingly, specific *engineering composition strategies* for performance enhancement in those detectors for ionizing radiation are required. Those strategies are listed in the following:

- Mixed compositions of halide perovskites which has proved to be more stable in ambient conditions.³³
- Substitution of the organic cation CH_3NH_3^+ (methylammonium) with $\text{CH}(\text{NH}_2)_2^+$ (formamidinium) broadening the optical absorption band thus allowing a superior stability of the hybrid perovskite³⁴.
- Replacement of methylammonium for an inorganic cation as Cs^+ , resulting in a higher thermal stability.³⁵⁻³⁶
- Utilization of layered halide perovskites of atom-thick sheets of metal halides arranged with strict crystallographic assembling and distributed by long organic ligands, the adjacent layers are stacked together by weak van der Waals forces increasing robustness to moisture.^{26, 30}

In terms of *morphological evolution*, both microcrystalline and single crystalline (SCs) samples demand a fine control of the crystallization process to further engineer the device morphology, surface coverage and uniformity. Several morphological optimization strategies have been developed for thin-films with less defects, less pinholes and grain boundaries.^{11, 37-39} Specifications on the experimental parameters

of some of the used techniques for film preparation were discussed in **section 1.3.4.3** and will be further examined in **Chapter 3** (Materials and Methods). Actually, one of the main emphasis of this thesis are the advantages of using perovskite SCs of MAPbBr₃ in comparison to perovskite microcrystalline films (MCs) which suffers from morphological disorders.¹³ SCs possess a low trap density, high mobility, low intrinsic carrier concentration and long diffusion length,⁴⁰ which make the material ideal for simultaneously, rapid and sensitive detection. Perovskite MCs films and SCs compounds can be implemented into devices in both vertical and lateral configuration (**Figure 2.3**). Vertical photoconductors have a small electrode spacing with a short carrier transit length which provide a fast response. On the other hand, a lateral photoconductor showed a slow response and high driving voltage due to their large electrode spacing thus the response speed is, sometimes, sacrificed.³⁰

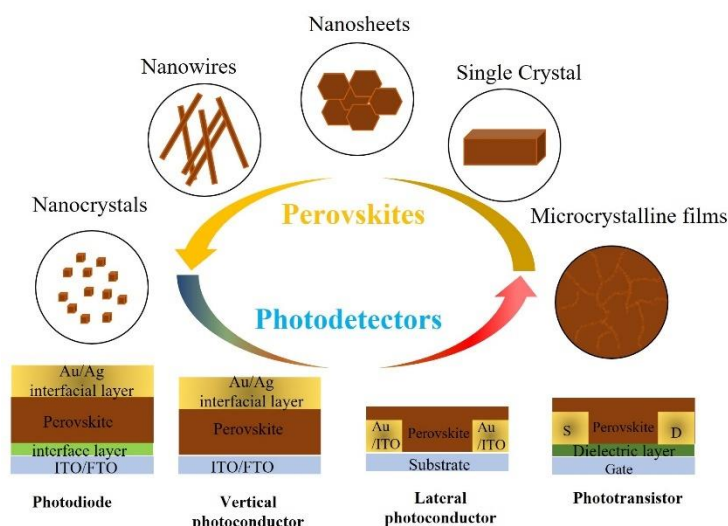


Figure 2.3. Schematic representation of perovskite-based photodetectors with different possible structural compositions and device architecture. Adapted with permission³⁰. Copyright 2016. The Royal Society of Chemistry.

The lateral configuration yields a better reproducibility and lower cost of fabrication in comparison to the vertical one.⁴¹⁻⁴² Additionally, the diode configuration (common architecture for direct conversion of X-rays) allows a better charge collection.⁴³⁻⁴⁴ A good charge collection efficiency relies on faster response and low driving voltages in an X-ray sensor. In fact, SeC detectors for X-ray detection with a diode configuration works at reverse bias to minimize the dark currents and to provide faster collection of charges. Finally, the sandwich-like topology observed in **Figure**

2.3 is usually constructed when light is explored and the presence of hole/electron transporting, blocking, or rectifying layers enhance the device performance.^{29, 45}

During the last fifteen years much work has been focused on amorphous MCs semiconductors and SCs as perovskite-based X-ray detectors in imaging applications.^{18, 20, 25, 28-29, 31, 40, 42-43, 45-58} The first report on the use of MAPbI₃ dates back to 2015, in here MAPbI₃ films were employed as sensitive material for detection of X-ray photons.⁵⁹ This work was followed by Wei et al., who reported about a sensitive X-ray detector made of MAPbBr₃ single crystal with a high sensitivity and environmental stability.⁶⁰ As a result of all the extensive research, specific requirements have been highlighted for the complete absorption of hard X-rays. In fact, due to the much stronger penetration capability of X and gamma (γ) rays a much thicker active layer is needed to stop radiation and to generate charges across the entire thickness of the semiconductor.⁶¹ Therefore, path lengths in the order of mm to cm for the γ -photons energy range (20 to 70 keV) are required. All these requirements may benefit the device by a drastic reduction of the defect density and an increment in the mobility lifetime product $\mu\tau$ ($\sim 1.0 \times 10^{-2} \text{ cm}^2 \text{ V}^{-1}$)⁶⁰ thus reduction of the surface/interfacial recombination.

Considering all this information related to the device composition and architecture, our approach was to start by studying two different compositions of MHPs in two different device architectures, firstly: vertical and symmetrical contacted MAPbBr₃ single crystals of $\sim 5 \times 5 \text{ cm}^2$ with higher crystallinity perovskite layers compared to their MCs counterpart. Secondly, asymmetrical-contacted MAPbI₃ thick-pellets using a short-term and low-cost powder sintering route with the aim to improve the performance and robustness of the existing process by using of rectifying layers as electrodes. **Chapter 3** describe the ITC (growth methodology) used to growing the SCs and **Chapter 4 and 6** summarize all the structural characterization techniques performed to the growth samples. In the case of the MAPbI₃ thick-pellets, **Chapter 3** described the soft-sintering procedure and **Chapter 5 and 8** presented some of the structural characteristics of the thick pellets.

2.1.2 Effects of Oxygen and Moisture

Common degradation pathways include oxygen and water exposure of the metal halide perovskite materials.^{6, 8, 62} Previous analyses pointed out that the perovskite material itself, decomposes into other species, causing some harm on the desired

optoelectronic properties. Aristidou et al. revealed how the combined action of light and molecular oxygen on the photoactive layer of MAPbI₃ may result in the decomposition of the perovskite and subsequent formation of PbI₂, I₂, and methylamine by ¹H-NMR spectroscopy.^{6, 8, 10, 12, 63-64} Other authors reported the influence of ambient atmosphere on the surface energy structure of perovskites, affirming that the exposure to oxygen gas induce a shift of the energetic vacuum level of the perovskite films, because of the formation of an oxygen-induced surface dipole.⁶ **Figure 2.4a** exhibits the faster visible decomposition of a MCs film of MAPbI₃ under higher humidity levels compared to their counterpart a MAPbI₃ SCs (**Figure 2.4b**) stored for months without any visible sign of sample degradation. Different mechanisms have been proposed for water infiltrates in MHPs materials. For instance, Müller et al. used infrared spectroscopy (IR) and Atomic Force Microscopy measurements (AFM) to prove the notion that water infiltrates through defects and grain boundaries, creating a high surface roughness showing a strong clear OH peak in the IR spectra (See **Figure 2.4c**).⁶⁵

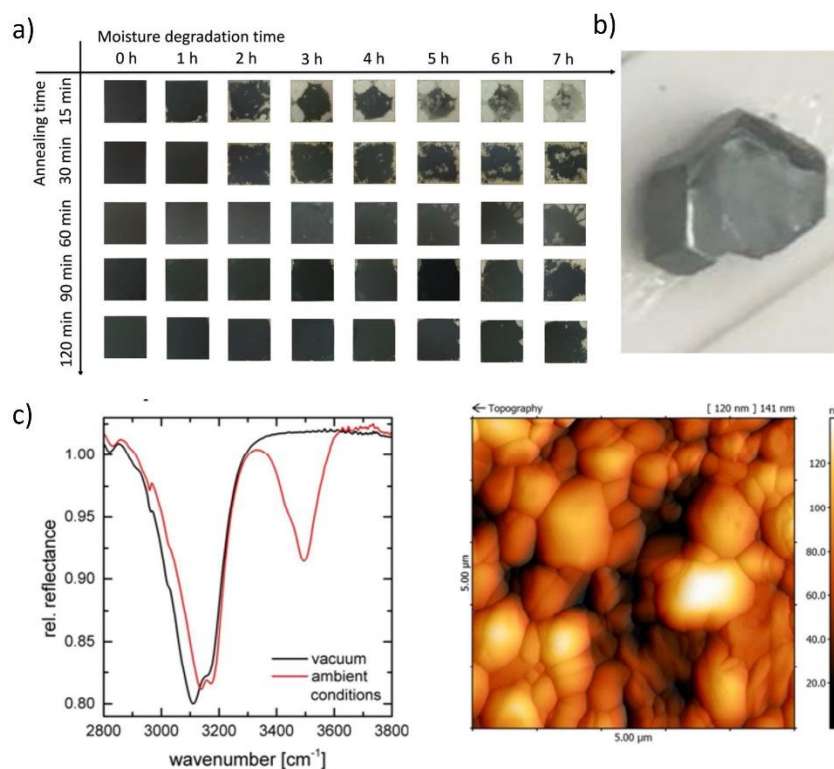


Figure 2.4. Consecutive images of the MAPbI₃ MCs films stored in 85% humidity for different times. The films were formed under different annealing time. b) A photograph of a MAPbI₃ SCs after storing in air without encapsulation for more than 2 years. Reproduced with permission.⁶⁶ Copyright 2016, The Royal Society of Chemistry c) Example of a relative reflectance spectra (of nonpolarized light at grazing incidence) of 300 nm thick MAPbI₃ on a thick Au layer measured in

vacuum and in ambient condition s(left panel). AFM measurement of the corresponding film in air (right panel). Reproduced with permission of ref.⁶⁵ Copyright 2015. American Chemical Society

Certainly, upon water exposure and due to the hygroscopic nature of the organic components, water molecules may diffuse into the perovskite matrix or form the $\text{MAPbI}_3 \cdot \text{H}_2\text{O}$ complex, acting as a charge trap center.^{6, 62} In microcrystalline perovskite films the grain and GBs of the thin amorphous intergranular layer are more sensitive to moisture^{4, 66} in comparison to SCs compounds.

The phenomenon of the rapid embedding of water into MAPbI_3 was observed in MCs samples (See **Chapter 3** for sample preparation). **Figure 2.5b** shows a top-view SEM image of a degraded MCs sample of MAPbI_3 measured under ambient conditions. In here, it is apparent that the open structure of the GBs is favorable for quick diffusion of moisture along the grains and into the MCs films. Oxygen and moisture creates numerous degradation pathways, **Figure 2.5c** shows clear signs of surface decomposition, which is a major challenge for their application on a commercial scale.⁹ Therefore, to ensure long-term stability of the device, preparation of perovskite layers is usually carried out under isolated atmosphere (in N_2 flow with H_2O , and O_2 levels < 0.5 ppm).

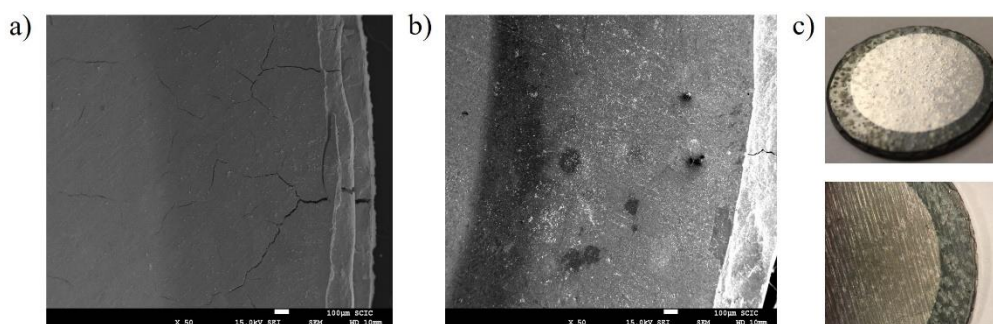


Figure 2.5. SEM top-view image of a MCs perovskite of MAPbI_3 a) fresh sample and b) degraded sample c) Picture of a MAPbI_3 pellet upon exposure of ambient (RH > 50 %).

One of our strategies to avoid sample degradation was using a constant N_2 flow and moisture control. A sample holder presented in **Figure 2.6** coupled to constant N_2 flow was employed for the longtime measurements. Lower reactivity and selective contacts/electrodes were also used to avoid intrinsic degradation. Reactive contacts may accelerate the degradation of perovskite bulk under external factors, such as moisture, oxygen, UV light, elevated temperatures and electric bias.⁵ In fact, the

reactivity at the perovskite/metal electrode interface is a common issue and despite the efforts made to identify the precise interfacial reactions limiting the device stability/performance. The topic is still controversial as it is not clear the techniques able to probe the perovskite/metal interface. Herein, Au electrodes were discarded due to the reported metal migration from the electrode inside the perovskite layer.⁶⁷ Chemical interaction and degradation has been observed in MAPbBr₃ single crystal when put into direct contact perovskite/Au.^{64, 68} Other low-cost commonly used contacting metals are Al and Ag, unfortunately, they have been found to promote irreversible degradation pathways when diffused ions from the perovskite react with the metal electrode creating metal–halide compounds and accumulating halide ion byproducts.⁶⁹ Even so, visual indications of corrosion of the metal electrode is present in both cases.⁷⁰ The use of Cr₂O₃/Cr as electrodes have been proposed to enhance the stability.^{16, 52} Therefore, Pt and Cr₂O₃/Cr were chosen as less reactive metals contact⁷¹ based on previous reports^{16, 33, 44, 55} as they do not degrade the perovskite films. Reinforcing that assumption, we found high reproducibility in our measurements with no visible degradation after using the N₂ flow and with low levels of H₂O, and O₂ (<1 ppm) during and after the data acquisition which allowed to discard contact reactions.

Another alternative to avoid sample degradation under O₂ and moisture is the encapsulation method. Encapsulating these devices is an alternative to address the stability issue without affecting the device lifetime and performance.⁷²

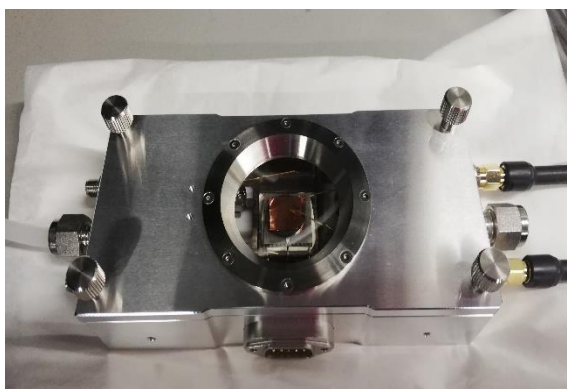


Figure 2.6. Sample holder used for all the electrical measurements with nitrogen flow system.

Nowadays the utilization of materials and structures with higher barrier performance for oxygen and moisture has been an effective alternative to overcome these questions and enhance device stability in solar cells, photodetectors and X-ray sensors.⁷³

2.1.3 Effects of the Temperature and UV-light

In addition to thermal and moisture degradation mechanism, exposure to light may cause device degradation related to chemical interactions between electrode layers/metal contact and the perovskite material. MHPs for radiation detection should be capable of sustained operation at controlled temperatures. Compact, room temperature X-ray detectors are of interest in many areas including diagnostic X-ray imaging, radiation protection and dosimetry. In the case of X-ray detectors based on perovskite materials, improving device photo-stability remains challenging, it has been reported that perovskite thin films begin to decompose at temperatures close to 140 °C in air⁷⁴ or at lower values (~ 85 °C) even in nitrogen atmosphere.⁷⁵ Although, occasionally, the device performance can be recovered when stored in the dark for a short time.⁷⁶ Leijtens et al., reported that the structural symmetry can be reduced at lower temperatures (orthorhombic phase), while higher temperatures allow the transitions to the cubic phase, which means that the material exists in the useful tetragonal and cubic phases at relevant temperatures (0–100 °C).⁷²

However, concerns about the volatility of the organic decomposition products have guided researchers to look for replacing strategies with inorganic cations.^{72, 77} The thermal stability can be improved by the incorporation of around a 20-30% of bromide in the composition.⁷⁸ In fact, this partial substitution of the relatively smaller Br atom for the bulky I anion promoted a more thermodynamically favorable structure at room temperature.⁷⁷⁻⁷⁹ In the case of single crystals with Br in the structure, several reports proved that SCs do not undergo thermal decomposition until temperatures in excess of 200°C,^{28, 80} which make them ideal for a radiation detector.

Wang et al. reported that MAPbI₃ SCs can be stored in ambient atmosphere for 2 years without any encapsulation looking black and shiny without notable degradation (See **Figure 2.4b**)⁶⁶ The SCs growth in this thesis (**Figure 2.7a**) were measured under 1 sun illumination (100 mW cm⁻²) for the charging transient experiment in **Chapter 7**.⁸¹ The charging transient analysis is an experimental technique based on transient polarization signals very similar to the well-known Sawyer-Tower experiments (See **Chapter 3**, charging measurements). **Figure 2.7a** displays a part of the circuit setup used during the illumination measurement of the single crystal of MAPbBr₃ and **Figure 2.7b** shows a SEM image of the top view of the SCs sample after the measurements with no visible sign of degradation.

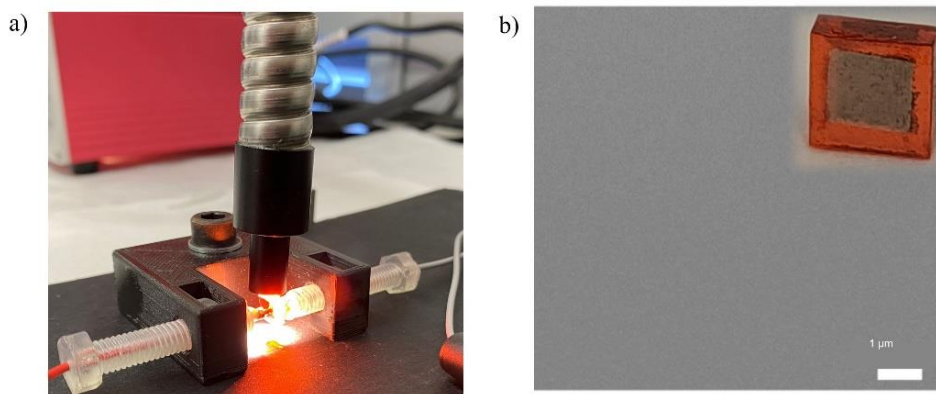


Figure 2.7. a) Example of the Sawyer-Tower setup for the charging measurements under 1 Sun illumination of SCs of MAPbBr₃. b) SEM image of a SCs of MAPbBr₃. In the inset the MAPbBr₃ contacted with Pt electrodes.

However, for the pellets studied in this thesis (MAPbI₃-MCs) light-induced degradation was examined when the samples were measured without N₂ flow at ambient temperature. This chemical reactivity has been studied and associated to the interaction between migrating ions and external contacts by exploring the j - V response in solar cells.^{10, 82} Light can also induce phase segregation,⁸³ enhance piezoelectricity,⁸⁴ and change dipole moments of the unit cell.⁸⁵ With all this observation of halides phase segregation one can hypothesize about the existence of mobile ions as another critical issue in perovskite materials.

So far, we have proved that perovskite materials, as soft matter systems, are sensible to oxygen, light, moisture, and temperature. Consequently, their application and commercialization are still a major bottleneck, especially in countries with high severe humidity conditions and high average temperatures. Therefore, new perovskite families with improved light and thermal stability should be proposed with variable architectures using an array of selective contact layers, which can introduce or eliminate degradation routes. The next section presents other significant factors affecting the dark current response of MHPs. The aim is to provide a coherent picture allowing to correlate the chemical composition with the defect redistribution within the device when an external bias is applied.

2.2 Effect of the electrical bias

X-ray detectors usually work under high electrical fields. Therefore, electrical bias-dependent degradation is another puzzling topic in perovskite materials used to this

purpose. The bias condition, usually, alter the internal fields leading to large variations in the current–voltage characteristics depending on the electrical history of the device.^{48, 86-87} Such biasing may also influence the long-term electrical stability of the device by promoting electrical stress and degradation pathways.⁸⁸

The electrical hysteresis phenomena (See **Figure 2.8a**) has been widely observed in solar cells through the current–voltage (j - V) measurements. It has been linked to external parameters such as scan rate, scan direction, pre-biasing voltage and light intensity, etc. Several reports have proposed strategies to resolve the hysteresis issue in hybrid perovskite solar cells,^{13, 71, 76, 84, 89-96}. Yet, it's well-known that the origin of the hysteresis cannot be attributed to only one underlying mechanism. Charge trapping, capacitive effects, ferroelectricity, and ion migration have been proposed (See **Figure 2.9**) as possible causes, but there is no conclusion or consensus about one theory that could explain all the phenomenology connected to the hysteresis phenomenon.

A number of assumptions and definitions have been proposed for a deeper comprehension of the dark current phenomena and the different conductive regimes found in a typical semiconductor device based on MHPs. In general, for a SeC device with n charge-carrier concentration, current density is proportional to the product of carrier mobility and intrinsic carrier concentration of the perovskite at a constant electrical field. When a negligible space-charge density throughout the bulk is assumed, the ohmic regime in which the current rises linearly with the voltage, is given by the Ohm's law. Current density is described as:

$$J = \sigma E = qn\mu \frac{V}{L} \quad (2),$$

In here, σ is the electronic conductivity; E is the electric field, q is the electronic charge and μ is the charge-carrier mobility. The electrical field is equal to $\frac{V}{L}$, where V is the applied voltage and L is the device thickness and the electronic conductivity is defined as $\sigma = qn\mu$.⁹⁷ Metal halide perovskites are known to present intrinsically high carrier concentration, which leads to relatively small resistivity (eg, MAPbI₃: $10^7 \Omega \text{ cm}$)⁹⁸⁻¹⁰⁰ with large dark current values.^{55, 98} Additionally, the ionic bonding nature of the material, predicts that ions tend to migrate under electrical bias (see **section 2.2.2: Ion migration**), which causes ionic conductivity, and thus increases the

current background leading to baseline drifting and deviations from Ohm's law.^{18, 101-102} When that happens and the space-charge region from both contacts overlap the drift current-density profile for a single carrier device is assumed to follow a different regime known as Space-Charge Limited Current (SCLC) and the Mott-Gurney law (See **Figure 2.8b**):

$$J = \frac{9}{8} \mu \epsilon_r \epsilon_0 \frac{V^2}{L^3} \quad (2.1),$$

where ϵ_r is the dielectric constant and ϵ_0 is the permittivity of free space

In fact, SCLC measurements are the most commonly used steady-state techniques to study the influence of mobile ion, defect densities and carrier mobilities in perovskites but their use is still controversial.¹⁰³

Duijnsteet et al., introduced a pulsed voltage space-charge limited current (PV-SCLC) measurement methodology,¹⁰³ with the aim of diminishing the motion of mobile ions and to further achieve reproducible current-voltage characteristics without hysteresis (**Figure 2.8b**). Other conductive regimes may occur when ($J \propto V^n$, $n > 1.5$ or $n > 2$) Child-Langmuir ballistic regime of SCLC¹⁰⁴ or trap-filled limited region,¹⁰³ respectively.

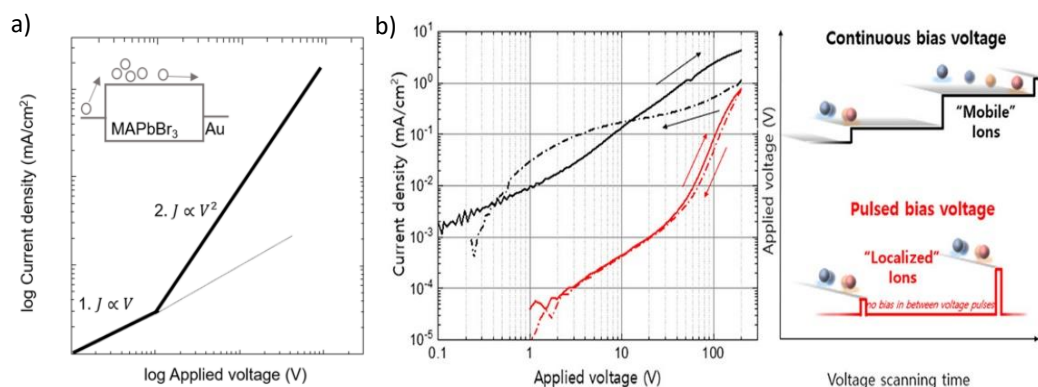


Figure 2.8. a) SCLC behavior for a trap-free semiconductor. Two charge transport regions are visible: (1. $J \propto V$) Ohmic region and (2. $J \propto V^2$) SCLC region b) Large hysteresis between forward (solid line) and reverse (dashed line) J - V traces during the SCLC measurement in a perovskite SCs. (Right): Schematic illustration of ion movement upon continuous bias application during the SCLC measurement. At positive voltage during the forward scan mobile ions drift toward the electrode interfaces. Mobile ions are still displaced toward the electrode interfaces during the reverse scan. (black label). In the PV-SCLC method no redistribution of mobile ions through the sample is observed (red label) conductivity. Reproduced with permission.¹⁰³ Copyright 2020. American Chemical Society

All this information helps to understand the trend of a dark j - V curve in a conventional halide perovskite. However, the analysis of the j - V response should be taken with caution because many artifacts and anomalous behavior have been reported.¹⁰⁵⁻¹⁰⁶ These puzzling peculiarities arise from the mixed ionic-electronic conductivity of this class of semiconductor.¹⁰⁷ Thus, many hypotheses have been formulated, some of them focused on capacitive effects⁹⁰ and others into slow transients in the injection current.¹⁰⁶ Although, an ionic origin is commonly assumed in the literature.¹⁰⁸⁻¹¹⁰ Therefore, radiation detectors with a desirable long-term electrical stability and a minimum dark current level can be only designed by considering the link between mobile ions and electronic conductivity. In order to unveil that, the next sections include a discussion on the electrical stability in radiation detectors based on perovskite materials, i.e., the dark current response and the influence on mobile ions on those levels of electric current.

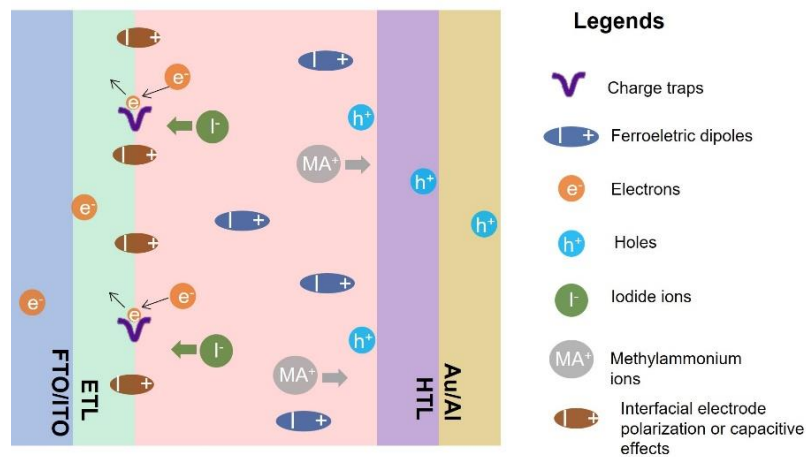


Figure 2.9. Schematic diagram shows the various ion/defects movements in a perovskite device structure that could possibly lead to hysteresis phenomenon during current-voltage characteristic measurements. The exact nature of each ion-movement processes and its degree of influence on hysteresis varies with respect to the device structure and materials involved. Reprinted with permission from⁹². Copyright 2018. Solar Energy Materials and Solar Cells.

2.2.1 Dark current

Another important parameter of a radiation detector is the dark current (leakage current) I_{dark} which is defined as the current flowing in absence of any radiation stimulus. In the **section 1.3 in Chapter 1** it is mentioned how important are electrical contacts to minimize leakage currents in a radiation detector. The “ideal” device should have the smallest possible dark current to reduce the noise, as the detector noise

determines the lowest detectable dose and the signal-to-noise ratio.^{28, 53} Usually in most radiation detectors based on semiconductor materials, background electronic noise is due to the fluctuation of the dark current.⁸⁶ Under bias, the main contributions to dark current result from (i) the presence of defective states, (ii) thermal charge carrier in the bulk and (iii) the injection of carriers at the electrodes interface. Kasap et al.⁸⁶ suggested an ideal value of dark current in SeC detectors between 0.1–1 nA cm⁻² but today's commercially available detectors have dark current < 50 nA cm⁻² close to the acceptable value of 10 nA cm⁻².²⁸ The origin of the leakage current is related to both the bulk volume and the surface of the detector. Therefore, great care should be taken in the fabrication of SeC detectors to avoid contamination of the surfaces, which could create leakage paths. For example, a few authors reported the use of guard rings which is a metal circle traditionally used to protect high impedance nodes in a circuit from surface leakage currents.³⁶

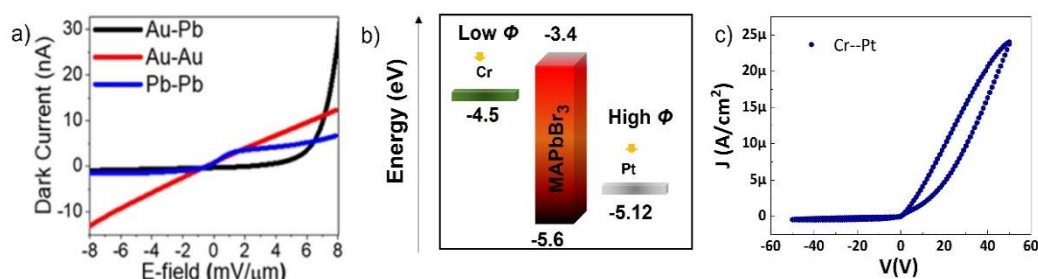


Figure 2.10. a) Example of the dark current as a function of electric field for a MAPbI₃ single-crystal devices with Pb–Pb (blue), Au–Au (red), and Au–Pb (black) lateral contacts. Adapted with permission.¹¹¹ Copyright 2020 American Chemical Society b) Energy band gap diagram showing the metal work function c) *j*-*V* characteristic curve for a MAPbI₃ microcrystalline sample with an asymmetric metal contact-perovskite configuration

Strategies to reduce dark current are extensively applied in X-ray detectors, the small bandgap (0.7 eV) of Germanium detectors which is one of the most useful sensors in the field, is related to the large thermally induced leakage current and does not allow to the standard high purity germanium (HPGe) to operate at room temperature. The result is that HPGe detectors must be cooled to reduce these levels to the point that the associated noise does not spoil their excellent energy resolution.^{56, 112} Another way to reduce dark current is to choose semiconductor materials with a wider band gap (e.g., greater than 1.5 eV), that could reduce the bulk-generated

leakage current allowing to operate at room temperature.¹¹³ Based on different reports,^{45, 53, 114} Shrestha et al. proposed blocking interfaces to minimize the dark current noise. They designed a SCs of MAPbI₃ lateral contacted with different work functions (Pb//MAPbI₃//Au device configuration) and the dark current on reverse bias showed to be lower by more than an order of magnitude in comparison to their symmetric counterpart Au– Au device (See **Figure 2.10a**).¹¹¹ Due to the rectifying nature of this configuration, an asymmetric face to face device Cr//MAPbI₃//Pt was developed in this thesis¹¹⁵ showing almost non hysteresis at reverse bias during the *j*-*V* scan measurement (See **Figure 2.10c**)

Finally, it has been observed by several authors^{63-64, 116} that the electrochemical-reaction occurring at the anode site: $\text{Au}_{(0)} + 2\text{I}^- \longrightarrow [\text{AuI}_2]^- + 2\text{V}_\text{I} + \text{h}^+$ and induced by the external polarization in MAPbI₃ SCs symmetrically contacted with Au, increase the dark current in the device. Hence, they reported the use of blocking layers between the electrodes and the SCs to suppress the dark current, at least, 3 orders of magnitude making possible to fabricate highly sensitive and fast response X-ray detectors.¹¹⁷ Undoubtedly, going through the mechanism behind the long-term dark current stability of X-ray detectors needs a closer look to the ion migration process. The next section intent to provide the recent efforts and related progress in this topic as well as the strategies developed with the goal of quantify ion migration parameters.

2.2.2 Ion Migration

Ionic motion strongly influences the electronic charge-carrier dynamics in MHPs. The existence of drifting and diffusing mobile ions makes the use of traditional electrical characterization techniques questionable, due to the electronic-ionic nature of this conductor. This section summarizes the origin of ion migration and its connection with the device electronic performance. It is also discussed some of the tools and electrical protocols designed for characterizing ion migration.

Ion migration occurs in MHPs crystalline materials in many circumstances. The soft ionic crystal structure easily collapses due to its ionic conductive nature, hence the migration of halide vacancies prevails compared to larger cations.^{13, 17} One of the first reports about the existence of iodoplumbates as mixed conductors in MAPbI₃ solar cells was published by Yang et al.¹¹⁸ Afterwards, Xiao et al., reported the observation of a field-switchable photovoltaic effect by the formation of reversible p–i–n structures induced by ion drift in the perovskite layer.¹¹⁹ In a recent report, Sakhatskyi et al.

showed the stability performance of different perovskite composition as a function of the expected ion diffusion coefficient.¹²⁰ These findings highlight that ionic transport is a process of hopping between equilibrium sites of the ions that occupy interstitials and defects. They point out that the migration of halide vacancies prevails compared to larger cations. Though, at long operation times and under external driving forces such as voltage, light, and temperature, organic cations, and metal electrode ions also diffuse through the perovskite material. (See **Figure 2.11**).

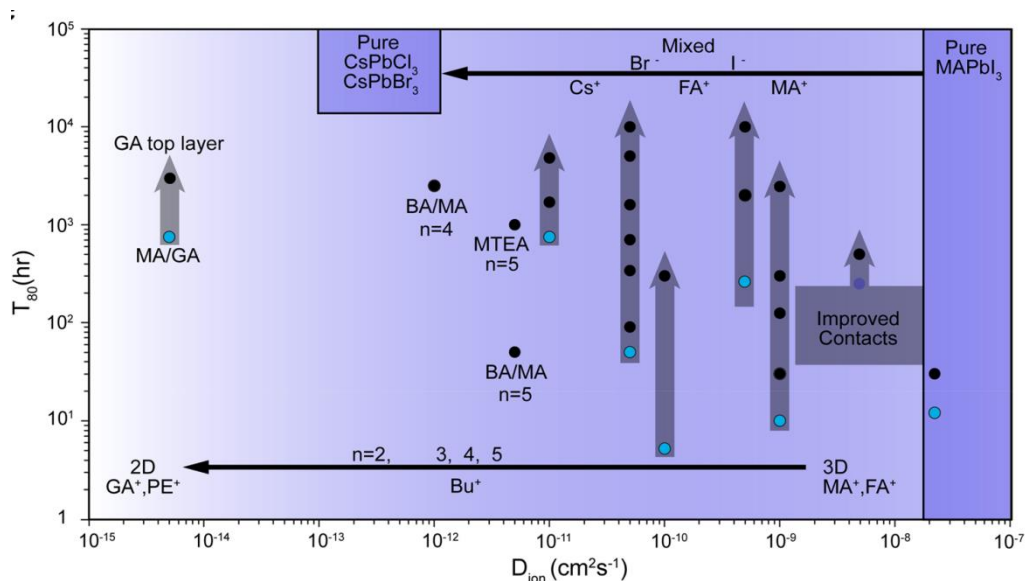


Figure 2.11. a) Stability performance (T_{80}) under 1 sun illumination condition and maximum power point tracking (MPPT) of selected literature examples as a function of the expected ion diffusion coefficient (D_{ion}). Reprinted with permission of ref.¹²⁰ Copyright 2022, American Chemical Society.

Other reports showed that mobile ionic species has the potential to profoundly disturb device characteristics, by shielding the bulk material from externally applied voltages and thus affecting the total electronic current injection, transport, and extraction.¹²¹⁻¹²⁵ In those reports, an important parameter is the activation energy (AE) which is the lowest free energy barrier that ions need to overcome to move from its initial position to an adjacent position.

Table 2.1 shows the activation energies calculated by computational methods by Azpiroz et al.¹⁰¹ Several investigations have shown defects with different activation energies in perovskite materials.¹³ Being the halide vacancies the one with the smallest AE it was suggested by numerous authors^{13, 19, 101, 126-127} to be halide vacancies the faster mobile ionic species. On the other hand, those AE values around ~ 0.5 and 0.8

eV for MA and Pb vacancies, respectively, were found to be the responsible to the slow response inherent to perovskites.¹²¹

Table 2.1 Calculated activation energies for the different point defects migrating of the in MAPbI₃ and MAPbBr₃ perovskite¹⁰¹

Defect	MAPbI ₃	MAPbBr ₃
	E _a (eV)	E _a (eV)
V _{I/Br}	0.08	0.09
V _{MA}	0.46	0.56
V _{Pb}	0.80	NR
I _i	0.08	NR

*NR: not reported

In **Figure 2.12** formation energies of all possible point defects in MAPbI₃ are presented from MA, Pb, I vacancies (V_{MA}, V_{Pb}, and V_I) and interstitials (MA_i, Pb_i, and I_i) to cation and anion substitutions. Depending on the chemical potential of the constituted element, formation energies of all point defects can be calculated.¹²⁸ Thus, ion migration can occur by vacancy migration, interstitial ion hopping or even other mechanisms, but the migration process itself is usually carried out through the internal defects such as Schottky and Frenkel defects (See **Figure 2.13**).¹²¹ The migration paths have been extensively studied showing other possibilities for ion migration such as lattice distortion or disorder caused by local charge accumulation or dissolution of impurities, lattice softening, piezoelectric effects and strain induced effect.^{22, 84, 92-93, 129} Grains and grain boundaries can be also, channels for ion motion resulting in poorer stability of the sample.¹²⁷ Still any change of the perovskite formulation can affect the crystal structure and the crystallinity nature of the perovskite.

Halogen ions are the highly mobile and reactive species, tending to diffuse out of the perovskite layer, reacting with some device components and inducing interfacial degradation.⁶⁴ Wang et al. reported some characteristic timescales of the kinetic phenomena in PSCs of MAPbI₃ and MAPbBr₃. They reported a time transport value over a distance of 100 nm in a MAPbI₃ film of 10⁻² s for the halide vacancy diffusion, a value between ~10-100 s for ions at the interface and ~1000 s for cation vacancy diffusion.¹²⁹ Indeed, the mobility of MA⁺ affect the optoelectronic properties and the long-term stability of many perovskites devices. Actually, intrinsic cations are also capable of significantly diffuse creating a spatial inhomogeneity under different stimulus such as bias, oxygen, and humidity environment.^{8, 110, 120, 126}

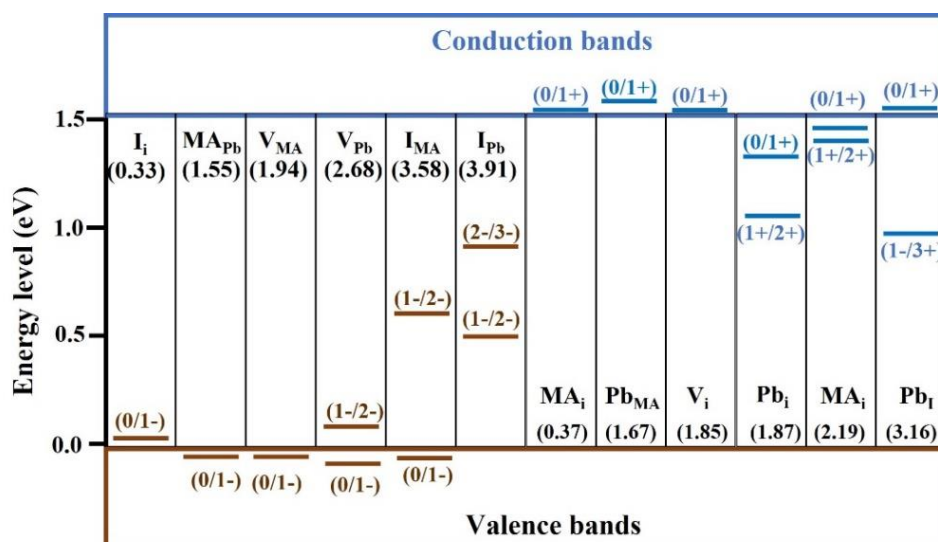


Figure 2.12. Calculated transition energy levels of point defects in $CH_3NH_3PbI_3$.¹²⁸ The formation energies of neutral defects are shown in parentheses. The acceptors/donors are ordered by the formation energies (from left to right) Adapted with permission.¹³⁰ Copyright 2018. Springer Nature.

Mapping ion migration is an additional challenging topic, numerous advanced characterization techniques including optical spectroscopy, electron spectrometry, mass spectrometry, atomic force microscopy, and electrical measurements have been used with this purpose. McGovern et al., used Transient Ion Drift (TID) to quantify the characteristics of mobile ions in $MAPbBr_3$ in order to compare them with in $MAPbI_3$ (See **Figure 2.14**). In that work they demonstrated a reduced activation energy, a reduced diffusion coefficient, and a reduced concentration for halide ions in $MAPbBr_3$ in comparison with $MAPbI_3$.¹³¹ Explanation to this experimental observation can be based on the stronger Pb–Br bond between atoms in $MAPbBr_3$ samples compared to the bond between Pb–I in I-based perovskites. This may create a lattice contraction suppressing the ion migration of the bulky MA^+ ion in Br-based perovskites. It has been also reported a smaller stronger hydrogen bonding to the surrounding Pb–Br₆ octahedra in $MAPbBr_3$.^{126, 131}

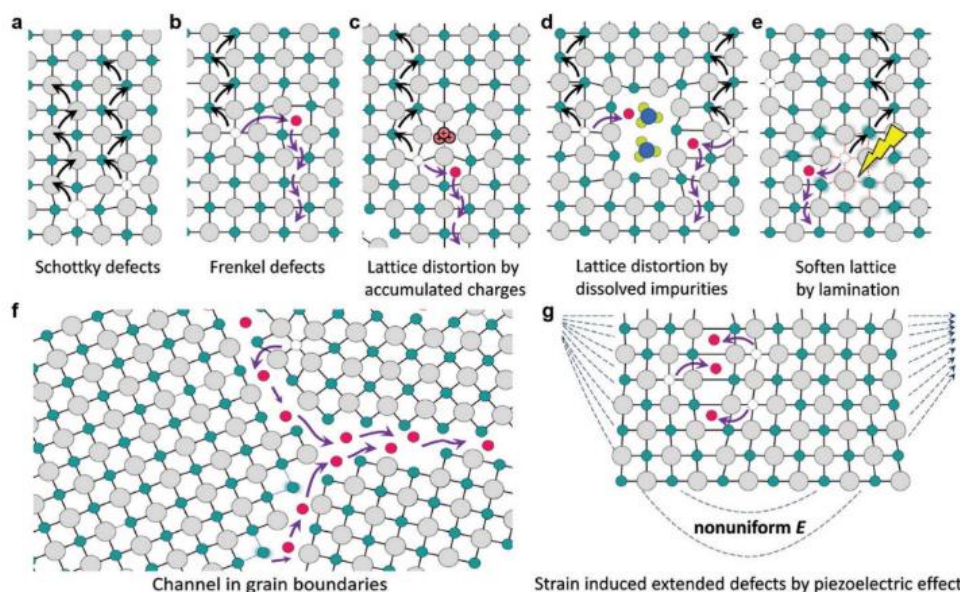


Figure 2.13. Ion migration paths in halide perovskites. a) Schottky and b) Frenkel defects. c) Lattice distortion by accumulated charges. d) Lattice distortion by dissolved impurities. e) Softened lattice by lamination. f) Channel in grain boundaries. g) Strain-induced extended defects by piezoelectric effect. Reproduced with permission.¹²⁷ Copyright 2016, American Chemical Society.

A similar approach was used in this study by recording the long-term current transient of different perovskite devices.^{126, 132} In here, we reported a coupling between electronic transport and ion kinetics exists that ultimately establishes the time scale of electronic current (See results and discussion in **Chapter 6 and 8**). We calculated ion migration providing an estimation of the intrinsic parameters such as the ionic mobility and diffusion coefficients.^{115, 132}

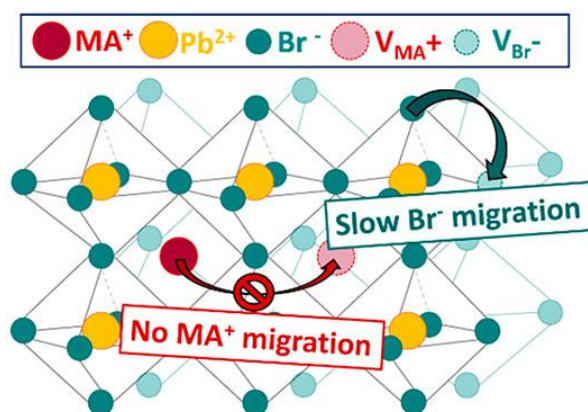


Figure 2.14. Comparison of mobile ions in MAPbBr_3 and MAPbI_3 showing the suppression of migration paths due to a reduced activation energy for bromide migration compared to iodine. Reprinted with permission of Ref.¹³¹ Copyright 2020, American Chemical Society.

Other approach that helps to quantify ion migration is Impedance Spectroscopy (IS) measurements. This is a robust, nondestructive method to study charge and ion transport processes.^{36, 40, 133} It has been extensively used as a powerful tool to understand the origin of photoinduced degradation in perovskite films or solar cells based on MAPbI₃.¹³⁴⁻¹³⁶

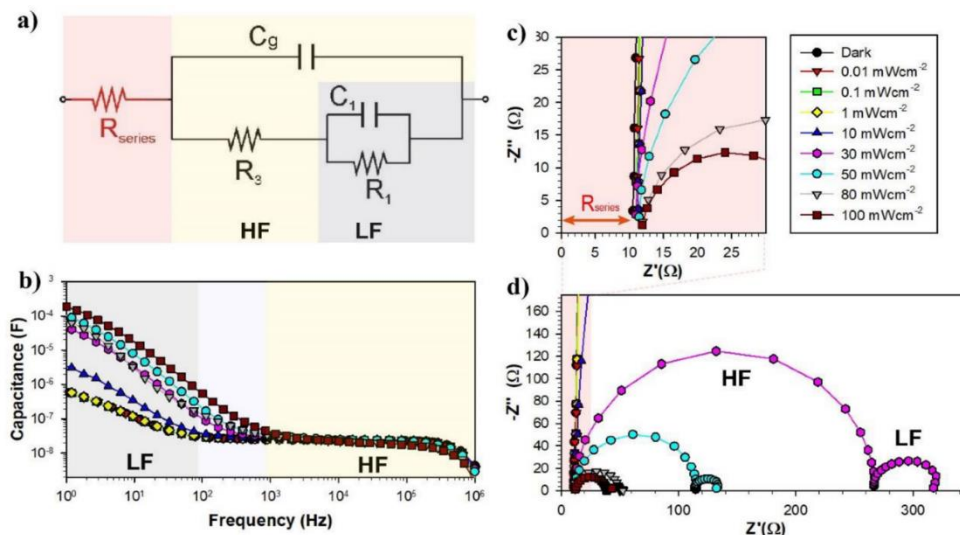


Figure 2.15. Comparison (a) Representative EC used to fit the data for MHP devices containing adequate extraction layers from the (b) capacitance frequency plots (c) and (d) complex impedance plot. Reprinted with permission of ref.¹³³ Copyright 2021. American Chemical Society

Figure 2.15 shows different features in the Nyquist plot (Impedance spectra, c and d) and the Bode plot (Capacitance response, b) that can be observed in a typical MAPI device under different illumination conditions.¹³³ Because the IS response usually corresponds to the least resistive pathways and a reduced number of elements are present in the spectra, simplified circuits, such as the one presented in **Figure 2.15a** are selected in order to extract equivalent electrical elements that cause the observed response and ultimately provide a physical interpretation.^{134, 137} The IS analysis usually covers the whole range of frequencies between 1 MHz and 10 mHz allowing to understand how to distinguish between electronic and ionic defects considering the time scales involved in the different process.¹⁰¹⁻¹⁰²

In any case, the number of possible research questions are endless toward clarifying the role ion transport in the degradation of PSCs. For example, Bag et al. were pioneers in studying the Warburg-like response in these materials.¹²² Moreover, Peng et al, calculated diffusion coefficients in the order of $\sim 10^{-8}$ cm² s⁻¹ in MAPbBr₃ single crystals by analyzing the low frequency response in IS.¹³⁸ Recently, Yan et al.

measured the Warburg resistance relating to ion migration to obtain the diffusion coefficient and activation energy of migration ion.¹⁷

In this respect, impedance measurements were carried out in ambient conditions¹⁶ (in **Chapter 4**) and under N₂ flow (in **Chapters 6 and 8**).^{115, 126} Results in those chapters showed high reproducibility of the electrical response by IS. This approach enables to study the mobile ions and how these defect species alter the internal electrical field, interact with the contact materials, or even modulate electronic properties. This mobile ionic dopant produces a sort of dynamic doping effect that locally vary the electronic conductivity (See about the IDD model in **Chapters 4 and 6**).¹¹⁵

Ultimately, the important question is how this ion migration governs the electronic current for the long-term operational stability of the perovskite-based detector. In this thesis we developed a robust electrical protocol with the aim of exploring the long-term stability response of device under polarization.¹³² **Figure 2.16** displays an example of the long-term current response under different biasing protocols of samples of MAPbI₃ with similar thickness. As a general trend, at the beginning of the transient the current rapidly increases with an exponential behavior until saturation to steady state. In the case of **Figure 2.16a**, this behavior is not clear; current does not seem to saturate and no reproducibility between cycles of polarization is observed under the different bias steps. Additionally, visible signs of surface degradation are observed in the measured sample in **Figure 2.16b**. A subsequent experiment was performed in **Figure 2.16c** and this time, the variability of responses was smaller compared to the first measurement. One explanation regarding the different current increases between transient protocols and cycles point out to the shorter relaxation times used, less than 3 hours for the first procedure and 4 hours for the second one. After 4 hours at short circuit condition (0 V-bias) the sample is in a completely relaxed state. In all cases, Cu-conductive tape of high quality was used on top of the pellets to ensure a better electrical contact. Still, the top image of **Figure 2.16b**. shows a degraded MAPbI₃ pellet after the first cycle of biasing experiments and the other two images below (**Figure 2.16b**) showed a homogenous surface at both side of the sample (Pt//Cr electrodes) and no visible surface degradation was seen for the second tested protocol.

We reported a high reproducibility for current registered at different cycles with the measurement protocol showed in (c).^{126, 132} Additionally, in **Chapter 8** we showed the effective ion mobility calculated from the analysis of the long-term dark current

response of MHPs of different crystallinity and composition by using the optimized protocol in **Figure 2.16c**.

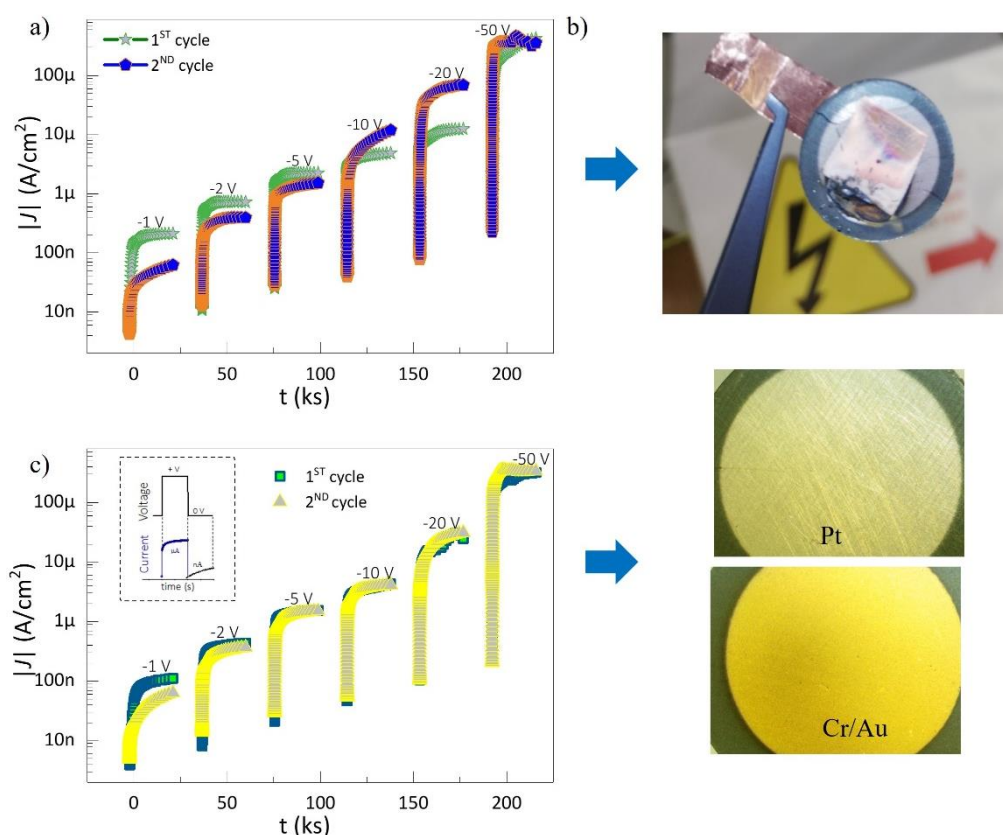


Figure 2.16. a) Long-term current response under consecutive bias of a MAPbI₃ thick pellet at room temperature (first biasing protocol). b) Image of the top view of a MAPbI₃ thick after the respective measurement protocol c) Long-term current response under consecutive bias for a MAPbI₃ thick pellet at room temperature (second biasing protocol). In the inset is shown the biasing protocol.

In conclusion, MHPs bring an unprecedented opportunity for radiation detection but ionic defects at the surfaces and grain boundaries are detrimental to both the perovskite-based detector efficacy and long-term stability. In this thesis, we have proven that MAPbBr₃-SCs perovskite is preferred when longtime measurements are required due to the higher structural stability. Moreover, controlling the exposure to light intensity, oxygen, and moisture by using constant N₂ flow and a Faraday cage allowed to reduce interfacial degradation in these materials. Regarding the chemical interactions between top metal contact and perovskite material, Pt and Cr as contact electrodes were chosen. Pt is one of the least reactive metals known towards the perovskite material, an inert material which does not react with the perovskite films,

being a better choice when preferring an inert enough substrate on perovskite films. Additionally, the use of $\text{Cr}_2\text{O}_3/\text{Cr}$ as electrodes have been proposed to enhance the stability in comparison to Au, Ag as metal contacts. Finally, from the electrical measurements it is highlighted the importance of designing robust measuring procedures in exploring thick perovskite electrical response.

Overall, in this PhD thesis we have shown that it is possible to obtain reproducible and reliable measurements to characterize ion migration and its influence on the dark current response of perovskite devices. Engineering the composition and architecture of the device by controlling the external interfaces allow us to discern the transport mechanisms of mobile species under variable electrical fields with the aim to create a coherent picture for the design of the next generation of X-ray detectors based on perovskite materials.

References

1. Choi, J. I. J.; Khan, M. E.; Hawash, Z.; Kim, K. J.; Lee, H.; Ono, L. K.; Qi, Y.; Kim, Y.-H.; Park, J. Y., Atomic-Scale View of Stability and Degradation of Single-Crystal MAPbBr_3 Surfaces. *J. Mater. Chem. A* **2019**, *7*, 20760-20766.
2. Bozano, L.; Carter, A.; Scott, J. C.; Malliaras, G. G.; Brock, P. J., Temperature- and Field-Dependent Electron and Hole Mobilities in Polymer Light-Emitting Diodes. *Appl. Phys. Lett.* **1999**, *74*, 1132-1134.
3. Zarazua, I.; Bisquert, J.; Garcia-Belmonte, G., Light-Induced Space-Charge Accumulation Zone as Photovoltaic Mechanism in Perovskite Solar Cells. *J. Phys. Chem. Lett.* **2016**, *7*, 525-528.
4. Xing, J.; Wang, Q.; Dong, Q.; Yuan, Y.; Fang, Y.; Huang, J., Ultrafast Ion Migration in Hybrid Perovskite Polycrystalline Thin Films under Light and Suppression in Single Crystals. *Phys. Chem. Chem. Phys.* **2016**, *18*, 30484-30490.
5. Roose, B.; Wang, Q.; Abate, A., The Role of Charge Selective Contacts in Perovskite Solar Cell Stability. *Adv. Energy Mater.* **2019**, *9*, 1803140.
6. Yang, J.; Yuan, Z.; Liu, X.; Braun, S.; Li, Y.; Tang, J.; Gao, F.; Duan, C.; Fahlman, M.; Bao, Q., Oxygen- and Water-Induced Energetics Degradation in Organometal Halide Perovskites. *ACS Appl Mater Interfaces* **2018**, *10*, 16225-16230.
7. Yang, L.; Li, Y.; Sun, Y.; Wang, W.; Shao, Z., Perovskite Oxides in Catalytic Combustion of Volatile Organic Compounds: Recent Advances and Future Prospects. *Energy Environ. Mater.* **2021**, *0*, 1-26.
8. Aristidou, N.; Sanchez-Molina, I.; Chotchuangchutchaval, T.; Brown, M.; Martinez, L.; Rath, T.; Haque, S. A., The Role of Oxygen in the Degradation of Methylammonium Lead Trihalide Perovskite Photoactive Layers. *Angewandte Chemie (International ed. in English)* **2015**, *54*, 8208-12.
9. Bick, D. S.; Kindsmüller, A.; Staikov, G.; Gunkel, F.; Müller, D.; Schneller, T.; Waser, R.; Valov, I., Stability and Degradation of Perovskite Electrocatalysts for Oxygen Evolution Reaction. *Electrochim. Acta* **2016**, *218*, 156-162.
10. Guerrero, A.; You, J.; Aranda, C.; Kang, Y. S.; Garcia-Belmonte, G.; Zhou, H.; Bisquert, J.; Yang, Y., Interfacial Degradation of Planar Lead Halide Perovskite Solar Cells. *ACS Nano* **2016**, *10*, 218-224.
11. Aranda, C.; Cristobal, C.; Shooshtari, L.; Li, C.; Huettner, S.; Guerrero, A., Formation Criteria of High Efficiency Perovskite Solar Cells under Ambient Conditions. *Sustainable Energy Fuels* **2017**, *1*, 540-547.
12. Xiao, S.; Zhang, K.; Zheng, S.; Yang, S., Good or Evil: What Is the Role of Water in Crystallization of Organometal Halide Perovskites? *Nanoscale Horizons* **2020**, *5*, 1147-1154.
13. Zhu, W.; Wang, S.; Zhang, X.; Wang, A.; Wu, C.; Hao, F., Ion Migration in Organic-Inorganic Hybrid Perovskite Solar Cells: Current Understanding and Perspectives. *Small* **2022**, *18*, 2105783.
14. Schileo, G.; Grancini, G., Halide Perovskites: Current Issues and New Strategies to Push Material and Device Stability. *Journal of Physics: Energy* **2020**, *2*, 021005.
15. Ellis, C. L. C.; Smith, E.; Javaid, H.; Berns, G.; Venkataraman, D., Chapter 6 - Ion Migration in Hybrid Perovskites: Evolving Understanding of a Dynamic Phenomenon. In *Perovskite Photovoltaics*, Thomas, S.; Thankappan, A., Eds. Academic Press: 2018; pp 163-196.
16. García-Batlle, M.; Baussens, O.; Amari, S.; Zaccaro, J.; Gros-Daillon, E.; Verilhac, J. M.; Guerrero, A.; Garcia-Belmonte, G., Moving Ions Vary Electronic Conductivity in Lead Bromide Perovskite Single Crystals through Dynamic Doping. *Adv. Electron. Mater.* **2020**, *6*, 2000485.

17. Yan, X.; Fan, W.; Cheng, F.; Sun, H.; Xu, C.; Wang, L.; Kang, Z.; Zhang, Y., Ion Migration in Hybrid Perovskites: Classification, Identification, and Manipulation. *Nano Today* **2022**, *44*, 101503.
18. Bertoluzzi, L.; Boyd, C. C.; Rolston, N.; Xu, J.; Prasanna, R.; O'Regan, B. C.; McGehee, M. D., Mobile Ion Concentration Measurement and Open-Access Band Diagram Simulation Platform for Halide Perovskite Solar Cells. *Joule* **2020**, *4*, 109-127.
19. Futscher, M. H.; Gangishetty, M. K.; Congreve, D. N.; Ehrler, B., Quantifying Mobile Ions and Electronic Defects in Perovskite-Based Devices with Temperature-Dependent Capacitance Measurements: Frequency Vs Time Domain. *J. Chem. Phys.* **2020**, *152*, 044202.
20. Kakavelakis, G.; Gedda, M.; Panagiotopoulos, A.; Kymakis, E.; Anthopoulos, T. D.; Petridis, K., Metal Halide Perovskites for High-Energy Radiation Detection. *Adv. Sci.* **2020**, *7*, 2002098.
21. Yoon, Y. J., et al., Reversible, Full-Color Luminescence by Post-Treatment of Perovskite Nanocrystals. *Joule* **2018**, *2*, 2105-2116.
22. Zhu, C., et al., Strain Engineering in Perovskite Solar Cells and Its Impacts on Carrier Dynamics. *Nat. Commun.* **2019**, *10*, 815.
23. Liu, Y., et al., A 1300 Mm² Ultrahigh-Performance Digital Imaging Assembly Using High-Quality Perovskite Single Crystals. *Adv. Mater.* **2018**, *30*, 1707314.
24. Senocrate, A.; Maier, J., Solid-State Ionics of Hybrid Halide Perovskites. *J. Am. Chem. Soc.* **2019**, *141*, 8382-8396.
25. Tsai, H.; Tisdale, J.; Shrestha, S.; Liu, F.; Nie, W., Emerging Lead-Halide Perovskite Semiconductor for Solid-State Detectors. In *Advanced X-Ray Detector Technologies: Design and Applications*, Iniewski, K., Ed. Springer International Publishing: Cham, 2022; pp 35-58.
26. Zhou, T.; Zhang, T., Recent Progress of Nanostructured Sensing Materials from 0d to 3d: Overview of Structure–Property–Application Relationship for Gas Sensors. *Small Methods* **2021**, *5*, 2100515.
27. Bao, C.; Yang, J.; Bai, S.; Xu, W.; Yan, Z.; Xu, Q.; Liu, J.; Zhang, W.; Gao, F., High Performance and Stable All-Inorganic Metal Halide Perovskite-Based Photodetectors for Optical Communication Applications. *Adv. Mater.* **2018**, *30*, 1803422.
28. Basiricò, L.; Ciavatti, A.; Fraboni, B., Solution-Grown Organic and Perovskite X-Ray Detectors: A New Paradigm for the Direct Detection of Ionizing Radiation. *Adv. Mater. Technol.* **2021**, *6*, 2000475.
29. He, Y., et al., CsPbBr₃ Perovskite Detectors with 1.4% Energy Resolution for High-Energy Γ -Rays. *Nat. Photon.* **2021**, *15*, 36.
30. Wang, H.; Kim, D. H., Perovskite-Based Photodetectors: Materials and Devices. *Chem. Soc. Rev.* **2017**, *46*, 5204-5236.
31. Tan, R.; Dryzhakov, B.; Charest, J.; Hu, B.; Ahmadi, M.; Lukosi, E., Improved Radiation Sensing with Methylammonium Lead Tribromide Perovskite Semiconductors. *Nucl. Instrum. Methods Phys. Res., Sect. A* **2021**, *986*, 164710.
32. Xu, Y., et al., Solution-Processed Epitaxial Growth of MAPbI₃ Single-Crystal Films for Highly Stable Photodetectors. *Front. Mater.* **2021**, *8*.
33. Wu, Y.; Wang, P.; Guan, Z.; Liu, J.; Wang, Z.; Zheng, Z.; Jin, S.; Dai, Y.; Whangbo, M.-H.; Huang, B., Enhancing the Photocatalytic Hydrogen Evolution Activity of Mixed-Halide Perovskite CH₃NH₃PbBr₃-XIX Achieved by Bandgap Funneling of Charge Carriers. *ACS Catal.* **2018**, *8*, 10349-10357.

34. Eperon, G. E.; Stranks, S. D.; Menelaou, C.; Johnston, M. B.; Herz, L. M.; Snaith, H. J., Formamidinium Lead Trihalide: A Broadly Tunable Perovskite for Efficient Planar Heterojunction Solar Cells. *Energy Environ. Sci.* **2014**, *7*, 982-988.
35. Wu, Y.; Li, X.; Wei, Y.; Gu, Y.; Zeng, H., Perovskite Photodetectors with Both Visible-Infrared Dual-Mode Response and Super-Narrowband Characteristics Towards Photo-Communication Encryption Application. *Nanoscale* **2018**, *10*, 359-365.
36. Almora, O.; Matt, G. J.; These, A.; Kanak, A.; Levchuk, I.; Shrestha, S.; Osvet, A.; Brabec, C. J.; Garcia-Belmonte, G., Surface Versus Bulk Currents and Ionic Space-Charge Effects in Cspbbr3 Single Crystals. *J. Phys. Chem. Lett.* **2022**, *13*, 3824-3830.
37. Fu, L.; Li, B.; Li, S.; Yin, L., Magnetic, Electronic, and Optical Properties of Perovskite Materials. In *Revolution of Perovskite: Synthesis, Properties and Applications*, Arul, N. S.; Nithya, V. D., Eds. Springer Singapore: Singapore, 2020; pp 43-59.
38. Stojanovic, B. D., Mechanochemical Synthesis of Ceramic Powders with Perovskite Structure. *J. Mater. Process. Technol.* **2003**, *143-144*, 78-81.
39. Yang, Y.; Yang, M.; Moore, David T.; Yan, Y.; Miller, Elisa M.; Zhu, K.; Beard, Matthew C., Top and Bottom Surfaces Limit Carrier Lifetime in Lead Iodide Perovskite Films. *Nat. Energy* **2017**, *2*, 16207.
40. Afroz, M. A.; Aranda, C. A.; Taylor, N. K.; Yukta; Yadav, P.; Tavakoli, M. M.; Saliba, M.; Satapathi, S., Impedance Spectroscopy for Metal Halide Perovskite Single Crystals: Recent Advances, Challenges, and Solutions. *ACS Energy Lett.* **2021**, 3275-3286.
41. Yu, W., et al., Single Crystal Hybrid Perovskite Field-Effect Transistors. *Nat. Commun.* **2018**, *9*, 5354.
42. Zhu, L.; Ran, R.; Tadé, M.; Wang, W.; Shao, Z., Perovskite Materials in Energy Storage and Conversion. *Asia-Pac. J. Chem. Eng.* **2016**, *11*, 338-369.
43. Wang, X.; Huang, Y.; Lei, W.; Li, Q.; Zhang, X.; Khan, Q.; Wang, B., Asymmetrical Photodetection Response of Methylammonium Lead Bromide Perovskite Single Crystal. *Cryst. Res. Technol.* **2017**, *52*, 1700115.
44. Xie, G.; Yang, X.; Duan, J.; Duan, Y.; Tang, Q., Bulk Pt/Cspbbr3 Schottky Junctions for Charge Boosting in Robust Triboelectric Nanogenerators. *J. Mater. Chem. A* **2020**, *8*, 11966-11975.
45. He, Y., et al., High Spectral Resolution of Gamma-Rays at Room Temperature by Perovskite Cspbbr3 Single Crystals. *Nat. Commun.* **2018**, *9*, 1609.
46. Maculan, G.; Sheikh, A. D.; Abdelhady, A. L.; Saidaminov, M. I.; Haque, M. A.; Murali, B.; Alarousu, E.; Mohammed, O. F.; Wu, T.; Bakr, O. M., Ch3nh3pbcl3 Single Crystals: Inverse Temperature Crystallization and Visible-Blind Uv-Photodetector. *J. Phys. Chem. Lett.* **2015**, *6*, 3781-3786.
47. Saidaminov, M. I., et al., High-Quality Bulk Hybrid Perovskite Single Crystals within Minutes by Inverse Temperature Crystallization. *Nat. Commun.* **2015**, *6*, 7586.
48. Shaikh, P. A.; Shi, D.; Retamal, J. R. D.; Sheikh, A. D.; Haque, M. A.; Kang, C.-F.; He, J.-H.; Bakr, O. M.; Wu, T., Schottky Junctions on Perovskite Single Crystals: Light-Modulated Dielectric Constant and Self-Biased Photodetection. *J. Mater. Chem. C* **2016**, *4*, 8304-8312.
49. Shrestha, S., et al., High-Performance Direct Conversion X-Ray Detectors Based on Sintered Hybrid Lead Triiodide Perovskite Wafers. *Nat. Photon.* **2017**, *11*, 436-440.
50. Xu, Y.; Jiao, B.; Song, T.-B.; Stoumpos, C. C.; He, Y.; Hadar, I.; Lin, W.; Jie, W.; Kanatzidis, M. G., Zero-Dimensional Cs2tei6 Perovskite: Solution-Processed Thick Films with High X-Ray Sensitivity. *ACS Photon.* **2019**, *6*, 196-203.

51. Zhuang, R., et al., Highly Sensitive X-Ray Detector Made of Layered Perovskite-Like $(\text{NH}_4)_3\text{Bi}_2\text{I}_9$ Single Crystal with Anisotropic Response. *Nat. Photon.* **2019**, *13*, 602-608.
52. Amari, S.; Verilhac, J.-M.; Gros D'Aillon, E.; Ibanez, A.; Zaccaro, J., Optimization of the Growth Conditions for High Quality $\text{CH}_3\text{NH}_3\text{PbBr}_3$ Hybrid Perovskite Single Crystals. *Cryst. Growth Des.* **2020**, *20*, 1665-1672.
53. Liu, Y., et al., Inch-Size 0d-Structured Lead-Free Perovskite Single Crystals for Highly Sensitive Stable X-Ray Imaging. *Matter* **2020**, *3*, 180-196.
54. Murali, B.; Kolli, H. K.; Yin, J.; Ketavath, R.; Bakr, O. M.; Mohammed, O. F., Single Crystals: The Next Big Wave of Perovskite Optoelectronics. *ACS Mater. Lett.* **2020**, *2*, 184-214.
55. Deumel, S., et al., High-Sensitivity High-Resolution X-Ray Imaging with Soft-Sintered Metal Halide Perovskites. *Nat. Electron.* **2021**, *4*, 681-688.
56. Tsoulfanidis, N.; Landsberger, S., *Measurement and Detection of Radiation*; CRC Press, 2021.
57. Liu, F.; Wu, R.; Wei, J.; Nie, W.; Mohite, A. D.; Brovelli, S.; Manna, L.; Li, H., Recent Progress in Halide Perovskite Radiation Detectors for Gamma-Ray Spectroscopy. *ACS Energy Lett.* **2022**, *7*, 1066-1085.
58. Wang, J.-X., et al., Nearly 100% Energy Transfer at the Interface of Metal-Organic Frameworks for X-Ray Imaging Scintillators. *Matter* **2022**, *5*, 253-265.
59. Yakunin, S., et al., Detection of X-Ray Photons by Solution-Processed Organic-Inorganic Perovskites. *Nat. Photon.* **2015**, *9*, 444-449.
60. Wei, H., et al., Sensitive X-Ray Detectors Made of Methylammonium Lead Tribromide Perovskite Single Crystals. *Nat. Photonics* **2016**, *10*, 333.
61. Heiss, W.; Brabec, C., Perovskites Target X-Ray Detection. *Nat. Photon.* **2016**, *10*, 288-289.
62. Ralaiarisoa, M.; Salzmann, I.; Zu, F.-S.; Koch, N., Effect of Water, Oxygen, and Air Exposure on $\text{CH}_3\text{NH}_3\text{PbI}_3\text{-XCl}_x$ Perovskite Surface Electronic Properties. *Adv. Electron. Mater.* **2018**, *4*, 1800307.
63. Zhao, L.; Kerner, R. A.; Xiao, Z.; Lin, Y. L.; Lee, K. M.; Schwartz, J.; Rand, B. P., Redox Chemistry Dominates the Degradation and Decomposition of Metal Halide Perovskite Optoelectronic Devices. *ACS Energy Lett.* **2016**, *1*, 595-602.
64. Pospisil, J.; Guerrero, A.; Zmeskal, O.; Weiter, M.; Gallardo, J. J.; Navas, J.; Garcia-Belmonte, G., Reversible Formation of Gold Halides in Single-Crystal Hybrid-Perovskite/Au Interface Upon Biasing and Effect on Electronic Carrier Injection. *Adv. Funct. Mater.* **2019**, *29*, 1900881.
65. Müller, C., et al., Water Infiltration in Methylammonium Lead Iodide Perovskite: Fast and Inconspicuous. *Chemistry of Materials* **2015**, *27*, 7835-7841.
66. Wang, Q.; Chen, B.; Liu, Y.; Deng, Y.; Bai, Y.; Dong, Q.; Huang, J., Scaling Behavior of Moisture-Induced Grain Degradation in Polycrystalline Hybrid Perovskite Thin Films. *Energy Environ. Sci.* **2017**, *10*, 516-522.
67. Domanski, K.; Correa-Baena, J.-P.; Mine, N.; Nazeeruddin, M. K.; Abate, A.; Saliba, M.; Tress, W.; Hagfeldt, A.; Grätzel, M., Not All That Glitters Is Gold: Metal-Migration-Induced Degradation in Perovskite Solar Cells. *ACS Nano* **2016**, *10*, 6306-6314.
68. Kovalenko, A.; Pospisil, J.; Krajcovic, J.; Weiter, M.; Guerrero, A.; Garcia-Belmonte, G., Interface Inductive Currents and Carrier Injection in Hybrid Perovskite Single Crystals. *Appl. Phys. Lett.* **2017**, *111*, 163504.

69. Lee, H.; Ko, D.; Lee, C., Direct Evidence of Ion-Migration-Induced Degradation of Ultrabright Perovskite Light-Emitting Diodes. *ACS Appl. Mater. Interfaces* **2019**, *11*, 11667-11673.
70. Sanehira, E. M.; Tremolet de Villers, B. J.; Schulz, P.; Reese, M. O.; Ferrere, S.; Zhu, K.; Lin, L. Y.; Berry, J. J.; Luther, J. M., Influence of Electrode Interfaces on the Stability of Perovskite Solar Cells: Reduced Degradation Using Moox/Al for Hole Collection. *ACS Energy Lett.* **2016**, *1*, 38-45.
71. Stumpp, M.; Ruess, R.; Müßener, J.; Schlettwein, D., Freezing the Polarization of $\text{CH}_3\text{NH}_3\text{PbI}_3$ and $\text{CH}_3\text{NH}_3\text{PbI}_3\text{-XClx}$ Perovskite Films. *Mater. Today Chem.* **2017**, *4*, 97-105.
72. Leijtens, T.; Bush, K.; Cheacharoen, R.; Beal, R.; Bowring, A.; McGehee, M. D., Towards Enabling Stable Lead Halide Perovskite Solar Cells; Interplay between Structural, Environmental, and Thermal Stability. *J. Mater. Chem. A* **2017**, *5*, 11483-11500.
73. Kaltenbrunner, M., et al., Flexible High Power-Per-Weight Perovskite Solar Cells with Chromium Oxide–Metal Contacts for Improved Stability in Air. *Nat Mater* **2015**, *14*, 1032-1039.
74. Supasai, T.; Rujisamphan, N.; Ullrich, K.; Chemseddine, A.; Dittrich, T., Formation of a Passivating $\text{CH}_3\text{NH}_3\text{PbI}_3/\text{PbI}_2$ Interface During Moderate Heating of $\text{CH}_3\text{NH}_3\text{PbI}_3$ Layers. *Appl. Phys. Lett.* **2013**, *103*, 183906.
75. Conings, B., et al., Intrinsic Thermal Instability of Methylammonium Lead Trihalide Perovskite. *Adv. Energy Mater.* **2015**, *5*, 1500477.
76. La Ferrara, V.; De Maria, A.; Rametta, G.; Delli Veneri, P., The Effect of Storage Cycle on Improvement in the Photovoltaic Parameters of Planar Triple Cation Perovskite Solar Cells. *Mater. Adv.* **2021**, *2*, 5396-5405.
77. Beal, R. E.; Slotcavage, D. J.; Leijtens, T.; Bowring, A. R.; Belisle, R. A.; Nguyen, W. H.; Burkhard, G. F.; Hoke, E. T.; McGehee, M. D., Cesium Lead Halide Perovskites with Improved Stability for Tandem Solar Cells. *J. Phys. Chem. Lett.* **2016**, *7*, 746-751.
78. Sutton, R. J., et al., Bandgap-Tunable Cesium Lead Halide Perovskites with High Thermal Stability for Efficient Solar Cells. *Adv. Energy Mater.* **2016**, *6*, 1502458.
79. Yin, W.-J.; Yan, Y.; Wei, S.-H., Anomalous Alloy Properties in Mixed Halide Perovskites. *J. Phys. Chem. LETT.* **2014**, *5*, 3625-3631.
80. Pan, Z.; Wu, L.; Jiang, J.; Shen, L.; Yao, K., Searching for High-Quality Halide Perovskite Single Crystals toward X-Ray Detection. *J. Phys. Chem. Lett.* **2022**, *13*, 2851-2861.
81. García-Batlle, M.; Zia, W.; Aranda, C. A.; Saliba, M.; Almora, O.; Guerrero, A.; Garcia-Belmonte, G., Observation of Long-Term Stable Response in MAPbBr_3 Single Crystals Monitored through Displacement Currents under Varying Illumination. *Solar RRL* **2022**, *n/a*, 2200173.
82. Almora, O.; Aranda, C.; Garcia-Belmonte, G., Do Capacitance Measurements Reveal Light-Induced Bulk Dielectric Changes in Photovoltaic Perovskites? *J. Phys. Chem. C* **2017**, *122*, 13450-13454.
83. Slotcavage, D. J.; Karunadasa, H. I.; McGehee, M. D., Light-Induced Phase Segregation in Halide-Perovskite Absorbers. *ACS Energy Lett.* **2016**, *1*, 1199-1205.
84. Ippili, S.; Jella, V.; Kim, J.; Hong, S.; Yoon, S.-G., Enhanced Piezoelectric Output Performance Via Control of Dielectrics in Fe^{2+} -Incorporated MAPbI_3 Perovskite Thin Films: Flexible Piezoelectric Generators. *Nano Energy* **2018**, *49*, 247-256.
85. Wu, X.; Yu, H.; Li, L.; Wang, F.; Xu, H.; Zhao, N., Composition-Dependent Light-Induced Dipole Moment Change in Organometal Halide Perovskites. *J. Phys. Chem. C* **2015**, *119*, 1253-1259.

86. Kasap, S. O., X-Ray Sensitivity of Photoconductors: Application to Stabilized a-Se. *J. Phys. D: Appl. Phys.* **2000**, *33*, 2853-2865.
87. Zheng, X.; Zhao, W.; Wang, P.; Tan, H.; Saidaminov, M. I.; Tie, S.; Chen, L.; Peng, Y.; Long, J.; Zhang, W.-H., Ultrasensitive and Stable X-Ray Detection Using Zero-Dimensional Lead-Free Perovskites. *J. Energy Chem.* **2020**, *49*, 299-306.
88. Leijtens, T.; Eperon, G. E.; Noel, N. K.; Habisreutinger, S. N.; Petrozza, A.; Snaith, H. J., Stability of Metal Halide Perovskite Solar Cells. *Adv. Energy Mater.* **2015**, *5*, 1500963.
89. Almora, O.; Aranda, C.; Zarazua, I.; Guerrero, A.; Garcia-Belmonte, G., Noncapacitive Hysteresis in Perovskite Solar Cells at Room Temperature. *ACS Energy Lett.* **2016**, *1*, 209–215.
90. Almora, O.; Zarazua, I.; Mas-Marza, E.; Mora-Sero, I.; Bisquert, J.; Garcia-Belmonte, G., Capacitive Dark Currents, Hysteresis, and Electrode Polarization in Lead Halide Perovskite Solar Cells. *J. Phys. Chem. Lett.* **2015**, *6*, 1645-1652.
91. Bisquert, J.; Guerrero, A.; Gonzales, C., Theory of Hysteresis in Halide Perovskites by Integration of the Equivalent Circuit. *ACS Phys. Chem. Au* **2021**, *1*, 25-44.
92. Elumalai, N. K.; Uddin, A., Hysteresis in Organic-Inorganic Hybrid Perovskite Solar Cells. *Sol. Energy Mater. Sol. Cells* **2016**, *157*, 476-509.
93. Fakharuddin, A.; Schmidt-Mende, L.; Garcia-Belmonte, G.; Jose, R.; Mora-Sero, I., Interfaces in Perovskite Solar Cells. *Adv. Energy Mater.* **2017**, *7*, 1700623.
94. Kim, S.-G.; Li, C.; Guerrero, A.; Yang, J.-M.; Zhong, Y.; Bisquert, J.; Huettner, S.; Park, N.-G., Potassium Ions as a Kinetic Controller in Ionic Double Layers for Hysteresis-Free Perovskite Solar Cells. *J. Mater. Chem. A* **2019**, *7*, 18807-18815.
95. Unger, E. L.; Hoke, E. T.; Bailie, C. D.; Nguyen, W. H.; Bowring, A. R.; Heumüller, T.; Christoforo, M. G.; McGehee, M. D., Hysteresis and Transient Behavior in Current-Voltage Measurements of Hybrid-Perovskite Absorber Solar Cells. *Energy Environ. Sci.* **2014**, *7*, 3690-3698.
96. Wei, J.; Zhao, Y.; Li, H.; Li, G.; Pan, J.; Xu, D.; Zhao, Q.; Yu, D., Hysteresis Analysis Based on the Ferroelectric Effect in Hybrid Perovskite Solar Cells. *J. Phys. Chem. Lett.* **2014**, *5*, 3937-3945.
97. Duijnste, E. A.; Le Corre, V. M.; Johnston, M. B.; Koster, L. J. A.; Lim, J.; Snaith, H. J., Understanding Dark Current-Voltage Characteristics in Metal-Halide Perovskite Single Crystals. *Phys. Rev. Appl.* **2021**, *15*, 014006.
98. Chen, Y.; Yi, H. T.; Wu, X.; Haroldson, R.; Gartstein, Y. N.; Rodionov, Y. I.; Tikhonov, K. S.; Zakhidov, A.; Zhu, X. Y.; Podzorov, V., Extended Carrier Lifetimes and Diffusion in Hybrid Perovskites Revealed by Hall Effect and Photoconductivity Measurements. *Nat. Commun.* **2016**, *7*, 12253.
99. Kiermasch, D.; Rieder, P.; Tvingstedt, K.; Baumann, A.; Dyakonov, V., Improved Charge Carrier Lifetime in Planar Perovskite Solar Cells by Bromine Doping. *Scientific reports* **2016**, *6*, 39333.
100. Wehrenfennig, C.; Eperon, G. E.; Johnston, M. B.; Snaith, H. J.; Herz, L. M., High Charge Carrier Mobilities and Lifetimes in Organolead Trihalide Perovskites. *Adv. Mater.* **2014**, *26*, 1584-1589.
101. Azpiroz, J. M.; Mosconi, E.; Bisquert, J.; De Angelis, F., Defects Migration in Methylammonium Lead Iodide and Their Role in Perovskite Solar Cells Operation. *Energy Environ. Sci.* **2015**, *8*, 2118-2127
102. Bisquert, J.; Garcia-Belmonte, G.; Guerrero, A., Ionic/Electronic Conduction and Capacitance of Halide Perovskite Materials. In *Perovskite Photovoltaics and Optoelectronics*, 2022; pp 173-213.

103. Duijnste, E. A.; Ball, J. M.; Le Corre, V. M.; Koster, L. J. A.; Snaith, H. J.; Lim, J., Toward Understanding Space-Charge Limited Current Measurements on Metal Halide Perovskites. *ACS Energy Lett.* **2020**, *5*, 376-384.
104. Almora, O.; Miravet, D.; García-Batlle, M.; Garcia-Belmonte, G., Ballistic-Like Space-Charge-Limited Currents in Halide Perovskites at Room Temperature. *Appl. Phys. Lett.* **2021**, *119*, 242107.
105. Ershov, M.; Liu, H. C.; Li, L.; Buchanan, M.; Wasilewski, Z. R.; Jonscher, A. K., Negative Capacitance Effect in Semiconductor Devices. *IEEE Trans. Electron Devices* **1998**, *45*, 2196-2206.
106. Ebadi, F.; Taghavinia, N.; Mohammadpour, R.; Hagfeldt, A.; Tress, W., Origin of Apparent Light-Enhanced and Negative Capacitance in Perovskite Solar Cells. *Nat. Commun.* **2019**, *10*, 1574.
107. Moia, D., et al., Ionic-to-Electronic Current Amplification in Hybrid Perovskite Solar Cells: Ionically Gated Transistor-Interface Circuit Model Explains Hysteresis and Impedance of Mixed Conducting Devices. *Energy Environm. Sci.* **2019**, *12*, 1296-1308.
108. Almora, O.; Guerrero, A.; Garcia-Belmonte, G., Ionic Charging by Local Imbalance at Interfaces in Hybrid Lead Halide Perovskites. *Appl. Phys. Lett.* **2016**, *108*, 043903.
109. Caram, J.; García-Batlle, M.; Almora, O.; Arce, R. D.; Guerrero, A.; Garcia-Belmonte, G., Direct Observation of Surface Polarization at Hybrid Perovskite/Au Interfaces by Dark Transient Experiments. *Appl. Phys. Lett.* **2020**, *116*, 183503.
110. Carrillo, J.; Guerrero, A.; Rahimnejad, S.; Almora, O.; Zarazua, I.; Mas-Marza, E.; Bisquert, J.; Garcia-Belmonte, G., Ionic Reactivity at Contacts and Aging of Methylammonium Lead Triiodide Perovskite Solar Cells. *Adv. Energy Mater.* **2016**, *6*, 1502246
111. Shrestha, S., et al., Role of the Metal–Semiconductor Interface in Halide Perovskite Devices for Radiation Photon Counting. *ACS Appl. Mater. Interfaces* **2020**, *12*, 45533-45540.
112. Knoll, G. F., *Radiation Detection and Measurement*; Wiley, 2010.
113. Wei, H.; Huang, J., Halide Lead Perovskites for Ionizing Radiation Detection. *Nat. Commun.* **2019**, *10*, 1066.
114. Tisdale, J. T.; Muckley, E.; Ahmadi, M.; Smith, T.; Seal, C.; Lukosi, E.; Ivanov, I. N.; Hu, B., Dynamic Impact of Electrode Materials on Interface of Single-Crystalline Methylammonium Lead Bromide Perovskite. *Adv. Mater. Interfaces* **2018**, *5*, 1800476.
115. García-Batlle, M.; Deumel, S.; Huerdler, J. E.; Tedde, S. F.; Guerrero, A.; Almora, O.; Garcia-Belmonte, G., Mobile Ion-Driven Modulation of Electronic Conductivity Explains Long-Timescale Electrical Response in Lead Iodide Perovskite Thick Pellets. *ACS Appl. Mater. Interfaces* **2021**, *13*, 35617-35624.
116. Song, Y., et al., Atomistic Surface Passivation of $\text{CH}_3\text{NH}_3\text{PbI}_3$ Perovskite Single Crystals for Highly Sensitive Coplanar-Structure X-Ray Detectors. *Research* **2020**, *2020*, 5958243.
117. Song, Y., et al., Elimination of Interfacial-Electrochemical-Reaction-Induced Polarization in Perovskite Single Crystals for Ultrasensitive and Stable X-Ray Detector Arrays. *Adv. Mater.* **2021**, *33*, 2103078.
118. Yang, T.-Y.; Gregori, G.; Pellet, N.; Grätzel, M.; Maier, J., The Significance of Ion Conduction in a Hybrid Organic–Inorganic Lead-Iodide-Based Perovskite Photosensitizer. *Angew. Chem., Int. Ed.* **2015**, *54*, 7905-7910.
119. Xiao, Z.; Yuan, Y.; Shao, Y.; Wang, Q.; Dong, Q.; Bi, C.; Sharma, P.; Gruverman, A.; Huang, J., Giant Switchable Photovoltaic Effect in Organometal Trihalide Perovskite Devices. *Nat Mater* **2015**, *14*, 193-8.

120. Sakhatskyi, K., et al., Assessing the Drawbacks and Benefits of Ion Migration in Lead Halide Perovskites. *ACS Energy Letters* **2022**, 3401-3414.
121. Azpiroz, J. M.; Mosconi, E.; Bisquert, J.; De Angelis, F., Defect Migration in Methylammonium Lead Iodide and Its Role in Perovskite Solar Cell Operation. *Energy Environ. Sci.* **2015**, *8*, 2118-2127.
122. Bag, M.; Renna, L. A.; Adhikari, R. Y.; Karak, S.; Liu, F.; Lahti, P. M.; Russell, T. P.; Tuominen, M. T.; Venkataraman, D., Kinetics of Ion Transport in Perovskite Active Layers and Its Implications for Active Layer Stability. *J. Am. Chem. Soc.* **2015**, *137*, 13130-13137.
123. Eames, C.; Frost, J. M.; Barnes, P. R. F.; O'Regan, B. C.; Walsh, A.; Islam, M. S., Ionic Transport in Hybrid Lead Iodide Perovskite Solar Cells. *Nat. Commun.* **2015**, *6*, 7497.
124. Richardson, G.; O'Kane, S. E. J.; Niemann, R. G.; Peltola, T. A.; Foster, J. M.; Cameron, P. J.; Walker, A. B., Can Slow-Moving Ions Explain Hysteresis in the Current–Voltage Curves of Perovskite Solar Cells? *Energy Environ. Sci.* **2016**, *9*, 1476-1485.
125. Li, D.; Wu, H.; Cheng, H.-C.; Wang, G.; Huang, Y.; Duan, X., Electronic and Ionic Transport Dynamics in Organolead Halide Perovskites. *ACS Nano* **2016**, *10*, 6933-6941.
126. García-Batlle, M.; Deumel, S.; Huerdler, J. E.; Tedde, S. F.; Almora, O.; Garcia-Belmonte, G., Effective Ion Mobility and Long-Term Dark Current of Metal Halide Perovskites with Different Crystallinities and Compositions. *Adv. Photon. Research* **2022**, *n/a*, 2200136.
127. Yuan, Y.; Huang, J., Ion Migration in Organometal Trihalide Perovskite and Its Impact on Photovoltaic Efficiency and Stability. *Accounts of chemical research* **2016**, *49*, 286-93.
128. Yin, W.-J.; Shi, T.; Yan, Y., Unusual Defect Physics in $\text{CH}_3\text{NH}_3\text{PbI}_3$ Perovskite Solar Cell Absorber. *Appl. Phys. Lett.* **2014**, *104*, 063903.
129. Wang, H.; Guerrero, A.; Bou, A.; Al-Mayouf, A. M.; Bisquert, J., Kinetic and Material Properties of Interfaces Governing Slow Response and Long Timescale Phenomena in Perovskite Solar Cells. *Energy Environ. Sci.* **2019**, *12*, 2054-2079.
130. Wang, F.; Bai, S.; Tress, W.; Hagfeldt, A.; Gao, F., Defects Engineering for High-Performance Perovskite Solar Cells. *npj Flexible Electron.* **2018**, *2*, 22.
131. McGovern, L.; Futscher, M. H.; Muscarella, L. A.; Ehrler, B., Understanding the Stability of MAPbBr_3 Versus MAPbI_3 : Suppression of Methylammonium Migration and Reduction of Halide Migration. *J. Phys. Chem. Lett.* **2020**, *11*, 7127-7132.
132. García-Batlle, M.; Mayén Guillén, J.; Chapran, M.; Baussens, O.; Zaccaro, J.; Gros Daillon, E.; Verilhac, J. M.; Guerrero, A.; Almora, O.; Garcia Belmonte, G., Coupling between Ion Drift and Kinetics of Electronic Current Transients in MAPbBr_3 Single Crystals. *ACS Energy Lett.* **2022**, *7*, 946–951.
133. Guerrero, A.; Bisquert, J.; Garcia-Belmonte, G., Impedance Spectroscopy of Metal Halide Perovskite Solar Cells from the Perspective of Equivalent Circuits. *Chem. Rev.* **2021**, *121*, 14430-14484.
134. Zarazua, I.; Han, G.; Boix, P. P.; Mhaisalkar, S.; Fabregat-Santiago, F.; Mora-Seró, I.; Bisquert, J.; Garcia-Belmonte, G., Surface Recombination and Collection Efficiency in Perovskite Solar Cells from Impedance Analysis. *J. Phys. Chem. Lett.* **2016**, *7*, 5105-5113.
135. Mora-Sero, I.; Garcia-Belmonte, G.; Boix, P. P.; Vazquez, M. A.; Bisquert, J., Impedance Spectroscopy Characterisation of Highly Efficient Silicon Solar Cells under Different Light Illumination Intensities. *Energy Environ. Sci.* **2009**, *2*, 678-686.

136. Almora, O.; Cho, K. T.; Aghazada, S.; Zimmermann, I.; Matt, G. J.; Brabec, C. J.; Nazeeruddin, M. K.; Garcia-Belmonte, G., Discerning Recombination Mechanisms and Ideality Factors through Impedance Analysis of High-Efficiency Perovskite Solar Cells. *Nano Energy* **2018**, *48*, 63-72.
137. Aranda, C.; Bisquert, J.; Guerrero, A., Impedance Spectroscopy of Perovskite/Contact Interface: Beneficial Chemical Reactivity Effect. *J. Chem. Phys.* **2019**, *151*, 124201.
138. Peng, W.; Aranda, C.; Bakr, O. M.; Garcia-Belmonte, G.; Bisquert, J.; Guerrero, A., Quantification of Ionic Diffusion in Lead Halide Perovskite Single Crystals. *ACS Energy Lett.* **2018**, *3*, 1477-1481.

Chapter 3. Materials and Methods

This chapter summarizes the materials and experimental procedures used for the processing of the perovskite devices based on MAPbI₃ and MAPbBr₃, developed during the course of this thesis and potentially used as X-ray detector. The Chapter is divided in four subsections: perovskites synthesis and device preparation, structural description, optical characterization, and electrical measurements.

3.1 Perovskite synthesis

All salts and solvents were used as received without any further purification, the perovskite precursor CH₃NH₃I (MAI) (> 99 wt. %) and CH₃NH₃Br (MABr) (> 99 wt. %) were purchased from Dyesol/Greatcell Solar while PbI₂ (99.99% wt. %) and PbBr₂ (99.99% wt. %) were bought from TCI America. Salts were stored in a glovebox under N₂ atmosphere. All solvents were purchased from Sigma Aldrich: Dimethylformamide (DMF) anhydrous, (99.8 wt. %) and Dimethylsulfoxide (DMSO) anhydrous (99.8 wt. %,) both, were stored in a glovebox under N₂ atmosphere. Sandpaper of different grain sizes [P1200 (15 μm), P2400 (10 μm) and P4000 (5 μm)] used in the polishing process was purchased from Escil Company, France. All syntheses were carried out in 20 ml reaction vials.

3.1.1 Single crystal (SCs) growth

Crystallization methods are based in a two-step process which includes nucleation and growth of a solid phase (See **Figure 3.1**). However, to growth a SCs it is not always an easy task. Materials of high quality and a well-controlled temperature technique is the best approach to achieve this goal.¹⁻² Among the different crystallization methods for the growth of SCs, the Inverse Temperature Crystallization (ITC), which has been introduced and deeply described in Chapter 1, was the selected procedure. ITC starts with a nucleation at the solution surface layer due to the effect of surface tension; then the growth of the nucleus into a crystal until it reaches a certain size when surface tension can no longer keep the crystal afloat. The obtained SCs usually exhibit a shiny mirror surface and a homogeneous regular shape. Our growth experiments were conducted by ITC, the perovskite precursors, CH₃NH₃Br, PbBr₂ were dissolved (1:1 mol. %) in DMF to obtain 1 M solutions of MAPbBr₃. All the solutions are then maintained at room temperature under stirring and then, filtered at

ambient conditions using PTFE filters with $0.2\ \mu\text{m}$ pore size to remove any insoluble particles.

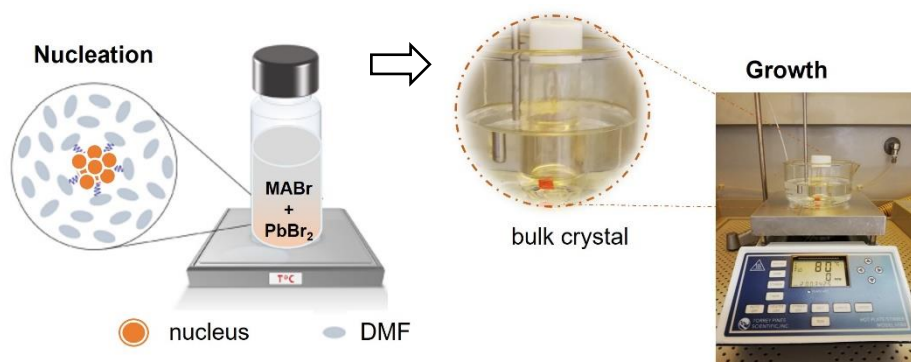


Figure 3.1. Schematic draw of the intermolecular interaction in the solution volume (left) during the nucleation process b) Growing process of a SCs of MAPbBr₃ in DMF by the ITC methodology (right).

An optimization of the growth procedures regarding the optimum temperature, volume of the vial, level of oil in the bath and heating rates (heat transfer rate), was required based on two growth protocols labeled as fast/unseeded and slow/seeded growth (See **Figure 3.2**). The *unseeded process* was similar to the one described in a previous work³ using a linear temperature ramp and fresh solution placed in the vial without any seed crystal.

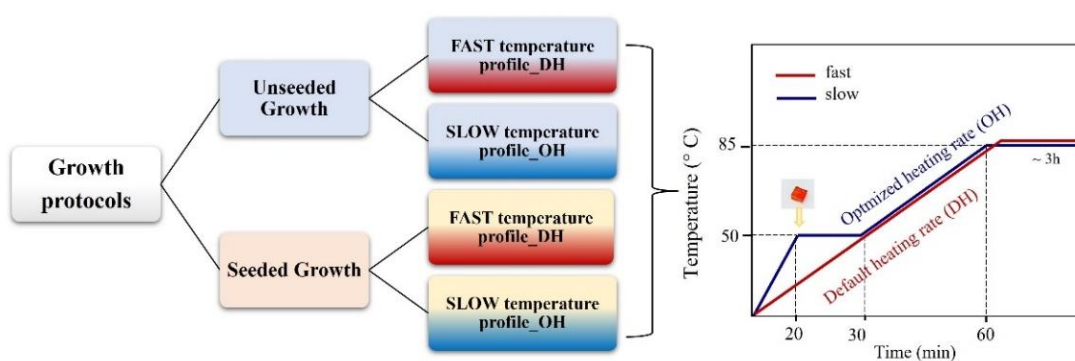


Figure 3.2. Schematic illustration of the different growth protocols investigated (left). Graphic representation of the ITC process of unseeded and seeded crystals with different heating rates (right).

The *fast/unseeded protocol*, derived from the ITC method was carried out using 3 mL of perovskite solutions placed in 20 mL of a glass flask vial in a silicon oil bath. In here, the temperature is abruptly brought from room to 80-85 °C leading to the spontaneous nucleation and growth of crystals.

Meanwhile, for the *seeded procedures* (See **Figure 3.2**), seeds must be first obtained by spontaneous nucleation and placed inside the vial once the temperature increase to $\sim 50^\circ\text{C}$ in the flasks to avoid dissolving the seed. In here, the crystal growth and the quality of the seed depends on the geometry of the vials and the temperature profile. In the *slow/seeded* procedure, the heating temperature profile is crucial and with the same perovskite solution, the temperature is first increased at 50°C , and then is kept for 20 mins at this temperature to place the seeds (**Figure 3.3c**) inside the flasks to avoid dissolving the seed (Fig **Figure 3.3a**). Finally, the solution is heated up, at a constant heating rate of 1°C/h for 3 hours, until $80\text{--}85^\circ\text{C}$. The various heating rates tested in the slow-seeded protocol are summarized in **Figure 3.3b**. Crystals obtained by this protocol are presented in the bar chart of **Figure 3.3d**. Those SCs are finally washed with warm DMF, then, placed in the vial, and transferred to the dry box with a nitrogen atmosphere.

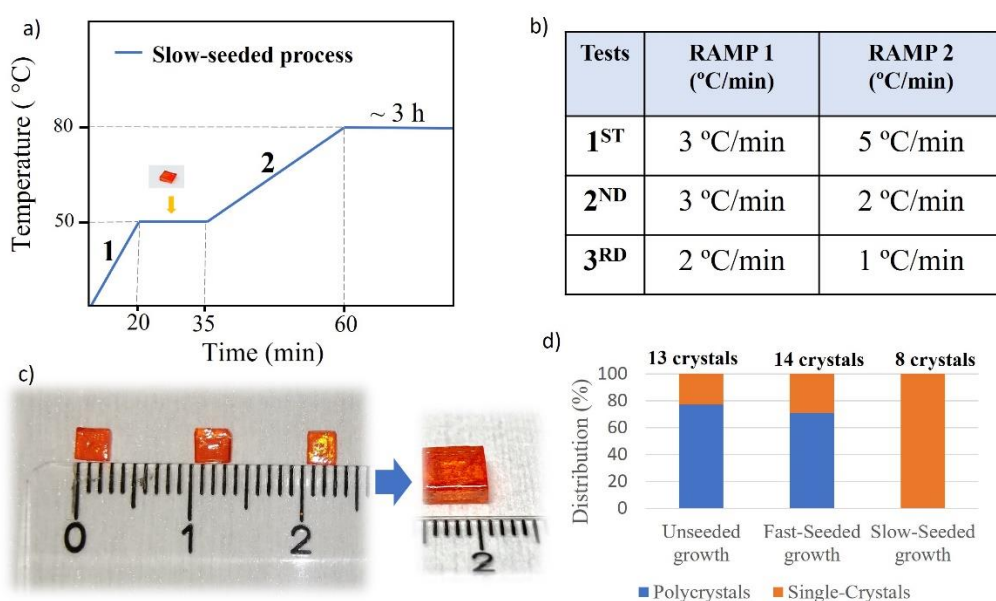


Figure 3.3. a) Schematic graph of the Slow-seeded protocol for the growth of MAPbBr₃ SCs. b) Optimized heating rates for the Slow-seeded protocol c) Seeds of MAPbBr₃ and bar chart showing the number of crystals growth.

As observed in **Figure 3.3** several high quality SCs samples were growth by this methodology. These samples were used for the charging experiments and long-term measurements in Chapter 7 and 8 respectively. On the other hand, SCs symmetrically contacted with Cr electrodes and provided by the Laboratory for Innovation in New Energy Technologies and Nanomaterials (LITEN), Atomic Energy Commission (CEA

Tech). These samples were used for Impedance Spectroscopy experiments in Chapter 4 and 6.

3.1.2 Soft-sintering procedure of Microcrystals (MCs)

MAPbX₃ (X=Br, I) MCs pellets of ≈1 mm thick asymmetrically contacted with evaporated Pt and Cr electrodes of 1 cm² area (see **Figure 3.4**). The pellets with a diameter of 15 mm and a thickness between 880 and 1,000 μm were produced using commercially available MAPbX₃ (X=Br, I) powders (Xi'an Polymer Light Technology).

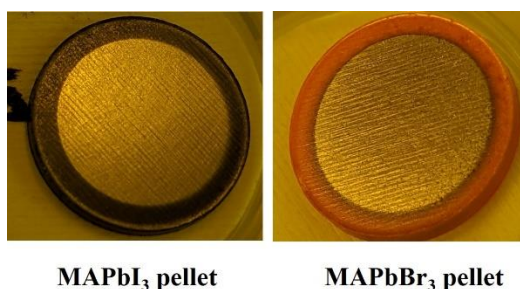


Figure 3.4. Top surface images of the perovskite MCs fabricated by the Soft-sintering procedure. Samples provided by Siemens Healthineers AG Technology Excellence, further information in ref⁴

The powder was sieved with a 50 μm mesh. For each composition, the powder was filled into a height-adjustable powder container (See **Figure 3.5**) and a cylinder of stainless steel with a polished surface was placed above this. Then, a hydraulic press (PerkinElmer company) applied up to 495 MPa. The soft sintering of the pellets was completed at a pressure of 110 MPa (2 t), applied for 30 min at a temperature of 70 °C. Finally, on the two-wafer faces, electrodes with an area of 1 cm² were deposited via physical vapor deposition. For that purpose, 100 nm Cr on one side and 100 nm Pt on the other side were sputtered.⁴ The results thick pellets with a thickness of around 1000 μm are observed in **Figure 3.4**. Samples were provided by Siemens Healthineers AG Technology Excellence.

Six thick-pellets of MAPbI₃ and four of MAPbBr₃ were prepared by this procedure. The pellets were used for Impedance Spectroscopy experiments and for the long-term transient measurements in Chapter 5. Further information about the structure and the optoelectronic response of the samples can be observed in Chapter 5 and 8.

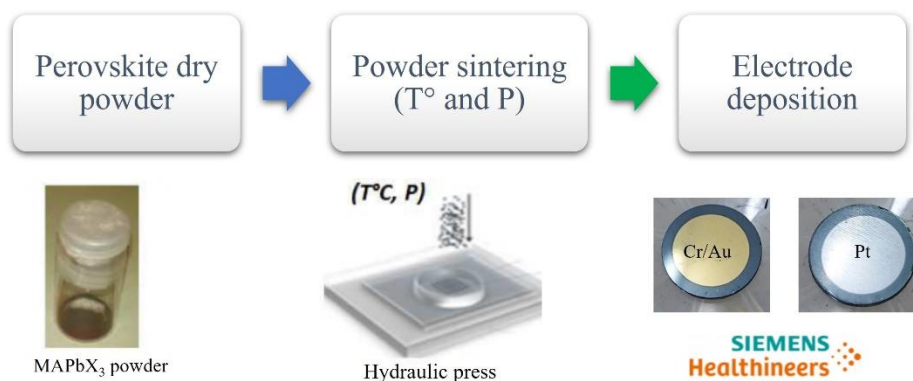


Figure 3.5. Schematic steps of the soft-sintering procedure for the preparation of MAPbX_3 ($X=\text{Br, I}$) perovskite devices. Method developed by Siemens Healthineers AG Technology Excellence. Additional information in ref.⁴⁻⁵

3.2 Device preparation

Various electrode configurations were employed in perovskite devices of MAPbBr_3 and MAPbI_3 prepared in this thesis. Table 3.1 showed the general characteristics of the samples studied, the electrical measurements and the corresponding chapter on results and discussion. In the case of MAPbBr_3 -SCs, Pt and Cr electrodes were evaporated at two opposite faces of the SCs, prior to that, the SCs were mechanically polished with sandpaper of different grain sizes, starting with this order: P1200 (15 μm), P2400 (10 μm) and P4000 (5 μm)]. For the MAPbX_3 ($X = \text{Br, I}$) micro-crystalline pellets (MCs) ~ 1 mm-thick, Pt and Cr electrodes were deposited via sputtering and vapor deposition respectively.

Table 3.1 Samples studied in this thesis

Sample	Crystallinity	Thickness	Electrodes (area)	Measurement procedure	Chapter
MAPbBr_3 (CEA-LITEN)	SCs	0.88 to 1 mm	Cr/Cr (12 mm ²)	Impedance Spectroscopy Long-term current transient experiments	4 and 6
MAPbBr_3 (INAM)	SCs	~ 1 mm	Pt/Pt (12 mm ²)	Charging transient experiments	7
MAPbBr_3 (SIEMENS)	MCs	~ 1202 μm	Pt/Cr (1 cm ²)	Long-term current transient experiments	8
MAPbI_3 (SIEMENS)	MCs	~ 1102 μm	Pt/Cr (1 cm ²)	Impedance Spectroscopy Long-term current transient experiments	5 and 8

3.3 Structural characterization techniques

3.3.1 X ray diffraction (XRD)

The X-ray diffraction technique is crucial in determining the lattice constant of the crystalline materials. Crystalline materials are three-dimensional diffraction gratings and have regular spacing (d) between planes of atoms which are in the same order as the wavelengths λ of X-rays. **Figure 3.6** shown the general setup for an X-ray measurement. The incident X-rays will reflect from the different planes of the crystalline material, causing them to interfere constructively and destructively at different angles (θ) according to the Bragg's law: $\lambda n = 2dsen\theta$ where n is refractive index of material.⁶ There are different methods to extract information related to the crystallinity of the samples. The XRD pattern of a SCs is obtained either by rotation of a single crystal with a fixed detector or using a position sensitive detector with a fixed crystal. For MCs samples the powder method (PXRD) is commonly selected, and it is usually performed with flat films in pinhole arrangement. We measured our samples by the PXRD method in an X-ray diffractometer (D8 Advance, Bruker-AXS) (Cu $K\alpha$, wavelength $\lambda=1.5406$ Å). The diffraction pattern in **Figure 3.6** shows a comparison between the XRD patterns of grounded powder samples and thin samples of MAPbBr₃ perovskite. The XRD pattern of a SCs compound allows to determine atomic positions, bond lengths and angles.⁷

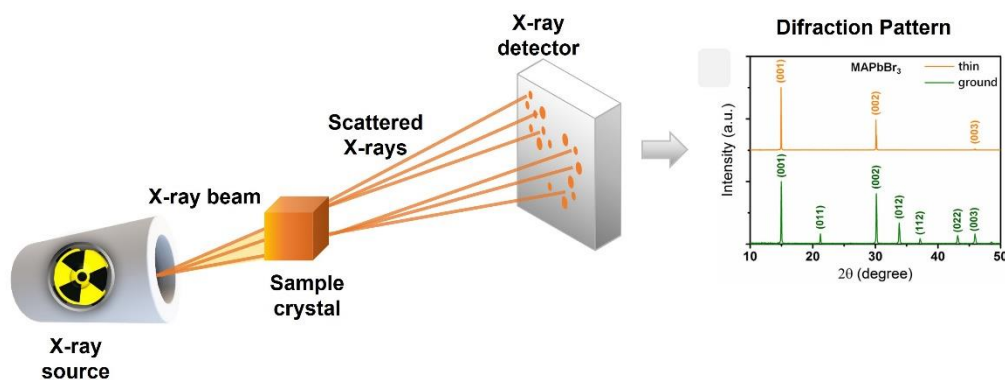


Figure 3.6. Schematic representation of a general X-ray setup with the corresponding diffraction pattern of a pure phase single crystal of MAPbBr₃

However, we also conducted high resolution 2D-XRD analysis in order to study the degree of crystallinity of the SCs using an X-ray diffractometer Agilent Super Nova

Atlas Dual Source (Cu-K α , wavelength $\lambda=1.5406 \text{ \AA}$). A rotation spectrum along the α cell axis can be measured in which only dots appear, and the absence of concentrically distributed circles is a clear sign that the material is not microcrystalline⁷ (See Chapter 7, Fig Supporting information).

3.3.2 Scanning Electron Microcopy (SEM) imaging and Laser Scanning Microscopy

SEM is a powerful tool that allows the physical observation at microscopic scales of surfaces and interfaces of several materials. In contrast to a traditional optical microscope, the electronic microscope can provide much higher resolution. For example, resolution for secondary electron image is close to 1.2 nm at 30 kV. This can reveal much information about the quality of the growth process: surface morphological features of the crystal related to the growth and quality of an interface or cleaved cross-section of a crystal.⁸ Using a focused beam of high-energy electrons, the signal is generated from the electron-sample interactions. A JEOL 7001F instrument equipped with an electron cannon of 0.1-30kV, FEG and EDX detector of Si (Li) for elemental analysis was employed for morphologies studies of the SCs growth.

Additionally, Laser Scanning Confocal Microcopy (LSCM) was also performed despite it is not the conventional technique for observing the surface area in SCs and is more frequently used for *ex vivo/in vitro* studies in biochemistry laboratories.⁹ LSCM (See **Figure 3.7**, left) has the advantage of possessing a highly optical resolution, the equipment Keyence VK-9710 has a light source (violet Laser: 408 nm) with an output of 0.9mW. **Figure 3.7** (right panel) shows the unsymmetrical surface of the different magnified areas of a bromide based SCs presumably due to dislocation growth mechanics during the solution growth.¹⁰ That was one of the main reason for the optimization of the solution growing protocols.

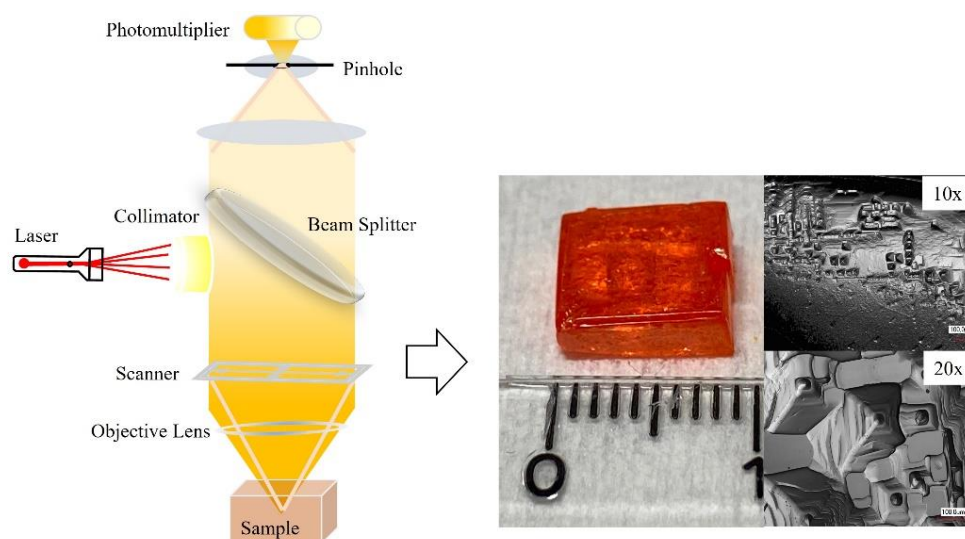


Figure 3.7. Schematic representation of the Laser Scanning Confocal Microscope showing a high-resolution image of the top view of a SCs of MAPbBr₃ without a polished surface.

3.4 Optical characterization techniques

3.4.1 Photoluminescence spectroscopy

Photoluminescence spectroscopy (PL) is the most commonly used characterization technique applied in studying fluorescence in a semiconductor material. The general electronic processes of the technique is showed in **Figure 3.8**: a sample is excited with a short wavelength light source, and the emission peak from a fluorescence material can be captured in the photoluminescence spectrum, which is also closely related to the bandgap of the material.¹¹ The PL measurements were carried out by a Horiba Fluorolog 3-11, using 405 nm of excitation source and, the photoluminescence peak position (~ 570 nm) of MAPbBr₃ is observed in the inset of **Figure 3.8** (right). Photoluminescence images of MAPbI₃-MCs and MAPbBr₃ -SCs are shown in the Supporting Information of Chapter 8.

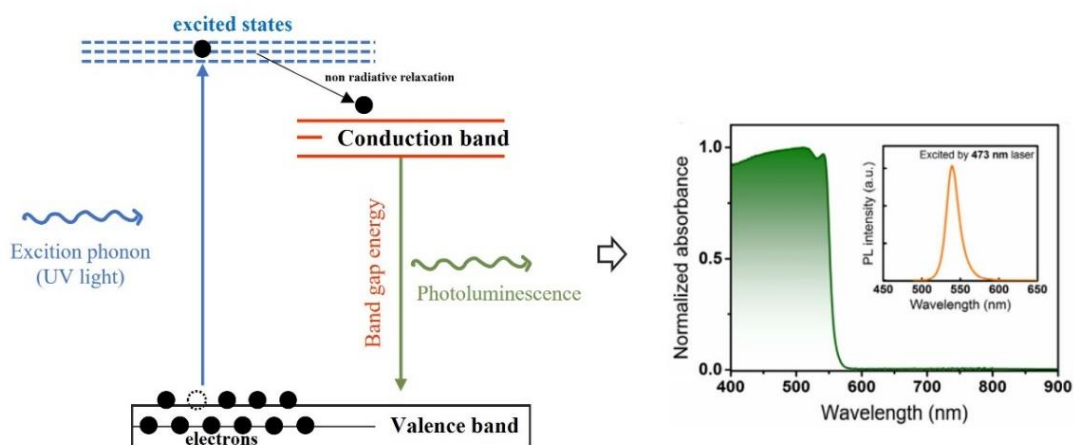


Figure 3.8. Schematic draw of the photoluminescence process

3.4.2 UV-vis absorption spectroscopy

Absorption spectroscopy (UV–Vis or UV/Vis) is the key technique to determine the bandgap of a semiconductor material. Usually, the spectrum can be measured in a transmission or absorption mode, where the transmitted light follows the Lambert–Beer law $A = \log\left(\frac{I_0}{I}\right) = \epsilon lc$ where here A is the measured absorbance, $\frac{I_0}{I}$ is the intensity ratio of the incident/transmitted light, l the path length through the sample and c the concentration of the absorbing species.¹² This technique also brings valuable information about the composition of perovskite sample. When the composition of the crystal varies, the color of the crystals also gradually changes. This change can be quantitatively measured in the UV-Vis absorption spectra by a calibration curve. The measurements were recorded by a Cary 500 Scan VARIAN spectrophotometer in the 250–800 nm wavelength range. An example of an UV-vis spectra can be observed in **Figure 3.8**. Nonetheless our UV-vis measurements are shown in the Supporting Information of Chapter 7 and 8.

3.5 Electrical measurements

All electrical experiments were performed at room temperature and under constant N₂ flow. In **Figure 2.6** is shown the sample holder system with nitrogen flow used during the measurement. Samples were stored in a dry glove box. The impedance measurements were carried out by using a PGSTAT-30 Autolab potentiostat equipped with impedance module. Samples were measured inside a metallic box acting as Faraday cage, in dark conditions between 10 mHz and 1 MHz, with a perturbation amplitude between 100-500mV.

For the charging measurements using a reference capacitor, a source measure unit Keithley Model 2612 was used as the voltage supply and an HP Digital Multimeter Model 34401A (input impedance > 10 GΩ) coupled through a FET input buffer model AD8244 (input impedance 10 TΩ) was used to record the polarization voltage signals. For the light condition a Broadband Halogen Fiber Optic lamp (150 W High-Output) with an irradiance level of 100 mW cm⁻² was used. For the long transients experiments a Keithley Model 2636B was used as both, voltage supply and digital multimeter to record the current transient response of the samples.

3.5.1 Dark current-voltage characteristics

In any semiconductor material as Pb-halide perovskites the current-voltage characteristic, or *j-V* curve, often provide insights into the internal working mechanism of the electronic devices and some means for evaluating the change in conductance (or inversely the impedance) of the element analyzed. Because perovskite is a mixed ionic-electronic conductor material, the current-voltage characteristics sometimes is difficult to document since the behavior could be erratically arbitrary at times. When an *j-V* sweep is repeated under the same conditions, the characteristics may differ from one measurement to another due to the effect of the slow-moving ionic species that modify the contacts (See **Figure 3.9**). The specific current-voltage characteristics of the samples studied in this thesis were measured using a source unit Keithley Model 2612. Devices were mounted in the sample holder presented in **Chapter 2** and were measured using in both reverse and forward bias at different scan rates 100-500 mV s⁻¹. For more information about the *j-V* measurements see Chapter 8.

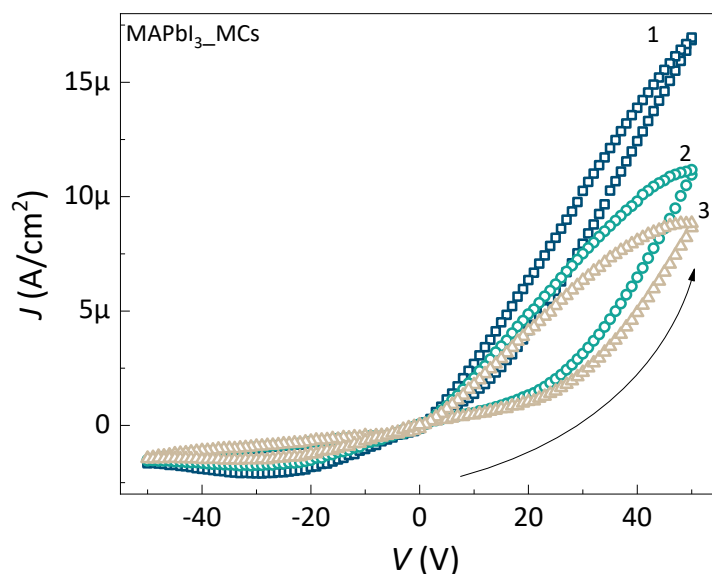


Figure 3.9. Current voltage characteristics of a MAPbI₃ thick pellet repeated under the same conditions.

3.5.2 Impedance Spectroscopy

Impedance spectroscopy is a well-known nondestructive characterization tool which is usually classified in the group of the small perturbation techniques. In this technique, the response of the sample to an electrical field is monitored as a function of determined frequency ranges ω , generally between 1 MHz (microseconds) to 10 mHz (seconds). Basically, the sample of interest is perturbed by an alternating voltage, but not irreversible-induced modifications are usually found during the measurement.¹³⁻¹⁴ It allows to extract physicochemical properties and electrical variables of the system under study. Additionally, one can extract, kinetic parameters, solution resistance, charge transport properties, etc. of electrochemical systems and solid-state devices.¹⁵⁻²³ **Figure 3.10** shows how to calculate the impedance Z : by applying a sinusoidal voltage \tilde{V} perturbation to a sample at different frequencies around a given steady state point, the flow of alternating current \tilde{j} can be obtained. The relation describes in equation 3 forms the complex impedance Z (Ωcm^2) in the frequency domain:

$$Z(\omega) = \frac{\tilde{V}(\omega)}{\tilde{j}(\omega)} \quad (3)$$

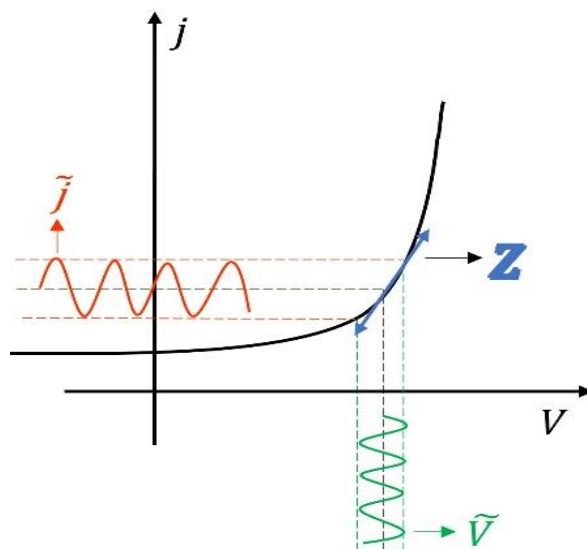


Figure 3.10. Schematic illustration of the IS technique. The voltage perturbation (green signal) around a given steady state point allow to obtain the resulting modulated current response (red signal).

The amplitude of the AC voltage signal is around a given steady-state and can be as low as 20 mV for perovskite thin-films or as high as 1 V for perovskite thick crystals. As can be observed in **Figure 3.10** this small perturbation technique also ensures a linear dependence between the $\tilde{V}(\omega)$ and the $\tilde{j}(\omega)$

The physical meaning of impedance is the complex resistance of the sample (time-varying or frequency-dependent), and the low frequency limit of the transfer function is the differential DC resistance at a given point in the $j - V$ curve. As a complex number the IS transfer function can be represented in the form of a Z -plot (Nyquist plot), and the IS data can be split in a real part of Z versus imaginary part of Z'' over the range of measured frequencies. This representation allows a better understanding of the internal mechanistic processes occurring on different characteristic timescales. These characteristic times can be represented in terms of combinations of passive electrical elements (See **Figure 3.11**). At the same time, these passive elements are electrical replicas of physical mechanisms occurring within the devices such diffusion-limited effects or capacitive behaviors.

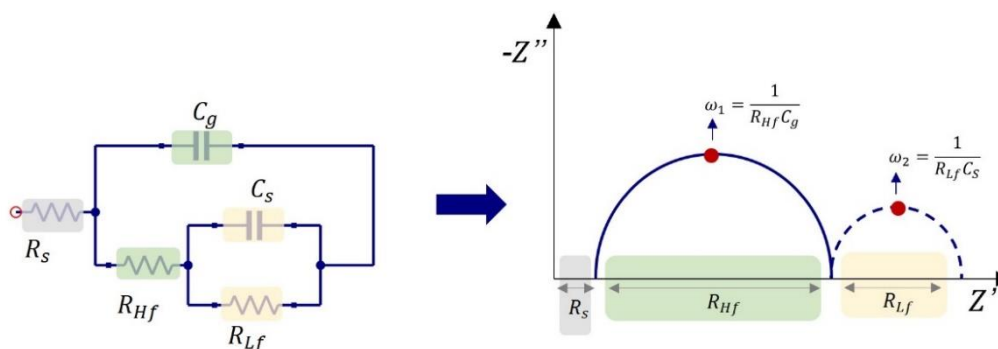


Figure 3.11. Schematic representation of the Impedance spectra (Nyquist plot representation) and the corresponding equivalent circuit with some of the electrical components: R_s series resistance, C_g geometric capacitance and R_{HF} , and R_{LF} the high-, and low-frequency resistances, respectively, the low-frequency capacitance usually labelled as surface capacitance C_s . Those components are used for the electrical model of a perovskite device for both, high frequency, and low frequency regions.

Figure 3.11 (right) shows a basic IS spectra a Z -plane response that basically consists of semicircles or arcs in the upper quadrant whose width is given by the high-frequency resistance R_{HF} (straight line arc) which is shifted along the x-axis by a value equal to the series resistance R_s . If other processes occur on a different timescale (longer times) the response in **Figure 3.11** can be much complex and a second arc can be observed in the upper quadrant whose width will be dependent of the low-frequency resistance R_{LF} (dash line arc). The maximum point of the semicircle corresponds to the maximum frequency of the imaginary part in the impedance plot (black dot) which is the inverse of the time constant formed by the product of the resistance and the capacitance for each frequency regions.

In **Figure 3.12(b)** another useful representation can be seen which is the frequency dependent capacitance (also known as combination Bode plot) and can be expressed as $C(\omega) = \frac{1}{i\omega Z(\omega)}$. This representation allows the identification of the type of capacitances being observed over the range of frequencies.

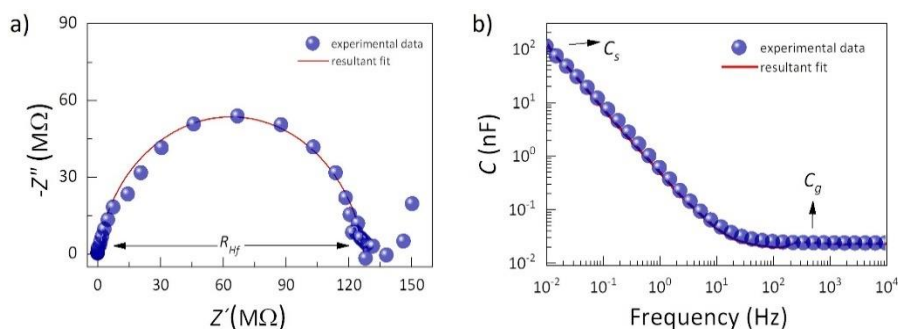


Figure 3.12. a) Impedance spectra and b) Capacitance response of a MAPbBr₃ perovskite single crystal

Recalling the capacitance versus frequency plot obtained in this thesis (**Figure 3.12**), two increments and one clear plateau is observed depending on the timescales (on the frequency). The high frequency response has been already correlated with perovskite dielectric processes and series resistance contributions and relate to the geometrical capacitance C_g , while the low-frequency response, surface capacitance C_s is attributed to interfacial processes, chemical reaction and so on.²⁴⁻²⁵ Capacitive features, usually, relates to charge storage mechanisms and may include the space charge capacitance, the chemical capacitance, bulk dielectric capacitance and surface state capacitance.²⁶⁻²⁹

IS has been one of the most helpful techniques applied during this thesis. The next chapters will present all the IS results and the physical models used for additional understanding of the long-term electronic behavior of perovskite devices of MAPbI₃-MCs and MAPbBr₃-SCs.

3.5.3 Long-term current transient experiments

As we mentioned in Chapter 1, X-ray detector based on direct conversion work under higher electrical fields. Therefore, it is of major importance to study the current response upon biasing. With that purpose, chronopotentiometry measurements were performed for long periods of time in dark. In **Figure 3.13** the general setup for the transient, measurements are shown. One can observe that, for the case of a MAPbBr₃ SCs the current response upon bias exponentially rises and finally saturates approaching steady-state values. **Figure 3.13b** displays the transient protocol designed for longer times of polarization. The consecutive step voltages were: 10, 20, 50, 80, 100 and 200 V and between each positive/negative bias the crystal is left to relaxes at

0 V (short-circuit condition) for ~ 3000 s approximately. In **Figure 3.13b** in the zero-bias condition the small current has the opposite sign and appears as an undershoot of the order of nA cm^{-2} . That negative current should exclusively obey the ion dynamic because and the decay time constants τ should reflect the dynamics of the diffusive ionic transport. The short circuit current can be observed in the Supporting Information of Chapter 6.

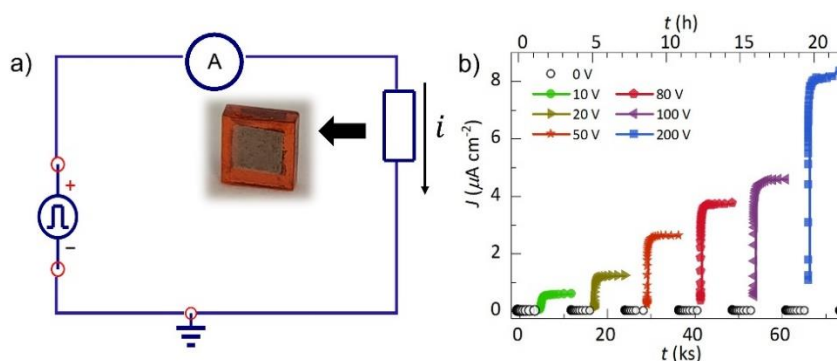


Figure 3.13. a) Experimental setup for the long-term current transient experiments b) Biasing protocol carried out under several long-time direct-current mode (DC) bias conditions in the ranges of ± 200 to 0 V

3.5.4 Charging transient experiments

The charging transient analysis is an experimental technique based on transient polarization signals very similar to the well-known Sawyer-Tower experiments. In this approach, a large square voltage signal is applied instead of an alternating small voltage perturbation and the resulting polarization is recorded by means of a reference capacitor under suppression of DC currents. **Figure 3.14a** indicate the rectangular voltage signal (V_{app}) applied to the sample C_x across a reference linear capacitor C_0 , with both capacitors in series connection. One important requirement is to select $C_0 \gg C_x$ in order to assure that the applied voltage principally drops within the perovskite sample. Only then, the charge storage in C_x (as in C_0) is $Q = C_0 V_0$, being V_0 the voltage at the reference capacitor. All the measurements are recorded with an ultrahigh input resistance or the order of $\sim \text{T}\Omega$ to avoid loading effects from the recording instrument. We used this setup in order to find the connection between the polarization and the charging of perovskite/contact interfaces for MAPbI_3 perovskite interdigitated films³⁰ and for MAPbBr_3 single crystals (See Chapter 7). As observed

in **Figure 3.14b**, the voltage at C_0 follows the bias perturbation steps in such a way that only a small portion drops at it, i.e., $V_0 \ll V_{app}$.

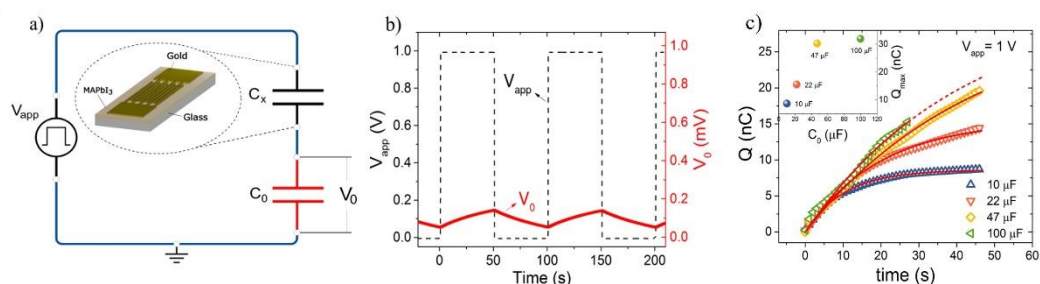


Figure 3.14. a) Example of the experimental circuit used for the charge transient measurements of a 320 nm thick MAPbI₃ film registered in dark conditions. b) Example of the charge transient response when a rectangular voltage pulse of 1V-height is applied across the sample. Note the scale differences with the induced voltage. c) Charge transients for long-time poling using different reference capacitors, The reference capacitor ranges $C_0 = 10 - 100 \mu\text{F}$, as indicated. In the inset: Q_{max} induced calculated from fitting to an exponential function. Reprinted with permission of reference.³⁰ Copyright 2020 AIP Publishing.

In our measurements the reference capacitor set-up suppresses direct current by monitoring exclusively displacements currents which can be corroborated by the collapse of the charge transients which is independent of the value of C_0 .

References

1. Yuan, Z.; Zhou, J.; Zhang, Y.; Ma, X.; Wang, J.; Dong, J.; Lu, F.; Han, D.; Kuang, B.; Wang, N., Growing Masni₃ Perovskite Single-Crystal Films by Inverse Temperature Crystallization. *J. Phys.: Condens. Matter* **2022**, *34*, 144009.
2. Liu, Y.; Yang, Z.; Liu, S., Recent Progress in Single-Crystalline Perovskite Research Including Crystal Preparation, Property Evaluation, and Applications. *Adv. Sci.* **2018**, *5*, 1700471.
3. Saidaminov, M. I., et al., High-Quality Bulk Hybrid Perovskite Single Crystals within Minutes by Inverse Temperature Crystallization. *Nat. Commun.* **2015**, *6*, 7586.
4. Deumel, S., et al., High-Sensitivity High-Resolution X-Ray Imaging with Soft-Sintered Metal Halide Perovskites. *Nat. Electron.* **2021**, *4*, 681-688.
5. Shrestha, S., et al., High-Performance Direct Conversion X-Ray Detectors Based on Sintered Hybrid Lead Triiodide Perovskite Wafers. *Nat. Photon.* **2017**, *11*, 436-440.
6. Yu, S.; Liu, P.; Xiao, S., A Review of Main Characterization Methods for Identifying Two-Dimensional Organic-Inorganic Halide Perovskites. *J. Mater. Sci.* **2021**, *56*, 11656-11681.
7. He, B. B., Introduction to Two-Dimensional X-Ray Diffraction. *Powder Diffraction* **2003**, *18*, 71-85.
8. Mohammed, A.; Abdullah, A., *Scanning Electron Microscopy (Sem): A Review*, 2019.
9. Canette, A.; Briandet, R., Microscopy | Confocal Laser Scanning Microscopy. In *Encyclopedia of Food Microbiology (Second Edition)*, Batt, C. A.; Tortorello, M. L., Eds. Academic Press: Oxford, 2014; pp 676-683.
10. Wang, X.; Huang, Y.; Lei, W.; Li, Q.; Zhang, X.; Khan, Q.; Wang, B., Asymmetrical Photodetection Response of Methylammonium Lead Bromide Perovskite Single Crystal. *Cryst. Res. Technol.* **2017**, *52*, 1700115.
11. Wang, F.; Liu, X.-K.; Gao, F., Chapter 1 - Fundamentals of Solar Cells and Light-Emitting Diodes. In *Advanced Nanomaterials for Solar Cells and Light Emitting Diodes*, Gao, F., Ed. Elsevier: 2019; pp 1-35.
12. Picollo, M.; Aceto, M.; Vitorino, T., Uv-Vis Spectroscopy. **2019**, *4*.
13. Guerrero, A.; Bisquert, J.; Garcia-Belmonte, G., Impedance Spectroscopy of Metal Halide Perovskite Solar Cells from the Perspective of Equivalent Circuits. *Chem. Rev.* **2021**, *121*, 14430-14484.
14. Wang, H.; Guerrero, A.; Bou, A.; Al-Mayouf, A. M.; Bisquert, J., Kinetic and Material Properties of Interfaces Governing Slow Response and Long Timescale Phenomena in Perovskite Solar Cells. *Energy Environ. Sci.* **2019**, *12*, 2054-2079.
15. Almora, O.; Cho, K. T.; Aghazada, S.; Zimmermann, I.; Matt, G. J.; Brabec, C. J.; Nazeeruddin, M. K.; Garcia-Belmonte, G., Discerning Recombination Mechanisms and Ideality Factors through Impedance Analysis of High-Efficiency Perovskite Solar Cells. *Nano Energy* **2018**, *48*, 63-72.
16. Aranda, C.; Bisquert, J.; Guerrero, A., Impedance Spectroscopy of Perovskite/Contact Interface: Beneficial Chemical Reactivity Effect. *J. Chem. Phys.* **2019**, *151*, 124201.
17. Bisquert, J.; Garcia-Belmonte, G.; Guerrero, A., Ionic/Electronic Conduction and Capacitance of Halide Perovskite Materials. In *Perovskite Photovoltaics and Optoelectronics*, 2022; pp 173-213.

18. Lopez-Varo, P.; Jiménez-Tejada, J. A.; García-Rosell, M.; Ravishankar, S.; Garcia-Belmonte, G.; Bisquert, J.; Almora, O., Device Physics of Hybrid Perovskite Solar Cells: Theory and Experiment. *Adv. Energy Mater.* **2018**, *8*, 1702772.
19. Mora-Sero, I.; Garcia-Belmonte, G.; Boix, P. P.; Vazquez, M. A.; Bisquert, J., Impedance Spectroscopy Characterisation of Highly Efficient Silicon Solar Cells under Different Light Illumination Intensities. *Energy Environ. Sci.* **2009**, *2*, 678-686.
20. Mora-Seró, I.; Luo, Y.; Garcia-Belmonte, G.; Bisquert, J.; Muñoz, D.; Voz, C.; Puigdollers, J.; Alcubilla, R., Recombination Rates in Heterojunction Silicon Solar Cells Analyzed by Impedance Spectroscopy at Forward Bias and under Illumination. *Sol. Energy Mater. Sol. Cells* **2008**, *92*, 505-509.
21. Tisdale, J. T.; Muckley, E.; Ahmadi, M.; Smith, T.; Seal, C.; Lukosi, E.; Ivanov, I. N.; Hu, B., Dynamic Impact of Electrode Materials on Interface of Single-Crystalline Methylammonium Lead Bromide Perovskite. *Adv. Mater. Interfaces* **2018**, *5*, 1800476.
22. Zarazua, I.; Han, G.; Boix, P. P.; Mhaisalkar, S.; Fabregat-Santiago, F.; Mora-Seró, I.; Bisquert, J.; Garcia-Belmonte, G., Surface Recombination and Collection Efficiency in Perovskite Solar Cells from Impedance Analysis. *J. Phys. Chem. Lett.* **2016**, *7*, 5105-5113.
23. Zarazua, I.; Sidhik, S.; López-Luke, T.; Esparza, D.; De la Rosa, E.; Reyes-Gomez, J.; Mora-Seró, I.; Garcia-Belmonte, G., Operating Mechanisms of Mesoscopic Perovskite Solar Cells through Impedance Spectroscopy and J-V Modeling. *J. Phys. Chem. Lett.* **2017**, *8*, 6073-6079.
24. Almora, O.; Aranda, C.; Garcia-Belmonte, G., Do Capacitance Measurements Reveal Light-Induced Bulk Dielectric Changes in Photovoltaic Perovskites? *J. Phys. Chem. C* **2017**, *122*, 13450-13454.
25. Almora, O.; Zarazua, I.; Mas-Marza, E.; Mora-Sero, I.; Bisquert, J.; Garcia-Belmonte, G., Capacitive Dark Currents, Hysteresis, and Electrode Polarization in Lead Halide Perovskite Solar Cells. *J. Phys. Chem. Lett.* **2015**, *6*, 1645-1652.
26. Bisquert, J., Chemical Capacitance of Nanostructured Semiconductors: Its Origin and Significance for Nanocomposite Solar Cells. *Phys. Chem. Chem. Phys.* **2003**, *5*, 5360-5364.
27. Ershov, M.; Liu, H. C.; Li, L.; Buchanan, M.; Wasilewski, Z. R.; Jonscher, A. K., Negative Capacitance Effect in Semiconductor Devices. *IEEE Trans. Electron Devices* **1998**, *45*, 2196-2206.
28. Ebadi, F.; Taghavinia, N.; Mohammadpour, R.; Hagfeldt, A.; Tress, W., Origin of Apparent Light-Enhanced and Negative Capacitance in Perovskite Solar Cells. *Nat. Commun.* **2019**, *10*, 1574.
29. Zarazua, I.; Bisquert, J.; Garcia-Belmonte, G., Light-Induced Space-Charge Accumulation Zone as Photovoltaic Mechanism in Perovskite Solar Cells. *The journal of physical chemistry letters* **2016**, *7*, 525-8.
30. Caram, J.; García-Batlle, M.; Almora, O.; Arce, R. D.; Guerrero, A.; Garcia-Belmonte, G., Direct Observation of Surface Polarization at Hybrid Perovskite/Au Interfaces by Dark Transient Experiments. *Appl. Phys. Lett.* **2020**, *116*, 183503.

Chapter 4: Publication 1

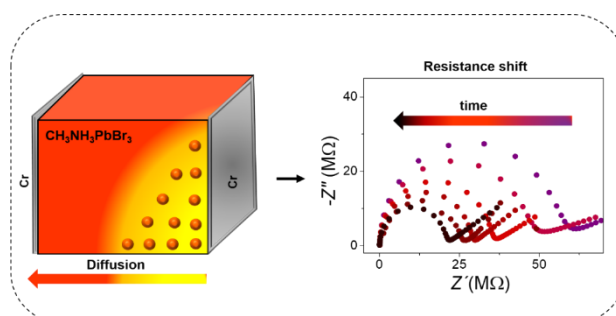
Marisé García-Battle, O. Baussens, S. Amari, J. Zaccaro, E. Gros-Daillon, J. M. Verilhac, A. Guerrero, G. Garcia-Belmonte, Moving Ions Vary Electronic Conductivity in Lead Bromide Perovskite Single Crystals through Dynamic Doping, *Adv. Electron. Mater.* **2020**, 6, 2000485, <https://doi.org/10.1002/aelm.202000485>

4.1 Candidate's contribution

Nature of Contribution	Extent of Contribution
<ul style="list-style-type: none"> • Performed the experimental measurements • Performed the fitting of experimental data • Wrote the experimental part of the manuscript • Contributed to reply to the referees 	50 %

4.2 Brief summary

In this work the impedance analysis of a set of high quality thick $\text{CH}_3\text{NH}_3\text{PbBr}_3$ single crystals contacted with more stable and less reacting chromium electrodes it is shown. We probe that the bias- and time-dependence of bulk resistance informs about the accumulation and relaxation dynamics of the moving ionic species. Our analysis extracts values for the ion diffusivity in the range of $10^{-8} \text{ cm}^2 \text{ s}^{-1}$ and ionic mobilities in the order of $10^{-6} \text{ V}^{-1}\text{cm}^2 \text{ s}^{-1}$. Our finding suggests that the interplay between ionic and electronic properties in perovskite materials relies upon a sort of dynamic doping effect caused by moving ions that act as dopants and locally vary the carrier density.



4.3 Published manuscript

Moving Ions Vary Electronic Conductivity in Lead Bromide Perovskite Single Crystals through Dynamic Doping

Marisé García-Batlle¹, Oriane Baussens², Smaïl Amari³, Julien Zaccaro⁴,
Eric Gros-Daillon², Jean-Marie Verilhac³, Antonio Guerrero¹,
and Germà Garcia-Belmonte^{1*}

¹ Institute of Advanced Materials (INAM), Universitat Jaume I, ES12006 Castelló, Spain

² Grenoble Alpes University, CEA, LETI, F38000 Grenoble, France

³ Grenoble Alpes University, CEA, LITEN, F38000 Grenoble, France

⁴ Grenoble Alpes University, CNRS, Grenoble INP, Institut Néel, F38042 Grenoble France

*Email: garciag@uji.es

5 October 2022

Abstract

Metal halide perovskite single crystals are being explored as functional materials for a variety of optoelectronic applications. Among others, solar cells, field effect transistors and X- and γ -ray detectors have shown improved performance and stability. However, a general uncertainty exists about the relevant mechanisms governing the electronic operation. This is caused by the presence of mobile ions and how these defect species alter the internal electrical field, interact with the contact materials or modulate electronic properties. Here, a set of high quality thick methylammonium lead tribromide single crystals contacted with low reactivity chromium electrodes are analyzed by impedance spectroscopy. Through examination of the sample resistance evolution with bias and releasing time, it is revealed that an interplay exists between the perovskite electronic conductivity and the defect distribution within the crystal bulk. Ion diffusion after bias removing changes the local doping density then governing the electronic transport. These findings indicate that the coupling between ionic and electronic properties relies upon a dynamic doping effect caused by moving ions that act as mobile dopants. In addition to electronic features, our analysis extracts values for the ion diffusivity in the range of $10^{-8} \text{ cm}^2 \text{ s}^{-1}$ in good agreement with other independent measurements.

1. Introduction

Apart from being used as light absorbing materials for photovoltaic applications,¹ hybrid perovskites have recently attracted much attention as sensitive layers for high-energy radiation detectors and imaging devices for medical diagnostics.² In some aspects, X- and γ -ray detection technologies face similar drawbacks when using perovskite materials as those previously encountered in solar cell engineering. One of them is caused by the presence of mobile ions and how these species alter the internal electrical field, interact with the contact materials or modulate electronic properties.³⁻⁶ Upon biasing, charged moving ions accumulate in the vicinity of the outer interfaces causing electrical field partial shielding.⁷⁻⁹ It has been also reported how intrinsic defects chemically react with the electrodes giving rise to losses in performance and device instabilities.¹⁰⁻¹¹

The occurrence of polarized interfaces in hybrid perovskite-based electronic devices were proposed¹² as an explaining mechanism for the measured excess capacitance at low frequencies. In dark conditions, mobile ions pile up at outer interfaces forming double layer-like structures in the vicinity of the perovskite/contact interface.¹³⁻¹⁴ Excess dark capacitance of order 1-10 $\mu\text{F cm}^{-2}$ can be readily explained in this way. In addition to purely electrostatic approaches for the interfacial phenomena, it is known that chemical reactions between mobile ions and contacting materials might give rise to the formation of dipole-like structures.¹⁵⁻¹⁶ Also deviations from stable electrical characteristics (i.e. hysteresis in J - V or non-ohmic response) have previously been correlated with the dynamics of migrating ions which interact with the contacts.^{14-15, 17} A survey about the chemical reactivity of the perovskite/contact materials can be found elsewhere.¹⁴ In this sense, the kinetics of electrode charging may be understood not only in terms of ion diffusion and double-layer formation, but also by interface reactivity forming local chemical bonds. Therefore, the variety of interfacial-related mechanisms, from purely electrostatic to chemically active, makes the interpretation of the registered electrical response largely dependent on the specific selected materials and device processing.

A strategy to progress in relating electric responses, operating mechanisms, and device architecture relies upon simplifying the probing structure mainly in two aspects. One of them, by using single-crystal samples instead of polycrystalline layers which introduce additional uncertainties with respect to the effects of grain boundaries and internal interfaces.¹⁸⁻²¹ The other simplification consists in selecting symmetrical samples with less reactive or passivated contacts, which improves reproducibility and limits outer interface influences on the overall electrical response.²² This last point is particularly important when long-time experiments are programmed. Commonly observed drifts and instabilities in the electrical response are not easily connected to well-identified evolving mechanisms, in such a way that the underlying uncertainty about governing processes persists.

Here, high quality methylammonium lead tribromide (MAPbBr₃) single crystals are contacted with chromium electrodes. Thermally evaporated chromium has been selected as a material that spontaneously oxidizes during sample preparation due to a very negative standard reduction potential, giving rise to a thin layer of Cr₂O₃.²³ The passivation of the interface occurs by Cr (III) formation making the electrode material less reactive than other metals as Au when put into contact with the perovskite layer.²⁴ Using Cr as metal contact has proved successful to increase the stability in record photovoltaic devices due to the deactivation of one of the possible degradation pathways.^{22, 24-25} Also for high sensitivity and long stability X-ray detectors, chromium-based contacts have been employed.²⁶⁻²⁷

For the purpose of this work, the use of more stable Cr contacts provides unambiguous access to the electrical dynamics of migrating ions in the bulk of the perovskite and their relaxation kinetics.²⁸ It is revealed here that there exists an interplay between the perovskite electronic conductivity and the defect distribution within the crystal bulk. It is shown how the ion dynamics effectively governs the electronic properties by changing the local doping density. These findings clearly indicate that the interplay between ionic and electronic properties in perovskite materials relies upon a sort of dynamic doping effect caused by moving ions that act as mobile dopants. In addition to electronic features, our analysis extracts values for the ion diffusivity in the range of 10⁻⁸ cm² s⁻¹ in good agreement with independent measurements.

2. Results

Single crystal MAPbBr₃ were prepared following the growth methodology detailed in a previous work.²⁹ Single crystals obtained have been characterized by cross polarized light, surface chemical etching to reveal dislocations and X-ray diffraction (fwhm with an average of 28.3 arc sec). By this method, a clear improvement in crystal quality is reached with higher transparency (~80%), minimized internal strains, and a low dislocation density in the range of 10⁴–10⁵ cm⁻².²⁹

We show here the general electrical behavior of single crystal perovskite samples of MAPbBr₃ with thickness ~1 mm, symmetrically contacted with Cr electrodes (see Supporting Information for sample details and below on experimental conditions). By examining Figure 1, one can infer that the current-voltage characteristics exhibits an approximate ohmic response within the selected voltage range. Accompanying the operation ohmic current, a hysteretic current appears as a consequence of the capacitive mechanisms occurring at low frequencies (see below for impedance analysis).¹⁰ It is remarkable the ohmic character of the characteristics in agreement with previous analysis on Cr-contacted perovskite devices.³⁰ On the contrary, Au metal as contact material yields much more featured responses.¹⁵

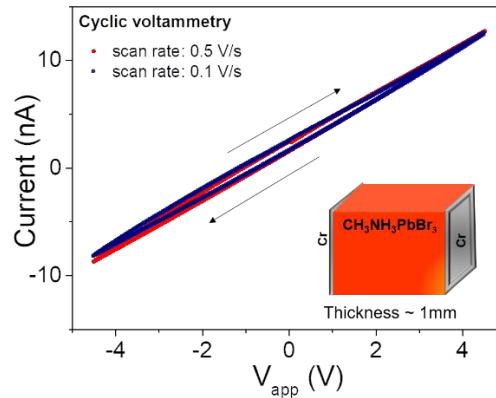


Figure 1. Example of current-voltage characteristics of MAPbBr₃ single crystals of thickness ~1 mm symmetrically contacted with Cr electrodes. The utilization of two different scan rates allows evidencing a small hysteric contribution caused by additional capacitive currents. Note the minutes time window for data registering.

All impedance measurements are performed at room temperature, in the dark and air ambient conditions. This experimental setup avoids the formation of an internal built-in potential as expected when asymmetrical (different work function) materials are used as selective contacting layers. One can observe in the impedance (Figure 2a) and capacitance (Figure 2b) responses, registered at zero-bias, two main features: at high- and intermediate-frequencies ($f > 100$ Hz) the geometrical capacitance C_g and sample resistance R dominate. This forms a semicircle in Figure 2a through the parallel combination RC_g . At lower frequencies the commonly reported excess capacitance increment $C_s \gg C_g$ is observed in Figure 2b, which is viewed as additional increment in the impedance plot. The low-frequency feature in the dark has been usually related to ionic polarization/dynamics within the crystal,¹² and is responsible for the $I - V$ distortion (hysteresis) in Figure 1. The spectra are analyzed and fitted in terms of the equivalent circuit given Figure S1 in Supporting Information.

One important question is to verify if the high-frequency impedance response actually stems from bulk mechanisms. To this end, an exhaustive test has been performed by varying the single crystal thickness. The diameter of the impedance arc should relate to the electronic conductivity $\sigma_e = qn\mu_e$, which establishes the sample (high-frequency) resistance as $R = L/\sigma_e A$, being q the elementary charge, n the carrier density gathering both electrons and holes, μ_e the electronic carrier mobility, L corresponds of the sample thickness, and A its effective area. $\sigma_e \gg \sigma_i$ by several orders of magnitude so as to establish the high-frequency resistive response. See below our discussion on the doping character of the samples. Similarly, the capacitive mechanism ought to scale with thickness as $C_g = \epsilon\epsilon_0 A/L$, being ϵ the dielectric constant and ϵ_0 the permittivity of the free space. As observed in Figure S2, the high-frequency capacitance exhibits no variation upon biasing or time. Therefore, the

parallel combination RC_g determines the high-frequency part of the spectra and is completely given by electronic transport and dielectric properties.

By examining Figure 2c and d, one can infer that both R and C_g scale following the predicted dependence on geometric factors. The dielectric constant $\varepsilon = 76 \pm 11$ extracted from linear fitting agrees with previous determinations for MAPbBr₃,³¹⁻³³ which resulted in values $\varepsilon \sim 60$ at 300 K. Also, the crystal electronic conductivity can be inferred from the linear relationship $R \propto L/A$. Here electronic conductivity of the measured single crystals is in the order of $10^{-8} \Omega^{-1} \text{cm}^{-1}$. High electronic mobility has been measured using laser time-of-flight techniques in our samples $\mu_e = 13 \text{ cm}^2 \text{V}^{-1} \text{s}^{-1}$,³⁴ in accordance with previous analysis on perovskite single crystals.³⁵ These mobility values allow us to infer a background carrier density $n = 1.3 \times 10^{10} \text{ cm}^{-3}$, that also agreed with previous estimations.²⁰ As both parameters linearly scale with the geometrical values, we conclude that the high-frequency part of the impedance response obeys bulk conductive and dielectric properties of MAPbBr₃ single crystals.

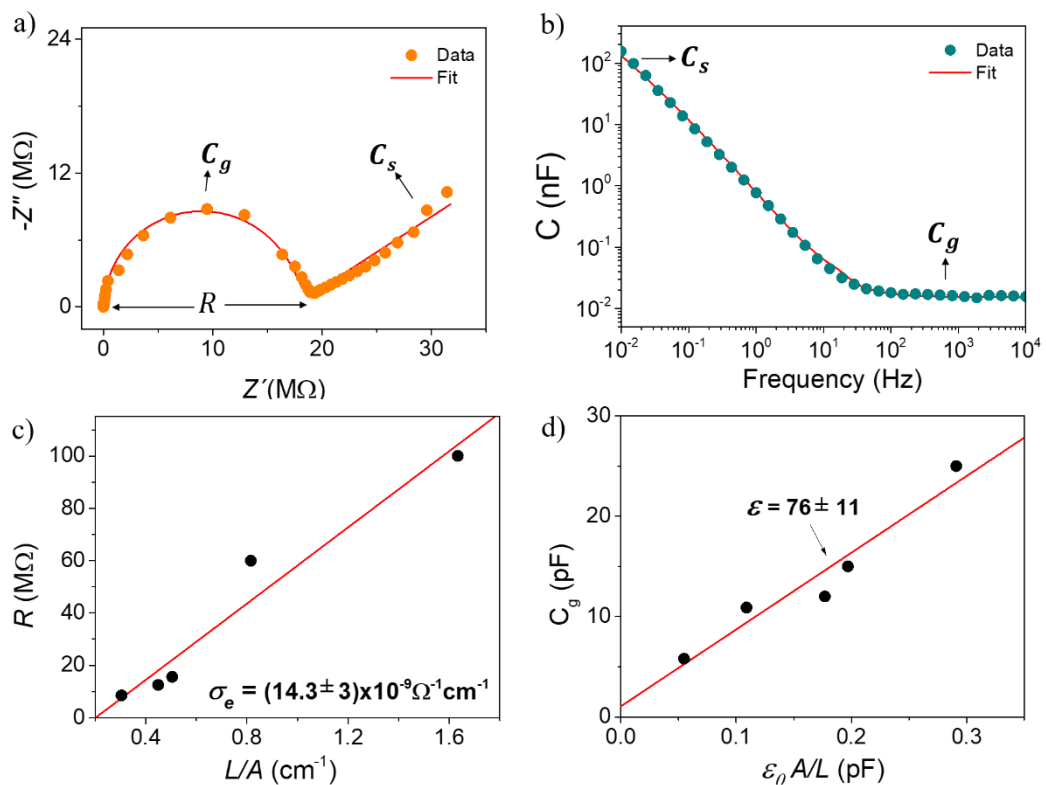


Figure 2. a) Example of the impedance response of MAPbBr₃ single crystals of thickness ~ 1 mm symmetrically contacted with Cr electrodes measured at 0 V in the dark (relaxed samples). Fits result by using the equivalent circuit of Figure S1. b) Capacitance spectrum. Scaling of the high-frequency c) resistance d) and capacitance for five samples of different thicknesses and electrode area, exhibiting linear relationship with geometrical parameters.

Having established the bulk origin for the experimental R and C_g values. We explore now the effects upon bias application. By examining Figure 3a, one can observe that biasing between 0 V and 5 V increases the main resistance (high-frequency part), which is related to the conduction properties of the perovskite crystal as discussed previously. In these experiments, impedance measurement was performed at a given applied voltage after 5 min of pre-conditioning time in the dark. Therefore, the total poling time at each bias is estimated to be of 20 min. It is noted that the linear low-frequency feature is less visible for >2 V-bias. After removing applied voltage, the samples are able to recover initial (equilibrium) response at 0 V-bias, although it takes a much longer time ~ 24 h as illustrated in Figure 3b. A detailed view of the decreasing high-frequency resistance for a time window of 5 h after removing 5 V-bias is shown in Figure 3c. It is noted that in addition to a well-defined semicircle, a line at low frequencies points to the occurrence of modulated resistive/capacitive contributions only observable at longer times.

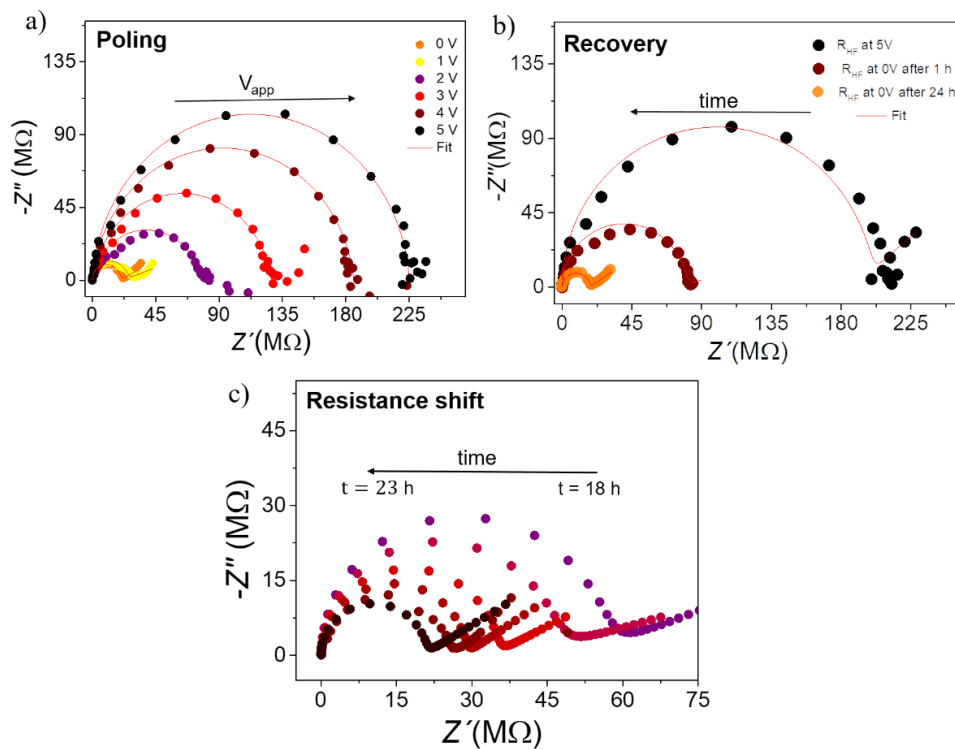


Figure 3. a) Variation of the impedance as a function of the increasing bias with total measuring time ~ 20 min at each voltage. b) Variation of the impedance after removing 5 V-bias and evolution with time. Note that the final (24 h) spectrum recovers the initial one at 0 V-bias in Figure 3a. c) Detailed view of the variation of the impedance after removing 5 V-bias and evolution with time for smaller impedances (five last hours of the experiment).

One can infer from our observations that sample resistance is a function, not only of the applied bias, but also of the poling and recovering time. While poling induces relatively quick responses with resistive increment as main result, equilibrium state needs much longer times to recover. The above explained impedance variation process was repeated several times to verify its cyclability (see reproducibility test in Figure S3). It is important to note that due to the use of Cr we are able to limit the interference of the contacts by chemical reactivity. Therefore, these findings suggest a plausible change in electrical driving force ultimately establishing the conductive character of the bromide perovskite crystals.

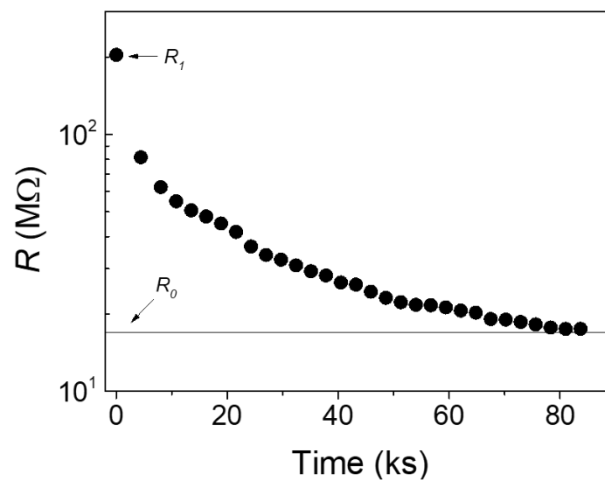


Figure 4. Variation of the resistance extracted from fitting of impedance spectra after bias removing at $t = 0$. Note the log scale in the vertical axis that informs on the complex function (non-exponential) of the resistance variation.

A complete series of impedance spectra allows calculating how the value of the high-frequency resistance recovers the equilibrium after bias is removed (see Figure 4). It is inferred that the resistance shows a large value R_1 at shorter recovering times and progressively attains a steady-state value R_0 after a long equilibration time of approximately 24 h. It is also seen that the resistance variation does not obey an exponential law.

In order to understand this variation, we propose a rationale that connects the decrease of the resistance with time with the increase in electronic doping of the perovskite bulk. Our hypothesis is that the carrier density n depends on the distribution of mobile ions within the crystal that act as moving dopants. This kind of correlation between mobile ion location within the crystal and electronic carrier density was previously postulated by Bisquert and co-workers in the case of the electrical switching of photoluminescence.³⁶

Upon long-time polarization, ion movement and accumulation produce a sort of dedoping effect giving rise to a reduced carrier density n_1 in a wide portion of the crystal,

and consequently yields larger resistance R_1 . After removing bias, ions take some time to return to their initial distribution which recovers the greater background value of the carrier density n_0 along the crystal bulk. That initial carrier density is understood as an equilibrium n_0 value for the sample at zero bias in the dark. From the evolution of the impedance with time, it is observed that $R_0 < R_1$, or equivalently $n_0 > n_1$. From the values in Figure 4, one can infer that electronic carrier density ratio n_0/n_1 attains values as high as ~ 12 , thus indicating that doping is reduced by approximately one order of magnitude upon 5 V-poling. The time evolution of the ionic-electronic coupling is schematically illustrated in Figure 5 through the dynamic doping process.

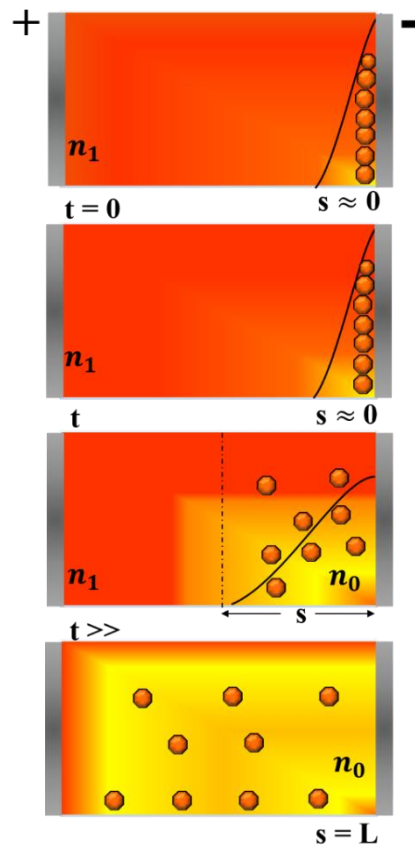


Figure 5. Schematic drawing of the ion polarization and rearrangement process (dynamic doping) by diffusion after bias removing. Initially, mobile ionic species accumulate following a narrow distribution near the contact. Here it is assumed that positively-charged defects dominate the concentration of mobile ions. Ion accumulation entails de-doping of electronic carriers within the crystal bulk with carrier density n_1 . At $t = 0$, external electrical field is removed so that ions are released and start diffusing. At a given releasing time t , the ion distribution width s spreads and provokes a progressive increment in the overall carrier density n . In the final stage, ions recover the equilibrium distribution and, consequently, the overall electronic carrier density returns to n_0 .

Let us consider that the rate at which n transits from n_1 to n_0 mimics the time scale of mobile ion re-distribution after releasing. For the sake of simplicity, we model the increase in average carrier density in relation to the effective size s occupied by moving ions. At shorter times, ion accumulation restricts to narrow layers in the vicinity of the contact (see Figure 5). Ideally, s evolves after bias removing from $s \approx 0$ to L . As a first approximation, one can assume that the effective size s divides the bulk into two zones of larger and smaller doping, forming a sort of semiconductor homojunction in which the boundary position varies with time. The real situation is of course much more complex and should include the exact distribution mobile ions and their contribution to local electronic doping.

For the sake of simplicity, an effective carrier density can be calculated as

$$n = \frac{1}{L} [n_0 s + n_1 (L - s)] \quad (1)$$

which includes two zones of different doping. It should be noted that two well-differentiated impedance arcs corresponding to each of the above-mentioned separate doping zones are hardly observable because of the rather small ratio $n_0/n_1 \sim 12$. After rearrangement, Equation (1) can be expressed as

$$n = n_1 \left(1 + \frac{\gamma s}{L} \right) \quad (2)$$

Here, γ represents a constant determined by the limiting doping states

$$\gamma = \frac{n_0 - n_1}{n_1} \quad (3)$$

that results by assuming $n(s = 0) = n_1$ and $n(s = L) = n_0$.

Let us also assume that doping ions initially accumulate following a narrow distribution near the contact that spreads as $s = \sigma$. Here σ stands for the distribution width. The accumulation occurs by effect of the applied electrical field because no built-in potential exists for symmetrically contacted samples. This ionic accumulation is expected by formation of a diffusion ion layer in the vicinity of the contacts and by very limited interfacial chemical interaction within the experimental time framework. When bias is removed, ions are released and tend to diffuse back to their equilibrium position in such a way that the mean square displacement of the ion distribution enlarges with time. The simple outlined model would entail diffusion takes place in 1D ($\delta = 1$), but the real situation should be more complex with diffusion dimensionality approaching larger values. Individual ion penetration path is in principle hemispherical. Therefore, the distribution width spreads by diffusion as

$$\sigma = \sqrt{2\delta Dt} \quad (4)$$

with D accounts for the ion diffusion coefficient, $\delta = 3$ for 3D diffusion, and t is the time.

Because the resistance ratio R_1/R equals the density ratio n/n_1 , one can derive by combining Equation (2) and (4), and $\delta = 3$ an expression for the time dependence of the resistance ratio as

$$\frac{R_1}{R} = 1 + \frac{\gamma}{L} \sqrt{6Dt} \quad (5)$$

which predicts a linear dependence as $\propto \sqrt{t}$ with slope determined by the diffusion coefficient.

The resistance extracted from impedance data fitting in Figure 4 is replotted in Figure 6 in accordance to the formulation of Equation (5), i.e. R_1/R as a function of \sqrt{t} .

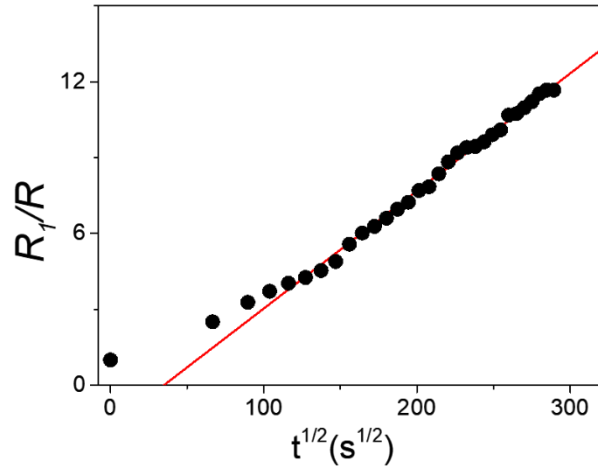


Figure 6. Variation of resistance ratio as a function of time following the relationship of Equation (5). Solid line represents a linear fitting.

As observed, a good linear relationship is reproduced between R_1/R and \sqrt{t} in accordance with our prediction for longer times. A deviation occurs at shorter times, presumably related to the simplicity of the model in Equation (5), unable to capture second order depolarization effects for greater moving ion concentrations. It is also questionable that our assumption $s = \sigma$ is valid for $s \ll L$. In any case, from the linear fitting slope in Figure 6 (valid for longer times) and the experimental parameters $L = 0.88$ mm and $\gamma = 10.67$, one can obtain a value for the ion diffusion coefficient that results in $D = 2.6 \times 10^{-8} \text{ cm}^2 \text{ s}^{-1}$. We note that reducing the diffusion dimensionality from $\delta = 3$ to $\delta = 1$ just enlarges the diffusion coefficient by a factor three. Whereas some studies have reported diffusivity values of native defects in organohalide perovskites of the order of those encountered in common solid-state ionic conductors, $D \approx 10^{-12} \text{ cm}^2 \text{ s}^{-1}$,³⁷⁻³⁹ other analysis gave much faster ion migration coefficients $D \approx 10^{-8}$ to $10^{-7} \text{ cm}^2 \text{ s}^{-1}$ in agreement with recent determinations and simulations of the diffusion coefficient.⁴⁰⁻⁴¹

3. Discussion

We remark that ionic diffusion coefficients in the order of 10^{-8} - $10^{-7} \text{ cm}^2 \text{ s}^{-1}$ explain the extremely slow relaxing time (~ 24 h) after bias removing in the studied perovskite thick single crystals. Similarly, it is also possible to estimate the short polarization time upon poling evidenced in Figure 3a. Resistance attains large values a few minutes after

bias application. From the estimated D and using the Einstein relation $\mu_i = qD/k_B T$, being μ_i the ionic mobility and $k_B T$ the thermal energy, one can estimate the ion transit time by electrical field drift upon application of 5 V-bias as $t_d = L^2/\mu_i V_{app}$. For our measurements, the transit time calculation results in polarization times of $t_d \sim 15$ min, which agrees with our general observation about the impedance dynamic change in Figure 3a. Therefore, it is concluded that polarization by ion movement (drift-driven) takes several minutes for 1 mm-thick single crystals, but requires much longer times when ions should be transported by diffusion. As observed by impedance measurement, ion distribution locally varies the electronic doping and the overall sample resistance. More importantly, it is the ion dynamics that governs the ultimate response time of the electronic transport in perovskite compounds through the dynamic doping process.

Also of importance is the comparison between electronic and ionic mobilities. As noted, electronic conductivity situates in values as high as $\mu_e = 13 \text{ cm}^2 \text{ V}^{-1} \text{ s}^{-1}$ for high quality single crystals. From our estimations, the ionic mobility results in $\mu_i = 1.0 \times 10^{-6} \text{ cm}^2 \text{ V}^{-1} \text{ s}^{-1}$, and therefore $\mu_e \gg \mu_i$ as expected. In order to achieve similar ionic and electronic conductivities $\sigma_e \approx \sigma_i$, mobile ion concentration as high as $1.7 \times 10^{17} \text{ cm}^{-3}$ would be necessary, which seems to be rather unlikely for good quality single crystals as those used here. Let us note for consistency that the electronic density is only enlarged by approximately one order of magnitude, from $n_0 = 1.3 \times 10^{10} \text{ cm}^{-3}$ down to $n_1 = 1.2 \times 10^9 \text{ cm}^{-3}$. So that this increment is hardly caused by large mobile ionic defect concentrations. Therefore, the initial assumption about the domination of electronic over ionic conductivity $\sigma_e \gg \sigma_i$ is consistent with our findings.

The dissimilar time response observed between poling and recovering without applied electrical field in terms of the intrinsic ionic dynamics allows us to preclude alternative explanation for the measurements. One might think about slow decomposition or doping by environmental molecules as H_2O or oxygen in a surface mechanism. These kinds of processes usually involve chemical reactivity, either with the perovskite or contact materials. However, such chemical interactions usually exhibit poor reversibility. For instance, hydrated phases have been studied by first-principle methods⁴² as one of the primary degradation or decomposition paths. For solar cells structures, electrical degradation takes place on a short time scale of 2–3 days of exposure.⁴³ Some authors have observed reversible responses upon drying,^{44–45} but the devices have to be exposed to dry nitrogen or high temperature for hours. Single crystals used here were always in ambient atmosphere and room temperature. If humidity was absorbed (water molecules diffusivity is much lower in mono- than in poly-crystals), they should have been kept inside in contradiction to the observed reversibility in Figure S3. Then the effect of extrinsic agents can be safely excluded.

Recalling now the general impedance response of Figure 2, the low-frequency feature manifested either as a linear increment (Figure 2a) or a capacitive step (Figure 2b) should be related to the dynamics of the ionic profile. The variation of the ion distribution within the time window corresponding to the measuring frequency give

rise to the reported capacitance increase because of ion accumulation C_5 . Consequently, there is a modulation of the electronic doping restricted within the crystal to affected zones. The final effect is an increment in the electronic resistance caused by the coupling between ion distribution variation and carrier density. As observed in Figure 2a, the modulation effect is more visible for longer releasing times (wider distributions of mobile ions) than in the case of narrow accumulations. It is also noted that diffusion characteristics are also present in the low-frequency impedance in the form of Warburg-like responses.⁴¹

In the following we speculate about the connection between specific ionic defects and electronic doping mechanisms. Due to the presence of three elements in the ABX_3 perovskite formulations and to the rich redox chemistry of halide-containing materials, a whole array of ionic defects (D) may be present in the crystals. The energy of defect formation has been extensively studied by theoretical calculations.⁴⁶⁻⁴⁸ Not only do they include the basic nine species arising from vacancies, interstitial elements and antisites but they also include their corresponding stable charged counterparts. Examples of negatively charged defects (D^-) compatible with low formation energies include halide interstitials (X_i^-) or Pb^{2+} vacancies (V_{Pb}^{2-}). Alternatively, examples of positively charged defects (D^+) include MA^+ interstitials (MA_i^+) and Pb^{2+} interstitial (Pb_i^+) or X^- vacancies (V_X^+). Among all these defects, V_X^+ is the mobile ion believed to have the lowest activation energy for migration. Whilst formation of these defects is accessible by theoretical means, they are very difficult to detect experimentally. As a consequence, accessible understanding of the defect density for the different defect species is always limited for given perovskite samples. Direct measurement of specific defect densities is out of the scope of this work⁴⁹⁻⁵⁰ and we next provide a general discussion on how the doping concentration is modified during the application and switching-off of an external bias.

A simple explanation would consist in assuming that halide vacancies V_X^+ dominate and establish the general background doping character. As V_X^+ is considered a shallow donor both for iodide and bromide perovskites,⁵¹⁻⁵² one can infer that n -type doping increases in zones in which the halide vacancy concentration is higher. Upon poling, accumulation of halide vacancies near the negative-biased contact is expected. As a consequence, this process forms an internal doping profile which implies that the perovskite bulk can be modeled as a sort of semiconductor homojunction with a mobile boundary between lower- and higher-doped regions in accordance with the simple structure sketched in Figure 5 of the dynamic doping process.

But obviously, the defect chemistry in hybrid perovskite compounds may be much richer. Since the application of an external voltage produces movement of charged defects and electronic carrier injection, defects can capture a hole/electron to form neutral states D^0 . Consequently, for negatively charged defects this would be $D^- + h^+ \rightarrow D^0$.⁴⁷ However, there will be a complementary redox semi-reaction (reduction) taking place simultaneously somewhere in the device which would increase the concentration of negatively charged species. For the previous example the

complementary reduction reaction can be represented as $D^0 + e^- \rightarrow D^-$. The overall result is that there will be no change in the background doping density. If the same halogen participates in both oxidation and reduction reaction, a Frenkel type reaction will be taking place ($Br_i^- + V_{Br}^+ \rightarrow Br^0$). It has been also reported that formation of new nonradiative defects in MAPbI₃ is only observed in the presence of injected electrons, suggesting that redox processes play a key role.⁵³

In any case, an increase in the measured resistance as a consequence of a reduction in doping density can only be explained by formation of separated regions with different doping densities, being the least doped region mainly responsible for the resistive response. This situation is the basis of the electrical model proposed in this work which is in good agreement with previous results in spatially resolved PL measurements.³⁶ Mobile ions will follow the external electrical field induced by the external voltage and will populate the region where they can modify the doping concentration. Upon switching-off the external voltage mobile ions (V_X^+) will move in the perovskite layer following the chemical potential generated from the highly populated region of mobile ions to the region with lower concentration of mobile ions. In the presence of an external voltage the density of electrons and holes will be the sum of the free carriers and the background densities in each region. Alternatively, in the absence of an applied voltage, supply of h^+/e^- to accomplish the opposite reactions will be reduced as only background doping is present in the perovskite layer. This by itself responds for the slower kinetics of the relaxation of ions after switching-off the voltage as both electrons and holes are involved in the bulk perovskite chemical reactions.

4. Conclusions

We report on the impedance analysis of a set of high quality thick CH₃NH₃PbBr₃ single crystals contacted with more stable and less reacting chromium electrodes. It is shown that the high-frequency circuit elements extracted from impedance are originated by the dielectric and electronic conduction properties of the sample bulk. The bias- and time-dependence of bulk resistance informs about the accumulation and relaxation dynamics of the moving ionic species. Our analysis extracts values for the ion diffusivity in the range of $10^{-8} \text{ cm}^2 \text{ s}^{-1}$ in good agreement with independent measurements. It is concluded that the interplay between ionic and electronic properties in perovskite materials relies upon a sort of dynamic doping effect caused by moving ions that act as dopants and locally vary the carrier density. These findings highlight the electronic-ionic coupling effect and reveals the mechanism through which such connection occurs.

5. Experimental Section

Crystal preparation. Self-supported CH₃NH₃PbBr₃ single crystal were fabricated using the inverse temperature protocol in dimethylformamide (DMF), and following the growth methodology detailed in a previous work.²⁹ Bare crystals have square shape

with typical lateral dimensions of $5 \times 5 \text{ mm}^2$ and a thickness of 2 mm. Crystals with different thicknesses ranging from 0.6 to 1.4 mm were subsequently fabricated by using a first rough mechano-chemical polishing and by decreasing progressively the sand paper roughness. Special attention has been paid to apply a constant pressure of 0.3 N on all the samples, in order to avoid any additional mechanical strains in the bulk of the crystals. In the final step, the crystals were finely polished to mirror grade quality on the (100) faces. Just after the polishing step, 100 nm thick chromium electrodes were evaporated on both faces through a mechanical shadow mask. Devices were stored in air without any encapsulation.

Impedance measurements. Impedance spectroscopy experiments were carried out by using a PGSTAT-30 Autolab potentiostat equipped with impedance module. All the samples were measured inside a metallic box acting as Faraday cage, in dark and air conditions between 10 mHz and 1 MHz, with a perturbation amplitude of 30 mV. Different potentials cycles were used mainly from 0 V to 5 V (forward polarization bias) and from 5 V to 0 V (reverse polarization bias). After each bias change, the sample was left to attain equilibrium during 5 minutes before starting a run. Each run lasted 13-15 minutes.

Supporting Information

Supporting Information is available from the Wiley Online Library or from the author.

Acknowledgments

We acknowledge support from Horizon 2020 project (grant number 871336 - PEROXIS). M. G.-B. acknowledges Generalitat Valenciana for a grant (number GRISOLIAP/2018/073). O. B. acknowledges Trixell for her PhD grant.

Conflict of Interest

The authors declare no conflict of interest.

Keywords

ion dynamics, hybrid perovskites, electronic conductivity, dynamic doping.

References

1. Green, M. A.; Dunlop, E. D.; Hohl-Ebinger, J.; Yoshita, M.; Kopidakis, N.; Ho-Baillie, A. W. Y., Solar Cell Efficiency Tables (Version 55). *Progress in Photovoltaics: Research and Applications* **2020**, *28*, 3-15.

2. Heiss, W.; Brabec, C., Perovskites Target X-Ray Detection. *Nature Photonics* **2016**, *10*, 288-289.
3. Unger, E. L.; Hoke, E. T.; Bailie, C. D.; Nguyen, W. H.; Bowring, A. R.; Heumuller, T.; Christoforo, M. G.; McGehee, M. D., Hysteresis and Transient Behavior in Current-Voltage Measurements of Hybrid-Perovskite Absorber Solar Cells. *Energy Environ. Sci.* **2014**, *7*, 3690-3698.
4. Azpiroz, J. M.; Mosconi, E.; Bisquert, J.; De Angelis, F., Defect Migration in Methylammonium Lead Iodide and Its Role in Perovskite Solar Cell Operation. *Energy & Environmental Science* **2015**, *8*, 2118-2127.
5. Meloni, S., et al., Ionic Polarization-Induced Current–Voltage Hysteresis in $\text{CH}_3\text{NH}_3\text{PbX}_3$ Perovskite Solar Cells. *Nat. Commun.* **2016**, *7*, 10334.
6. Hoke, E. T.; Slotcavage, D. J.; Dohner, E. R.; Bowring, A. R.; Karunadasa, H. I.; McGehee, M. D., Reversible Photo-Induced Trap Formation in Mixed-Halide Hybrid Perovskites for Photovoltaics. *Chemical Science* **2015**, *6*, 613-617.
7. Jiang, C.-S., et al., Carrier Separation and Transport in Perovskite Solar Cells Studied by Nanometre-Scale Profiling of Electrical Potential. *Nature Communications* **2015**, *6*, 8397.
8. Bergmann, V. W.; Guo, Y.; Tanaka, H.; Hermes, I. M.; Li, D.; Klasen, A.; Bretschneider, S. A.; Nakamura, E.; Berger, R.; Weber, S. A. L., Local Time-Dependent Charging in a Perovskite Solar Cell. *ACS Appl. Mater. Interfaces* **2016**, *8*, 19402-19409.
9. Ahmadi, M.; Collins, L.; Higgins, K.; Kim, D.; Lukosi, E.; Kalinin, S. V., Spatially Resolved Carrier Dynamics at MAPbBr_3 Single Crystal–Electrode Interface. *ACS Applied Materials & Interfaces* **2019**, *11*, 41551-41560.
10. Almora, O.; Aranda, C.; Zarazua, I.; Guerrero, A.; Garcia-Belmonte, G., Noncapacitive Hysteresis in Perovskite Solar Cells at Room Temperature. *ACS Energy Lett.* **2016**, *1*, 209–215.
11. Wang, J., et al., Investigation of Electrode Electrochemical Reactions in $\text{CH}_3\text{NH}_3\text{PbBr}_3$ Perovskite Single-Crystal Field-Effect Transistors. **2019**, *31*, 1902618.
12. Almora, O.; Zarazua, I.; Mas-Marza, E.; Mora-Sero, I.; Bisquert, J.; Garcia-Belmonte, G., Capacitive Dark Currents, Hysteresis, and Electrode Polarization in Lead Halide Perovskite Solar Cells. *J. Phys. Chem. Lett.* **2015**, *6*, 1645-1652.
13. Almora, O.; Guerrero, A.; Garcia-Belmonte, G., Ionic Charging by Local Imbalance at Interfaces in Hybrid Lead Halide Perovskites. *Applied Physics Letters* **2016**, *108*, 043903.
14. Wang, H.; Guerrero, A.; Bou, A.; Al-Mayouf, A. M.; Bisquert, J., Kinetic and Material Properties of Interfaces Governing Slow Response and Long Timescale Phenomena in Perovskite Solar Cells. *Energy & Environmental Science* **2019**, *12*, 2054-2079.
15. Pospisil, J.; Guerrero, A.; Zmeskal, O.; Weiter, M.; Gallardo, J. J.; Navas, J.; Garcia-Belmonte, G., Reversible Formation of Gold Halides in Single-Crystal Hybrid-Perovskite/Au Interface Upon Biasing and Effect on Electronic Carrier Injection. *Advanced Functional Materials* **2019**, *29*, 1900881.

16. Carrillo, J.; Guerrero, A.; Rahimnejad, S.; Almora, O.; Zarazua, I.; Mas-Marza, E.; Bisquert, J.; Garcia-Belmonte, G., Ionic Reactivity at Contacts and Aging of Methylammonium Lead Triiodide Perovskite Solar Cells. *Adv. Energy Mater.* **2016**, *6*, 1502246
17. Solanki, A.; Guerrero, A.; Zhang, Q.; Bisquert, J.; Sum, T. C., Interfacial Mechanism for Efficient Resistive Switching in Ruddlesden–Popper Perovskites for Non-Volatile Memories. *The Journal of Physical Chemistry Letters* **2020**, *11*, 463-470.
18. Liu, Y., et al., Two-Inch-Sized Perovskite $\text{Ch}_3\text{nh}_3\text{pbx}_3$ (X = Cl, Br, I) Crystals: Growth and Characterization. *Adv. Mater.* **2015**, *27*, 5176-5183.
19. Peng, W., et al., Solution-Grown Monocrystalline Hybrid Perovskite Films for Hole-Transporter-Free Solar Cells. *Adv. Mater.* **2016**, *28*, 3383-3390.
20. Saidaminov, M. I., et al., High-Quality Bulk Hybrid Perovskite Single Crystals within Minutes by Inverse Temperature Crystallization. *Nature Communications* **2015**, *6*, 7586.
21. Kovalenko, A.; Pospisil, J.; Krajcovic, J.; Weiter, M.; Guerrero, A.; Garcia-Belmonte, G., Interface Inductive Currents and Carrier Injection in Hybrid Perovskite Single Crystals. *Appl. Phys. Lett.* **2017**, *111*, 163504.
22. Kaltenbrunner, M., et al., Flexible High Power-Per-Weight Perovskite Solar Cells with Chromium Oxide–Metal Contacts for Improved Stability in Air. *Nature Materials* **2015**, *14*, 1032-1039.
23. Jordan, L. R.; Betts, A. J.; Dahm, K. L.; Dearnley, P. A.; Wright, G. A., Corrosion and Passivation Mechanism of Chromium Diboride Coatings on Stainless Steel. *Corrosion Science* **2005**, *47*, 1085-1096.
24. Guerrero, A.; You, J.; Aranda, C.; Kang, Y. S.; Garcia-Belmonte, G.; Zhou, H.; Bisquert, J.; Yang, Y., Interfacial Degradation of Planar Lead Halide Perovskite Solar Cells. *ACS Nano* **2016**, *10*, 218-224.
25. Bai, S., et al., Planar Perovskite Solar Cells with Long-Term Stability Using Ionic Liquid Additives. *Nature* **2019**, *571*, 245-250.
26. Thirimanne, H. M., et al., High Sensitivity Organic Inorganic Hybrid X-Ray Detectors with Direct Transduction and Broadband Response. *Nature Communications* **2018**, *9*, 2926.
27. Basiricò, L.; Senanayak, S. P.; Ciavatti, A.; Abdi-Jalebi, M.; Fraboni, B.; Siringhaus, H., Detection of X-Rays by Solution-Processed Cesium-Containing Mixed Triple Cation Perovskite Thin Films. *Advanced Functional Materials* **2019**, *29*, 1902346.
28. Weber, S. A. L.; Hermes, I. M.; Turren-Cruz, S.-H.; Gort, C.; Bergmann, V. W.; Gilson, L.; Hagfeldt, A.; Graetzel, M.; Tress, W.; Berger, R., How the Formation of Interfacial Charge Causes Hysteresis in Perovskite Solar Cells. *Energy & Environmental Science* **2018**, *11*, 2404-2413.
29. Amari, S.; Verilhac, J.-M.; Gros D'Aillon, E.; Ibanez, A.; Zaccaro, J., Optimization of the Growth Conditions for High Quality $\text{Ch}_3\text{nh}_3\text{pbbr}_3$ Hybrid Perovskite Single Crystals. *Crystal Growth & Design* **2020**, *20*, 1665-1672.

30. Tisdale, J. T.; Muckley, E.; Ahmadi, M.; Smith, T.; Seal, C.; Lukosi, E.; Ivanov, I. N.; Hu, B., Dynamic Impact of Electrode Materials on Interface of Single-Crystalline Methylammonium Lead Bromide Perovskite. *Adv. Mater. Interfaces* **2018**, *5*, 1800476.
31. Onoda-Yamamuro, N.; Matsuo, T.; Suga, H., Dielectric Study of $\text{Ch}_3\text{nh}_3\text{pbx}_3$ ($X = \text{Cl}, \text{Br}, \text{I}$). *Journal of Physics and Chemistry of Solids* **1992**, *53*, 935-939.
32. Govinda, S., et al., Behavior of Methylammonium Dipoles in Mapbx_3 ($X = \text{Br}$ and I). *The Journal of Physical Chemistry Letters* **2017**, *8*, 4113-4121.
33. Wilson, J. N.; Frost, J. M.; Wallace, S. K.; Walsh, A., Dielectric and Ferroic Properties of Metal Halide Perovskites. *APL Mater.* **2019**, *7*, 010901.
34. Baussens, O.; Maturana, L.; Amari, S.; Verilhac, J.; Hirsch, L.; Gros-Daillon, E., Transport Properties of $\text{Ch}_3\text{nh}_3\text{pbbr}_3$ Single Crystals for Medical X-Ray Detection Applications. *Appl. Phys. Lett.* **2020**, submitted.
35. Shi, D., et al., Low Trap-State Density and Long Carrier Diffusion in Organolead Trihalide Perovskite Single Crystals. *Science* **2015**, *347*, 519-522.
36. Li, C.; Guerrero, A.; Huettner, S.; Bisquert, J., Unravelling the Role of Vacancies in Lead Halide Perovskite through Electrical Switching of Photoluminescence. *Nat. Commun.* **2018**, *9*, 5113.
37. Eames, C.; Frost, J. M.; Barnes, P. R. F.; O'Regan, B. C.; Walsh, A.; Islam, M. S., Ionic Transport in Hybrid Lead Iodide Perovskite Solar Cells. *Nature Communications* **2015**, *6*, 7497.
38. Bag, M.; Renna, L. A.; Adhikari, R. Y.; Karak, S.; Liu, F.; Lahti, P. M.; Russell, T. P.; Tuominen, M. T.; Venkataraman, D., Kinetics of Ion Transport in Perovskite Active Layers and Its Implications for Active Layer Stability. *Journal of the American Chemical Society* **2015**, *137*, 13130-13137.
39. Richardson, G.; O'Kane, S. E. J.; Niemann, R. G.; Peltola, T. A.; Foster, J. M.; Cameron, P. J.; Walker, A. B., Can Slow-Moving Ions Explain Hysteresis in the Current–Voltage Curves of Perovskite Solar Cells? *Energy & Environmental Science* **2016**, *9*, 1476-1485.
40. Yang, T.-Y.; Gregori, G.; Pellet, N.; Grätzel, M.; Maier, J., The Significance of Ion Conduction in a Hybrid Organic–Inorganic Lead-Iodide-Based Perovskite Photosensitizer. *Angewandte Chemie International Edition* **2015**, *54*, 7905-7910.
41. Peng, W.; Aranda, C.; Bakr, O. M.; Garcia-Belmonte, G.; Bisquert, J.; Guerrero, A., Quantification of Ionic Diffusion in Lead Halide Perovskite Single Crystals. *ACS Energy Letters* **2018**, *3*, 1477-1481.
42. Kye, Y.-H.; Yu, C.-J.; Jong, U.-G.; Chen, Y.; Walsh, A., Critical Role of Water in Defect Aggregation and Chemical Degradation of Perovskite Solar Cells. *The Journal of Physical Chemistry Letters* **2018**, *9*, 2196-2201.
43. Marronnier, A.; Lee, H.; Lee, H.; Kim, M.; Eypert, C.; Gaston, J.-P.; Roma, G.; Tondelier, D.; Geffroy, B.; Bonnassieux, Y., Electrical and Optical

Degradation Study of Methylammonium-Based Perovskite Materials under Ambient Conditions. *Solar Energy Materials and Solar Cells* **2018**, *178*, 179-185.

44. Leguy, A. M. A., et al., Reversible Hydration of $\text{CH}_3\text{NH}_3\text{PbI}_3$ in Films, Single Crystals, and Solar Cells. *Chemistry of Materials* **2015**, *27*, 3397-3407.

45. García-Fernández, A.; Moradi, Z.; Bermúdez-García, J. M.; Sánchez-Andújar, M.; Gimeno, V. A.; Castro-García, S.; Señarís-Rodríguez, M. A.; Mas-Marzá, E.; Garcia-Belmonte, G.; Fabregat-Santiago, F., Effect of Environmental Humidity on the Electrical Properties of Lead Halide Perovskites. *The Journal of Physical Chemistry C* **2019**, *123*, 2011-2018.

46. Meggiolaro, D.; Mosconi, E.; De Angelis, F., Modeling the Interaction of Molecular Iodine with MAPbI_3 : A Probe of Lead-Halide Perovskites Defect Chemistry. *ACS Energy Letters* **2018**, *3*, 447-451.

47. Whalley, L. D.; Crespo-Otero, R.; Walsh, A., H-Center and V-Center Defects in Hybrid Halide Perovskites. *ACS Energy Letters* **2017**, *2*, 2713-2714.

48. Motti, S. G.; Meggiolaro, D.; Barker, A. J.; Mosconi, E.; Perini, C. A. R.; Ball, J. M.; Gandini, M.; Kim, M.; De Angelis, F.; Petrozza, A., Controlling Competing Photochemical Reactions Stabilizes Perovskite Solar Cells. *Nature Photonics* **2019**, *13*, 532-539.

49. deQuilettes, D. W.; Frohna, K.; Emin, D.; Kirchartz, T.; Bulovic, V.; Ginger, D. S.; Stranks, S. D., Charge-Carrier Recombination in Halide Perovskites. *Chemical Reviews* **2019**, *119*, 11007-11019.

50. Bertoluzzi, L.; Boyd, C. C.; Rolston, N.; Xu, J.; Prasanna, R.; O'Regan, B. C.; McGehee, M. D., Mobile Ion Concentration Measurement and Open-Access Band Diagram Simulation Platform for Halide Perovskite Solar Cells. *Joule* **2020**, *4*, 109-127.

51. Yin, W.-J.; Shi, T.; Yan, Y., Unusual Defect Physics in $\text{CH}_3\text{NH}_3\text{PbI}_3$ Perovskite Solar Cell Absorber. *Appl. Phys. Lett.* **2014**, *104*, 063903.

52. Motti, S. G.; Meggiolaro, D.; Martani, S.; Sorrentino, R.; Barker, A. J.; De Angelis, F.; Petrozza, A., Defect Activity in Lead Halide Perovskites. *Adv. Mater.* **2019**, *31*, 1901183.

53. Birkhold, S. T.; Pecht, J. T.; Liu, H.; Giridharagopal, R.; Eperon, G. E.; Schmidt-Mende, L.; Li, X.; Ginger, D. S., Interplay of Mobile Ions and Injected Carriers Creates Recombination Centers in Metal Halide Perovskites under Bias. *ACS Energy Letters* **2018**, *3*, 1279-1286.

4.4 Supplemental Information

Moving Ions Vary Electronic Conductivity in Lead Bromide Perovskite Single Crystals through Dynamic Doping

Marisé García-Batlle¹, Oriane Baussens², Smaïl Amari³, Julien Zaccaro⁴,
Eric Gros-Daillon², Jean-Marie Verilhac³, Antonio Guerrero¹,
and Germà Garcia-Belmonte^{1*}

¹ Institute of Advanced Materials (INAM), Universitat Jaume I, ES12006 Castelló, Spain






² Grenoble Alpes University, CEA, LETI, F38000 Grenoble, France

³ Grenoble Alpes University, CEA, LITEN, F38000 Grenoble, France

⁴ Grenoble Alpes University, CNRS, Grenoble INP, Institut Néel, F38042 Grenoble France

*Email: garciag@uji.es

Table S1: Summary table of samples studied with their dimensions and properties. Further information about the characterization techniques in ref [29] main text.

N ame	Crys tallinity	Crystal dimensions (mm³)	Elect rode surface (mm²)	Resist ivity (10⁸ Ω.cm)	Picture
R X10	SC	3.93×3.87×0.61	12.1	3.40	
R X11	SC	6.64×5.81×0.88	28.9	3.60	
R X5B	SC	4.10×2.00×0.89	5.5	2.50	
R X16	SC	5.70×4.80×0.88	19.6	1.10	
R X15	SC	5.13×5.72×1.35	22.1	5.5	

*SC: Single crystal

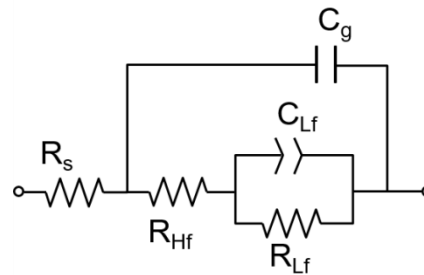


Figure S1 Equivalent circuit used to fit the IS data measured in the dark of the MAPbBr₃ perovskite single crystal, with series resistance R_s , C_g geometric capacitance and R_{HF} , and R_{LF} the high-, and low-frequency resistances, respectively. C_{Lf} is the low-frequency capacitance usually labelled as surface capacitance C_s .

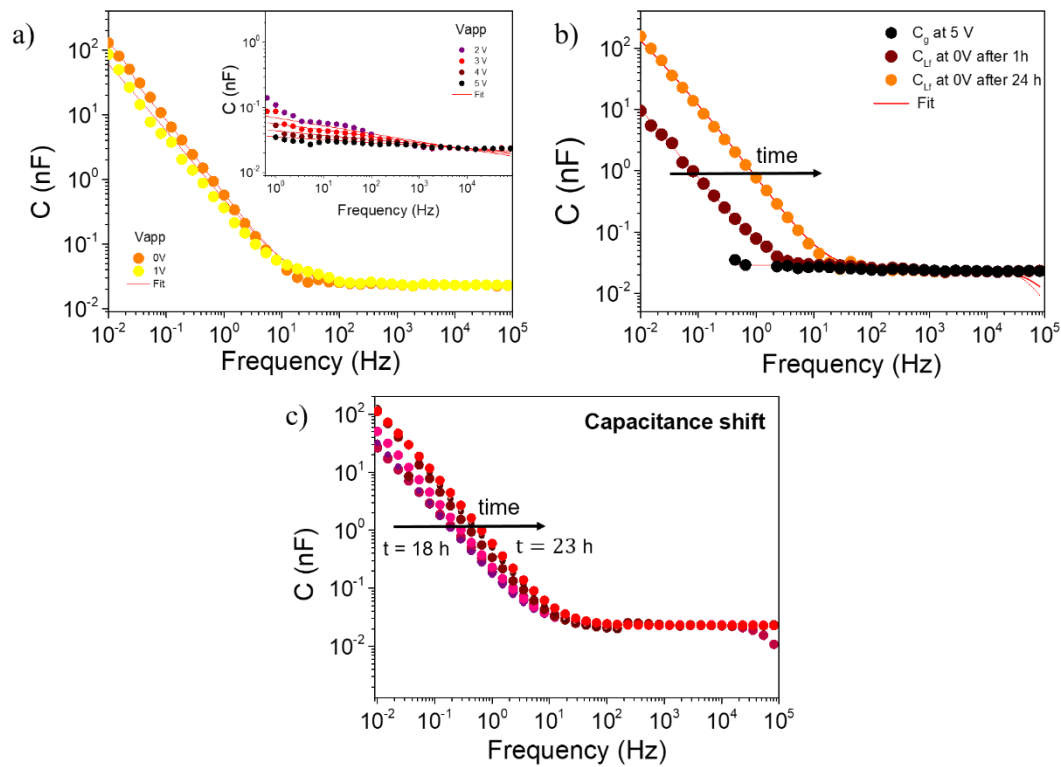


Figure S2 a) Variation of the capacitance spectra as a function of the bias with total measuring time ~ 20 min. b) Variation of the low frequency capacitance after removing 5 V-bias and evolution with time. c) Detailed view of the variation of the capacitance after removing 5 V-bias and evolution with time during the final hours of the experiment. Note that in all cases the geometrical capacitance value, which corresponds to the high-frequency plateau, remains unaltered.

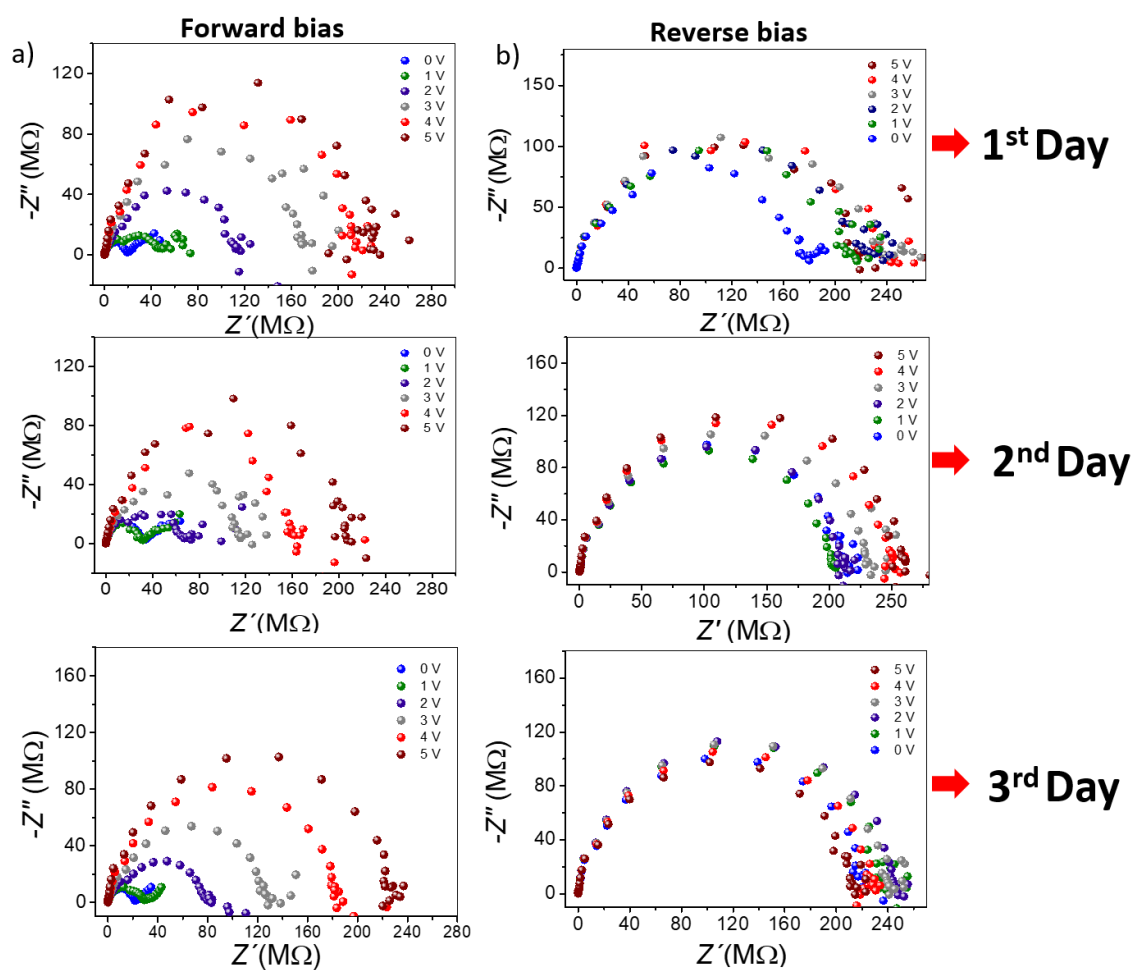


Figure S3 Reproducibility test of the forward and reverse polarization cycling. Variation of the impedance spectra of a $\text{CH}_3\text{NH}_3\text{PbBr}_3$ single-crystal during different polarization cycles (3 days). a) The right panels show the impedance change for increasing bias from 0 V to 5 V (forward polarization). b) The left panels show the minor changes produced during reverse polarization bias from 5 V to 0 V. The measuring time between each applied bias is about 20 min. After each forward/reverse polarization cycle, the sample was left to recovery during ~ 24 hours at 0 V. The same measurements were performed several times to verify its cyclability. In all cases the initial background, low-impedance response is recovered at 0 V.

Chapter 5: Publication 2

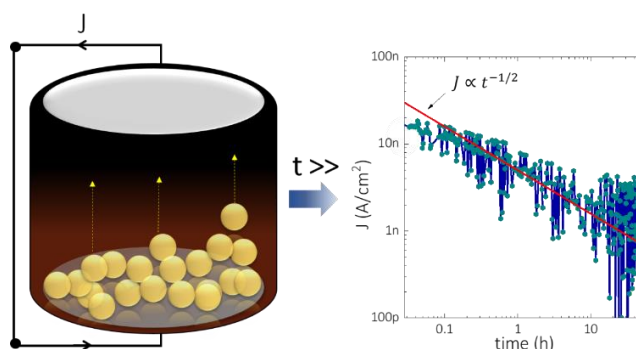
Marisé García-Batlle, Sarah Deumel, Judith E. Huerdler, Sandro F. Tedde, Antonio Guerrero, Osbel Almora, Germà Garcia-Belmonte, Mobile Ion-Driven Modulation of Electronic Conductivity Explains Long-Timescale Electrical Response in Lead Iodide Perovskite Thick Pellets, *ACS Appl. Mater. Interfaces* **2021**, 13, 35617, <https://doi.org/10.1021/acsami.1c06046>

5.1 Candidate's contribution

Nature of Contribution	Extent of Contribution
<ul style="list-style-type: none"> Performed the IS experiments to identify diffusion mechanisms. Performed the long-time transients' measurements Performed the fitting of all the experimental data. Wrote the experimental part and the first draft of results and discussion of the manuscripts Contributed to reply to the referees 	50 %

5.2 Brief summary

In here, MAPbI₃ thick pellets are analyzed by recording the long timescale diffusion patterns at zero bias and the resistance evolution at short circuit condition. A \sqrt{t} –dependence is encountered which is a fingerprint of diffusive transport. This time dependence is simultaneously obeyed by current relaxation and impedance recovering. Both independent observations of diffusion patterns reinforce the validity of our explanation of the ionic-electronic interplay between mobile ions that act as dopants and electronic carriers. Electronic doping profile changes depending on the actual ion bulk distribution.



5.3 Published manuscript

Mobile Ion-Driven Modulation of Electronic Conductivity Explains Long Timescale Electrical Response in Lead Iodide Perovskite Thick Pellets

Marisé García-Battle¹, Sarah Deumel^{2,3}, Judith E. Huerdler², Sandro F. Tedde², Antonio Guerrero¹, Osbel Almora¹, and Germà Garcia-Belmonte^{1*}

Institute of Advanced Materials (INAM), Universitat Jaume I, ES12006 Castelló, Spain

² *Siemens Healthineers AG, Technology Excellence, Guenther-Scharowsky-Strasse 1, 91058 Erlangen, Germany*

³ *Institute-Materials for Electronics and Energy Technology (i-MEET), Department of Materials Science and Engineering, Friedrich-Alexander-Universitaet Erlangen-Nuernberg, Energy Campus Nuernberg, Fuertherstraße 250, Nuernberg 90429, Germany*

*Email: garciag@uji.es

5 October 2022

Keywords

Perovskites, ion migration, electronic conductivity, dynamic doping, X-ray detection

Abstract

The favorable optoelectronic properties of metal halide perovskites have been applied to X- and γ -ray detection, solar energy and optoelectronics. Large electronic mobility, reduced recombination losses of the electron-hole pairs and high sensitivity upon ionizing irradiation have fostered great attention on technological realizations. Nevertheless, the recognized mixed ionic-electronic transport properties of hybrid perovskites possess severe limitations as far as long timescale instabilities and degradation issues are faced. Several effects are attributed to the presence of mobile ions such as shielding of the internal electrical field upon biasing and chemical interaction between intrinsic moving defects and electrode materials. Ion-originated modulations of electronic properties constitute an essential piece of knowledge to further progress into the halide perovskite device physics and operating modes. Here,

ionic current and electronic impedance of lead iodide perovskite thick pellets are independently monitored showing self-consistent patterns. Our findings point to a coupling of ionic and electronic properties as a *dynamic doping* effect caused by moving ions that act as mobile dopants. Electronic doping profile changes within the bulk as a function of the actual ion inner distribution, then producing a specific time-dependence in the electronic conductivity that reproduces time patterns of the type $\propto \sqrt{t}$, a clear fingerprint of diffusive transport. Values for the iodine-related defect diffusivity in the range of $D_{ion} \sim 10^{-8} \text{ cm}^2 \text{ s}^{-1}$, which corresponds to ionic mobilities of about $\mu_{ion} \sim 10^{-6} \text{ cm}^2 \text{ V}^{-1} \text{ s}^{-1}$, are encountered. Technological realizations based on thick perovskite layers would benefit from that fundamental information, as far as long timescale current stabilization is concerned.

Introduction

The significant success achieved by hybrid organic-inorganic lead halide perovskites is attributed to their outstanding light harvesting and charge carrier collection properties. This has motivated intensive research for photovoltaic applications¹ and, among other subjects, for high energy radiation detectors and imaging devices for medical diagnostics. For instance, it is well known that $\text{CH}_3\text{NH}_3\text{PbI}_3$ (MAPI) shows promising sensitivity for ionizing radiation detection with competitive values compared to standard technologies.² Similarly, the favorable optoelectronic properties of similar perovskites have been widely studied for X- and γ -ray detection, and complete devices have been proved.³⁻⁴ Current realizations of perovskite-based radiation detectors are typically made of bulky devices with absorber thicknesses up to millimeters to stop high-energy X-ray photons, poly-to-monocrystalline morphology and asymmetric metallic contacts.⁵⁻⁷ These structural features differ from those encountered in thin film perovskite photovoltaics, where much is currently known about the electronic characterization and modeling of the charge carrier transport properties.⁸⁻⁹ Nevertheless, the mixed ionic-electronic transport properties of hybrid perovskites are still a puzzling subject of research either for solar or radiation devices. Moreover, there are not too many studies on the long timescale electric response of ionizing energy detectors based on thick perovskite layers³ and further understanding of their working mechanisms is certainly needed.¹⁰

Classical modeling of semiconductor devices considers mobile electronic carriers while includes the influence of fixed ionic defects determining electronic doping profile. Usually, transport properties of ionic species play a minor role on the overall short-term operation. Yet, drift and diffusion of dopants¹¹⁻¹² or intrinsic defects¹³⁻¹⁴ constitute well-known degradation mechanisms in traditional solar cells and other electronic devices. Degradation typically occurs during long-term operational conditions and the involved ionic species come either from electrodes, or intermediate layers in hetero structures, or result from the product of the reactivity of the materials. Importantly, the mobility μ_{ion} of these ionic species in traditional semiconductor materials is many orders of magnitude lower than typical values ($\mu_{el} \sim 100 \text{ cm}^2 \text{ V}^{-1} \text{ s}^{-1}$) of the electronic mobility.⁹

As an example of an optoelectronic device in which the interplay between electronic and ionic kinetic properties plays a determining role, we can cite light-emitting electrochemical cells.¹⁵ Here the ionic charge dynamics is essential to explain the time evolution of the light power emission as those materials are mixed ionic-electronic conductors.¹⁶ For this kind of disordered organic devices, electronic mobilities are intrinsically lower ($\mu_{el} \sim 10^{-5} \text{ cm}^2 \text{ V}^{-1} \text{ s}^{-1}$) because of the polaronic character of the carrier transport in amorphous organic films,¹⁷ approaching the expected ion mobilities $\mu_{ion} \sim 10^{-8} - 10^{-5} \text{ cm}^2 \text{ V}^{-1} \text{ s}^{-1}$ in these materials.¹⁵ Also oxygen-vacancy transport in oxides¹⁸ is known to play a determining role in memristive devices to tailor electrical resistance for data storage and neuromorphic applications.¹⁹

For halide perovskite compounds, the dual ionic-electronic character of charge transport complicates the device modeling and forces the consideration of both faster and slower mechanisms, related to electronic and ionic kinetics, respectively.²⁰⁻²¹ It is known that several intrinsic defects (vacancies and interstitials as V_I^+ , MA_i^+ , V_{MA}^- , or I_i^- in the case of MAPI)²²⁻²³ possess nonnegligible transport properties.²⁴⁻²⁵ Several effects are attributed to the presence of mobile ions such as alteration of the internal electrical field upon biasing, through contact charge accumulation and shielding.²⁶⁻²⁸ It is also reported the chemical interaction between intrinsic moving defects and electrode materials giving rise to losses in performance and device instabilities.²⁹⁻³⁰

Moreover, the electronic and ionic dynamics relates through coupling of either recombination or conduction electronic carrier properties with defect distribution

within the active layer. In this line, it was suggested for perovskite solar cells that carrier recombination flux is highly dependent on the local ionic environment, in such a way that upon operation ions move to reduce recombination resistance, slowing down as a consequence non-radiative recombination rate.³¹⁻³² Also change of doping profile upon poling has been revealed by means of Mott-Schottky analysis, signaling an interplay between ion distribution and electronic density.³³ Even more interesting is the observation of electronic conductivity modulation in connection with ionic migration. For example, the time dependence of the electrical current in MAPI pellets with planar symmetrical electrodes has been correlated with the drift of the photoluminescence front upon biasing. The effect is explained by a sort of ion-induced modification of the doping profile in which the drift of vacancies establishes the local electron and hole concentration and consequently the steady-state electronic conductivity properties.³⁴ In other cases, ion diffusion, instead of drift, has been claimed as a suitable explanation of the impedance relaxation at zero-bias.³⁵ This last approach has permitted the estimation of the ion diffusion coefficient ($D_{ion} \sim 10^{-8} \text{ cm}^2 \text{ s}^{-1}$) in thick lead bromide perovskite single crystals.

Hence, the coupling between ionic and electronic properties in halide perovskites is a central issue that has mobilized many efforts and fostered important research during the last years.³⁶⁻³⁷ Although some partial and/or indirect correlations between ionic and electronic mechanisms have been proposed or invoked as explanatory rationales of the device operation, an unambiguous observation of those mixed ionic-electronic interplays is still obscure.³⁸⁻⁴¹ However, deciphering ion-originated modulations of electronic properties might constitute an essential piece of knowledge to further progress into the halide perovskite device physics and operating modes. Also, specific technological applications as solar cells, light-emitting diodes or X- and γ -detectors would benefit from that fundamental information, particularly when long timescale functioning, and degradation paths became an issue.

In this work, the electrical response of ~ 1 mm-thick $\text{CH}_3\text{NH}_3\text{PbI}_3$ microcrystalline pellets upon biasing is explored by registering current transients and impedance spectra. Very long-time experiments have been programmed that observe clear ion diffusion trends in the range of one day. Simultaneously, the electronic conductivity is monitored that reproduces the same time patterns of the type $\propto \sqrt{t}$, a clear fingerprint

of diffusive transport. Our findings point to couple ionic and electronic properties as a *dynamic doping* effect caused by moving ions that act as mobile dopants. Ion diffusion after bias removing changes then the local doping density governing as a consequence the electronic transport. That approach allows extracting values for the ion diffusivity in the range of $D_{ion} \sim 10^{-8} \text{ cm}^2 \text{ s}^{-1}$, which corresponds to ion mobilities of about $\mu_{ion} \sim 10^{-6} \text{ cm}^2 \text{ V}^{-1} \text{ s}^{-1}$ by assuming the Einstein's relation, in good agreement with other independent measurements

Results and Discussion

The samples under consideration were ~ 1 mm-thick MAPI microcrystalline pellets asymmetrically contacted with evaporated Pt and Cr electrodes of 1 cm^2 area. The fabrication details, basic morphology, and optoelectronic characterization can be found in Table S1 of the Supporting information. Experimental section also summarizes used instrumentation and methods.

Short-time current transients. We first check the sample response to voltage steps (inset of Figure 1b). The current transients after applying different positive biases during 500 s are presented in Figure 1a. The electronic current is delayed during the first 200 s, presumably due to the reordering of the ionic density.⁴² During the transient, the electronic charge carriers may be influenced by the ionic drift, which generates an ionic current with the same polarity as that of the electronic current. Eventually, the ions accumulate near the perovskite–electrode interfaces increasing the ion-induced built-in electric field leading to the simultaneous operation of drift and diffusion currents before the ion accumulation reaches the equilibrium conditions.⁴³⁻⁴⁴ Maximum currents upon bias application are registered in the range of $\mu\text{A cm}^{-2}$ (Figure 1a). Subsequently, after the positive biasing, the device is then kept at a short-circuit (0V-bias) condition to observe the relaxation current, as presented in Figure 1b.

When the external bias is removed, a small undershoot current appears of the order of nA cm^{-2} with the opposite sign (Figure 1b and Figure S1b). That negative current is the fingerprint of initial ion displacement to recover equilibrium distribution, as remarked previously.⁴² Note that electronic displacement currents should response faster ($\sim \mu\text{s}$) within the scales of the dielectric relaxation time (see later on this concern). Zero-volt current registering is then a way of observing ionic migration

without the perturbing contribution of electronic carriers. It is observed that the ionic current decay occurs in two steps: firstly, a quick response during a few seconds and afterwards a slower relaxation in a timescale of tens to hundreds of seconds. These processes may correspond to the slow reduction of the ionic built-in field, which drifts backwards the ions at the same time that they diffuse to restore equilibrium.⁴² Negative overshoot currents are always situated in the range of nA cm^{-2} (see Figure 1b). The slower transient response can be fitted using an exponential decay to obtain a characteristic time constant $\tau_{st} \sim 200$ s (Figure S1b).

One might think about an ionic relaxation process involving long distances within the perovskite thick layers. An estimation of the ion diffusion coefficient easily results by using the next expression,

$$D_{ion} = \frac{L_{diff}^2}{\tau} \quad (1)$$

where $L_{diff} = 0.55$ mm is the effective diffusion length that here corresponds to half of the layer thickness because the structural symmetry. By including typical response times in Figure 1b into Equation 1, a hypothetical value for the short timescale diffusion coefficient results $D_{ion}^{st} \sim 1.5 \times 10^{-5} \text{ cm}^2 \text{ s}^{-1}$. We note it is far from those reported for common solid-state ionic conductors, $D_{ion} \sim 10^{-12} \text{ cm}^2 \text{ s}^{-1}$,⁴⁵⁻⁴⁷ and even from previous reported faster ion migration coefficient $D_{ion} \sim 10^{-8} - 10^{-9} \text{ cm}^2 \text{ s}^{-1}$ in lead halide perovskites.^{35, 48-49} Similarly, the Einstein's equation can be used to deduce a characteristic mobility as

$$\mu_{ion} = \frac{q D_{ion}}{k_B T} \quad (2)$$

where q is the elementary charge, k_B stands for the Boltzmann constant, and T is the absolute temperature. From Equation 2, the previous estimation would entail $\mu_{ion}^{st} \sim 6 \times 10^4 \text{ cm}^2 \text{ V}^{-1} \text{ s}^{-1}$, which is far above previous determinations of ionic mobility in MAPI,^{8, 50} (see Table S2). Consequently, the unphysical inferred values of D_{ion}^{st} and μ_{ion}^{st} indicate that the characteristic time scale of $\tau_{st} \sim 200$ s should involve ionic displacements confined within much narrow regions. For this time scale, diffusion within the pellet competes with the remaining effects of the ionic built-in field, which governs the early stages of the relaxation towards equilibrium.

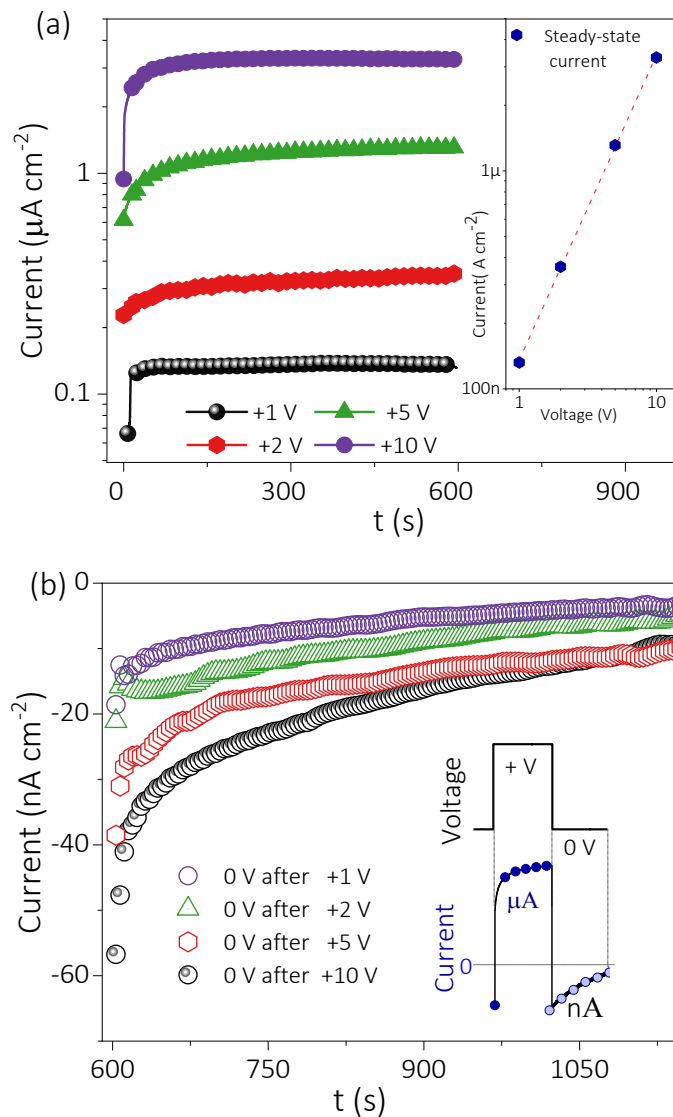


Figure 1 a) Short-time current transients registered at different positive applied biases. In the inset, there is the corresponding variation of the steady-state current (dots) and linear fit (dashed line). b) Relaxation current registered after the positive biasing when the device is kept at short-circuit condition (0 V-bias). Similar responses are obtained for negative biasing. The inset in (b) schemes the order of magnitude and sign of the current transients.

Long-time current transients. The above discussion suggests that ionic diffusion would require a longer timescale at short-circuit (0 V-bias), where the drift component due to the ionic built-in field can be neglected. Only then, the decay time constants can

reflect the dynamics of the diffusive ionic transport within the whole layer thickness.^{35, 42} Therefore, an experiment similar to that previously schemed in the inset of Figure 1b was performed in a timescale of days, as illustrated in Figure 2. Replicas of this experiment are shown in Figure S2.

The current during forward biasing was recorded during approximately one day, before switching to short-circuit conditions, when the current was measured for around two days. During the polarization at +10 V, an increment of the drift current is observed which seems to saturate at $t \gg 5 \times 10^4$ s. Subsequently, after removing applied bias, a non-diffusing regime can be first observed for $t < 400$ s, preceding a clear $1/\sqrt{t}$ law for $t \gg 400$ s. It is well-known that time dependences of the type \sqrt{t} can be taken as an indication for the occurrence of diffusion mechanisms.⁴⁸ As observed in Figure 2, the small ionic current is masked by a noisy component that dominates at longer times $t < 5 \times 10^4$ s. Despite the noise of order ~ 1 nA cm⁻², the diffusive component is clearly identified. Unfortunately, the reduced signal-to-noise ratio precludes reproducing these experiments using lower bias values.

The observed diffusive long-term current decrease can be assumed to have a characteristic ionic diffusion time $\tau_{lt} \geq 5 \times 10^4$ s. Thus, by using Equation 1 and 2, one can estimate an upper limit for the long-timescale ionic diffusion coefficient and mobility, which result of order $D_{ion}^{lt} \sim 10^{-8}$ cm² s⁻¹ and $\mu_{ion}^{lt} \sim 10^{-6}$ cm V⁻¹ s⁻¹, respectively. These values are evidently closer to those previously reported,^{35, 48-49} suggesting that the ionic current transient observed in Figure 2 is a fingerprint of an ionic diffusion mechanisms involving the entire pellet's bulk.

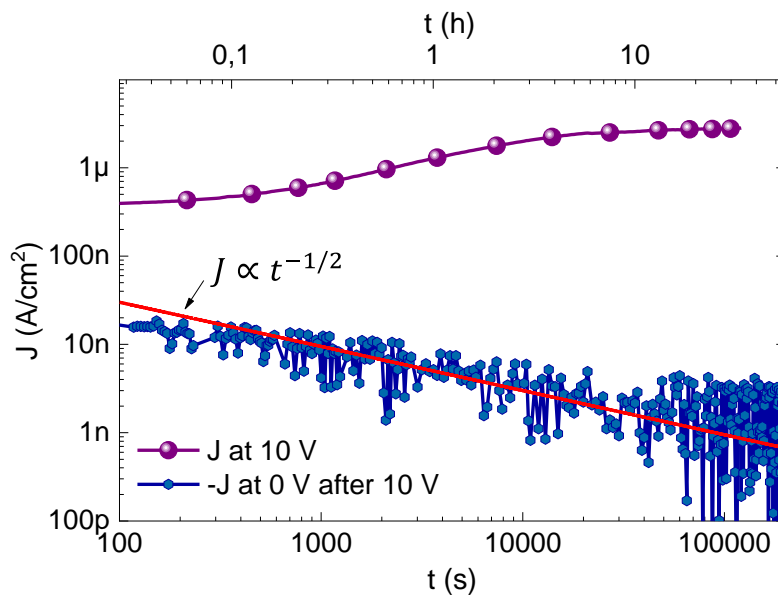


Figure 2. Long-time current transients of a MAPI pellets in the dark, under the applied external 10 V bias and subsequent zero bias, as indicated. The solid red line corresponds to a fit to a $1/\sqrt{t}$ decay law.

Long-time impedance recovery. The previous analysis relies on monitoring small currents (1-10 nA cm⁻²), poorly distinguishable from noise at longer times. An experimental way of augmenting the signal-to-noise ratio consists of measuring the current response to a perturbative stimulus at several stages during the system relaxation at zero-bias. This is obviously the measurement of the impedance spectroscopy IS response of the MAPI thick pellets (in the frequency domain within $10^{-2} \text{ Hz} < f < 10^6 \text{ Hz}$). The small voltage alternating-current (AC) mode perturbation (20 mV) is superimposed to the direct-current (DC) mode bias (0 V). Because of the small AC and DC values, the experiment is always carried out within the ohmic electronic response regime.¹⁰ As each impedance spectrum takes about 900 s to be registered, this procedure is a manner of exploring the electronic conduction state of the active layer at different times. By examining Figure 3a, one can observe typical impedance spectra of perovskite-based devices, which comprises a resistor-capacitor (RC) coupled sub-circuit at higher frequencies. As discussed previously,³⁵ these circuit elements represent the geometrical (dielectric) capacitance $C_g = \epsilon\epsilon_0 A/L$ and the electronic resistance $R = L/\sigma_{el}A$, being A the active area, ϵ is the dielectric constant, ϵ_0 the vacuum permittivity, and σ_{el} accounts for the electronic conductivity. It is worth

noting that the characteristic response time for this RC_g circuit always lies within those values typical for electronic dielectric relaxation timescales⁵¹ $\tau_{die} \sim 10 \mu\text{s}$, reinforcing the electronic origin of the high-frequency impedance response. The whole spectra are analyzed and fitted in terms of the equivalent circuit given in Figure S3.

A detailed view of the high-frequency resistance variation at zero-bias for 12 h after removing +10 V-bias can be observed in the IS plot of Figure 3a. Once short-circuit (0 V bias) DC conditions are imposed, the samples are able to slowly recover initial (equilibrium) response. By examining Figure 3a, one can infer that the sample resistance not only is a function of the applied bias, but also of the poling and recovering time. A closer examination of the variation of the resistance extracted from fitting at zero bias is presented in Figure 3b. The resistance shows a large initial value R_1 at shorter recovering times (less electronic conductive state) and progressively reduces to attain a steady-state value R_0 (background state) after a long equilibration time of 12 h. Such a reduction in bulk resistance is interpreted in terms of the increment in electronic carrier density n , which relates to the electronic conductivity as $\sigma_{el} = q\mu_{el}n$. The limiting resistances R_1 and R_0 give rise to an increase in carrier density from $n_1 = 9 \times 10^8 \text{ cm}^{-3}$ up to $n_0 = 7 \times 10^9 \text{ cm}^{-3}$, by assuming typical values for the electronic mobility as $\mu_{el} = 10 \text{ cm}^2 \text{ V}^{-1} \text{ s}^{-1}$. Similar behavior is observed for negative biasing (see Figure S4).

Our findings move us to consider that the redistribution of ionic species along the layer bulk is accompanied by the change in electronic carrier density. The mechanism can be viewed a sort of *dynamic doping* process in which mobile ions act as dopants able to locally alter the doping density. An alternative explanation of the resistance variation of Figure 3b (not explored here) would imply a hypothetical ion-driven modulation of the electronic mobility.

A model of the dynamic doping process accounting for the resistance variation is outlined in the Figure S5 in the Supporting information. Our approach simplifies the complex situation by considering a sharp front separating two zones of high and low carrier density that shifts as the ions diffuse to recover the equilibrium ion concentration (background electronic conduction state). A simple expression is thereby derived as

$$\frac{R - R_0}{R_1 - R_0} = 1 - \frac{3\sqrt{2D_{ion}t}}{L} \quad (3)$$

which assumes a 1D diffusion process with Gaussian ion distribution, and predicts a time dependence of the kind \sqrt{t} , keeping then the diffusive character as previously observed for ionic depolarization currents in Figure 2. Therefore, the resistance in Figure 3b can be normalized as $(R - R_0)/(R_1 - R_0)$ and plotted as a function of \sqrt{t} , as presented in Figure 3c. By examining this plot, a linear trend is clearly obeyed with a slope including the ion diffusivity as $3\sqrt{2D_{ion}}/L$, as derived from the analytical model of Equation 3 and purposely outlined in the Supporting information. After resistance normalization, very similar trends are reproduced independent of the voltage sign in Figure 3c. The kinetic independence on bias sign would indicate a bulk origin, rather than interfacial, for the mechanism behind the observed electrical response. We note that a deviation from the linear behavior occurs at shorter times ($t < 5 \times 10^3$ s) in Figure 3c, for which the simplicity of the model disregards second order depolarization effects for greater moving ion concentrations. For shorter times, the driving force for ion displacement should certainly incorporate other mechanisms as the relaxation of the ionic built-in voltage should include drift-driven processes in addition to the simple diffusion, in such a way that the \sqrt{t} -dependence is no longer obeyed. In any case, the linear response part in Figure 3c seems to reinforce the predominance of diffusion mechanisms for $t > 5 \times 10^3$ s of short-circuit regime after polarization.

From the linear fitting slope in Figure 3c (valid for longer times) and the experimental parameter $L = 1.1$ mm, one can obtain a value for the ion diffusion coefficient that results in $D_{ion} = (3 \pm 1) \times 10^{-8} \text{ cm}^2 \text{ s}^{-1}$, averaging over several relaxation experiments. We remark that the order of magnitude obtained for D_{ion} is in agreement with values reported for the diffusion coefficient of iodine-related defects. By nuclear magnetic resonance (NMR),⁵²⁻⁵³ values of order $10^{-9} \text{ cm}^2 \text{ s}^{-1}$ were obtained for I^- , while MA^+ exhibited smaller values in the range of 10^{-15} - $10^{-12} \text{ cm}^2 \text{ s}^{-1}$. From drift current accompanied by electrical switching of luminescence,³⁴ I^- diffusivity is obtained to be around 5×10^{-8} - $6 \times 10^{-9} \text{ cm}^2 \text{ s}^{-1}$. Also, current transient⁵⁴ and capacitance transient⁵⁵ analyses gave rise to diffusion coefficient of order 10^{-8} - $10^{-9} \text{ cm}^2 \text{ s}^{-1}$ for I^- . In addition, impedance analysis of the low-frequency diffusion patterns yielded similar values.⁴⁹ Therefore, we also assume that the relatively fast ion diffusion coefficient

encountered here $D_{ion} \sim 10^{-8} \text{ cm}^2 \text{ s}^{-1}$ should be related to the transport of mobile iodine defects. Other possible moving ions as MA^+ and Pb^{2+} should certainly exhibit much lower values.^{48, 56}

As a consequence, it is inferred that iodine vacancies V_I^+ dominate and establish the general background doping character. As halide vacancies are considered a shallow donor both for iodide and bromide perovskites,^{23, 57} a n -type doping character should be larger in zones in which the iodine vacancy concentration increases. Upon biasing, formation of reach-zones of iodine vacancies near the negatively-biased contact is expected, and contrary for the positive contact. Large part of the layer bulk undergoes a de-doping process as dopant ions accumulate at the contacts. Therefore, an internal doping profile is formed that implies that the perovskite bulk can be modeled as a sort of semiconductor homojunction with a mobile boundary between lower- and higher-doped regions in accordance with the model outlined in the Supporting Information. This is what we denote as *dynamic doping* process.

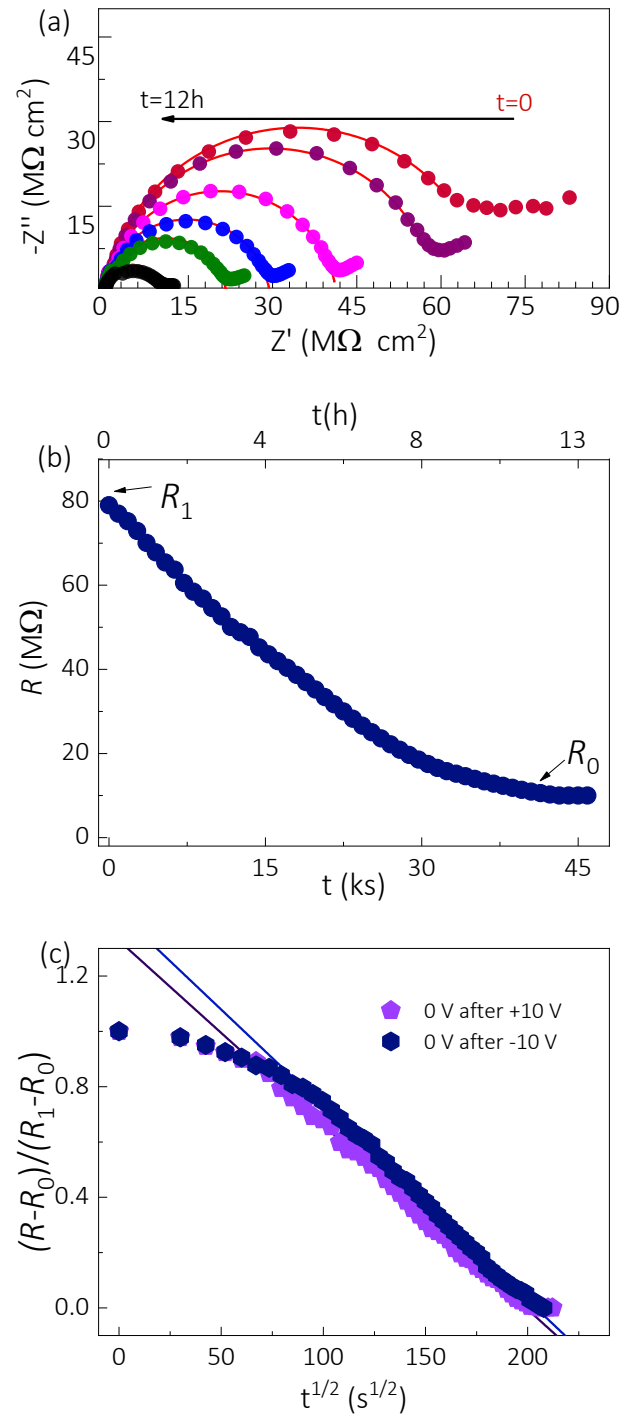


Figure 3. a) Variation of the impedance at zero bias after removing +10 V bias and evolution with time. The dots correspond to the experimental data obtained at different time instants: 0 h (red), + 2 h (purple), +5 h (pink), +7 h (blue), +9 h (green), 12 h (black). The red solid lines correspond to the fittings to the equivalent circuit in Figure S2. b) Long-time relaxation experiments (~12 h) showing the variation of the sample resistance extracted from impedance spectra analysis as a function of time measured at zero bias. A transition between initial large resistance R_1 down to small resistance R_0 is observed. c) Variation of the normalized resistance as a function of time following the relationship of Equation 3, for relaxation experiments performed at zero bias after previous long-term positive and negative bias. The blue/purple solid lines represent linear fittings.

Conclusions

Summarizing our results, we indicate that the present study reveals several features to be included into a simulation of the general device operation of thick perovskite layers. (1) On the one hand, long timescale diffusion patterns are encountered which follows a \sqrt{t} –dependence. This unambiguously signals the fingerprint of diffusive transport. (2) That time dependence is simultaneously obeyed by current relaxation (Figure 2) and impedance recovering (Figure 3). While long-time negative current undershoot at zero bias exclusively registers the ion displacement, the impedance captures the electronic small perturbation response at different depolarization stages. That independent observation of diffusion patterns reinforces the validity of our explanation. (3) As a consequence, an ionic-electronic interplay should exist between mobile ions that act as dopants and electronic carriers. Electronic doping profile changes depending on the actual ion bulk distribution. This is the essence of the *dynamic doping* mechanism formulated here. (4) The kinetics of ionic depolarization is a multistep process. It starts by an initial collapse of the ion diffusion layer ($\tau_{diff} \sim 200$ s), built-up after biasing. Afterwards, long-range diffusion occurs involving much longer times ($\tau_L \sim 10^5$ s). From the analysis the ion diffusion coefficient is extracted which lies within the range of 10^{-8} cm² s⁻¹, presumable connected to the iodine defect transport.

We have proposed here a connection between ionic and electronic properties that allow progressing into the halide perovskite device physics and operating modes.

Technological realizations as solar cells, light-emitting diodes and, particularly, X- and γ -detectors would benefit from that fundamental information, as far as long timescale functioning and current stabilization under biasing is concerned.

Experimental

Sample preparation: The samples under consideration were ~1 mm-thick MAPI microcrystalline pellets with a diameter of 15 mm. The pellets were made by a soft-sintering process, which is described in detail in ref.⁷ The microcrystalline MAPI powder is commercially available from Xi'an Polymer Light Technology Corp. It was filled into a powder container with adjustable height, and a polished cylinder was placed above it. The hydraulic press (Perkin Elmer) applies a pressure of 55 MPa (1t) for 30 min at 70 °C. On the resulting pellet 2 electrodes (Pt, Cr) with a thickness of around 100 nm were deposited via physical vapor deposition. Their active area is 1 cm².

Structural and optical characterization techniques: Through measurements of Scanning Electron Microscopy the polycrystalline nature of the perovskite pellet is observed (Fig S6a). The X-ray Diffraction pattern (Fig S6b) shows the most prominent peaks with the (110), (220), and (310) peaks at 14.1°, 28.4°, and 32.1°. The peaks indicate the tetragonal MAPbI₃-phase with an *I4cm* space group. These values are in good agreement with comparative XRD data of a typical MAPI film.⁵⁸⁻⁵⁹

Electrical Measurements: The chronoamperometry experiments, as well as the impedance spectroscopy (IS) characterizations were made with a PGSTAT302N potentiostat from Metrohm AUTOLAB. Measurements of current and impedance were carried out at several long-time DC bias conditions in the range of ±10 V to 0 V. The samples were kept in the dark with N₂ circulation in order to prevent from humidity- or oxygen-induced degradation.

Associated contents

Supporting Information

The supporting information is available free of charge at

Sample preparation and characterization, general current transients and impedance analysis, model for resistance relaxation.

Notes

The authors declare no competing financial interest.

Acknowledgments

This work has received funding from the European Union's Horizon 2020 research and innovation program under the Photonics Public Private Partnership (www.photonics21.org) with the project PEROXIS under the grant agreement N° 871336. M. G.-B. acknowledges Generalitat Valenciana for a grant (number GRISOLIAP/2018/073).

References

1. Green, M. A.; Dunlop, E. D.; Hohl-Ebinger, J.; Yoshita, M.; Kopidakis, N.; Hao, X., Solar Cell Efficiency Tables (Version 56). *Progress in Photovoltaics: Research and Applications* **2020**, *28*, 629-638.
2. Heiss, W.; Brabec, C., Perovskites Target X-Ray Detection. *Nature Photonics* **2016**, *10*, 288-289.
3. Wei, H., et al., Sensitive X-Ray Detectors Made of Methylammonium Lead Tribromide Perovskite Single Crystals. *Nature Photonics* **2016**, *10*, 333-339.
4. Murali, B.; Kolli, H. K.; Yin, J.; Ketavath, R.; Bakr, O. M.; Mohammed, O. F., Single Crystals: The Next Big Wave of Perovskite Optoelectronics. *ACS Materials Letters* **2020**, *2*, 184-214.
5. He, Y., et al., High Spectral Resolution of Gamma-Rays at Room Temperature by Perovskite CsPbBr₃ Single Crystals. *Nature Communications* **2018**, *9*, 1609.
6. He, Y., et al., CsPbBr₃ Perovskite Detectors with 1.4% Energy Resolution for High-Energy Γ -Rays. *Nature Photonics* **2021**, *15*, 36-42.
7. Deumel, S., et al., Sub-Nanogray X-Ray Imaging with Soft-Sintered Methylammonium Lead Triiodide Perovskites. *Nature Electronics* **2021**, submitted.
8. Motta, C.; El-Mellouhi, F.; Sanvito, S., Charge Carrier Mobility in Hybrid Halide Perovskites. *Scientific Reports* **2015**, *5*, 12746.
9. Herz, L. M., Charge-Carrier Mobilities in Metal Halide Perovskites: Fundamental Mechanisms and Limits. *ACS Energy Letters* **2017**, *2*, 1539-1548.
10. Duijnste, E. A.; Le Corre, V. M.; Johnston, M. B.; Koster, L. J. A.; Lim, J.; Snaith, H. J., Understanding Dark Current-Voltage Characteristics in Metal-Halide Perovskite Single Crystals. *Physical Review Applied* **2021**, *15*, 014006.
11. Takada, J.; Yamaguchi, M.; Fukada, N.; Nishimura, K.; Tawada, Y., Thermal Degradation of a-Si:H Solar Cells by Dopant Diffusion. *Japanese Journal of Applied Physics* **1987**, *26*, 889-892.
12. Feldmann, F.; Schön, J.; Niess, J.; Lerch, W.; Hermle, M., Studying Dopant Diffusion from Poly-Si Passivating Contacts. *Solar Energy Materials and Solar Cells* **2019**, *200*, 109978.
13. Schmidt, J., Light-Induced Degradation in Crystalline Silicon Solar Cells. *Solid State Phenomena* **2003**, *95-96*, 187-196.
14. Adey, J.; Jones, R.; Palmer, D. W.; Briddon, P. R.; Öberg, S., Degradation of Boron-Doped Czochralski-Grown Silicon Solar Cells. *Physical Review Letters* **2004**, *93*, 055504.
15. van Reenen, S.; Janssen, R. A. J.; Kemerink, M., Doping Dynamics in Light-Emitting Electrochemical Cells. *Organic Electronics* **2011**, *12*, 1746-1753.
16. Lenes, M.; Garcia-Belmonte, G.; Tordera, D.; Pertegás, A.; Bisquert, J.; Bolink, H. J., Operating Modes of Sandwiched Light-Emitting Electrochemical Cells. *Advanced Functional Materials* **2011**, *21*, 1581-1586.

17. Brütting, W.; Adachi, C., *Physics of Organic Semiconductors*. Wiley-VCH: Weinheim, 2012.
18. Gunkel, F.; Christensen, D. V.; Chen, Y. Z.; Pryds, N., Oxygen Vacancies: The (in)Visible Friend of Oxide Electronics. *Applied Physics Letters* **2020**, *116*, 120505.
19. Waser, R.; Dittmann, R.; Staikov, G.; Szot, K., Redox-Based Resistive Switching Memories – Nanoionic Mechanisms, Prospects, and Challenges. *Advanced Materials* **2009**, *21*, 2632-2663.
20. Almora, O., et al., Ionic Dipolar Switching Hinders Charge Collection in Perovskite Solar Cells with Normal and Inverted Hysteresis. *Solar Energy Materials and Solar Cells* **2019**, *195*, 291-298.
21. Bertoluzzi, L.; Boyd, C. C.; Rolston, N.; Xu, J.; Prasanna, R.; O'Regan, B. C.; McGehee, M. D., Mobile Ion Concentration Measurement and Open-Access Band Diagram Simulation Platform for Halide Perovskite Solar Cells. *Joule* **2020**, *4*, 109-127.
22. Buin, A.; Comin, R.; Xu, J.; Ip, A. H.; Sargent, E. H., Halide-Dependent Electronic Structure of Organolead Perovskite Materials. *Chemistry of Materials* **2015**, *27*, 4405-4412.
23. Yin, W.-J.; Shi, T.; Yan, Y., Unusual Defect Physics in $\text{CH}_3\text{NH}_3\text{PbI}_3$ Perovskite Solar Cell Absorber. *Applied Physics Letters* **2014**, *104*, 063903.
24. Azpiroz, J. M.; Mosconi, E.; Bisquert, J.; De Angelis, F., Defect Migration in Methylammonium Lead Iodide and Its Role in Perovskite Solar Cell Operation. *Energy & Environmental Science* **2015**, *8*, 2118-2127.
25. Yang, D.; Ming, W.; Shi, H.; Zhang, L.; Du, M.-H., Fast Diffusion of Native Defects and Impurities in Perovskite Solar Cell Material $\text{CH}_3\text{NH}_3\text{PbI}_3$. *Chemistry of Materials* **2016**, *28*, 4349-4357.
26. Bergmann, V. W.; Guo, Y.; Tanaka, H.; Hermes, I. M.; Li, D.; Klasen, A.; Bretschneider, S. A.; Nakamura, E.; Berger, R.; Weber, S. A. L., Local Time-Dependent Charging in a Perovskite Solar Cell. *ACS Applied Materials & Interfaces* **2016**, *8*, 19402-19409.
27. Ahmadi, M.; Collins, L.; Higgins, K.; Kim, D.; Lukosi, E.; Kalinin, S. V., Spatially Resolved Carrier Dynamics at MAPbBr_3 Single Crystal–Electrode Interface. *ACS Applied Materials & Interfaces* **2019**, *11*, 41551-41560.
28. Zhu, T.-Y.; Shu, D.-J., Role of Ionic Charge Accumulation in Perovskite Solar Cell: Carrier Transfer in Bulk and Extraction at Interface. *The Journal of Physical Chemistry C* **2019**, *123*, 5312-5320.
29. Pospisil, J.; Guerrero, A.; Zmeskal, O.; Weiter, M.; Gallardo, J. J.; Navas, J.; Garcia-Belmonte, G., Reversible Formation of Gold Halides in Single-Crystal Hybrid-Perovskite/Au Interface Upon Biasing and Effect on Electronic Carrier Injection. *Advanced Functional Materials* **2019**, *29*, 1900881.
30. Wang, J., et al., Investigation of Electrode Electrochemical Reactions in $\text{CH}_3\text{NH}_3\text{PbBr}_3$ Perovskite Single-Crystal Field-Effect Transistors. *Advanced Materials* **2019**, *31*, 1902618.
31. Pockett, A.; Eperon, G. E.; Sakai, N.; Snaith, H. J.; Peter, L. M.; Cameron, P. J., Microseconds, Milliseconds and Seconds: Deconvoluting the Dynamic Behaviour of Planar Perovskite Solar Cells. *Physical Chemistry Chemical Physics* **2017**, *19*, 5959-5970.
32. Yang, C., et al., MAPbI_3 Single Crystals Free from Hole-Trapping Centers for Enhanced Photodetectivity. *ACS Energy Letters* **2019**, *4*, 2579-2584.
33. Fischer, M.; Tvingstedt, K.; Baumann, A.; Dyakonov, V., Doping Profile in Planar Hybrid Perovskite Solar Cells Identifying Mobile Ions. *ACS Applied Energy Materials* **2018**, *1*, 5129-5134.
34. Li, C.; Guerrero, A.; Huettner, S.; Bisquert, J., Unravelling the Role of Vacancies in Lead Halide Perovskite through Electrical Switching of Photoluminescence. *Nature Communications* **2018**, *9*, 5113.
35. García-Batlle, M.; Baussens, O.; Amari, S.; Zaccaro, J.; Gros-Daillon, E.; Verilhac, J.-M.; Guerrero, A.; Garcia-Belmonte, G., Moving Ions Vary Electronic

Conductivity in Lead Bromide Perovskite Single Crystals through Dynamic Doping. *Advanced Electronic Materials* **2020**, *6*, 2000485.

36. Wang, H.; Guerrero, A.; Bou, A.; Al-Mayouf, A. M.; Bisquert, J., Kinetic and Material Properties of Interfaces Governing Slow Response and Long Timescale Phenomena in Perovskite Solar Cells. *Energy & Environmental Science* **2019**, *12*, 2054-2079.

37. Liu, J.; Hu, M.; Dai, Z.; Que, W.; Padture, N. P.; Zhou, Y., Correlations between Electrochemical Ion Migration and Anomalous Device Behaviors in Perovskite Solar Cells. *ACS Energy Letters* **2021**, 1003-1014.

38. Lopez-Varo, P.; Jiménez-Tejada, J. A.; García-Rosell, M.; Ravishankar, S.; Garcia-Belmonte, G.; Bisquert, J.; Almora, O., Device Physics of Hybrid Perovskite Solar Cells: Theory and Experiment. *Advanced Energy Materials* **2018**, *8*, 1702772.

39. Kerner, R. A.; Rand, B. P., Ionic–Electronic Ambipolar Transport in Metal Halide Perovskites: Can Electronic Conductivity Limit Ionic Diffusion? *The Journal of Physical Chemistry Letters* **2018**, *9*, 132-137.

40. Reichert, S.; An, Q.; Woo, Y.-W.; Walsh, A.; Vaynzof, Y.; Deibel, C., Probing the Ionic Defect Landscape in Halide Perovskite Solar Cells. *Nature Communications* **2020**, *11*, 6098.

41. Moia, D., et al., Ionic-to-Electronic Current Amplification in Hybrid Perovskite Solar Cells: Ionically Gated Transistor-Interface Circuit Model Explains Hysteresis and Impedance of Mixed Conducting Devices. *Energy & Environmental Science* **2019**, *12*, 1296-1308.

42. Li, D.; Wu, H.; Cheng, H.-C.; Wang, G.; Huang, Y.; Duan, X., Electronic and Ionic Transport Dynamics in Organolead Halide Perovskites. *ACS Nano* **2016**, *10*, 6933-6941.

43. Xiao, Z.; Yuan, Y.; Shao, Y.; Wang, Q.; Dong, Q.; Bi, C.; Sharma, P.; Gruverman, A.; Huang, J., Giant Switchable Photovoltaic Effect in Organometal Trihalide Perovskite Devices. *Nature Materials* **2015**, *14*, 193-198.

44. Zhao, Y., et al., Anomalous Large Interface Charge in Polarity-Switchable Photovoltaic Devices: An Indication of Mobile Ions in Organic–Inorganic Halide Perovskites. *Energy & Environmental Science* **2015**, *8*, 1256-1260.

45. Eames, C.; Frost, J. M.; Barnes, P. R. F.; O'Regan, B. C.; Walsh, A.; Islam, M. S., Ionic Transport in Hybrid Lead Iodide Perovskite Solar Cells. *Nature Communications* **2015**, *6*, 7497.

46. Bag, M.; Renna, L. A.; Adhikari, R. Y.; Karak, S.; Liu, F.; Lahti, P. M.; Russell, T. P.; Tuominen, M. T.; Venkataraman, D., Kinetics of Ion Transport in Perovskite Active Layers and Its Implications for Active Layer Stability. *Journal of the American Chemical Society* **2015**, *137*, 13130-13137.

47. Richardson, G.; O'Kane, S. E. J.; Niemann, R. G.; Peltola, T. A.; Foster, J. M.; Cameron, P. J.; Walker, A. B., Can Slow-Moving Ions Explain Hysteresis in the Current–Voltage Curves of Perovskite Solar Cells? *Energy & Environmental Science* **2016**, *9*, 1476-1485.

48. Yang, T.-Y.; Gregori, G.; Pellet, N.; Grätzel, M.; Maier, J., The Significance of Ion Conduction in a Hybrid Organic–Inorganic Lead-Iodide-Based Perovskite Photosensitizer. *Angewandte Chemie International Edition* **2015**, *54*, 7905-7910.

49. Peng, W.; Aranda, C.; Bakr, O. M.; Garcia-Belmonte, G.; Bisquert, J.; Guerrero, A., Quantification of Ionic Diffusion in Lead Halide Perovskite Single Crystals. *ACS Energy Letters* **2018**, *3*, 1477-1481.

50. Savenije, T. J., et al., Thermally Activated Exciton Dissociation and Recombination Control the Carrier Dynamics in Organometal Halide Perovskite. *The Journal of Physical Chemistry Letters* **2014**, *5*, 2189-2194.

51. Almora, O.; Garcia-Belmonte, G., Light Capacitances in Silicon and Perovskite Solar Cells. *Solar Energy* **2019**, *189*, 103-110.

52. Senocrate, A.; Moudrakovski, I.; Acartürk, T.; Merkle, R.; Kim, G. Y.; Starke, U.; Grätzel, M.; Maier, J., Slow CH_3NH_3^+ Diffusion in $\text{CH}_3\text{NH}_3\text{PbI}_3$ under Light Measured by

Solid-State Nmr and Tracer Diffusion. *The Journal of Physical Chemistry C* **2018**, *122*, 21803-21806.

53. Senocrate, A.; Moudrakovski, I.; Kim, G. Y.; Yang, T.-Y.; Gregori, G.; Grätzel, M.; Maier, J., The Nature of Ion Conduction in Methylammonium Lead Iodide: A Multimethod Approach. *Angewandte Chemie International Edition* **2017**, *56*, 7755-7759.

54. Bertoluzzi, L.; Belisle, R. A.; Bush, K. A.; Cheacharoen, R.; McGehee, M. D.; O'Regan, B. C., In Situ Measurement of Electric-Field Screening in Hysteresis-Free Ptaa/Fa0.83cs0.17pb(I0.83br0.17)3/C60 Perovskite Solar Cells Gives an Ion Mobility of $\sim 3 \times 10^{-7}$ Cm²/(V S), 2 Orders of Magnitude Faster Than Reported for Metal-Oxide-Contacted Perovskite Cells with Hysteresis. *Journal of the American Chemical Society* **2018**, *140*, 12775-12784.

55. Futscher, M. H.; Lee, J. M.; McGovern, L.; Muscarella, L. A.; Wang, T.; Haider, M. I.; Fakharuddin, A.; Schmidt-Mende, L.; Ehrler, B., Quantification of Ion Migration in Ch3nh3pbI3 Perovskite Solar Cells by Transient Capacitance Measurements. *Materials Horizons* **2019**, *6*, 1497-1503.

56. Weber, S. A. L.; Hermes, I. M.; Turren-Cruz, S.-H.; Gort, C.; Bergmann, V. W.; Gilson, L.; Hagfeldt, A.; Graetzel, M.; Tress, W.; Berger, R., How the Formation of Interfacial Charge Causes Hysteresis in Perovskite Solar Cells. *Energy & Environmental Science* **2018**, *11*, 2404-2413.

57. Motti, S. G.; Meggiolaro, D.; Martani, S.; Sorrentino, R.; Barker, A. J.; De Angelis, F.; Petrozza, A., Defect Activity in Lead Halide Perovskites. *Advanced Materials* **2019**, *31*, 1901183.

58. Phillips, L. J.; Rashed, A. M.; Treharne, R. E.; Kay, J.; Yates, P.; Mitrovic, I. Z.; Weerakkody, A.; Hall, S.; Durose, K., Maximizing the Optical Performance of Planar Ch3nh3pbI3 Hybrid Perovskite Heterojunction Stacks. *Solar Energy Materials and Solar Cells* **2016**, *147*, 327-333.

59. Aranda, C.; Cristobal, C.; Shooshtari, L.; Li, C.; Huettner, S.; Guerrero, A., Formation Criteria of High Efficiency Perovskite Solar Cells under Ambient Conditions. *Sustainable Energy & Fuels* **2017**, *1*, 540-547.

5.4 Supplemental Information

Mobile Ion-Driven Modulation of Electronic Conductivity Explains Long Timescale Electrical Response in Lead Iodide Perovskite Thick Pellets

Marisé García-Batlle¹, Sarah Deumel^{2,3}, Judith E. Huerdler², Sandro F. Tedde², Antonio Guerrero¹, Osbel Almora¹, and Germà Garcia-Belmonte^{1*}

¹ Institute of Advanced Materials (INAM), Universitat Jaume I, ESI2006 Castelló, Spain

² Siemens Healthineers AG, Technology Excellence, Guenther-Scharowsky-Strasse 1, 91058 Erlangen, Germany

³ Institute-Materials for Electronics and Energy Technology (i-MEET), Department of Materials Science and Engineering, Friedrich-Alexander-Universitaet Erlangen-Nuernberg, Energy Campus Nuernberg, Fuertherstraße 250, Nuernberg 90429, Germany

garciag@uji.es

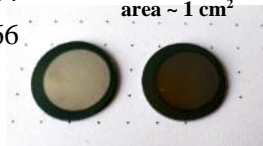
Table S1 Characteristics of the samples studied								
Sample name	Press time (min)	Press temperature (°C)	Press weight (Kg)	Pressure (MPa)	Pellet weight (mg)	Pellet thickness (µm)	Pellet Density (%)	Contacts
1	30	70	1000	55.5	516.6	1102	64	Pt/Cr electrodes area ~ 1 cm ² 
2	30	70	1000	55.5	527.9	1083	66	

Table S2 Summary of ionic mobility in Metal Halide Perovskites (~300 K)			
μ_{ion} (cm ² V ⁻¹ s ⁻¹)	Measurement technique	Ref.	Estimation of D_{ion} (cm ² s ⁻¹) by Einstein's relation ⁶
1×10^{-6}	EIS	2-4	2.6×10^{-8}
5×10^{-8}	PLQ	5	1.5×10^{-10}
1.5×10^{-9}	SDP	6	3.8×10^{-11}
10^{-9}	NMR spectroscopy	7-8	10^{-11}
10^{-8} - 10^{-9}	SDSP photocurrent transient	9	2.5×10^{-10} - 10^{-11}
10^{-9}	PTIR microscopy	10	10^{-11}

Column 2 lists the technique used to determine the mobility value (Electrochemical Impedance Spectroscopy (EIS) ; Nuclear magnetic resonance (NMR); Photothermal induced resonance (PTIR) microscopy; PL quenching method (PLQ); Step-dwell-step-probe (SDSP) photocurrent transient.

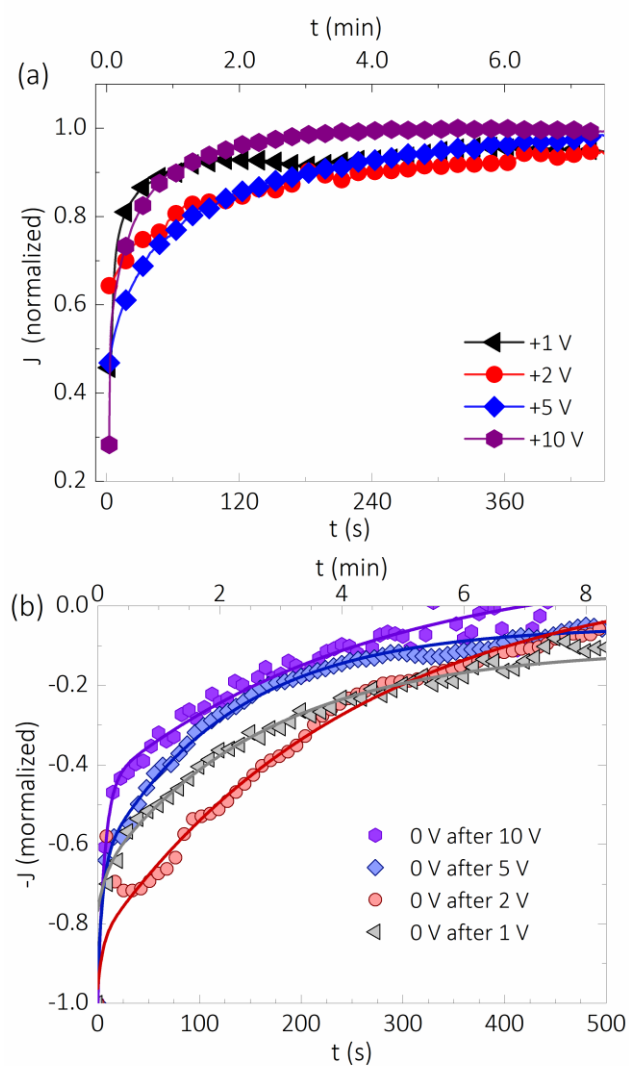


Figure S1. Short-time normalized current transients for a MAPI pellet in the dark at (a) forward +1, +2, +5, +10 V bias and (b) zero bias after polarization during 500 s, as indicated. The inset in (a) schemes the order of magnitude and sign of the current transients. The original current transients can be found in Figure 1.

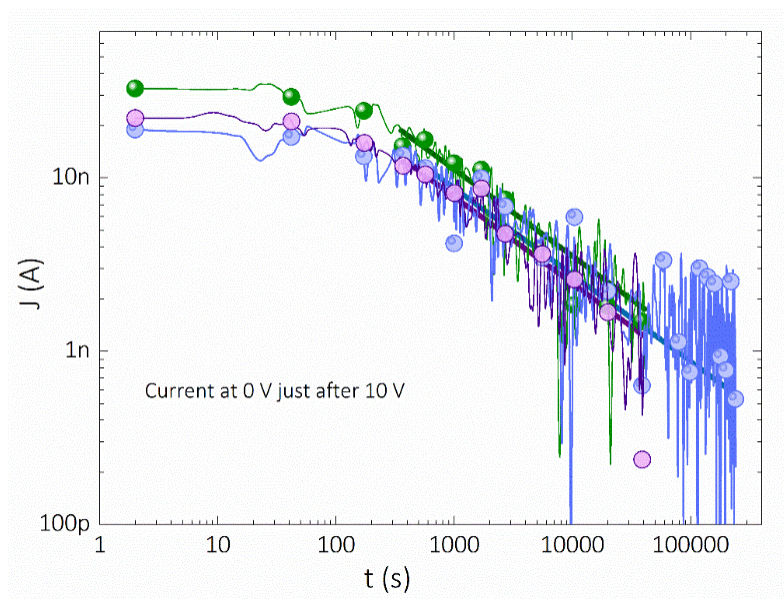


Figure S2. Sequence of experiments of long-time current transients of MAPI pellets in the dark, under the applied external 10 V bias and subsequent zero bias, as indicated. The solid line corresponds to a fit to a $1/\sqrt{t}$ decay law restricted to the range of significant signal-to-noise ratio.

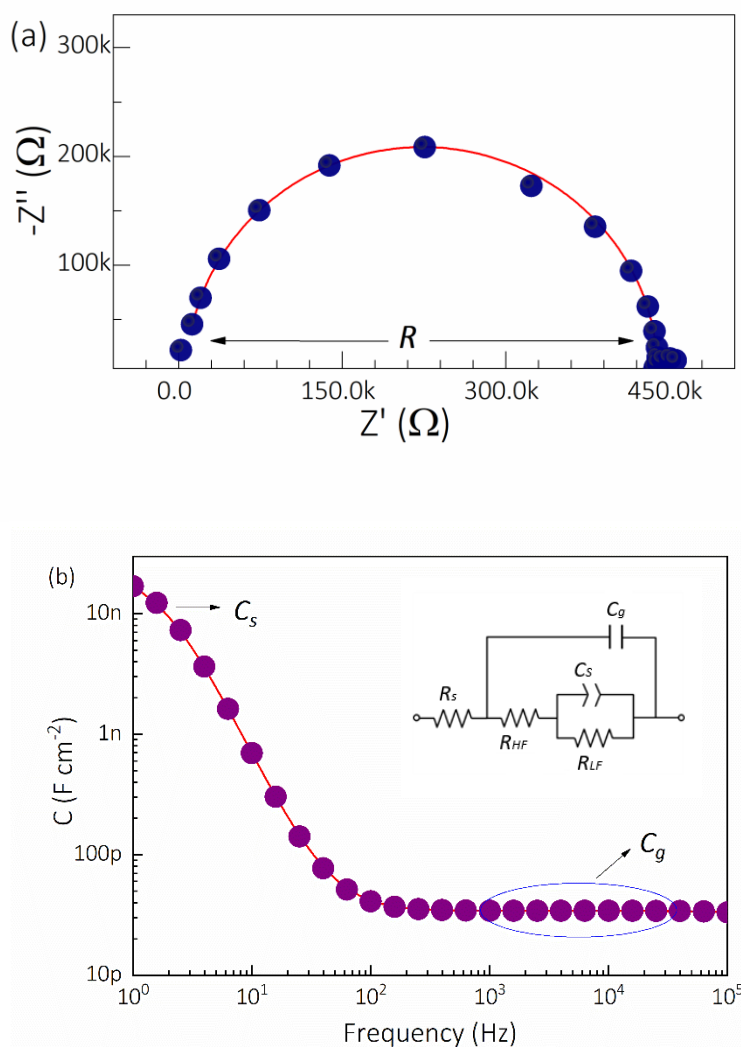


Figure S3. Example of the a) impedance response and b) Capacitance spectrum of MAPI-pellets of thickness ~ 1 mm asymmetrically contacted with Pt/Cr electrodes measured at 0 V in the dark (relaxed samples). Fits (solid line) result by using the equivalent circuit in the inset: with series resistance R_s , C_g geometric capacitance and R_{HF} , and R_{LF} the high-, and low-frequency resistances, respectively. The low-frequency capacitance usually labelled as surface capacitance C_s .

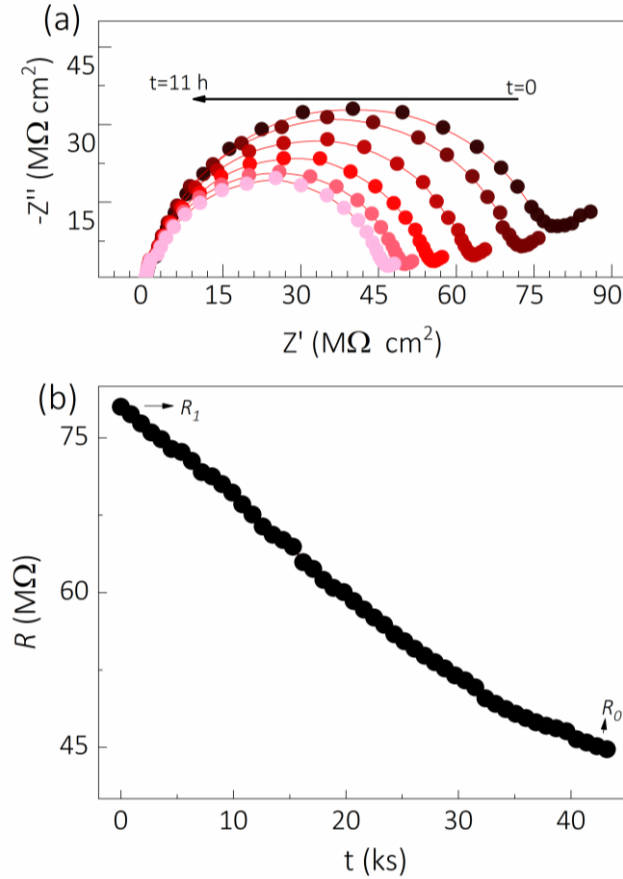


Figure S4. a) Variation of the impedance at zero bias after removing -10 V bias and evolution with time. b) Long-time relaxation experiments (~ 11 h) showing the variation of the sample resistance extracted from impedance spectra analysis as a function of time measured at zero bias.

Model for resistance relaxation.

For the sake of simplicity, one can calculate the total sample resistance as the contribution of two zones of different doping as depicted in Figure S5.

$$R = R_h + R_l \quad (1)$$

in such a way that $R_h = s/\sigma_h A$ and $R_l = (L - s)/\sigma_l A$. Here, L stands for the sample thickness, s indicates the width of the high doping region, σ_h and σ_l correspond to the electronic conductivity of high and low doping-density regions, respectively, and A is the effective sample area. We assume here the ohmic character of the electrical response as inferred from the linear dependences of the steady-state I - V curve (Figure 1a inset). It should be noted that two well-differentiated impedance arcs corresponding to each of the above-mentioned separate doping zones are hardly observable because of the rather small ratio R_h/R_l . After rearrangement, Equation (1) can be expressed in terms of the limiting values of the sample resistance R_1 and R_0 , which corresponds to the initial and final resistances, respectively. If we assume that $R_1 = L/\sigma_l A$, i.e. the low doping region occupies the whole thickness for shorter relaxing times and, seemingly, $R_0 = L/\sigma_h A$,

indicating high doping spreading along the entire bulk at longer times, one can derive readily that

$$R = R_1 - (R_1 - R_0) \frac{s}{L} \quad (2)$$

This linear expression as a function of s is illustrated in Figure S3b. Equation (2) can be normalized by the resistance step $R_1 - R_0$ giving rise to the following simple expression

$$\frac{R-R_0}{R_1-R_0} = 1 - \frac{s}{L} \quad (3)$$

that again predicts a linear dependence of the sample resistance with the width of the high doping zone s .

Let us also assume that ions initially accumulate following a narrow distribution near the contact with w standing for the distribution width. The accumulation occurs by effect of the applied electrical field. This ionic accumulation is expected by formation of a diffusion ion layer in the vicinity of the contacts and by very limited interfacial chemical interaction within the experimental time framework. Mobile ions depleted from the layer bulk induce a sort of electronic de-doping, reducing as a consequence the doping level and producing higher resistance. When bias is removed, ions are released and tend to diffuse back to their equilibrium position in such a way that the mean square displacement of the ion distribution enlarges with time. The simple outlined model would entail diffusion takes place in 1D ($\delta = 1$), but the real situation might be more complex with diffusion dimensionality approaching larger values because of the polycrystalline structure. For the sake of simplicity, let's assume that the distribution width spreads by diffusion as

$$w = \sqrt{2\delta Dt} \quad (4)$$

with D accounts for the ion diffusion coefficient, $\delta = 1$ for 1D diffusion, and t is the time. Equation 4 informs on how the high doping region width s extends within the perovskite layer bulk as the ion distribution spreads to attain initial homogeneity.

An additional component of the model concerns the relation between the width of the high doping zone s and the spread of the ion distribution w . For a Gaussian distribution, one can observe that nearly 99% of the ions concentrates within $3w$ as to assume that $s = 3w$. We recognize that this is in fact an oversimplification of a complex problem that should include concrete ion distributions and how they influence the local doping density. In any case, one can derive a simple linear expression for the variation of the resistance that suffices for our purposes.

By combining Equation (3) and (4), and $\delta = 1$ an expression for the time dependence of the normalized resistance step results as

$$\frac{R-R_0}{R_1-R_0} = 1 - \frac{3\sqrt{2Dt}}{L} \quad (5)$$

which predicts a linear dependence as $\propto \sqrt{t}$ with slope determined by the diffusion coefficient.

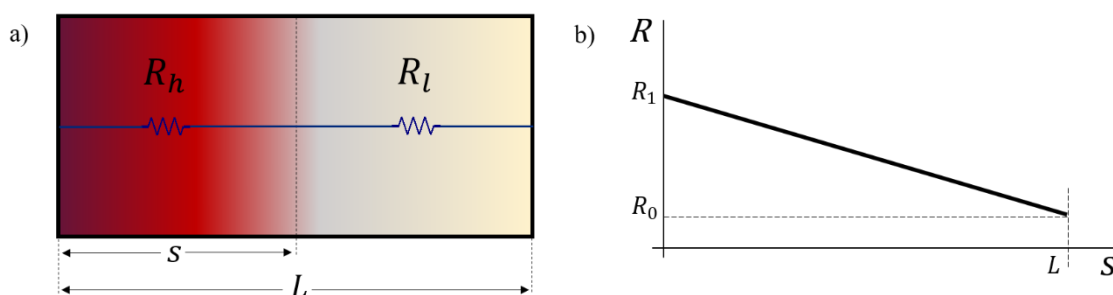


Figure S5. a) Model of the bulk resistance which splits it into two contributions $R = R_h + R_l$ of high- and low-doping separated regions. As the ionic charge moves to the right to attain equilibrium, the high-doping region width s progresses reducing the total sample resistance. b) Change of the total resistance as a function of s , exhibiting a linear dependence from R_1 at $s = 0$ down to R_0 at $s = L$, being L the sample thickness.

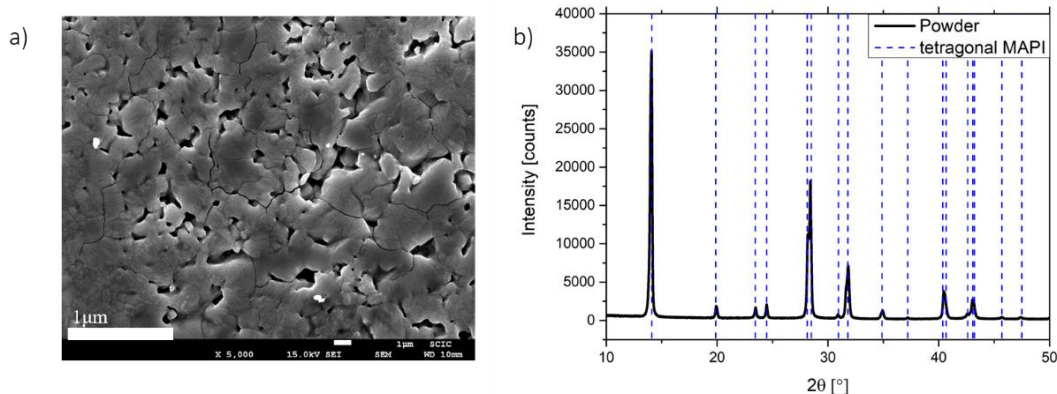


Figure S6 a) Scanning Electron Microscopy image showing the surfaces of the Sample 1 (MAPI pellet) b) X-Ray diffraction pattern of the used MAPbI₃ powder. The peaks indicate the tetragonal MAPbI₃-phase with an $I4cm$ space group (see main text).

References

1. Deumel, S.; Breemen, A. v.; Gelinck, G.; Peeters, B.; Maas, J.; Verbeek, R.; Akkerman, H.; Meulenkamp, E.; Huedler, J. E.; Acharya, M.; García-Batlle, M.; Almora, O.; Guerrero, A.; Garcia-Belmonte, G.; Heiss, W.; Schmidt, O.; Tedde, S. F., Sub-Nanogray X-Ray Imaging with Soft-Sintered Methylammonium Lead Triiodide Perovskites. *Nature Electronics* **2021**, submitted.
2. García-Batlle, M.; Baussens, O.; Amari, S.; Zaccaro, J.; Gros-Daillon, E.; Verilhac, J.-M.; Guerrero, A.; Garcia-Belmonte, G., Moving Ions Vary Electronic Conductivity in Lead Bromide Perovskite Single Crystals through Dynamic Doping. *Advanced Electronic Materials* **2020**, *6*, 2000485.
3. Yang, T.-Y.; Gregori, G.; Pellet, N.; Grätzel, M.; Maier, J., The Significance of Ion Conduction in a Hybrid Organic–Inorganic Lead-Iodide-Based Perovskite Photosensitizer. *Angewandte Chemie International Edition* **2015**, *54*, 7905-7910.
4. Peng, W.; Aranda, C.; Bakr, O. M.; Garcia-Belmonte, G.; Bisquert, J.; Guerrero, A., Quantification of Ionic Diffusion in Lead Halide Perovskite Single Crystals. *ACS Energy Letters* **2018**, *3*, 1477-1481.

5. Li, C.; Guerrero, A.; Huettner, S.; Bisquert, J., Unravelling the Role of Vacancies in Lead Halide Perovskite through Electrical Switching of Photoluminescence. *Nature Communications* **2018**, *9*, 5113.
6. Belisle, R. A.; Nguyen, W. H.; Bowring, A. R.; Calado, P.; Li, X.; Irvine, S. J. C.; McGehee, M. D.; Barnes, P. R. F.; O'Regan, B. C., Interpretation of Inverted Photocurrent Transients in Organic Lead Halide Perovskite Solar Cells: Proof of the Field Screening by Mobile Ions and Determination of the Space Charge Layer Widths. *Energy & Environmental Science* **2017**, *10*, 192-204.
7. Senocrate, A.; Moudrakovski, I.; Acartürk, T.; Merkle, R.; Kim, G. Y.; Starke, U.; Grätzel, M.; Maier, J., Slow CH_3NH_3^+ Diffusion in $\text{CH}_3\text{NH}_3\text{PbI}_3$ under Light Measured by Solid-State Nmr and Tracer Diffusion. *The Journal of Physical Chemistry C* **2018**, *122*, 21803-21806.
8. Senocrate, A.; Moudrakovski, I.; Kim, G. Y.; Yang, T.-Y.; Gregori, G.; Grätzel, M.; Maier, J., The Nature of Ion Conduction in Methylammonium Lead Iodide: A Multimethod Approach. *Angewandte Chemie International Edition* **2017**, *56*, 7755-7759.
9. Bertoluzzi, L.; Belisle, R. A.; Bush, K. A.; Cheacharoen, R.; McGehee, M. D.; O'Regan, B. C., In Situ Measurement of Electric-Field Screening in Hysteresis-Free $\text{Pb}(\text{MA})_{0.83}\text{Cs}_{0.17}\text{Pb}(\text{I}_{0.83}\text{Br}_{0.17})_3/\text{C60}$ Perovskite Solar Cells Gives an Ion Mobility of $\sim 3 \times 10^{-7} \text{ cm}^2/(\text{V s})$, 2 Orders of Magnitude Faster Than Reported for Metal-Oxide-Contacted Perovskite Cells with Hysteresis. *Journal of the American Chemical Society* **2018**, *140*, 12775-12784.
10. Yuan, Y.; Chae, J.; Shao, Y.; Wang, Q.; Xiao, Z.; Centrone, A.; Huang, J., Photovoltaic Switching Mechanism in Lateral Structure Hybrid Perovskite Solar Cells. *Advanced Energy Materials* **2015**, *5*, 1500615.

Chapter 6: Publication 3

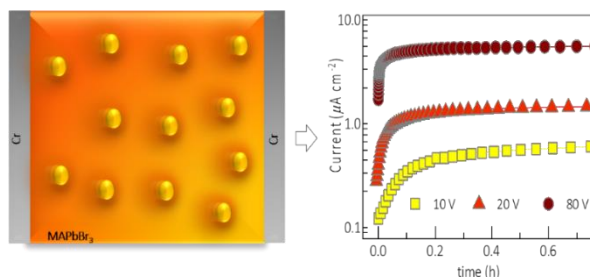
Marisé García-Batlle, J. Mayén Guillén, M. Chapran, O. Baussens, J. Zaccaro, E. Gros Daillon, J. M. Verilhac, A. Guerrero, O. Almora, G. Garcia Belmonte, Coupling between Ion Drift and Kinetics of Electronic Current Transients in MAPbBr₃ Single Crystals, *ACS Energy Lett.* **2022**, 7, 946, <https://doi.org/10.1021/acseenergylett.1c02578>

6.1 Candidate's contribution

Nature of Contribution	Extent of Contribution
<ul style="list-style-type: none"> Carried out all the drift transients' experiments and the fitting of the experimental data Performed all the characterization techniques Contributed to interpretation of the results Wrote the first draft of the manuscripts. 	50 %

6.2 Brief summary

Symmetrically contacted millimeters-thick MAPbBr₃ samples were studied using a measurement protocol robust and reliable focused on the longtime response towards steady-state current in cycles of biasing routines. Reproducible responses of the current transient upon bias application exhibits exponential increment. IS measurements allowed to estimate ionic mobility by using the IDD model while the formalism of the BVM regime of SCLC was used to explain the relaxation times $t_r \propto V^{-3/2}$. We found that the ionic currents are negligible in comparison to the total currents in our samples, for the measured bias and time ranges. The mobile ions, however, influence significantly the long-time electronic transport process via the modification of the charge density profile.



6.3 Published manuscript

Coupling between Ion Drift and Kinetics of Electronic Current Transients in MAPbBr₃ Single Crystals

Marisé García-Batlle¹, Javier Mayén Guillén², Marian Chapran³, Oriane Baussens³, Julien Zaccaro⁴, Jean-Marie Verilhac², Eric Gros-Daillon³, Antonio Guerrero¹, Osbel Almora^{1*} and Germà Garcia-Belmonte^{1*}

¹ *Institute of Advanced Materials (INAM), Universitat Jaume I, 12006 Castelló, Spain*

² *Grenoble Alpes University, CEA, LITEN, DTNM, F38000 Grenoble, France*

³ *Grenoble Alpes University, CEA, LETI, DOPT, F38000 Grenoble, France*

⁴ *Grenoble Alpes University, CNRS, Grenoble INP, Institut Néel, F38042 Grenoble, France*

*Email: almora@uji.es, garcia@uji.es

5 October 2022

Abstract

The optoelectronic properties of halide perovskite materials have fostered their utilization in many applications. Unravelling their working mechanisms remains challenging due to their mixed ionic-electronic conductive nature. By registering, with high reproducibility, the long-time current transient response of a set of single-crystal methylammonium lead tribromide samples, the ion migration process was proved. Sample biasing experiments (ionic drift), with characteristic times exhibiting a voltage dependence as $\propto V^{-3/2}$, is interpreted with an ionic migration model obeying a ballistic-like voltage-dependent mobility (BVM) regime of space-charge-limited current. The ionic kinetics effectively modify the long-time electronic current evolution, while the steady-state electronic currents behave nearly ohmic. Using the ionic dynamic doping model (IDD) for the recovering current at zero bias (ion diffusion), the ionic mobility is estimated to be $\sim 10^{-6} \text{ cm}^2 \text{ V}^{-1} \text{ s}^{-1}$. Our findings suggest that ionic currents are negligible in comparison to the electronic currents, however influencing them via changes in the charge density profile.

The outstanding and versatile optoelectronic properties of halide perovskite thin films, most typically based on methylammonium lead triiodide, have allowed their utilization in many applications such as solar cells, light-emitting diodes, photodetectors, and lasers.¹⁻² In the case of halide perovskite single crystals (SC), the promising sensitivity and favorable characteristics (high absorption coefficient, long carrier diffusion length, and long carrier lifetime) have motivated arduous research in the field of high-energy radiation detectors.³⁻⁵ Particularly, the use of methylammonium lead tribromide (MAPbBr₃) SCs for radiation detectors has recently shown significant progress⁶⁻⁸ due to their easy solution-based fabrication methods and the resulting high crystalline quality and material stability.⁹⁻¹¹ Nevertheless, unravelling the working mechanisms of halide perovskite-based devices remains challenging due to their mixed ionic-electronic conductive nature, which usually complicates the comprehension of certain response features.¹²⁻¹³ Moreover, understanding ion-originated modulations of the electronic properties is essential to further progress into the physics and operating modes of halide perovskite device.¹⁴⁻¹⁶

The ion migration in MAPbBr₃ SCs has been investigated through different methods (see Table S1 in the Supporting Information).¹⁷⁻²⁰ Several hypotheses have been suggested to distinguish ionic from electronic contributions to the measured current density (J) flowing through perovskite-based samples.²⁰⁻²⁵ Nevertheless, there are no conclusive evidence nor consensus on the most appropriate model. The major issues are the overlapping in time scales of both ionic and electronic phenomena, giving rise to the so-called hysteresis of halide perovskites,²⁶ and the materials reactivity causing performance degradation. Both phenomena hinder the interpretation of many experiments due to signal instability, lack of reproducibility and strong dependency on several parameters, such as the applied voltage (V), polarization history, temperature (T)²⁷ and moisture. Accordingly, for any study on the electrical response of mixed ionic-electronic halide perovskite it is essential to (i) identify a state (or regime) where one of the two contributions can be negligible, (ii) validate reproducibility and (iii) check whether material or interface degradation may affect the conclusions.

In order to explore purely electronic currents, one can either analyze a signal so fast that the ions cannot follow or so slow that a steady-state is attained and the ionic

displacement currents no longer contribute to the total direct-current-mode (DC) flux of charge carriers. High-frequency perturbation studies are an example of fast signal where the mobile ions are kept “frozen” in homogeneous quasi-equilibrium state. As such these studies are useful for evaluating the electronic phenomena without ionic contributions to the current or the charge density profile. However, they do not correspond to a realistic situation for device operation. In practical applications, the total DC currents are affected by the coupled contributions of electrons and ions to the charge density profile, hence defining the magnitude and time evolution of the total current.

In this work, an experiment is presented that consists in registering the long-time current transient response to different biases for a set of MAPbBr₃ SC samples, symmetrically contacted with chromium electrodes. The measured current exhibits exponential rise until saturation at the steady-state. On the other hand, relaxation under zero bias for enough time allows reaching equilibrium, which ensures negligible electrostatic potential energy before subsequent biasing. Thereby, a specific biasing protocol is followed that guarantees sufficient stability and permits high reproducibility. Ion migration is proved by either electrical field drift (current transient experiments) or ion diffusion (zero-bias impedance spectroscopy). As expected, dissimilar times scales are encountered for ion movement because of a change in transporting driving force. Experiments are analyzed either by means of the ionic dynamic doping model (IDD)^{17, 21} or the model of ballistic-like voltage-dependent mobility (BVM)²⁸ regime of space-charge-limited currents (SCLC) accounting for the separate regimes of ion diffusion and ion drift, respectively. Our findings suggest an ionic-electronic coupling in which purely electronic currents are measured that follow the slow kinetics of mobile ion redistribution. Ionic mobility values in the order of $\mu_i \sim 10^{-6} \text{ cm}^2 \text{ V}^{-1} \text{ s}^{-1}$ result in a consistent way through our analysis.

Experimental methods. Single-crystals of MAPbBr₃ were prepared following the inverse temperature crystallization (ITC) growth method.¹⁰ The precursors MABr and PbBr₂ were dissolved in N,N-dimethylformamide (DMF) with an equimolar ratio. The precursor solution containing a seed crystal was placed in an oil bath which temperature was programmatically raised from room temperature to 85°C. Finally, the

obtained high quality MAPbBr₃ single crystals were polished and then contacted with chromium electrodes. It has been selected because it spontaneously oxidizes during sample preparation giving rise to a thin layer of Cr₂O₃,²⁹ preserving the contact from rapid chemical degradation. The thicknesses L of the samples ranged from 0.96 to 2.20 mm. The evaporated electrodes had an active area A of ~ 20 mm².

The single crystals were characterized by optical transmission spectroscopy (Fig S1) and X-ray powder diffraction (Fig S2). The transmission spectrum was recorded on a Perkins-Elmer Lambda 900 spectrometer, using an unpolarized beam. Polished samples were mounted in front of an aperture with a diameter of 2 mm. The optical band gap, extracted from Tauc plot, shows value of 2.21 eV. Structural characterizations were made using a D8 Endeavor diffractometer equipped with a Johansonn monochromator. Single-crystal was grinded into powder and measured in Bragg-Brentano θ - 2θ geometry. The diffractogram reveals the standard cubic space group Pm3m of MAPbBr₃ crystals with lattice dimension $a=5.928$ Å, and without any trace of secondary phase.

Chronoamperometry experiments were carried out with a Source Measure Unit Keithley Model 2612B and impedance spectroscopy (IS) measurements were conducted with a PGSTAT302N potentiostat from Metrohm AUTOLAB. Current measurements were carried out under several long-time direct-current mode (DC) bias conditions in the ranges of ± 200 to 0 V. The samples were kept in the dark at 300 K with N₂ circulation for preventing humidity- and oxygen-induced degradations.

Measurement of current transients. The J - V characteristics of MAPbBr₃ SC samples are shown in Figure S3 in the supporting information (SI). One can infer from the linearity of the J - V response an ohmic behavior in the selected voltage range, without significant evidence of hysteretic current contribution. In fact, at the used scan rate of 90 mV/s, the electronic current is instantly observed due to a much faster speed of electrons/holes compared with that of ions.³⁰ However, it is not evident that the J - V responses have necessarily reached the steady-state regime, which might require much longer polarization times.

Figure 1a displays the current response of a MAPbBr₃ SC sample upon the application (solid dots) and removal (open dots) of step voltages (10, 20, 50, 80, 100

and 200 V). In this biasing protocol, after each 9600 s-interval of positive bias, the crystal relaxes at 0 V for 3000 s. At this zero-bias, a small current undershoot appears of the order of nA cm^{-2} with the opposite sign and long decay time (See Figure S4). As expected, that negative current seems to exclusively obey the ion dynamics.³⁰

In the zero bias, recovering experiment, the IS spectra were measured as a function of time t after a DC polarization of 10 V and fitted to the equivalent circuit of Figure S5. The high frequency resistance (R) values were normalized and shown to follow a trend $R \propto t^{1/2}$ (see Figure S6), in agreement with the IDD model (see section S2 and Discussion section).^{17, 21}

It is of major importance to study the drift current upon biasing. In Figure 1a, the electronic current density (J_e) exponentially rises and finally saturates approaching steady-state values J_0 at long times (10-1000 s). We interpret the current level as being originated by electronic (electrons and holes) carrier. However, such long response times suggest us that the kinetics of current saturation is governed by the slow movement of ionic species, then entailing a coupling between electronic drift and ionic transport. The J_0 - V shown in Figure 1b for four samples of different thicknesses along with a J - V curve (Figure S3) for comparison. From the allometric fitting, a $J_0 \propto V^n$ law is extracted with the power $n = 0.96 \pm 0.07$, which is more likely due to the occurrence of an ohmic conduction regime for the electronic carriers. It is also worth noting that fast J - V curves exhibit lower current values than those extracted from the steady-state regime.

As shown in Figure 1c, the measurement procedure from 10 V to 200 V-bias was repeated three consecutive times. Note that the steady-state current slightly increases between cycles while keeping the biasing protocol. Replicas of this experiment with other samples of similar thickness are shown in Figure S7 in SI.

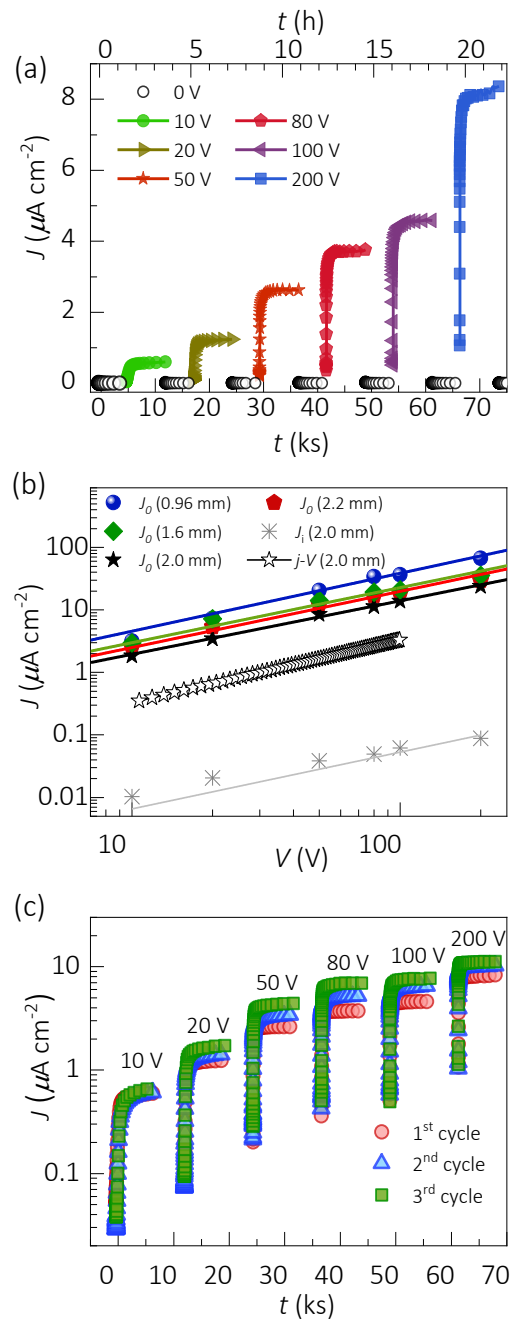


Figure 1. Long-time current evolution upon a biasing protocol for a ~2 mm-thick MAPbBr₃ SC sample. a) Full biasing routine of one cycle: after each bias, the device is kept under short-circuit (0 V bias) conditions to observe the relaxation current (Figure S4, SI). (b) Variation of the saturation current of four SC of different thicknesses are shown with the corresponding linear fit (solid lines), one of the J - V curves registered at high scan rates and the ionic drift currents J_i immediately obtained after bias removal (Figure S3, SI). (c) Biasing responses of three consecutive cycles. Replicas of this experiment with other samples are shown in Figure S7.

To quantify the ionic kinetics and estimate ionic transport parameters under different biases, we explored the shape and magnitude of the current transients. **Figure 2a** shows the current response (dots) with the corresponding exponential fittings (lines) for the first cycle (see fitting results for the other two cycles in Figure S8). The exponential rise can be explicitly expressed as $J_e(t) = J_0(1 - \exp[-t/\tau])$ where τ signals the time constant of the ion migration process. Since τ only accounts for 63% of the variation, we rather use the total characteristic time $t_t = 4\tau$ which corresponds to 98% of the transition to the steady-state. Then, by plotting the resulting time constants as a function of the applied bias at the power of $-3/2$, a clear $t_t \propto V^{-3/2}$ relationship is identified in **Figure 2b**. Importantly, also illustrated in **Figure 2b**, this behavior is even observed after 3 consecutive cycles of measurement, indicating a significant reproducibility.

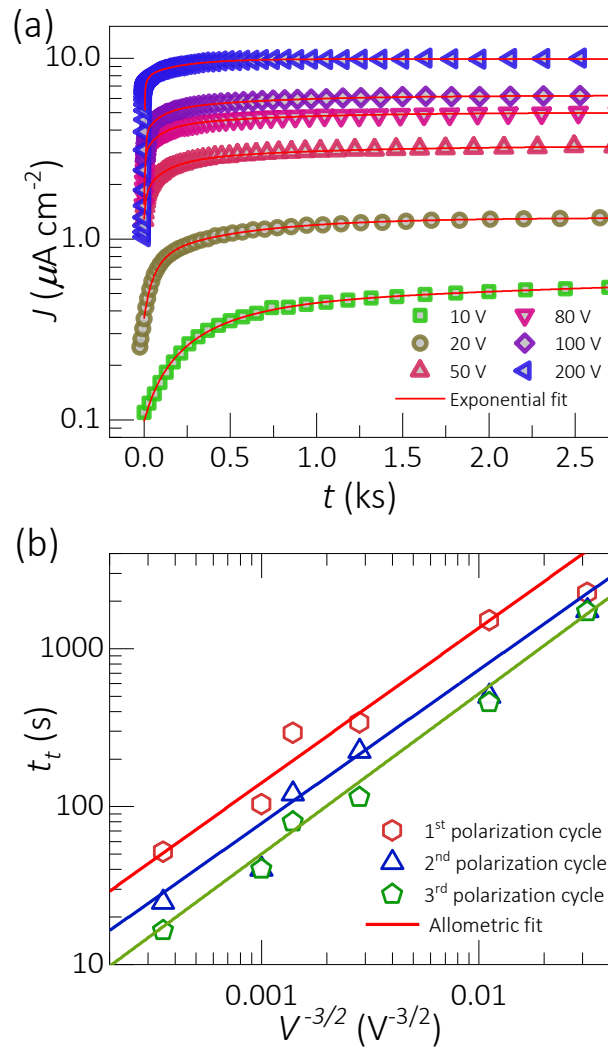


Figure 2. Parameterization of the long-time current transient response to different voltage steps during the first cycle of measurement of a ~ 2 mm-thick MAPbBr_3 SC sample: (a) experimental current transient (dots) and exponential fittings (lines), and (b) corresponding characteristic ionic relaxation time constants as a function of the applied voltage.

Analysis of ionic transit time. The long-time current transient experiments result in two main trends: $J_0 \propto V^n$, with $n \sim 1$ and $t_t \propto V^{-3/2}$. The ohmic behavior of the saturated current as a function of voltage indicates that, once the steady-state is attained, there is no significant influence of the actual charge density profile on the electronic currents. Importantly, that ohmic regime is obeyed irrespective of the sample thickness (Figure 1b). Hence, J_0 variation on biasing cycle (Figure 1c) is either caused by (i) an

interface phenomenon which merely modified the contact resistance and/or (ii) a bulk issue directly associated with the homogeneous change of defect density.

Ionic mobility can be directly evaluated by analyzing the resistance response under the diffusion-controlled relaxation at $V = 0$ V. By using the IDD model (see Section S2),^{17, 21} the evolution of R with time from the IS characterization results in a ionic diffusion coefficient as $D_i = (3.1 \pm 0.4) \times 10^{-8} \text{ cm}^2\text{s}^{-1}$, which corresponds to ion mobilities of about $\mu_i = (1.20 \pm 0.15) \times 10^{-6} \text{ cm}^2 \text{ V}^{-1} \text{ s}^{-1}$ by using the Einstein's relation (equation S8). Moreover, the crystal electronic conductivity can be inferred from the linear relationship $R \propto L/A$ (see Figure S9), and results in $\sigma_e = (20 \pm 5) \times 10^{-8} \Omega^{-1} \text{ cm}^{-1}$, also in agreement with previous reports.²¹ Besides, high electronic mobility (μ_e) has been measured using laser time-of-flight techniques in our samples being $\mu_e = 17 \text{ cm}^2 \text{ V}^{-1} \text{ s}^{-1}$ (see Figure S10) with a similar procedure as the one previously reported.¹⁹ Note therefore the huge difference in mobility between ionic species and electronic carriers. In fact, it makes sense to estimate the order of magnitude of the ionic drift currents from the maximum diffusion currents in each short-circuit period of the experiments (from Figure S4). The comparison is made in Figure 1b, which indicates that J is greater than J_i by more than two orders of magnitude. This would entail that ionic currents, although present, should be negligible as part of the total current measured during the relaxation towards the steady-state (i.e. $J_i \ll J$), which have to be considered as being mainly dominated by electronic carriers ($J \simeq J_e$). The difference in current level should also apply for the respective conductivity.¹³ However, the measured time constants within the range of 10-1000 s (Figure 2b) readily suggest that the transition towards the steady-state carries the information of the ionic kinetics.

The behavior of the ionic-related relaxation times $t_i \propto V^{-3/2}$ resembles that of the τ_{tof} in the classic Child-Langmuir law³¹⁻³² for the ballistic SCLC (see section S3), which suggests the occurrence of ionic currents with a $J_i \propto V^{3/2}$ trend. The ballistic SCLC tackles the space charge modification when the electrostatic energy is totally converted into kinetic energy upon application of an external electric field. Consequently, the drift velocity relates with the electrostatic potential as $v_d \propto \phi^{1/2}$ producing characteristic behaviors in the current ($J \propto V^{3/2}$), the potential versus position ($\phi \propto x^{4/3}$) and the time of flight ($\tau_{tof} \propto V^{-3/2}$). This deviates from the ohmic behavior where $v_d \propto \phi$, hence $J \propto V$, $\phi \propto x$ and $\tau_{tof} \propto V^{-1}$, giving rise to the simpler form $\tau_{tof} = L^2/\mu V$. The ballistic regime,

on the other hand, only applies to vacuum,³¹⁻³² low temperature,³³ or short enough distance³⁴ and time scale conditions.³⁵⁻³⁸ For more typical perovskite samples at room temperature, the ballistic-like voltage-dependent mobility (BVM)²⁸ assumes instead $v_d \propto (d\phi/dx)^{1/2}$, which results in $J \propto V^{3/2}$, $\phi \propto x^{5/3}$ and $\tau_{tof} \propto V^{-3/2}$. Considering the BVM formalism, the slow kinetics from our experiments would imply an ionic time-of-flight $\tau_{tof,i} \propto V^{-3/2}$ due to a maximum ionic drift velocity $v_{d,i} \propto V^{1/2}$ allowing us to describe consistently the observed ionic time-of-flight values as²⁸

$$\tau_{tof} = \frac{L^4 Q N}{\epsilon_0 \epsilon_r \mu \sqrt{2V_0}} V^{-3/2} \quad (1)$$

where L is the distance between electrodes; ϵ_0 , the vacuum permittivity; ϵ_r , the dielectric constant; V_0 , the onset potential for the BVM- regime; Q , the charge and N is an effective homogeneous density of charge carriers (mostly mobile ions in this case). The $\tau_{tof,i}$ values calculated from Equation (1) are shown in Figure 3 for a MAPbBr₃ single crystal in conditions similar to those of the experiment. It can be seen that mobile ions with $\mu_i \sim 10^{-6} \text{ cm}^2 \text{ V}^{-1} \text{ s}^{-1}$ (from the IDD model) reproduce $\tau_{tof,i} \sim 10^3 \text{ s}$ (from the experiment) with reasonably low values of charge concentration $N \sim 10^{11} \text{ cm}^{-3}$ for a single crystal sample. Here we have assumed unity for the charge Q as it corresponds to fast, bromide-related mobile ionic species. It is also noticeable that the electronic density calculated from the conductivity $\sigma_e = 20 \times 10^{-8} \text{ } \Omega^{-1} \text{ cm}^{-1}$ results in values as low as $n = 7 \times 10^{10} \text{ cm}^{-3}$, comparable with the ionic concentration estimated from Figure 3, i.e. $n \approx N$, consistent with the IDD model outlined in Sec. S2. However, it should be noted that only ionic species acting as electronic dopants contribute to the increment in electronic conductivity, in such a way that N might just constitute a part of the total mobile ions. Contrastingly, electronic charge carriers with $\mu_e = 17 \text{ cm}^2 \text{ V}^{-1} \text{ s}^{-1}$, would require unrealistically large doping density $n > 10^{18} \text{ cm}^{-3}$ for a single crystal to relax in the order of ks. The different ways in which the drift velocity of electrons and ions relate to the voltage can explain the electronic currents following an ionic relaxation.

The electronic J_0 values show nearly ohmic character, which may indicate that the electronic drift velocity is linear with the field. Then, one can take $v_{d,e} \propto V$ with a kinetic in the range of μs , and a final bulk distribution of the electrostatic potential that is linear ($\phi \propto x$). The behavior of $v_{d,e}$ is evidenced through electronic time-of-flight

techniques in Figure S10 and a possible description of the potential is schemed in the energy diagram of Figure S11. The ionic induced band bending of the bulky perovskite as $\varphi \propto x^{5/3}$ could favor the charge collection during the relaxation period. At steady state, a seemingly ohmic behavior occurs in the bulk and a larger current is reported possibly due to the IDD effect where the bias induced accumulation of ions towards the interfaces eases the transport.

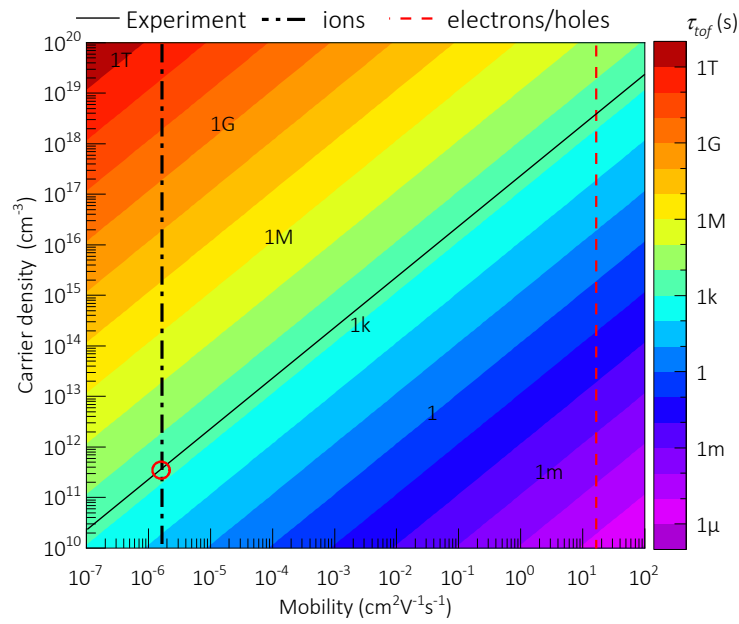


Figure 3: Time of flight (right-hand color bar) as a function of mobility and effective charge carrier density for the BVM regime of SCLC as in Equation (1) at $V=100$ V as for a MAPbBr_3 single crystal with $L = 2$ mm, $\epsilon_r = 76$,²¹ $V_0 = 10$ V. Note that the charge carrier density axis may refer to either ionic or electronic charge carriers in each case.

Our findings indicate that a coupling between ionic and electronic currents exists in such a way that the slower species (ions) condition the value of the measured current, which is actually determined by the faster carriers (electrons/holes). Consequently, ionic movement establishes the kinetics of the electronic response. Whatever the interplay mechanism is behind the current transients, it is clear from Figure 1a that

homogeneous distribution of ions at zero bias hinders the charge extraction at short times, while the applied bias favors the current flowing at longer times. The latter effect can be possibly due to (i) an increment of the effective doping in the bulk perovskite via field ionization, (ii) a local increment of effective doping caused by ion redistribution (dynamic doping), (iii) a reduction of contact barriers towards the electrodes via electrode polarization, or (iv) a combination of these effects. Elucidation of the effective mechanism occurring in perovskite-based devices needs an exhaustive analysis of different structures (electrodes, active material, buffer layers...) aimed at creating a coherent picture.

In summary, symmetrically contacted millimeters-thick MAPbBr₃ samples were studied using a measurement protocol focused on the long-time response towards steady-state current in cycles of biasing routines. This protocol has proven to be robust and reliable by delivering reproducible responses, regardless of possible ionic-related hysteresis and instability issues. Current transient upon bias application exhibits exponential increment. The behavior of the steady-state electronic drift currents suggests a seemingly ohmic conductivity for electronic charge carriers. However, the most-likely ionic-related relaxation times follow a $t_t \propto V^{-3/2}$ trend up to the order of hours, which can be modeled with the formalism of the BVM regime of SCLC. Furthermore, we also studied the diffusion relaxation via IS measurements which allowed us estimating the ionic mobility by using the IDD model. By combining the BVM and the IDD models, it is suggested that the ionic currents are negligible in comparison to the total currents in our samples, for the measured bias and time ranges. The mobile ions, however, influence significantly the long-time electronic transport process via the modification of the charge density profile.

Data available on request from the authors.

Supporting Information.

Sample preparation and structural, optical and electrical data is available. Ionic dynamic model and ballistic-like voltage-dependent mobility model outlined.

Acknowledgments

This work has received funding from the European Union's Horizon 2020 research and innovation program under the Photonics Public Private Partnership (www.photonics21.org) with the project PEROXIS under the grant agreement N° 871336. M. G.-B. acknowledges Generalitat Valenciana for a grant (number GRISOLIAP/2018/073).

References

1. Kim, H.; Han, J. S.; Choi, J.; Kim, S. Y.; Jang, H. W., Halide Perovskites for Applications Beyond Photovoltaics. *Small Methods* **2018**, *2*, 1700310.
2. Almora, O., et al., Device Performance of Emerging Photovoltaic Materials (Version 2). *Adv. Energy Mater.* **2021**, 2102526.
3. Heiss, W.; Brabec, C., Perovskites Target X-Ray Detection. *Nat. Photonics* **2016**, *10*, 288-289.
4. He, Y., et al., High Spectral Resolution of Gamma-Rays at Room Temperature by Perovskite CsPbBr₃ Single Crystals. *Nat. Commun.* **2018**, *9*, 1609.
5. Deumel, S., et al., High-Sensitivity High-Resolution X-Ray Imaging with Soft-Sintered Metal Halide Perovskites. *Nat. Electron.* **2021**, *4*, 681-688.
6. Tan, R.; Dryzhakov, B.; Charest, J.; Hu, B.; Ahmadi, M.; Lukosi, E., Improved Radiation Sensing with Methylammonium Lead Tribromide Perovskite Semiconductors. *Nuclear Instruments and Methods in Physics Research Section A: Accelerators, Spectrometers, Detectors and Associated Equipment* **2021**, 986, 164710.
7. Pan, W.; Wei, H.; Yang, B., Development of Halide Perovskite Single Crystal for Radiation Detection Applications. *Front. Chem.* **2020**, *8*.
8. Wei, H., et al., Sensitive X-Ray Detectors Made of Methylammonium Lead Tribromide Perovskite Single Crystals. *Nat. Photonics* **2016**, *10*, 333-339.
9. Saidaminov, M. I., et al., High-Quality Bulk Hybrid Perovskite Single Crystals within Minutes by Inverse Temperature Crystallization. *Nature communications* **2015**, *6*, 7586.
10. Amari, S.; Verilhac, J.-M.; Gros D'Aillon, E.; Ibanez, A.; Zaccaro, J., Optimization of the Growth Conditions for High Quality CH₃NH₃PbBr₃ Hybrid Perovskite Single Crystals. *Crystal Growth & Design* **2020**, *20*, 1665-1672.
11. Feng, A.; Jiang, X.; Zhang, X.; Zheng, X.; Zheng, W.; Mohammed, O. F.; Chen, Z.; Bakr, O. M., Shape Control of Metal Halide Perovskite Single Crystals: From Bulk to Nanoscale. *Chem. Mater.* **2020**, *32*, 7602-7617.
12. Futscher, M. H.; Milić, J. V., Mixed Conductivity of Hybrid Halide Perovskites: Emerging Opportunities and Challenges. *Front. Energy Res.* **2021**, *9*.

13. Wang, H.; Guerrero, A.; Bou, A.; Al-Mayouf, A. M.; Bisquert, J., Kinetic and Material Properties of Interfaces Governing Slow Response and Long Timescale Phenomena in Perovskite Solar Cells. *Energy Environ. Sci.* **2019**, *12*, 2054-2079.
14. Murali, B.; Kolli, H. K.; Yin, J.; Ketavath, R.; Bakr, O. M.; Mohammed, O. F., Single Crystals: The Next Big Wave of Perovskite Optoelectronics. *ACS Mater. Lett.* **2020**, *2*, 184-214.
15. Duijnste, E. A.; Le Corre, V. M.; Johnston, M. B.; Koster, L. J. A.; Lim, J.; Snaith, H. J., Understanding Dark Current-Voltage Characteristics in Metal-Halide Perovskite Single Crystals. *Phys. Rev. Appl.* **2021**, *15*, 014006.
16. Li, C.; Guerrero, A.; Huettner, S.; Bisquert, J., Unravelling the Role of Vacancies in Lead Halide Perovskite through Electrical Switching of Photoluminescence. *Nat. Commun.* **2018**, *9*, 5113.
17. Afroz, M. A.; Aranda, C. A.; Tailor, N. K.; Yukta; Yadav, P.; Tavakoli, M. M.; Saliba, M.; Satapathi, S., Impedance Spectroscopy for Metal Halide Perovskite Single Crystals: Recent Advances, Challenges, and Solutions. *ACS Energy Letters* **2021**, 3275-3286.
18. Musiienko, A.; Pipek, J.; Praus, P.; Brynza, M.; Belas, E.; Dryzhakov, B.; Du, M.-H.; Ahmadi, M.; Grill, R., Deciphering the Effect of Traps on Electronic Charge Transport Properties of Methylammonium Lead Tribromide Perovskite. *Sci. Adv.* **2020**, *6*, eabb6393.
19. Baussens, O.; Maturana, L.; Amari, S.; Zaccaro, J.; Verilhac, J.-M.; Hirsch, L.; Gros-Daillon, E., An Insight into the Charge Carriers Transport Properties and Electric Field Distribution of $\text{CH}_3\text{NH}_3\text{PbBr}_3$ Thick Single Crystals. *Appl. Phys. Lett.* **2020**, *117*, 041904.
20. Peng, W.; Aranda, C.; Bakr, O. M.; Garcia-Belmonte, G.; Bisquert, J.; Guerrero, A., Quantification of Ionic Diffusion in Lead Halide Perovskite Single Crystals. *ACS Energy Lett.* **2018**, *3*, 1477-1481.
21. García-Battle, M.; Baussens, O.; Amari, S.; Zaccaro, J.; Gros-Daillon, E.; Verilhac, J. M.; Guerrero, A.; Garcia-Belmonte, G., Moving Ions Vary Electronic Conductivity in Lead Bromide Perovskite Single Crystals through Dynamic Doping. *Adv. Electron. Mater.* **2020**, *6*, 2000485.

22. García-Batlle, M.; Deumel, S.; Huerdler, J. E.; Tedde, S. F.; Guerrero, A.; Almora, O.; Garcia-Belmonte, G., Mobile Ion-Driven Modulation of Electronic Conductivity Explains Long-Timescale Electrical Response in Lead Iodide Perovskite Thick Pellets. *ACS Appl. Mater. Interfaces* **2021**, *13*, 35617-35624.
23. Wei, D., et al., Ion-Migration Inhibition by the Cation– Π Interaction in Perovskite Materials for Efficient and Stable Perovskite Solar Cells. *Adv. Mater.* **2018**, *30*, 1707583.
24. Xiao, Z.; Yuan, Y.; Shao, Y.; Wang, Q.; Dong, Q.; Bi, C.; Sharma, P.; Gruverman, A.; Huang, J., Giant Switchable Photovoltaic Effect in Organometal Trihalide Perovskite Devices. *Nat. Mater.* **2015**, *14*, 193.
25. Unger, E. L.; Hoke, E. T.; Bailie, C. D.; Nguyen, W. H.; Bowring, A. R.; Heumüller, T.; Christoforo, M. G.; McGehee, M. D., Hysteresis and Transient Behavior in Current–Voltage Measurements of Hybrid-Perovskite Absorber Solar Cells. *Energy Environ. Sci.* **2014**, *7*, 3690-3698.
26. Snaith, H. J.; Abate, A.; Ball, J. M.; Eperon, G. E.; Leijtens, T.; Noel, N. K.; Stranks, S. D.; Wang, J. T.-W.; Wojciechowski, K.; Zhang, W., Anomalous Hysteresis in Perovskite Solar Cells. *J. Phys. Chem. Lett.* **2014**, *5*, 1511-1515.
27. Mahapatra, A.; Parikh, N.; Kumari, H.; Pandey, M. K.; Kumar, M.; Prochowicz, D.; Kalam, A.; Tavakoli, M. M.; Yadav, P., Reducing Ion Migration in Methylammonium Lead Tri-Bromide Single Crystal Via Lead Sulfate Passivation. *J. Appl. Phys.* **2020**, *127*, 185501.
28. Almora, O.; Miravet, D.; García-Batlle, M.; Garcia-Belmonte, G., Ballistic-Like Space-Charge-Limited Currents in Halide Perovskites at Room Temperature. *Appl. Phys. Lett.* **2021**, *119*, 242107.
29. Guerrero, A.; You, J.; Aranda, C.; Kang, Y. S.; Garcia-Belmonte, G.; Zhou, H.; Bisquert, J.; Yang, Y., Interfacial Degradation of Planar Lead Halide Perovskite Solar Cells. *ACS Nano* **2016**, *10*, 218-224.
30. Li, D.; Wu, H.; Cheng, H. C.; Wang, G.; Huang, Y.; Duan, X., Electronic and Ionic Transport Dynamics in Organolead Halide Perovskites. *ACS Nano* **2016**, *10*, 6933.
31. Child, C. D., Discharge from Hot Cao. *Phys. Rev. (Series I)* **1911**, *32*, 492-511.

32. Langmuir, I., The Effect of Space Charge and Residual Gases on Thermionic Currents in High Vacuum. *Phys. Rev.* **1913**, 2, 450-486.
33. Shur, M. S., Ballistic Transport in a Semiconductor with Collisions. *IEEE Trans. Electron Devices* **1981**, 28, 1120-1130.
34. Rhew, J.-H.; Lundstrom, M. S., Drift-Diffusion Equation for Ballistic Transport in Nanoscale Metal-Oxide-Semiconductor Field Effect Transistors. *J. Appl. Phys.* **2002**, 92, 5196-5202.
35. Hess, K.; Iafrate, G. J., Theory and Applications of near Ballistic Transport in Semiconductors. *Proc. IEEE* **1988**, 76, 519-532.
36. Sung, J., et al., Long-Range Ballistic Propagation of Carriers in Methylammonium Lead Iodide Perovskite Thin Films. *Nat. Physics* **2020**, 16, 171-176.
37. Sung, J.; Macpherson, S.; Rao, A., Enhanced Ballistic Transport of Charge Carriers in Alloyed and K-Passivated Alloyed Perovskite Thin Films. *J. Phys. Chem. Lett.* **2020**, 11, 5402-5406.
38. Guo, Z.; Wan, Y.; Yang, M.; Snaider, J.; Zhu, K.; Huang, L., Long-Range Hot-Carrier Transport in Hybrid Perovskites Visualized by Ultrafast Microscopy. *Science* **2017**, 356, 59-62.

6.4 Supplemental Information

Coupling between Ion Drift and Kinetics of Electronic Current Transients in MAPbBr₃ Single Crystals

Marisé García-Batlle¹, Javier Mayén Guillén², Marian Chapran³, Oriane Baussens³, Julien Zaccaro⁴, Jean-Marie Verilhac², Eric Gros-Daillon³, Antonio Guerrero¹, Osbel Almora^{1*} and Germà Garcia-Belmonte^{1*}

¹ *Institute of Advanced Materials (INAM), Universitat Jaume I, 12006 Castelló, Spain*

² *Grenoble Alpes University, CEA, LITEN, DTNM, F38000 Grenoble, France*

³ *Grenoble Alpes University, CEA, LETI, DOPT, F38000 Grenoble, France*

⁴ *Grenoble Alpes University, CNRS, Grenoble INP, Institut Néel, F38042 Grenoble, France*

*Email: almora@uji.es, garcia@uji.es

5 October 2022

Table S1 Report on parameterization of ion migration in Hybrid Perovskite Materials (~300 K)				
Methods	Architecture/thickness	Contacts/Composition	Parameters μ_i : ion mobility ($\text{cm}^2 \text{V}^{-1} \text{s}^{-1}$) D_i : diffusion coefficient ($\text{cm}^2 \text{s}^{-1}$)	Ref
ToF spectroscopy and Monte Carlo simulation	SCs_2 mm-thick	Cr / MAPbBr ₃ /Cr Au / MAPbBr ₃ /Au	$\mu_i = 10^{-7}$	1
PL quenching method	film_350 nm	Au/MAPbI ₃ /Au	$\mu_i = 9.1 \times 10^{-7}$ $D_i = 5 \text{ to } 6 \times 10^{-9}$	2
Nuclear magnetic resonance (NMR) spectroscopy	PCs_1 mm-thick	Gr/MAPbI ₃ /Gr	$D_i = 2 \times 10^{-9}$	3
Step-dwell-step-probe (SDSP) photocurrent transient.	film_400 nm	ITO/PTAA/FAPI/ C60/BCP/Ag	$\mu_i = 3 \times 10^{-7}$	4
Photothermal induced resonance (PTIR) microscopy	film_300 nm	Au/MAPbI ₃ /Au	$\mu_i = 1.5 \times 10^{-9}$	5
Chronoamperometry measurements	PCs_1mm-thick	Pt/MAPbI ₃ /Cr	$D_i = 3 \times 10^{-8}$ $\mu_i = 10^{-6}$	6
Impedance spectroscopy (IS)	PCs_0.6 mm-thick	Gr/MAPbI ₃ /Gr	$D_i = 2.4 \times 10^{-8}$	7
	SCs_1 μm -thick	TiO ₂ /MAPbBr ₃ / Au	$D_i = 1.8 \times 10^{-8}$	8
	SCs_1mm-thick	Cr / MAPbBr ₃ /Cr	$D_i = 2.6 \times 10^{-8}$ $\mu_i = 1 \times 10^{-6}$	9
Chronoamperometry measurements and Impedance spectroscopy*	SCs_1-2 mm	Cr / MAPbBr ₃ /Cr	$D_i = 3.1 \times 10^{-8}$ $\mu_i = 1.2 \times 10^{-6}$	this work

Column 2 lists the morphology of the perovskite devices being SCs: Single Crystals, PCs: Polycrystals

S1. Further experiments

METHODS

I. MAPbBr₃ SCs growth & device fabrication

MAPbBr₃ SCs were grown via Modified Inverse Temperature Crystallization (MITC) method. The growth process was similar to the one described in a previous work¹⁰ using linear 5°C/h temperature ramp. A seed was first obtained by spontaneous nucleation and used subsequently for crystal growth. At the end of the growth process, SCs of 4 mm × 4 mm × 2 mm on average were obtained. They were mechanically polished to mirror grade quality and Cr electrodes were thermally evaporated on opposite sides.

II. XRD

A D8 Endeavor diffractometer equipped with a Johansonn monochromator working in Bragg-Brentano θ - 2θ geometry was used (Cu K α $\lambda = 1.5406 \text{ \AA}$). An acquisition time of 2.5 s was set using 0.01° step, 2θ values ranging from 5° to 90°.

III. UV-Visible spectroscopy & Tauc plot

For transmittance data, a Perkin Elmer Lambda 900 UV-Vis-NIR spectrometer was used with a wavelength range of 400-600 nm, a 0.1 nm step and equipped with a Tungsten lamp. Tauc plot were charted using equation 1, 2, 3 and 4, where α is the absorption coefficient, h is the Planck constant, ν is the photon frequency, E_g is the band gap energy, B is a constant, γ is a factor depending on the nature of the electron transition and equal to 1/2 or 2 for the direct and indirect transition band gaps (here $\gamma = 1/2$),¹¹ c is the speed of light, A is the absorbance, T is the transmittance, d is the sample thickness and e is the elementary charge. In the Tauc plot, E_g was extracted at the intersection between the x axis and the linear fitting of the linear part in the onset region.

$$(\alpha h\nu)^{\frac{1}{\gamma}} = B(h\nu - E_g) \quad (\text{S1})$$

$$h\nu = \frac{hc}{\lambda 10^{-9} e} \quad (\text{S2})$$

$$\alpha = \frac{\ln(10) A}{d} \quad (\text{S3})$$

$$A = -\log T \quad (\text{S4})$$

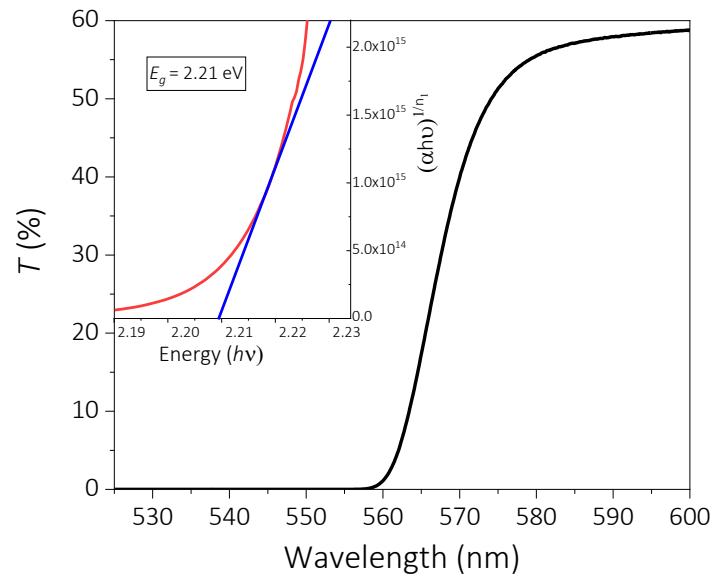


Figure S1. Transmittance spectre of MAPbBr₃ SC via UV-visible spectroscopy (SC thickness = 0.97 mm) In the inset : Tauc plot of MAPbBr₃ SC for band gap determination ($E_g = 2.21$ eV)

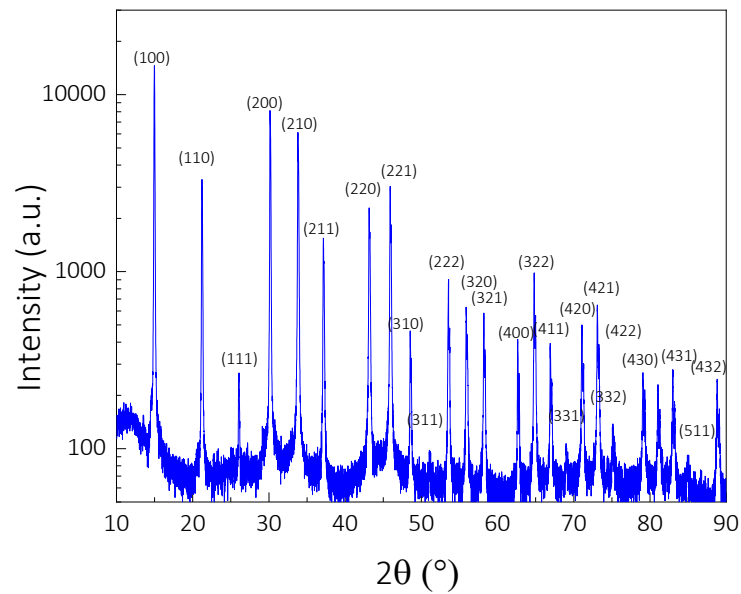


Figure S2. PXRD diffractogram in log scale of crushed MAPbBr₃ SC showing cubic crystal lattice (lattice parameter = 5.928 ± 0.003 Å) and no other parasitic phases.

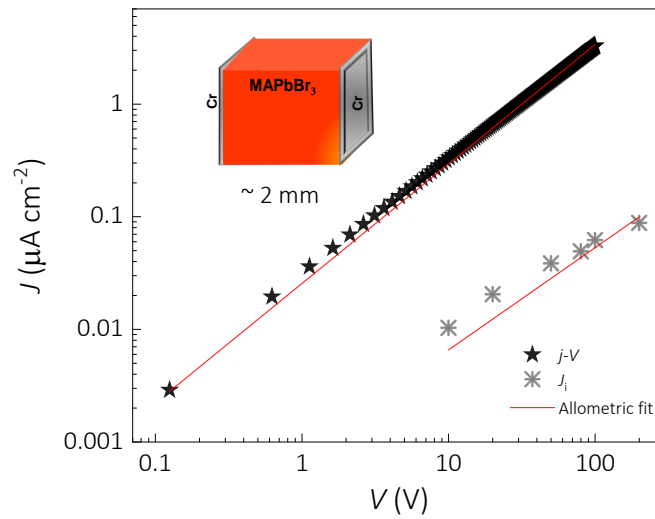


Figure S3. Comparison between the current–voltage characteristics (j - V) with scan rate of 90 mV/s and step: 1 V and the ionic drift currents J_i immediately obtained after bias removal of 2 mm-thick MAPbBr₃ SC symmetrically contacted with Cr electrodes. It is remarkable the ohmic character of the characteristics j - V curve, in agreement with previous analysis on Cr-contacted perovskite device.^{9, 12-13}

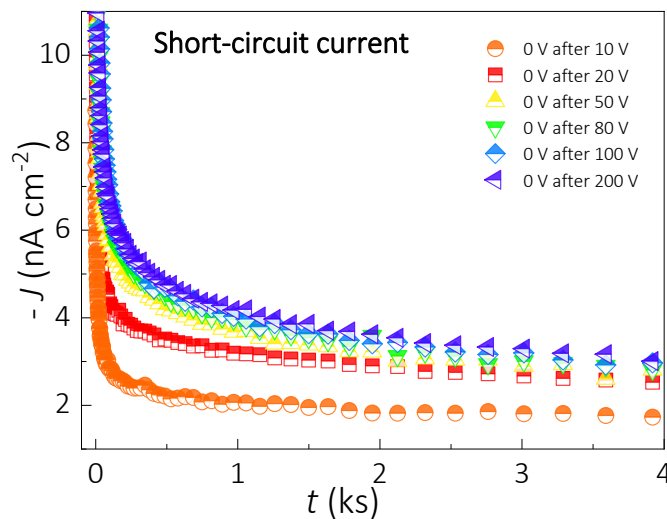


Figure S4. a) Current transient response to short-circuit condition (0 V-bias voltage) of a MAPbBr₃ SC symmetrically contacted with evaporated Cr electrodes.

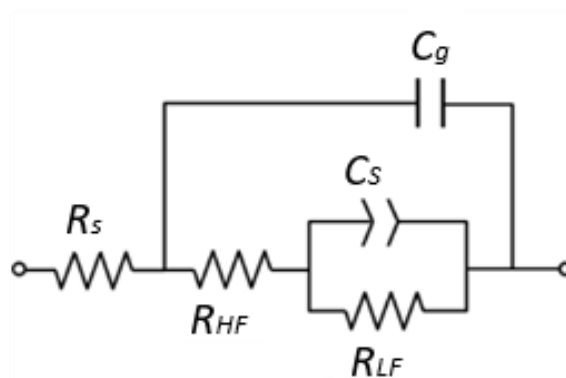


Figure S5. Equivalent circuit used to fit the impedance spectra: with series resistance R_s , C_g geometric capacitance and R_{HF} , and R_{LF} the high-, and low-frequency resistances, respectively. The low-frequency capacitance usually labelled as surface capacitance C_s .

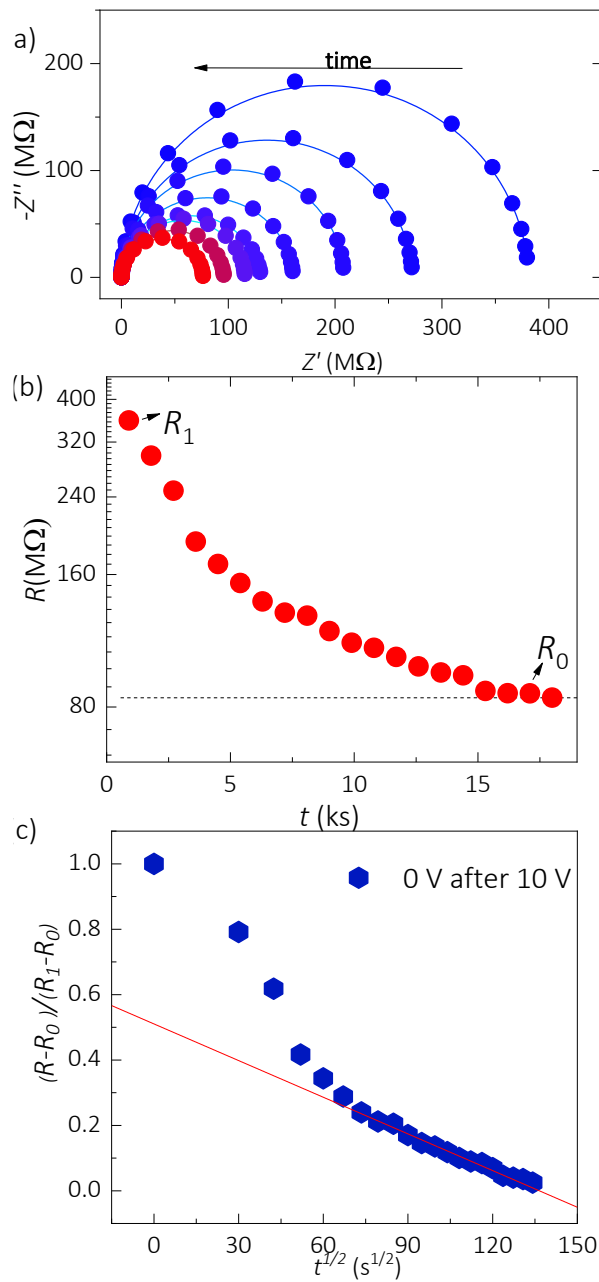


Figure S6. Variation of the impedance after removing 10 V bias and evolution with time b) Variation of the resistance extracted from fitting impedance spectra after bias removal at $t = 0$. Note the log scale in the vertical axis that informs on the complex function (non-exponential) of the resistance variation c) Variation of resistance ratio as a function of time following the relationship in equation (5) Solid line represents a linear fitting.

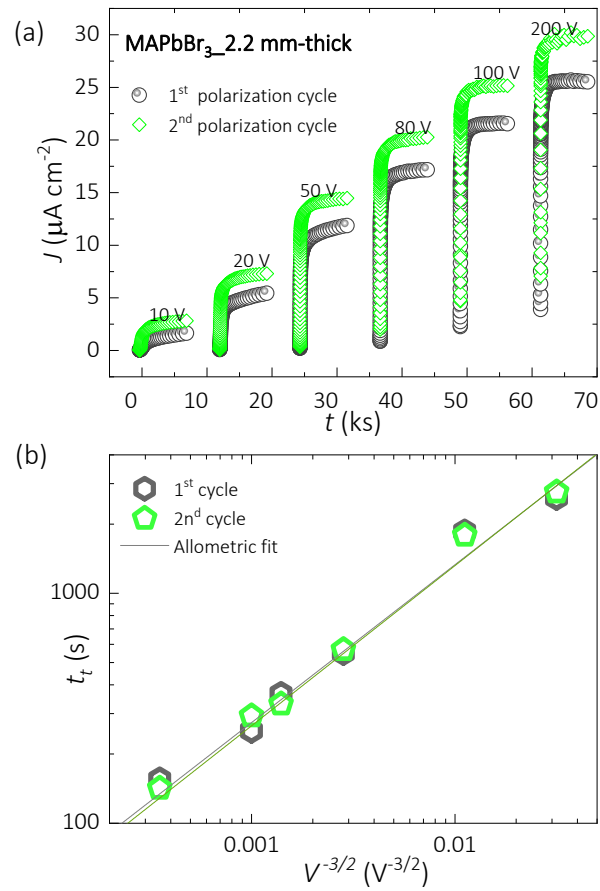


Figure S7. a) Long-time current transient's response to voltage steps of a 2.2 mm thick MAPbBr₃ SC- symmetrically contacted with evaporated Cr electrodes and b) corresponding characteristic ionic relaxation time constants as a function of the applied voltage.

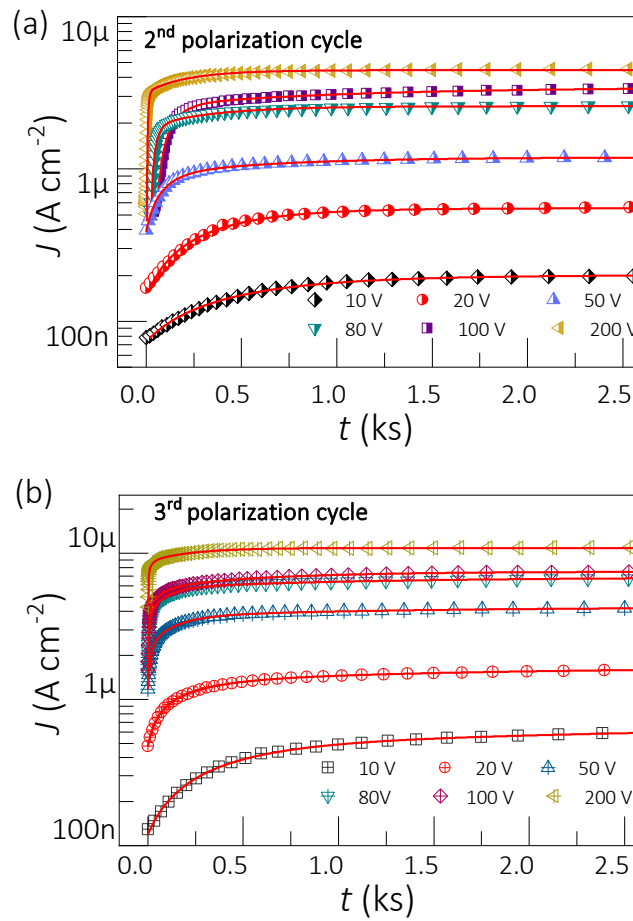


Figure S8. a) Long-time current transient response to different voltage steps during the 2nd and b) 3rd cycle of measurement of ~2 mm-thick MAPbBr₃ SC.

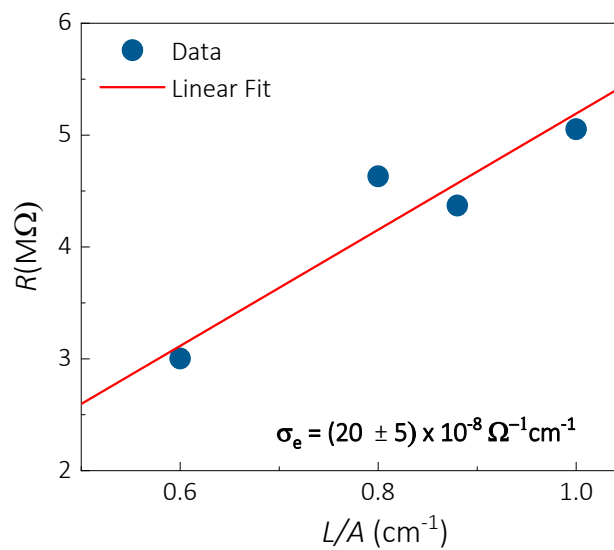


Figure S9. Scaling of the high-frequency resistance for four samples of different thicknesses and electrode area ratio, exhibiting linear relationship with geometrical parameter

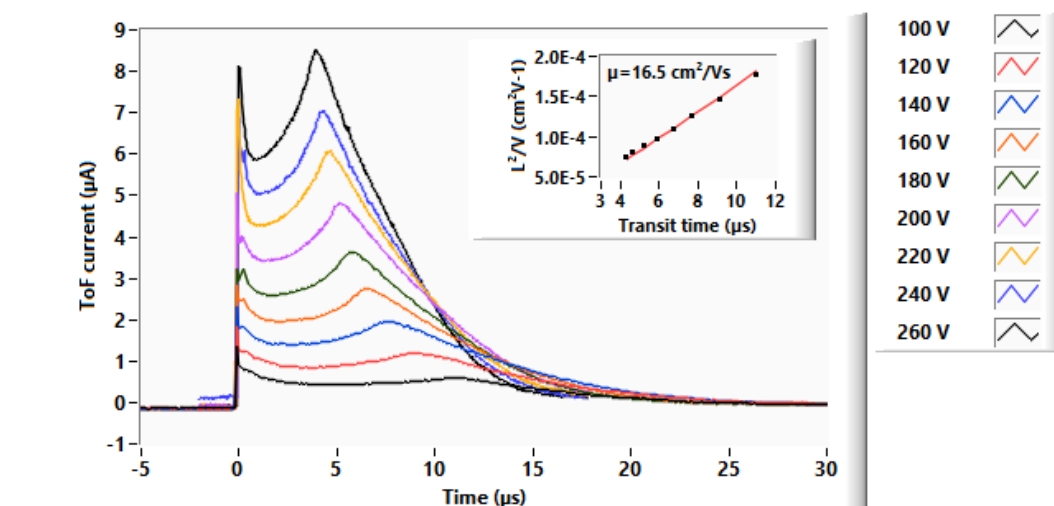


Figure S10. Hole time-of-flight (ToF) for a MAPbBr₃ single crystal (thickness 1.33 mm)

S2. Ionic Dynamic Doping (IDD) model

The IDD model,^{6,9} relies on the way the redistribution of ionic species along the layer bulk modulate the electronic carrier density. Mobile ions acts as dopants and locally alter the doping density by a dynamic doping process. Therefore, the resistance variation can be explained in terms of the increase in electronic carrier density. A detailed view of the high-frequency resistance decrease under 0-V bias can be observed in Figure S6a. By extracting the fitting parameters in Figure S6b the resistance shows a large initial value R_1 at shorter relaxing times and a steady-state value R_0 (background state) after a long equilibration time. A simple expression based in the IDD model⁶ is thereby derived where R_1 and R_0 are the limiting resistances which can be normalized by the resistance step ($R_1 - R_0$)

$$\frac{R - R_0}{R_1 - R_0} = 1 - \frac{s}{L} \quad (\text{S5})$$

where L and s stands for the sample thickness and the width of the high doping region respectively. The normalized resistance is formulated as a linear function of s giving rise to the expression (S5), that again predicts a linear dependence of the sample resistance with the width of the high doping zone s .

Let us also assume that ions initially accumulate following a narrow distribution near the contact with w standing for the distribution width. The accumulation occurs by effect of the applied electrical field. This ionic accumulation is expected by formation of a diffusion ion layer in the vicinity of the contacts and by very limited interfacial chemical interaction within the experimental time framework. Mobile ions depleted from the layer bulk induce a sort of electronic de-doping, reducing as a consequence the doping level and producing higher resistance. When bias is removed, ions are released and tend to diffuse back to their equilibrium position in such a way that the mean square displacement of the ion distribution enlarges with time. The simple outlined model would entail diffusion takes place in 1D ($\delta = 1$), but the real situation might be more complex with diffusion dimensionality approaching larger values because of the polycrystalline structure. For the sake of simplicity, let's assume that the distribution width spreads by diffusion as

$$w = \sqrt{2\delta Dt} \quad (\text{S6})$$

with D accounts for the ion diffusion coefficient, $\delta = 1$ for 1D diffusion, and t is the time. Equation S6 informs on how the high doping region width s extends within the perovskite layer bulk as the ion distribution spreads to attain initial homogeneity.

An additional component of the model concerns the relation between the width of the high doping zone s and the spread of the ion distribution w . For a Gaussian distribution,

one can observe that nearly 99% of the ions concentrates within $3w$ as to assume that $s = 3w$. We recognize that this is in fact an oversimplification of a complex problem that should include concrete ion distributions and how they influence the local doping density. In any case, one can derive a simple linear expression for the variation of the resistance that suffices for our purposes.

By combining Equation (S5) and (S6), and $\delta = 1$ an expression for the time dependence of the normalized resistance step results as

$$\frac{R - R_0}{R_1 - R_0} = 1 - \frac{3\sqrt{2Dt}}{L} \quad (\text{S7})$$

which predicts a linear dependence as $\propto \sqrt{t}$ with slope determined by the diffusion coefficient. One can also obtain a value for the ion diffusion coefficient by assuming the Einstein's relation, equation

$$\mu_{ion} = \frac{q D_{ion}}{k_B T} \quad (\text{S8})$$

where q is the elementary charge, k_B stands for the Boltzmann constant, and T is the absolute temperature. It's important to mentioned that due to the simplicity related to the model, a deviation occurs at shorter times, presumably unable to capture second order depolarization effects for greater moving ion concentrations.

S3. Ballistic-like voltage-dependent mobility (BVM) model of space-charge-limited current (SCLC)

In the classic mobility regime of SCLC, the drift velocity is a function of the electric field ξ and the bias- and space-independent constant mobility μ as

$$v_d = \mu_0 \xi \quad (\text{S9})$$

Equation (S9) results in the Mott-Gurney law¹⁴ where the current density is quadratic with the external applied voltage ($J \propto V^2$), the electrostatic potential behaves with the position as $\varphi \propto x^{3/2}$ and the time of flight can be approximated to $\tau_{tof} \propto V^{-2}$.

In the BVM model,¹⁵ the mobility is taken as function of the field, and thus the bias, as

$$\mu_0 = \mu \sqrt{\frac{V_0}{L\xi}} \quad (\text{S10})$$

where L is the distance between electrodes, V_0 is the onset voltage for the BVM regime, μ is the threshold mobility for the transition between ohmic and SCLC regime and the absolute field value is considered as $|\xi| = |d\varphi/dx|$ at each position x in between the electrodes and $|\xi| \approx V/L$ at the active electrode. A deduction with an expression for V_0 is presented in the original publication¹⁵ under two main assumptions: (i) the larger L_i the larger μ , where L_i is Frenkel's equation¹⁶ for the distance between the ions and their local potential maxima upon application of an external field; and (ii) the smaller L_D the larger μ , where L_D is a Debye length for the accumulation of mobile ions towards the electrodes.

By substituting Equation (S10) in (S9), the BVM drift velocity results as

$$v_d = \mu \sqrt{\frac{V_0}{L}} \xi \quad (\text{S11})$$

Equation (S10) can also be approximated as a particular case of Poole-Frenkel¹⁶⁻¹⁸ ionized-trap-mediated transport when field dependent charge carrier density $n \propto \xi$ and for narrow ranges of ξ .¹⁵ Furthermore, Equation (S10) can be substituted in the expression for the associated total current density

$$J = Q n v_d \quad (\text{S12})$$

where Q charge. Taking N from equations (S12) and (S10), the Poisson equation can be solved for $v_d \propto (d\varphi/dx)^{1/2}$ trend such as that of Equation (S10), which results in a potential

$$\varphi = \frac{3}{5} \left(\frac{3}{2}\right)^{\frac{2}{3}} \left(\frac{J}{\epsilon_0 \epsilon_r \mu \sqrt{V_0}} \sqrt{\frac{L}{V_0}}\right)^{\frac{2}{3}} x^{\frac{5}{3}} \quad (\text{S13})$$

The possible effect of a potential as Equation (S13) is presented in Figure S11. Moreover, after evaluating Equation (S13) at $x = L$ where $\varphi = V$, and since $\sqrt{500/243} \approx \sqrt{2}$, the current density results

$$J = \frac{\epsilon_0 \epsilon_r \mu}{L^3} \sqrt{2V_0} V^{3/2} \quad (\text{S14})$$

where ϵ_0 is the vacuum permittivity and ϵ_r the dielectric constant. Subsequently, from the definition of time of flight

$$\tau_{tof} = \frac{L}{v_d} \quad (\text{S15})$$

one can substitute (S14) and (S12) in (S15) to obtain the BVM approximation of the time of flight as

$$\tau_{tof} = \frac{9L^4 QN}{4\epsilon_0 \epsilon_r \mu \sqrt{V_0}} V^{-3/2} \quad (\text{S16})$$

where N is now an effective homogeneous charge carrier density. Typical τ_{tof} values of the BVM model are presented in Figure 3a of the main manuscript.

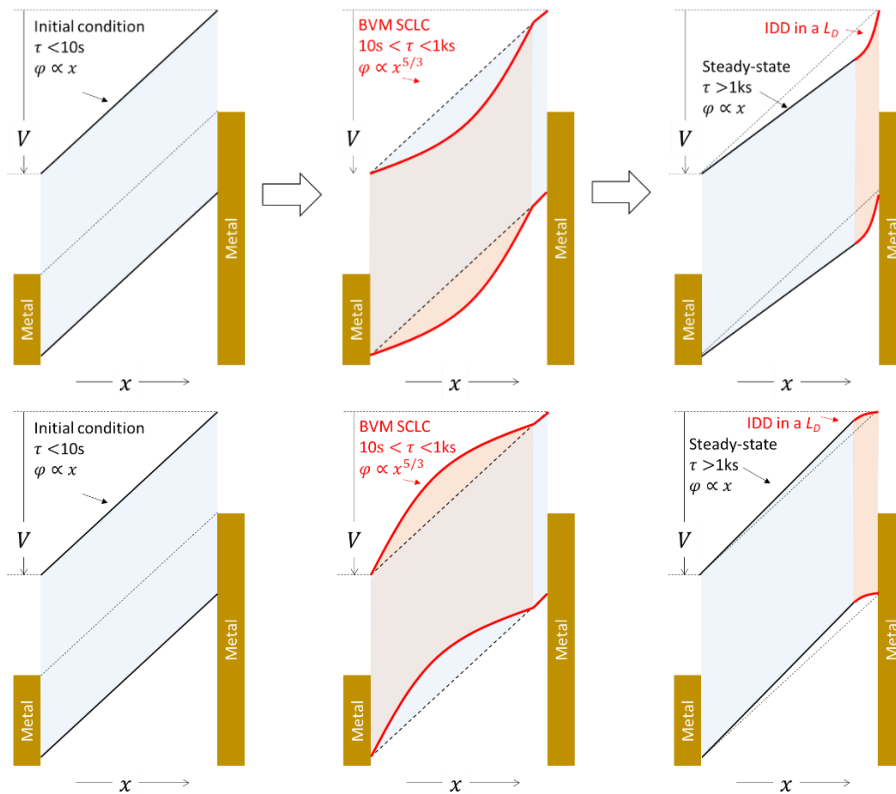


Figure S11. Proposed energy diagram of the evolution of transport for electron (top) and hole (bottom) charge carriers. From an initially ohmic behaviour, the mobile ions modify the space charge to create BVM SCLC within characteristic times \sim ks and subsequently pile up towards the electrodes resulting in a bulkily ohmic transport eased by interface ionic dynamic doping.

References

1. Musiienko, A.; Pipek, J.; Praus, P.; Brynza, M.; Belas, E.; Dryzhakov, B.; Du, M.-H.; Ahmadi, M.; Grill, R., Deciphering the Effect of Traps on Electronic Charge Transport Properties of Methylammonium Lead Tribromide Perovskite. *Sci. Adv.*, **6**, eabb6393.
2. Li, C.; Guerrero, A.; Huettner, S.; Bisquert, J., Unravelling the Role of Vacancies in Lead Halide Perovskite through Electrical Switching of Photoluminescence. *Nat. Commun.* **2018**, *9*, 5113.
3. Senocrate, A.; Moudrakovski, I.; Kim, G. Y.; Yang, T. Y.; Gregori, G.; Grätzel, M.; Maier, J., The Nature of Ion Conduction in Methylammonium Lead Iodide: A Multimethod Approach. *Angew. Chem., Int. Ed.* **2017**, *56*, 7755.
4. Bertoluzzi, L.; Belisle, R. A.; Bush, K. A.; Cheacharoen, R.; McGehee, M. D.; O'Regan, B. C., In Situ Measurement of Electric-Field Screening in Hysteresis-Free Ptaa/Fa0.83cs0.17pb(I0.83br0.17)3/C60 Perovskite Solar Cells Gives an Ion Mobility of $\sim 3 \times 10^{-7}$ Cm²/(V S), 2 Orders of Magnitude Faster Than Reported for Metal-Oxide-Contacted Perovskite Cells with Hysteresis. *J. Am. Chem. Soc.* **2018**, *140*, 12775.
5. Yuan, Y.; Chae, J.; Shao, Y.; Wang, Q.; Xiao, Z.; Centrone, A.; Huang, J., Photovoltaic Switching Mechanism in Lateral Structure Hybrid Perovskite Solar Cells. *Adv. Energy Mater.* **2015**, *5*, 1500615.
6. García-Batlle, M.; Deumel, S.; Huedler, J. E.; Tedde, S. F.; Guerrero, A.; Almora, O.; Garcia-Belmonte, G., Mobile Ion-Driven Modulation of Electronic Conductivity Explains Long-Timescale Electrical Response in Lead Iodide Perovskite Thick Pellets. *ACS Appl. Mater. Interfaces* **2021**, *13*, 35617-35624.
7. Yang, T.-Y.; Gregori, G.; Pellet, N.; Grätzel, M.; Maier, J., The Significance of Ion Conduction in a Hybrid Organic-Inorganic Lead-Iodide-Based Perovskite Photosensitizer. *Angew. Chem., Int. Ed.* **2015**, *54*, 7905-7910.
8. Peng, W.; Aranda, C.; Bakr, O. M.; Garcia-Belmonte, G.; Bisquert, J.; Guerrero, A., Quantification of Ionic Diffusion in Lead Halide Perovskite Single Crystals. *ACS Energy Lett.* **2018**, *3*, 1477-1481.
9. García-Batlle, M.; Baussens, O.; Amari, S.; Zaccaro, J.; Gros-Daillon, E.; Verilhac, J.-M.; Guerrero, A.; Garcia-Belmonte, G., Moving Ions Vary Electronic Conductivity in Lead Bromide Perovskite Single Crystals through Dynamic Doping. *Adv. Electron. Mater.* **2020**, *6*, 2000485.
10. Amari, S.; Verilhac, J.-M.; Gros D'Aillon, E.; Ibanez, A.; Zaccaro, J., Optimization of the Growth Conditions for High Quality Ch₃nh₃pbbr₃ Hybrid Perovskite Single Crystals. *Crystal Growth & Design* **2020**, *20*, 1665-1672.
11. Makuła, P.; Pacia, M.; Macyk, W., How to Correctly Determine the Band Gap Energy of Modified Semiconductor Photocatalysts Based on Uv-Vis Spectra. *J. Phys. Chem. Lett.* **2018**, *9*, 6814-6817.
12. Baussens, O.; Maturana, L.; Amari, S.; Zaccaro, J.; Verilhac, J.-M.; Hirsch, L.; Gros-Daillon, E., An Insight into the Charge Carriers Transport Properties and Electric Field Distribution of Ch₃nh₃pbbr₃ Thick Single Crystals. *Appl. Phys. Lett.* **2020**, *117*, 041904.
13. Tisdale, J. T.; Muckley, E.; Ahmadi, M.; Smith, T.; Seal, C.; Lukosi, E.; Ivanov, I. N.; Hu, B., Dynamic Impact of Electrode Materials on Interface of Single-Crystalline Methylammonium Lead Bromide Perovskite. *Adv. Mater. Interfaces* **2018**, *5*, 1800476.
14. Mott, N. F.; Gurney, R. W., *Electronic Processes in Ionic Crystals*; Clarendon Press: California, USA, 1940.

15. Almora, O.; Miravet, D.; García-Batlle, M.; Garcia-Belmonte, G., Ballistic-Like Space-Charge-Limited Currents in Halide Perovskites at Room Temperature. *Appl. Phys. Lett.* **2021**, *119*, 242107.
16. Frenkel, J., On Pre-Breakdown Phenomena in Insulators and Electronic Semiconductors. *Phys. Rev.* **1938**, *54*, 647-648.
17. Sze, S. M.; Ng, K. K., *Physics of Semiconductor Devices*, 3rd ed.; John Wiley & Sons: Hoboken, New Jersey, USA, 2007, p 832.
18. Murgatroyd, P. N., Theory of Space-Charge-Limited Current Enhanced by Frenkel Effect. *J. Phys. D: Appl. Phys.* **1970**, *3*, 151-156.

Chapter 7: Publication 4

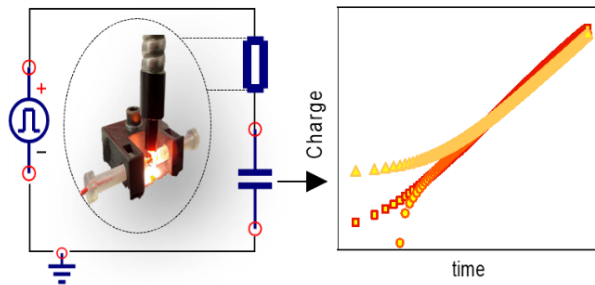
Marisé García-Battle, Waqas Zia, Clara A. Aranda, Michael Saliba, Osbel Almora, Antonio Guerrero, Germà Garcia-Belmonte, Observation of Long-Term Stable Response in MAPbBr₃ Single Crystals Monitored through Displacement Currents under Varying Illumination. **2022**. *Sol. RRL* 2200173. <https://doi.org/10.1002/solr.202200173>

7.1 Candidate's contribution

Nature of Contribution	Extent of Contribution
<ul style="list-style-type: none"> • Growth of the single crystal's samples • Contributed to UV-absorbance, XRD PL, and SEM analysis. • Carried out all the charging transients' measurements • Contributed to interpretation of the results • Wrote first draft of the manuscript • Contributed to the reply to the referees 	60 %

7.2 Brief summary

A fundamental difference is reported here when flowing currents are registered either directly or indirectly using an induced potential across a SCs sample of MAPbBr₃ perovskite. Displacement currents are monitoring by the use of different reference capacitors C_0 . A better understanding of the charging mechanisms at the contacts and the surface carrier kinetics is provided. We highlight the need of a robust and reliable electrical setup establishing the steady-state current across the device to further progress into the halide perovskite device physics and operating modes.



7.3 Published manuscript

Observation of Long-time Stable Response in MAPbBr₃ Single Crystals Monitored through Displacement Currents under Varying Illumination

Marisé García-Batlle^{1*}, Waqas Zia,^{2,3} Clara Aranda,^{2,3} Michael Saliba,^{2,3} Osbel Almora¹, Antonio Guerrero¹, and Germà Garcia-Belmonte^{1*}

¹*Institute of Advanced Materials (INAM), Universitat Jaume I, 12006 Castelló, Spain*

²*Institut für Photovoltaik (ipv), Sekretariat Pfaffenwaldring 47, 70569 Stuttgart, Germany*

³*Helmholtz Young Investigator Group*

*Email: garciag@uji.es, batlle@uji.es

Keywords: halide perovskites, impedance spectroscopy, transient experiments, direct current

5 October 2022

Abstract

Long-life of perovskite devices in working conditions remains as the bottle-neck for technology application. Stable charge carriers' transport together with non-reactive contact materials contribute to the increase of the device operation time. Still an appropriate model for transport carrier mechanisms is needed because of the complex ionic-electronic interplay. In this work, methylammonium lead bromide perovskite single crystals are used to analyze the current flowing across the perovskite sample after biasing. Two methods are performed: (i) direct measurement using an amperemeter and (ii) indirect method by means of an induced potential in a reference capacitor. Because of the continuity of the current, the latest method measures direct current through the sample by monitoring displacements currents. Intriguing features are observed: the displacement currents result in stable and highly reproducible responses for long-time biasing (~2000 s), while the direct measurements produce larger and exponentially-raising current dependence on time. These findings highlight

the nontrivial effect of contacting and measuring procedures in exploring thick perovskite electrical response.

Introduction: Perovskite materials have exceptional properties such as high carrier mobility,¹ long diffusion lengths, strong solar absorption, low non-radiative carrier recombination rate as well as facile fabrication.² They have been successfully used in many optoelectronic applications, such as solar cells, lasers, LEDs or sensors.³ Recently, metal halide perovskite single crystals (SCs) have attracted great attention as high efficiency photodetectors.⁴⁻⁷ Their unique combination of semiconducting properties and the large cross section for energetic photon as well as specific detectivity⁸ make them highly attractive candidates for X- and γ - rays detection.

However, long-time operation requires stable charge carrier transport properties to optimize charge collection and increase spatial resolution.⁹ Previous studies with perovskite SCs have reported that ions migrate under an external electric field causing the accumulation of mobile ionic species at the interfaces. This modulates the net built-in electric field, changing the injection barriers for electronic carriers.¹⁰⁻¹¹ The presence of moving ions modifies the current-voltage curves in perovskite solar cells, in addition to electronic mechanisms.¹²⁻¹⁴ In particular, slow redistribution of ions are responsible for the hysteretic behavior.¹⁵⁻¹⁶

Because of the recognized influence of ion migration, several hypotheses have been suggested to distinguish ionic from electronic contributions to the measured current density flowing across the samples.^{11, 17-21} Moreover, ionic transport has been investigated by different methods.^{9, 18, 22-23} Nevertheless, there are no conclusive evidence nor consensus on the most appropriate model when the analysis of direct current is addressed.²⁴⁻²⁶ Very recently, the use of a guard ring electrode configuration,²⁷ which avoids recollection of crystal surface currents, has allowed to identify bulk transport up to ten times lower than surface contributions.²⁸ Those last findings may indicate a dependence of measured current on the contact configuration and registering method.

Here, we select perovskite SCs of methylammonium lead bromide (MAPbBr₃), which exhibit environmental stability,²⁹⁻³⁰ symmetrically contacted with Pt electrodes. By using this configuration, the effects of grain boundaries and internal interfaces can

be discarded and, more importantly, the less reactive Pt metal is used,³¹⁻³² compared to Au, Ag or even Cr, that react with the perovskite layer, reducing irreversible degradation.³³ Pt contacts have been already employed for highly-sensitive, long-term stable X-ray imaging systems.³⁴ Due to the contacting symmetrical configuration, the perovskite layer is not subject to any internal built-in potential that would otherwise afflict contact metals with different work functions.³⁵

The experimental procedure to study current mechanisms is based on transient charging signals. Our measurements record displacement currents i_{dis} in a reference capacitor C_0 , as sketched in Fig. 1a, induced by the direct current i_{dir} flowing through the sample. This method monitors the voltage V_0 across C_0 such that the charge at the reference capacitor results as $Q = C_0 V_0$. Because the current continuity, $i_{dir} = i_{dis}$ at any time. This method is in contrast to the measurement of direct currents as depicted in Fig. 1b using an amperemeter. Although it would be expected that both techniques monitor similar transport properties (electrical current through thick MAPbBr₃ SCs), it is observed here significant differences between the time evolution and level of the current depending on the measuring method. While the use of the reference capacitor set-up results in highly stable responses for long-time biasing (~2000 s), the direct measurements produce larger and more-featured current dependence on time. Our findings shed new light on the otherwise elusive analysis of electrical properties of perovskite materials, highlighting the nontrivial effect of contacting and measuring procedures.

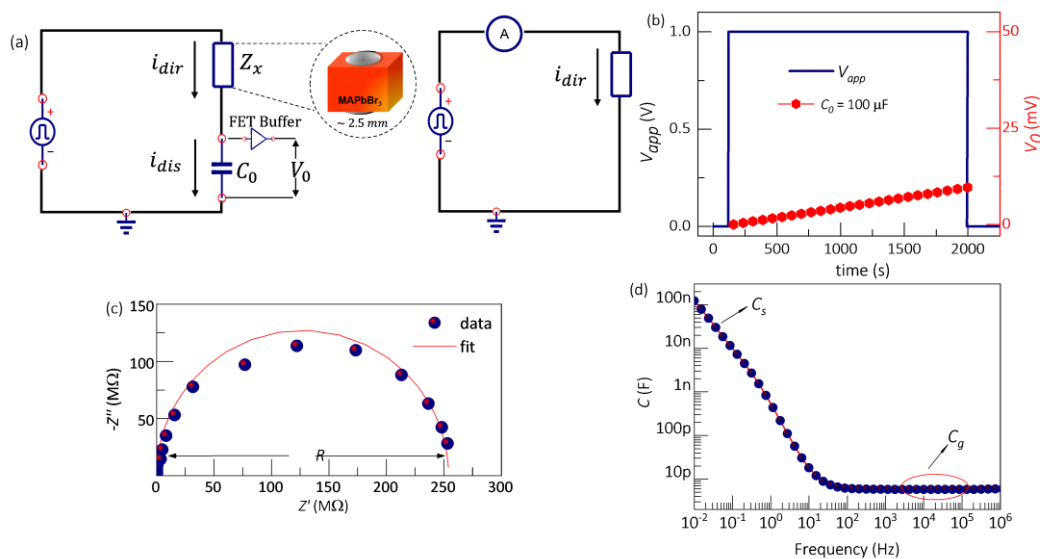


Figure 1. a) Experimental setup used to record charge transient measurements (*left*) and direct electronic currents (*right*) of a 2 mm-thick MAPbBr₃ SCs. b) Charge transient response of a ~ 2 mm thick MAPbBr₃ SCs in the dark conditions. Note that the applied rectangular pulse (V_{app}) of 1 V-height is compared with the induced voltage V_0 (note the scale differences) c) Impedance response and d) capacitance spectrum of a 2 mm-thick MAPbBr₃ SCs, measured at 0 V-bias in dark. Fig S10 in the Supporting Information shows the equivalent circuit used to fits the impedance spectra

Results and discussion: In Fig. S1 we show the general electrical behavior of a single-crystal perovskite sample of MAPbBr₃. The ohmic character (slope ~ 1) observed in the i - V curve is remarkable and agrees with some previous studies of symmetrical SCs perovskite-based devices,^{9, 11, 36-37} but not necessarily true for longer times.¹⁰ Note that the typical measuring time of the i - V curve characteristics situates at ~ 100 s. Fig 1(a) shows the configuration of the set-up circuit for the measurement of charge at the reference capacitor. Here a step voltage pulse (V_{app}) is applied to the sample Z_x (which is modelled by a parallel combination of C_x and R_x) across a linear reference capacitor C_0 , with both elements in series connection. Here C_x and R_x account for the low-frequency capacitance and shunt resistance of the sample, respectively. The analysis is meaningful if applied voltage principally drops within the perovskite sample, i.e. $V_0 \ll V_{app}$. This is accomplished when $C_0 \gg C_x$ and the measuring time is restricted to $t \ll R_x C_0$ (see transfer function in Sec. 2 of the Supporting Information). Thereupon, the charge storage in C_0 is $Q = C_0 V_0$, being V_0 the voltage at the reference capacitor (see Fig. 1b), which is recorded through an

ultrahigh input resistance unity gain field-effect-transistor buffer with 10 T Ω to avoid loading effects from the recording instrument. As observed in Fig. 1b, the voltage at C_0 follows the bias perturbation steps by just a small amount. It is worth noting that displacement current in the reference capacitor equals the current flowing in the sample for $t \gg R_x C_x$. Hence a simple calculation (see Sec. 2 in the SI) allows deriving the induced charge Q in C_0 as $Q(t) = V_{app}(1 - e^{-t/R_x C_0})/R_x$ that for shorter times simply results in $Q(t) = V_{app}t/R_x$. In other words, our procedure allows indirectly measuring the current through the sample as $i = V_{app}/R_x$ that is simply integrated in C_0 .

An estimation of the elements R_x and C_x can be derived from the impedance and capacitance spectra, registered at zero bias of MAPbBr₃ SCs s shown in Fig. 1c, d. The trends exhibited agree with prior measurements in SCs reported in previous works.¹⁰⁻¹¹ From the impedance spectra [Fig1(c)], one can observe at high and intermediate frequencies ($f > 100$ Hz) the sample shunt resistance R and the geometrical capacitance $C_g \approx 6.3$ pF dominate the response, in the Nyquist plot this can be identified as a semicircle through the parallel combination RC_g . However, a low-frequency feature is observed by analyzing the capacitance response, which is commonly known as excess capacitance C_s .³⁸⁻³⁹ This excess capacitance $C_s \gg C_g$ accounts for the increase in charge density near the interfaces, and it exceeds by several orders of magnitude that occurring in the bulk. In the dark, this low frequency capacitance exhibits a thickness-independent trend and has been related to ionic polarization/dynamics within the material.³⁸⁻⁴⁰ Note, however, that the actual R_x and C_x may slightly differ from the values $C_s \approx 100$ nF and $R \approx 250$ M Ω because of the dissimilar explored time window. In any case, the time constant $R_x C_x \approx 100$ s, much shorter than the measuring times used here.

Figure 2(a) shows the charge transients signals obtained in the dark using the setup in Fig. 1(a) and reference capacitors within the range of $C_0 = 1 - 470$ μ F, which were previously checked using impedance analysis (see Fig. S6). For the reference capacitors spectra, one can observe a plateau at the frequencies ($f < 1$ kHz) which is the region of interest. By analyzing the voltage response in Fig. S5 upon application of 1 V-bias step, it is inferred that V_0 inversely scales with the reference capacitor, as

expected. The condition $V_0 \ll V_{app}$ is accomplished in this case when V_0 attains values $\ll 1$ V. By examining Fig. S7(a), the polarization charge $Q = C_0 V_0$ results independent on the reference capacitor when $C_0 < 10 \mu\text{F}$. Lower capacitance values do not assure that the applied voltage principally drops within the perovskite sample, because the condition $t \ll R_x C_0$ is no longer accomplished. Therefore, using larger values of C_0 all response curves collapse in most of the transient for the explored time windows (up to 2000 s). From the estimations of the long-time accumulated charge Q_{Lt} , in Fig S7(b), one can see that it attains values within the range of ~ 1100 nC (after ~ 2000 s). Note that lower charge values are encountered for smaller values of C_0 as expected. It is then concluded here that the charge induced in the reference capacitor stems from the perovskite shunt resistance upon long-time (~ 2000 s) biasing, as demonstrated by the collapse of the transient charge signals as far as $C_0 > 10 \mu\text{F}$. High reproducibility is also noticed despite long-time biasing periods. Recalling now the impedance spectra in Fig. 1(d), a geometrical capacitance $C_g \approx 5$ pF and a bias $V_{app} = 1$ V in dark condition implies a charge $Q_b = C_g V_{app}$ approximately equal to 5 pC, which does not match those encountered from Fig. S7. Such a huge value ($Q \sim 1100$ nC) cannot be linked then to the polarization of the perovskite bulk.

Now let us analyze the charge transient signal under an irradiance intensity of 100 mW cm^{-2} (see Fig. S8). As inferred from our previous results in dark condition, the use of a large enough reference capacitor ensures that the voltage mainly drops at the perovskite SCs. Under illumination, only values of $C_0 > 100 \mu\text{F}$ can be used to obtain coherent transient measurements (collapse of the charge transient into a single response) as observed in Fig. 2a. By comparing the charging transient response, both in dark and light in Fig. 2a, one can infer a good linear relationship between Q and t for the time window explored. By fitting, it is parameterized as $Q(t) = it$ as previously derived with slope 1. Therefore, a value for the constant charging current i results in (0.51 ± 0.06) nA in the dark and (4.87 ± 0.03) nA under continuous light irradiation. It is inferred then that light enhances current through the perovskite sample by reducing the shunt resistance (photoresistive effect) by approximately one order of magnitude. More importantly, one can state that both dark and light currents exhibit an extremely stable and reproducible response, in contrast to that obtained through direct current analysis as next explained.

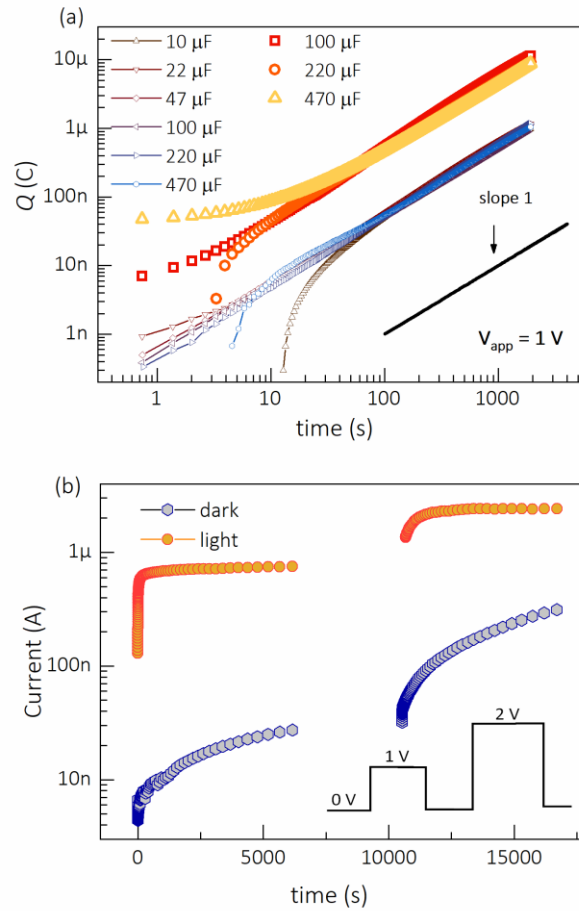


Figure 2. a) Comparison between the charge transient response in the dark condition with the charge transient response in light condition (100 mW cm^{-2}) under 1 applied bias. The solid black line corresponds to an allometric fit (slope 1). b) Electronic currents transient response in the dark and light conditions upon two different biases for a $\sim 2.5 \text{ mm}$ thick MAPbBr_3 SCs sample. Noted that the electronic current exponentially rises until steady-state values upon a biasing protocol (in the inset) at long times.

To elucidate the origin of those currents measured by dielectric displacement at C_0 , we explore electronic currents plotted in Fig. 2b, in which the long-time current response upon the direct application of voltage steps to the sample in dark conditions are shown. The general protocol of measurement in Fig. 2b is based on previous reports,¹⁰ once the crystals are polarized for 3 hours, are then left to relax at 0 V for 2 hours. As recently reported, direct currents originate from a drift of electronic species kinetically controlled by migrating ions.¹⁰ However, a significant difference appears in comparison to the charging method: currents are no longer constant but increase

with time. For times of ~ 2000 s and 1 V-bias, electronic dark current achieves values approximately equal to 10 nA, much greater than that registered through C_0 . If charge transients are programmed for even longer time (see Fig. S9), the same linear relationship is still observed. Under illumination, the differences are even larger: direct measurement attains ~ 800 nA while the reference capacitor set-up yields only ~ 5 nA. We note then that the measurement of induced potentials, which registers displacement currents in C_0 and, indirectly, constant current across shunt resistor. Our findings point to the significant influence of the method employed for charge extraction at the contacts that enlarge recombination currents. This is suggested by the drastic reduction in measured current under illumination when the reference capacitor set-up is used in comparison with the direct one. While long-range flowing current is reduced by a factor of 20 with the capacitor set-up, under illumination that suppression attains even larger values ($i_{dir}/i_{dis} \sim 160$). Those comparisons move us to conjecture about the different charging nature of the contacts. In one case (direct current measurement), low contact is directly grounded what assures sufficient and rapid removing of interfacial charges by the measuring set-up. On the contrary, with the reference capacitor method arriving charges should remain at the contacts (to maintain the measured voltage) which promotes the occurrence of additional mechanism such as enhancement of surface recombination currents. Although our findings are certainly very preliminary and a more systematic analysis is needed, they seem to point out the determining role of the charging at the contacts (interfacial carrier density) to establish the steady-state current flow. We can even propose a change in the current-governing process: capacitor set-up effectively registers minimum bulk conduction currents resulting after large surface carrier recombination, while direct measurement does not activate such as interfacial mechanisms and produces, as a consequence, larger measured currents.

Summary: A fundamental difference is reported here when flowing currents are registered either directly or indirectly using an induced potential. The use of the reference capacitor set-up suppresses direct current by monitoring exclusively displacements currents in C_0 . This is corroborated by the collapse of the charge transients, in which the polarization voltages stem from current flowing through the shunt resistance. Under illumination, excess electronic carriers are generated then

enlarging currents by a photoresistive effect. Our findings alert us on the variability in the measured electrical current across the sample depending on the experimental method, which may be used to guide us in the pursuit of a robust electrical model that accounts for contact mechanisms (at the end responsible of the measured electrical characteristics in perovskite-based devices) in addition to bulk conduction. A better understanding of the charging mechanisms at the contacts and how the surface carrier kinetics intervene in establishing the steady-state current allows us to progress into the halide perovskite device physics and operating modes.

Experimental Section: Solution Growth: All materials used for the preparation of the SCs were used as received: $\text{CH}_3\text{NH}_3\text{Br}$ (> 99 wt. %) and PbBr_2 (99.999 wt. %) was purchased from Dyesol and TCI America, respectively, dimethylformamide (DMF) (anhydrous, 99.8 wt. %) were purchased from Sigma-Aldrich. Salts were stored in a glovebox under N_2 atmosphere. Among the different methods for the growth of MAPbBr_3 SCs, the Inverse Temperature Crystallization (ITC) in DMF was used through which the obtained SCs exhibit a cubic shape, see Fig S1 inset, that makes them suited for the fabrication of devices. For the growth experiments, the perovskite precursors, $\text{CH}_3\text{NH}_3\text{Br}$, PbBr_2 were dissolved (1:1 mol. %) in DMF to obtain 1 M solutions of MAPbBr_3 . All the solutions were first maintained at room temperature under stirring and then, filtered using PTFE filters with 0.2 μm pore size to remove any insoluble particles. Two growth protocols were investigated labeled as fast/unseeded and slow/seeded growth. The process was similar to the one described in a previous work³⁶ using a linear temperature ramp. Seeds must be first obtained by spontaneous nucleation and used subsequently for crystal growth, the quality of the seed depends on the geometry of the vials and the temperature profile. For the fast/unseeded protocol, derived from the ITC method,^{36, 41} 3 mL of perovskite solutions are placed in 20 mL glass flask vial, using a silicon oil bath, the temperature is abruptly brought from room to 80-85 °C leading to the spontaneous nucleation and growth of crystals. In the slow/seeded procedure, the heating temperature profile is crucial. With the same perovskite solution, the temperature is first increased at 50 °C, and then is kept for 20 mins at this temperature to place the seeds inside the flasks to avoid dissolving the seed. Finally, the solution is heated up, at a constant heating rate

of 10 °C/h for 3 hours, until 80-85 °C. The crystals obtained are washed with warm DMF, then, placed in the vial, and transferred to the dry box with a nitrogen atmosphere. In the end, SCs were mechanically polished with three different sandpaper [P1200 (15 μm), P2400 (10 μm) and P4000 (5 μm)] and Pt electrodes were sputtered at two opposite faces.

Device preparation and optical characterization: Interface-mediated mechanisms are recognized to constitute issues of primary concern at the perovskite/metal electrode interface.⁴² It has been reported that Platinum is a preferably significantly inert material which does not react with the perovskite films.⁴³⁻⁴⁴ Then, Pt was sputtered (~30 nm) at opposites sides of the SCs and Au was thermally evaporated (100 nm) on top of Pt, at 6×10^{-6} mbar, to protect the metallic contact. The SCs were characterized by UV-vis absorption spectra in Cary 500 Scan VARIAN spectrophotometer (250-900 nm), obtaining the distinctive spectra with the corresponding absorption edge at for MAPbBr₃ with a bandgap of 2.18 eV (see Tauc plot, inset Fig. S2). The photoluminescence measurements were collected by a Fluorolog3-11 Horiba, using a 405 nm excitation source, the photoluminescence peak position (~ 570 nm) of MAPbBr₃ is observed in Fig S2 and match the values reported earlier for the same single crystals.^{41, 45} Also, Fig. S3 shows the XRD patterns of MAPbBr₃ obtained with a D8 Endeavor diffractometer equipped with a Johansonn monochromator. The SCs was grinded into powder and measured in Bragg-Brentano θ - 2θ geometry. The diffractogram reveals the standard cubic space group Pm3m of MAPbBr₃ crystals with lattice dimension $a=5.928$ Å, and without any trace of the secondary phase. Using an X-ray diffractometer Agilent Super Nova Atlas Dual Source (Cu-K α , wavelength $\lambda=1.5406$ Å) an XRD-2D rotation spectrum along the α cell axis were measured. In Fig S4 only dots appear, the absence of concentrically distributed circles is a clear sign that the material is not polycrystalline.⁴⁶ For the light condition measurements, a Si photodiode was used to calibrate the system and transient curves were performed under 1 sun illumination (100 mW cm^{-2}) using an OSL2-High-Intensity Fiber-Coupled Illuminator (Thorlabs).

Electrical Measurements: All electrical experiments were performed at room temperature in the air. Direct impedance measurements were carried out by using a PGSTAT-30 Autolab potentiostat equipped with impedance module. Samples were

measured inside a shielded cryostat Alpha dielectric E4991A Novocontrol acting as Faraday cage, in dark conditions between 10 mHz and 1 MHz, with a perturbation amplitude of 1 V. For the charging measurements using a reference capacitor, a source measure unit Keithley Model 2612 was used as the voltage supply and the polarization voltage signals, in Fig. S5, were recorded with a HP Digital Multimeter Model 34401A (input impedance $> 10 \text{ G}\Omega$) coupled through a FET input buffer model AD8244 (input impedance $10 \text{ T}\Omega$). The thicknesses of the samples are around $\sim 2.5 \text{ mm}$, and the evaporated electrodes had an active area of $\sim 13 \text{ mm}^2$. A Broadband Halogen Fiber Optic lamp (150 W High-Output) with an irradiance level of 100 mW cm^{-2} was used.

Supporting Information: see the supporting material for additional information on sample preparation and set-up checking and transfer function calculation.

Data available upon request from the authors.

Acknowledgments

This work has received funding from the European Union's Horizon 2020 research and innovation program under the Photonics Public Private Partnership (www.photonics21.org) with the project PEROXIS under Grant Agreement No. 871336. G.G.-B. acknowledges the financial support from Ministerio de Ciencia e Innovación (Spain) under project No. PID2019-107348GB-100. M. G.-B. acknowledges the support for the research stay from Generalitat Valenciana (BEFPI2020) under the grant number (GRISOLIAP/2018/073). We also acknowledge SCIC from UJI for Pt deposition. Funding for open access charge: CRUE-Universitat Jaume I.

References

1. Green, M. A.; Ho-Baillie, A.; Snaith, H. J., The Emergence of Perovskite Solar Cells. *Nat. Photon.* **2014**, *8*, 506-514.
2. Onoda-Yamamuro, N.; Matsuo, T.; Suga, H., Dielectric Study of $\text{Ch}_3\text{nh}_3\text{pbx}_3$ (X = Cl, Br, I). *J. Phys. Chem. Solids* **1992**, *53*, 935-939.
3. Futscher, M. H.; Gangishetty, M. K.; Congreve, D. N.; Ehrler, B., Quantifying Mobile Ions and Electronic Defects in Perovskite-Based Devices with Temperature-

Dependent Capacitance Measurements: Frequency Vs Time Domain. *J. Chem. Phys.* **2020**, *152*, 044202.

4. Afroz, M. A.; Aranda, C. A.; Tailor, N. K.; Yukta; Yadav, P.; Tavakoli, M. M.; Saliba, M.; Satapathi, S., Impedance Spectroscopy for Metal Halide Perovskite Single Crystals: Recent Advances, Challenges, and Solutions. *ACS Energy Lett.* **2021**, 3275-3286.

5. He, Y., et al., CsPbBr₃ Perovskite Detectors with 1.4% Energy Resolution for High-Energy Γ -Rays. *Nat. Photon.* **2021**, *15*, 36.

6. Liu, Y.; Yang, Z.; Liu, S., Recent Progress in Single-Crystalline Perovskite Research Including Crystal Preparation, Property Evaluation, and Applications. *Adv. Sci.* **2018**, *5*, 1700471.

7. Wei, H., et al., Sensitive X-Ray Detectors Made of Methylammonium Lead Tribromide Perovskite Single Crystals. *Nat. Photonics* **2016**, *10*, 333.

8. Liu, Y., et al., A 1300 Mm² Ultrahigh-Performance Digital Imaging Assembly Using High-Quality Perovskite Single Crystals. *Adv. Mater.* **2018**, *30*, 1707314.

9. Baussens, O.; Maturana, L.; Amari, S.; Zaccaro, J.; Verilhac, J.-M.; Hirsch, L.; Gros-Daillon, E., An Insight into the Charge Carriers Transport Properties and Electric Field Distribution of CH₃NH₃PbBr₃ Thick Single Crystals. *Appl. Phys. Lett.* **2020**, *117*, 041904.

10. García-Batlle, M.; Mayén Guillén, J.; Chapran, M.; Baussens, O.; Zaccaro, J.; Gros Daillon, E.; Verilhac, J. M.; Guerrero, A.; Almora, O.; Garcia Belmonte, G., Coupling between Ion Drift and Kinetics of Electronic Current Transients in MAPbBr₃ Single Crystals. *ACS Energy Lett.* **2022**, *7*, 946–951.

11. García-Batlle, M.; Baussens, O.; Amari, S.; Zaccaro, J.; Gros-Daillon, E.; Verilhac, J. M.; Guerrero, A.; Garcia-Belmonte, G., Moving Ions Vary Electronic Conductivity in Lead Bromide Perovskite Single Crystals through Dynamic Doping. *Adv. Electron. Mater.* **2020**, *6*, 2000485.

12. Tress, W.; Marinova, N.; Moehl, T.; Zakeeruddin, S. M.; Nazeeruddin, M. K.; Grätzel, M., Understanding the Rate-Dependent J–V Hysteresis, Slow Time Component, and Aging in CH₃NH₃PbI₃ Perovskite Solar Cells: The Role of a Compensated Electric Field. *Energy Environ. Sci.* **2015**, *8*, 995-1004.

13. Gottesman, R.; Haltzi, E.; Gouda, L.; Tirosh, S.; Bouhadana, Y.; Zaban, A.; Mosconi, E.; De Angelis, F., Extremely Slow Photoconductivity Response of CH₃NH₃PbI₃ Perovskites Suggesting Structural Changes under Working Conditions. *J. Phys. Chem. Lett.* **2014**, *5*, 2662-2669.

14. Ebadi, F.; Taghavinia, N.; Mohammadpour, R.; Hagfeldt, A.; Tress, W., Origin of Apparent Light-Enhanced and Negative Capacitance in Perovskite Solar Cells. *Nat. Commun.* **2019**, *10*, 1574.
15. Azpiroz, J. M.; Mosconi, E.; Bisquert, J.; De Angelis, F., Defects Migration in Methylammonium Lead Iodide and Their Role in Perovskite Solar Cells Operation. *Energy Environ. Sci.* **2015**, *8*, 2118-2127
16. Eames, C.; Frost, J. M.; Barnes, P. R. F.; O'Regan, B. C.; Walsh, A.; Islam, M. S., Ionic Transport in Hybrid Lead Iodide Perovskite Solar Cells. *Nat. Commun.* **2015**, *6*, 7497.
17. García-Batlle, M.; Deumel, S.; Huedler, J. E.; Tedde, S. F.; Guerrero, A.; Almora, O.; Garcia-Belmonte, G., Mobile Ion-Driven Modulation of Electronic Conductivity Explains Long-Timescale Electrical Response in Lead Iodide Perovskite Thick Pellets. *ACS Appl. Mater. Interfaces* **2021**, *13*, 35617-35624.
18. Peng, W.; Aranda, C.; Bakr, O. M.; Garcia-Belmonte, G.; Bisquert, J.; Guerrero, A., Quantification of Ionic Diffusion in Lead Halide Perovskite Single Crystals. *ACS Energy Lett.* **2018**, *3*, 1477-1481.
19. Wei, D., et al., Ion-Migration Inhibition by the Cation– Π Interaction in Perovskite Materials for Efficient and Stable Perovskite Solar Cells. *Adv. Mater.* **2018**, *30*, 1707583.
20. Unger, E. L.; Hoke, E. T.; Bailie, C. D.; Nguyen, W. H.; Bowring, A. R.; Heumüller, T.; Christoforo, M. G.; McGehee, M. D., Hysteresis and Transient Behavior in Current–Voltage Measurements of Hybrid-Perovskite Absorber Solar Cells. *Energy Environ. Sci.* **2014**, *7*, 3690-3698.
21. Xiao, Z.; Yuan, Y.; Shao, Y.; Wang, Q.; Dong, Q.; Bi, C.; Sharma, P.; Gruverman, A.; Huang, J., Giant Switchable Photovoltaic Effect in Organometal Trihalide Perovskite Devices. *Nat Mater* **2015**, *14*, 193-8.
22. Afroz, M. A.; Aranda, C. A.; Tailor, N. K.; Yukta; Yadav, P.; Tavakoli, M. M.; Saliba, M.; Satapathi, S., Impedance Spectroscopy for Metal Halide Perovskite Single Crystals: Recent Advances, Challenges, and Solutions. *ACS Energy Letters* **2021**, 3275-3286.
23. Musiienko, A.; Pipek, J.; Praus, P.; Brynza, M.; Belas, E.; Dryzhakov, B.; Du, M.-H.; Ahmadi, M.; Grill, R., Deciphering the Effect of Traps on Electronic Charge Transport Properties of Methylammonium Lead Tribromide Perovskite. *Sci. Adv.* **2020**, *6*, eabb6393.
24. Futscher, M. H.; Milić, J. V., Mixed Conductivity of Hybrid Halide Perovskites: Emerging Opportunities and Challenges. *Front. Energy Res.* **2021**, *9*.

25. Wang, H.; Guerrero, A.; Bou, A.; Al-Mayouf, A. M.; Bisquert, J., Kinetic and Material Properties of Interfaces Governing Slow Response and Long Timescale Phenomena in Perovskite Solar Cells. *Energy Environ. Sci.* **2019**, *12*, 2054-2079.
26. Duijnste, E. A.; Le Corre, V. M.; Johnston, M. B.; Koster, L. J. A.; Lim, J.; Snaith, H. J., Understanding Dark Current-Voltage Characteristics in Metal-Halide Perovskite Single Crystals. *Phys. Rev. Appl.* **2021**, *15*, 014006.
27. Wei, H.; DeSantis, D.; Wei, W.; Deng, Y.; Guo, D.; Savenije, T. J.; Cao, L.; Huang, J., Dopant Compensation in Alloyed $\text{CH}_3\text{NH}_3\text{PbBr}_3\text{-XCl}_x$ Perovskite Single Crystals for Gamma-Ray Spectroscopy. *Nat. Mater.* **2017**, *16*, 826-833.
28. Almora, O.; Matt, G. J.; These, A.; Kanak, A.; Levchuk, I.; Shrestha, S.; Osvet, A.; Brabec, C. J.; Garcia-Belmonte, G., Surface Versus Bulk Currents and Ionic Space-Charge Effects in Cspbbr_3 Single Crystals. *J. Phys. Chem. Lett.* **2022**, *13*, 3824-3830.
29. Choi, J. I. J.; Khan, M. E.; Hawash, Z.; Kim, K. J.; Lee, H.; Ono, L. K.; Qi, Y.; Kim, Y.-H.; Park, J. Y., Atomic-Scale View of Stability and Degradation of Single-Crystal Mapbbr_3 Surfaces. *J. Mater. Chem. A* **2019**, *7*, 20760-20766.
30. Wang, C.; Ecker, B. R.; Wei, H.; Huang, J.; Gao, Y., Environmental Surface Stability of the Mapbbr_3 Single Crystal. *The Journal of Physical Chemistry C* **2018**, *122*, 3513-3522.
31. Fakharuddin, A.; Schmidt-Mende, L.; Garcia-Belmonte, G.; Jose, R.; Mora-Sero, I., Interfaces in Perovskite Solar Cells. *Adv. Energy Mater.* **2017**, *7*, 1700623.
32. Guerrero, A.; You, J.; Aranda, C.; Kang, Y. S.; Garcia-Belmonte, G.; Zhou, H.; Bisquert, J.; Yang, Y., Interfacial Degradation of Planar Lead Halide Perovskite Solar Cells. *ACS Nano* **2016**, *10*, 218-224.
33. Roose, B.; Wang, Q.; Abate, A., The Role of Charge Selective Contacts in Perovskite Solar Cell Stability. *Adv. Energy Mater.* **2019**, *9*, 1803140.
34. Deumel, S., et al., High-Sensitivity High-Resolution X-Ray Imaging with Soft-Sintered Metal Halide Perovskites. *Nat. Electron.* **2021**, *4*, 681-688.
35. He, Y., et al., High Spectral Resolution of Gamma-Rays at Room Temperature by Perovskite Cspbbr_3 Single Crystals. *Nat. Commun.* **2018**, *9*, 1609.
36. Amari, S.; Verilhac, J.-M.; Gros D'Aillon, E.; Ibanez, A.; Zaccaro, J., Optimization of the Growth Conditions for High Quality $\text{CH}_3\text{NH}_3\text{PbBr}_3$ Hybrid Perovskite Single Crystals. *Cryst. Growth Des.* **2020**, *20*, 1665-1672.
37. Tisdale, J. T.; Muckley, E.; Ahmadi, M.; Smith, T.; Seal, C.; Lukosi, E.; Ivanov, I. N.; Hu, B., Dynamic Impact of Electrode Materials on Interface of Single-Crystalline Methylammonium Lead Bromide Perovskite. *Adv. Mater. Interfaces* **2018**, *5*, 1800476.

38. Almora, O.; Guerrero, A.; Garcia-Belmonte, G., Ionic Charging by Local Imbalance at Interfaces in Hybrid Lead Halide Perovskites. *Appl. Phys. Lett.* **2016**, *108*, 043903.
39. Almora, O.; Zarazua, I.; Mas-Marza, E.; Mora-Sero, I.; Bisquert, J.; Garcia-Belmonte, G., Capacitive Dark Currents, Hysteresis, and Electrode Polarization in Lead Halide Perovskite Solar Cells. *J. Phys. Chem. Lett.* **2015**, *6*, 1645-1652.
40. Caram, J.; García-Batlle, M.; Almora, O.; Arce, R. D.; Guerrero, A.; Garcia-Belmonte, G., Direct Observation of Surface Polarization at Hybrid Perovskite/Au Interfaces by Dark Transient Experiments. *Appl. Phys. Lett.* **2020**, *116*, 183503.
41. Saidaminov, M. I., et al., High-Quality Bulk Hybrid Perovskite Single Crystals within Minutes by Inverse Temperature Crystallization. *Nature communications* **2015**, *6*, 7586.
42. Zhao, L.; Kerner, R. A.; Xiao, Z.; Lin, Y. L.; Lee, K. M.; Schwartz, J.; Rand, B. P., Redox Chemistry Dominates the Degradation and Decomposition of Metal Halide Perovskite Optoelectronic Devices. *ACS Energy Lett.* **2016**, *1*, 595-602.
43. Shaikh, P. A.; Shi, D.; Retamal, J. R. D.; Sheikh, A. D.; Haque, M. A.; Kang, C.-F.; He, J.-H.; Bakr, O. M.; Wu, T., Schottky Junctions on Perovskite Single Crystals: Light-Modulated Dielectric Constant and Self-Biased Photodetection. *J. Mater. Chem. C* **2016**, *4*, 8304-8312.
44. Stumpp, M.; Ruess, R.; Müßener, J.; Schlettwein, D., Freezing the Polarization of $\text{CH}_3\text{NH}_3\text{PbI}_3$ and $\text{CH}_3\text{NH}_3\text{PbI}_3\text{-XCl}_x$ Perovskite Films. *Mater. Today Chem.* **2017**, *4*, 97-105.
45. Shi, D., et al., Low Trap-State Density and Long Carrier Diffusion in Organolead Trihalide Perovskite Single Crystals. *Science* **2015**, *347*, 519-522.
46. Widjonarko, N., Introduction to Advanced X-Ray Diffraction Techniques for Polymeric Thin Films. *Coatings* **2016**, *6*, 54.

7.4 Supplemental Information

Observation of Long-time Stable Response in MAPbBr₃ Single Crystals Monitored through Displacement Currents under Varying Illumination

Marisé García-Batlle^{1*}, Waqas Zia,^{2,3} Clara Aranda,^{2,3} Michael Saliba,^{2,3} Osbel Almora¹, Antonio Guerrero¹, and Germà Garcia-Belmonte^{1*}

¹*Institute of Advanced Materials (INAM), Universitat Jaume I, 12006 Castelló, Spain*

²*Institut für Photovoltaik (ipv), Sekretariat Pfaffenwaldring 47, 70569 Stuttgart, Germany*

³*Helmholtz Young Investigator Group*

*Email: garciag@uji.es batlle@uji.es

5 October 2022

S1 Crystal characterization and electrical response.

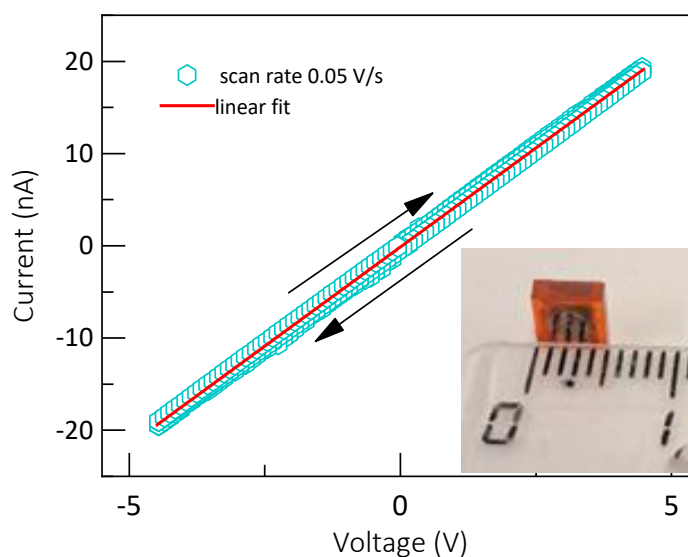


Figure S1. Example of current-voltage response, exhibiting an approximate ohmic behavior within the selected voltage range, of a MAPbBr₃ single crystals of thickness ≈ 2.5 mm. In the

inset: Image of a MAPbBr₃ single crystal symmetrically face-to-face contacted with Pt of dimensions ~5 mm x 5 mm and 2.45 mm-thick

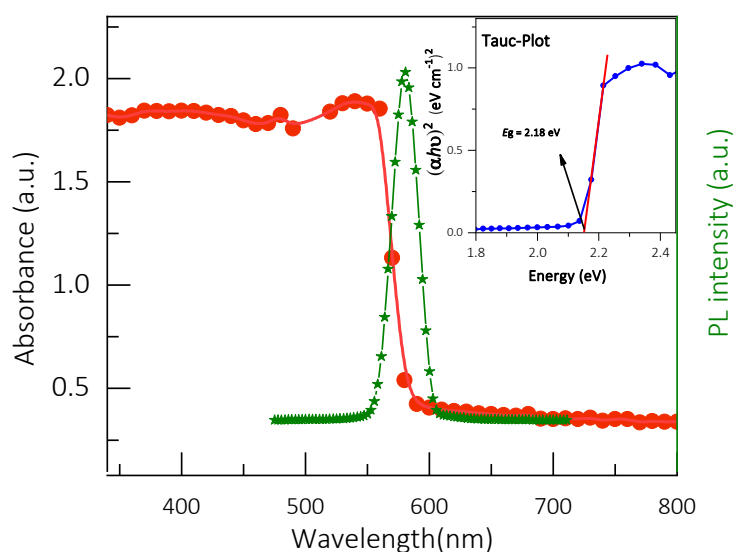


Figure S2. Transmittance and PL spectra ($\lambda_{\text{exc}} = 405$ nm) of MAPbBr₃ SCs via UV-visible spectroscopy (SCs thickness = 2.5 mm). In the inset: Tauc plot of MAPbBr₃ SC for band gap determination ($E_g = 2.18$ eV). This value is in good agreement with those found in the literature¹

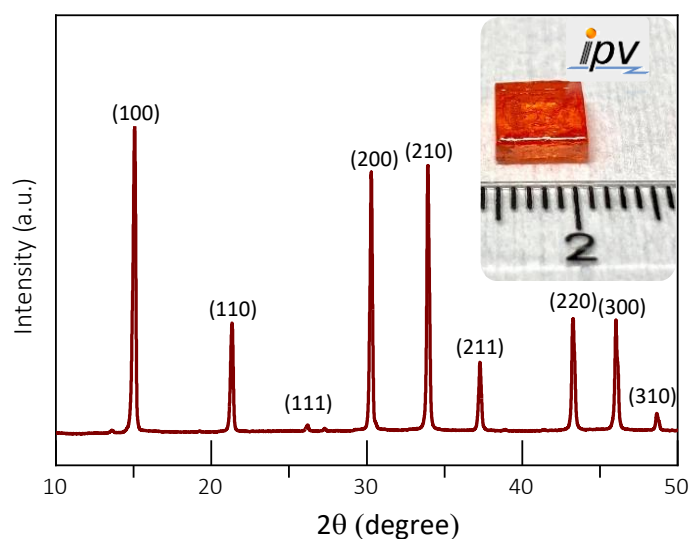


Figure S3. Image of the PXRD diffractogram of MAPbBr₃ SC at 300 K showing cubic crystal lattice (Pm3m space group) and no other parasitic phases. The diffractogram shows the (100), (110), and (200) (210) peaks at 15.0°, 21.21°, and 30.12° and 33.78° respectively. These values are in good agreement with those found in the literature². In the inset: Image of a MAPbBr₃ single crystal

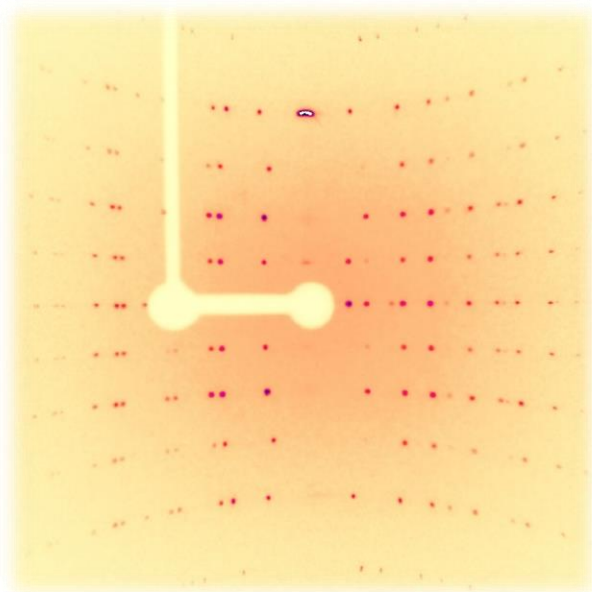


Figure S4. Rotation XRD spectra along α cell axis of a crystal measured with Cu radiation. The absence of concentric circles supports the monocrystalline nature of the crystal.

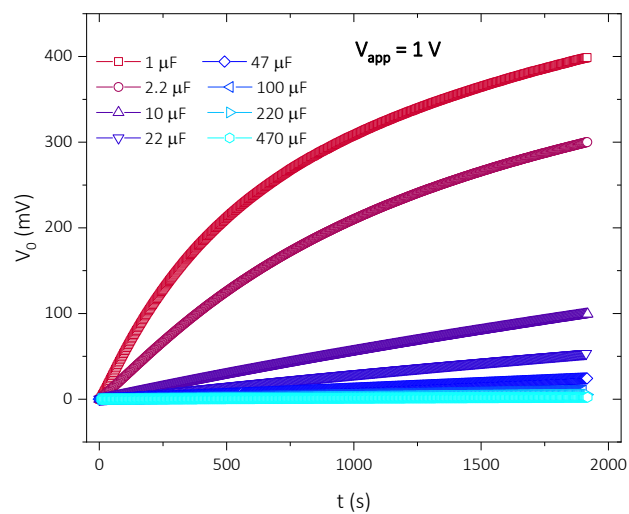


Figure S5. Polarization voltage signals for a MAPbBr SCs with 1 V applied bias in the dark conditions. The reference capacitor ranges $C_0 = 1 - 470 \mu\text{F}$, as indicated.

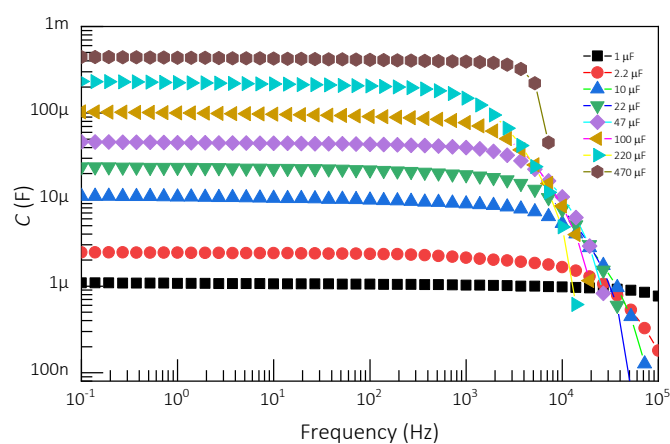


Figure S6. Capacitance spectra of the different reference capacitor used ($C_0 = 1 - 470 \mu\text{F}$) and. Note the plateau at lower frequencies.

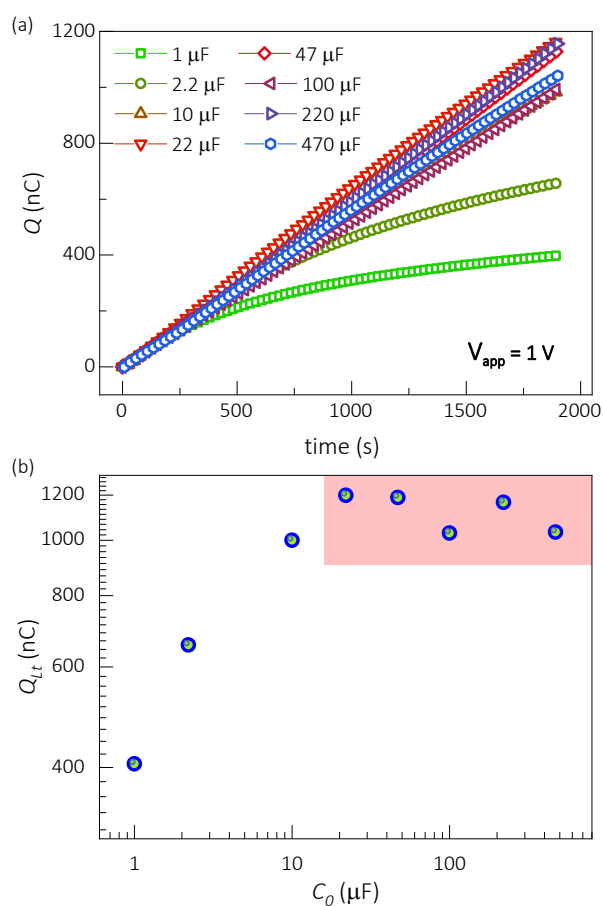


Figure S7. Charge transient signals in dark conditions of a 2 mm-thick MAPbBr₃ SCs under 1 V-bias using a wide-ranging of reference capacitors ($C_0 = 1 - 470 \mu\text{F}$). b) Long-time accumulated charge induced by long-time biasing as a function of the reference capacitor of a 2 mm-thick MAPbBr₃ SCs in dark conditions. Note the average value of Q_{Lt} in the shaded rectangle.

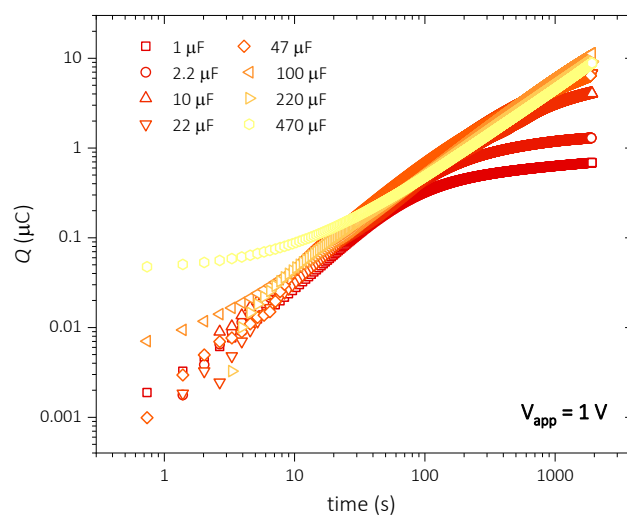


Figure S8. Charge transients for a MAPbBr₃ SCs with 1 V applied bias in the light conditions (100 mW cm^{-2}) induced for long-time poling using different reference capacitors

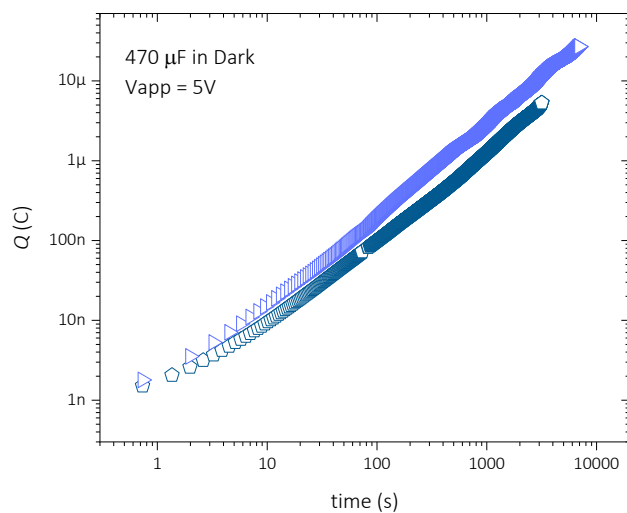


Figure S9. Charge transients for a MAPbBr SCs with 5 V applied bias in the dark conditions induced for long-time poling using a larger reference capacitor.

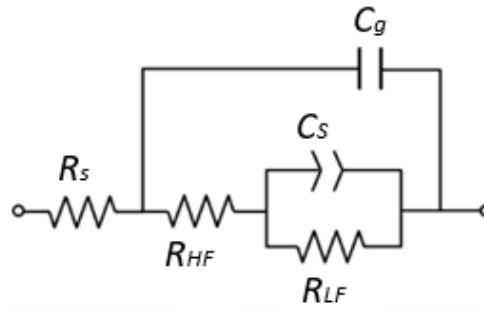
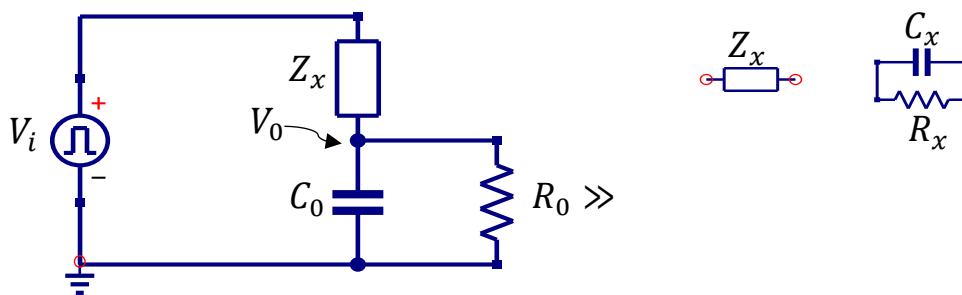


Fig S10: Equivalent circuit used to fit the impedance spectra in Fig 1: with R_s series resistance, C_g geometric capacitance and R_{HF} , and R_{LF} the high-, and low-frequency resistances, respectively. The low-frequency capacitance usually labelled as surface capacitance C_s .

S2 Transfer function

Calculation of the measuring transfer function: A practical model accounting for the time response of the measuring setup is drawn in the following equivalent circuit. As observed this equivalent circuit contains, in addition to the sample low-frequency elements, external elements as the reference capacitor and the voltage source. This circuit explores the low-frequency behavior of the more general equivalent circuit of



Here, $Z_x = R_x || C_x$ being R_x and C_x the perovskite shunt resistance and low-frequency capacitor, respectively ($Z_x = \frac{R_x}{1+j\omega R_x C_x}$), C_0 correspond to the reference capacitor connected in series and R_0 the extremely high input impedance ($10 \text{ T}\Omega$) of the FET buffer. The ratio between the measured voltage V_0 and the applied bias V_i can be explicit as a transfer function that corresponds to an alternating perturbation of frequency ω :

$$\frac{V_0}{V_i} = \frac{1}{\frac{R_x}{1+j\omega R_x C_x} + \frac{1}{j\omega C_0}} \cdot \frac{1}{j\omega C_0}$$

then

$$\frac{V_0}{V_i} = \frac{1 + j\omega R_x C_x}{1 + j\omega R_x (C_x + C_0)}$$

that in the case of $C_0 \gg C_x$, can be approximated to

$$\frac{V_0}{V_i} = \frac{1 + j\omega R_x C_x}{1 + j\omega R_x C_0}$$

and can be plotted as shown in Fig S11

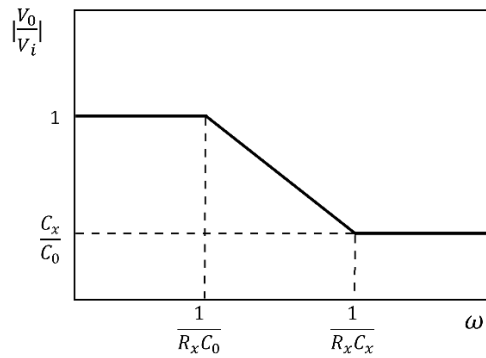


Figure S11. Change of the voltage ratio as a function of the frequency ω , showing the characteristic frequencies of the measuring transfer function.

Therefore, the high-frequency limit corresponds to the ratio C_x/C_0 , as assumed in the main text. The low-frequency limit equals 1, indicating that in the long-time (exciding the measuring time window) V_0 should approach V_i . The important cutoff frequency of the transfer function is determined by the time constant $R_x C_0$, that in our experiments result in orders of magnitude longer than the time scale of the saturated signal.

To conclude, for times approaching $\sim R_x C_0$ the charging transient at C_0 follows the exponential trend, which indicates the exponential charging of the reference capacitor through the sample shunt resistance.

$$Q(t) = Q_0(1 - e^{-t/R_x C_0})$$

References

1. Saidaminov, M. I., et al., High-Quality Bulk Hybrid Perovskite Single Crystals within Minutes by Inverse Temperature Crystallization. *Nat. Commun.* **2015**, *6*, 7586.
2. Wang, K.-H.; Li, L.-C.; Shellaiah, M.; Wen Sun, K., Structural and Photophysical Properties of Methylammonium Lead Tribromide (Mapbbr₃) Single Crystals. *Sci. Rep.* **2017**, *7*, 13643.

Chapter 8: Publication 5

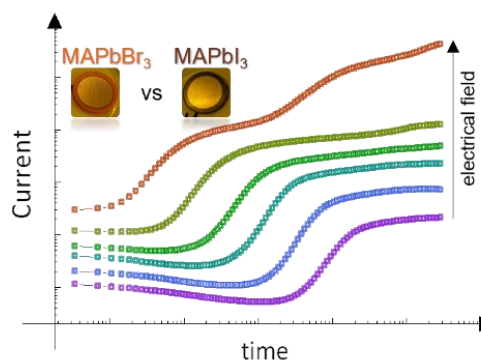
Marisé García-Batlle, Sarah Deumel, Judith E. Huerdler, Sandro F. Tedde, Osbel Almora, and **Germà Garcia-Belmonte**, Effective Ion Mobility and Long-Term Dark Current of Metal-Halide Perovskites of Different Crystallinities and Compositions, *Adv. Photonics Res.* **2022**, 2200136. <https://doi.org/10.1002/adpr.202200136>

8.1 Candidate's contribution

Nature of Contribution	Extent of Contribution
<ul style="list-style-type: none"> • Growth of the single crystal's samples • Performed all the structural and optical characterization techniques. • Carried out all the long-time transients' measurements • Contributed to interpretation of the results • Wrote first draft of the manuscript • Contributed to the reply to the referees 	50 %

8.2 Brief summary

Long-term dark current is explored here for a set of lead-halide perovskite thick samples of different crystallinity and composition. The general trend: dark current exhibits an exponential-like rise that reaches steady-state depending on the applied electrical field. The coupling between ionic drift and the time-scale of the electronic current is highlighted. Ionic drift mobility is calculated through ion time-of-flight at different applied bias. Dissimilar trends for μ dependence on the electrical field is found for MAPbI₃ and MAPbBr₃ hypothetically connected to the chemistry of the defect formation



8.3 Published manuscript

Effective Ion Mobility and Long-Term Dark Current of Metal-Halide Perovskites of Different Crystallinity and Composition

Marisé García-Batlle¹, Sarah Deumel², Judith E. Huerdler², Sandro F. Tedde², Osbel Almora¹, and Germà Garcia-Belmonte^{1*}

¹ *Institute of Advanced Materials (INAM), Universitat Jaume I, 12006 Castelló, Spain*

² *Siemens Healthineers AG, Technology Excellence, Guenther-Scharowsky-Strasse 1, 91058 Erlangen, Germany*

*E-mail: garciag@uji.es

5 octubre 2022

Abstract

Ion transport properties in metal-halide perovskite still constitute a subject of intense research because of the evident connection between mobile defects and device performance and operation degradation. In the specific case of X-ray detectors, dark current level and instability are regarded to be connected to the ion migration upon bias application. Different compositions (MAPbBr₃ and MAPbI₃) and structures (single- and micro-crystalline) are checked by the analysis of long-term dark current evolution. In all cases, electronic current increases with time before reaching a steady-state value within a response time (from 10⁴ s down to 10 s) that strongly depends on the applied bias. Our findings corroborate the existence of a coupling between electronic transport and ion kinetics that ultimately establishes the time scale of electronic current. Effective ion mobility μ_i is extracted for a range of applied electrical field ξ and several perovskite compositions. While ion mobility results field-independent in the case of MAPbI₃, a clear field-enhancement is observed for MAPbBr₃ ($\partial\mu_i/\partial\xi > 0$), irrespective of the crystallinity. Both perovskite compounds present effective ion mobility in the range of $\mu_i \approx 10^{-7}$ – 10^{-6} cm² V⁻¹ s⁻¹, in accordance with previous analyses. The ξ -dependence of the ion mobility is related to

the lower ionic concentration of the bromide compound. Slower-migrating defect drift is suppressed in the case of MAPbBr₃, in opposition to that observed here for MAPbI₃.

1. Introduction

Perovskites have been explored in almost all fields of material science.¹⁻² Considerable efforts have been made on examining the causes of hysteresis in the current–voltage curves,³⁻⁵ the nature of charge traps, defects,⁶⁻⁷ grain boundaries,⁸ origins of ion migration,⁹⁻¹¹ not only in the field of solar cells and light emitters devices,¹² but also as key materials in fuel cells¹³ and electrodes for water electrolyzers.¹⁴ By tailoring the composition of the perovskite compounds, a variety of physical properties appears, such as ferroelectric,¹⁵ dielectric, piezoelectric, magnetic,¹⁶ catalytic,¹⁷ photovoltaic, electronic-ionic-conduction,¹⁸ and superconducting properties.¹⁹

Recently, metal halide perovskite materials (HP) have been successfully used in X-ray imaging and ionizing radiation detectors.²⁰⁻²¹ Using their optoelectronic properties, the compounds can be tuned to adapt desired functionalities. The chemical formula APbX₃ (where A is a cation and X the halide anion) comprises reasonably high-Z elements which are helpful to stop high-energy radiation photons. HPs exhibit the so-called defect tolerance which is connected to the transport properties allowing to maximize the product of the charge mobility and carrier lifetime by minimizing the bulk/surface defect density.²²⁻²⁴ Furthermore, direct semiconductor radiation detectors based on Pb-halide perovskites can be grown and processed in solution at relatively low temperature and from low-cost basic raw materials.²⁵⁻²⁶

Fast and efficient detection of hard X- and γ -ray with high energy resolution is critical for medical and industrial applications.²⁷ The direct conversion X-ray detectors transform the incident X-ray photons directly into electrical signals, and present an advantage in terms of high spatial resolution in comparison to indirect detectors as CsI.²⁸ Besides optimization in material composition and device architecture, the current conventional direct detectors, such as amorphous selenium (α -Se),²⁹ suffer from their low mobility–lifetime ($\mu\tau$) product and small atomic number which limit their sensitivity.^{24, 30} In contrast, HPs exhibit large $\mu\tau$ -product and strong stopping power. However, the persistent drawback of ion migration results in deleterious and instable dark current.³¹⁻³³ In fact, induced dark current and also photocurrent drift

under a large electric field negatively alter the intrinsically good performance as X-ray detectors.³⁴

Significant progress has been reported about substrates, selective electrodes, and stable sensing layers for accurate detection. Highly sensitive active nanolayers has been tested for gas based detectors to increase the long-term current stability.³⁵ The use of noble metals such as Pd and Pt on the host materials has been examined for sensitivity improvement.³⁶ Other strategies for sensing performances are based on controlling the defect chemistry, from ion-doping/loading techniques³⁷ for stability enhancement³⁸ to atomistic surface passivation to heal the surface defects,³⁹⁻⁴⁰ introducing charge transport layers at the outer interfaces,³⁴ which may, potentially, inhibit the ion migration. However, dark current has been reported in perovskite-based detectors, with values larger than those registered with commercial devices,²⁹⁻³⁰ over which the photocurrent should be detected. Moreover, such a dark current under continuous biasing exhibits instability, which is detrimental to the transient response of the X-ray detectors.³⁴ Ultimately, dark current values are too large to achieve high quality images, with high resolution and contrast for accurate diagnosis.⁴¹ Therefore, it is essential to obtain high dark resistivity through further progress in material composition engineering and device architecture. Also crucial is to achieve a deep understanding on how ion migration governs the electronic current for the long-term operational stability of the detector.⁴²⁻⁴³

In this work, chronoamperometry experiments are performed to study the long-term current transient response of different compositions of single-crystal (SC) and micro-crystalline (MC) perovskite samples of MAPbBr₃ and MAPbI₃ at room temperature. Dissimilar current responses are encountered for the bromide-based perovskite samples and the iodine ones. Our findings corroborate the existence of a coupling between electronic transport and ion kinetics that ultimately establishes the time scale of electronic dark current.¹⁰ In all cases, electronic current increases with time before reaching a steady-state value within a response time (from 10⁴ s down to 10 s) that strongly depends on the applied bias. We highlight that fitting the long-term dark current transient curve provides an estimation of the intrinsic parameters such as the ionic mobility which is in the range of $\mu_i \approx 10^{-7}$ – 10^{-6} cm² V⁻¹ s⁻¹ for the studied samples.

2. Results and Discussion

MAPbBr₃-SC of ~2 mm-thick symmetrically face-to-face contacted with Cr electrodes and MC samples of ~1 mm-thick of MAPbX₃ (X⁻: Br⁻, I⁻) asymmetrically-contacted with Pt and Cr electrodes were investigated in the dark by registering the long-term current transient response after voltage biasing, as shown in Figure 1. The transients were measured by following a previously used protocol,¹⁰ by application of a forward bias for SC, symmetrically-contacted samples and a reverse bias (Pt positively- and Cr negatively-contacted) for MC samples, followed by a zero-bias equilibration period (see Figure S1) of ~3000 s. In Figure S2, the used biasing protocol for each sample is shown, which exhibit sufficient reproducibility. An increasing trend in the current transient can be seen (Figure 1), although some particularities were observed, at different times scales, depending on the sample composition and crystallinity.

By first examining the global transient response of a MAPbBr₃-SC (Figure 1a) under continuous application of forward bias, the current increases from a rather constant value at shorter times ($t < 1-10$ s), and finally saturates approaching steady-state values J_1 at longer times. This behavior has been noticed previously in MAPbBr₃ single-crystal samples¹⁰ and agrees with the evidence that the higher the bias the faster the current increase. In Figure 1b, an additional feature appears during the transient of a MAPbBr₃-MC sample under reverse bias. At the beginning of the transient for $t < 5-50$ s, a slight decrease of the current is observed, while for $t > 100$ s an exponential growth can be identified, as in the case of SC, that finally reaches a current steady state J_1 . As observed, the initial decrease represents a minor feature of the overall current evolution.

Figure 1c displays the more complex current transient response of a MAPbI₃-MC sample. Once more, for shorter times ($t < 50$ s) initial current tend to slightly decrease. Afterwards, the current grows and seems to saturate at J_1 . This is consistent with previous observations in Figure 1 a and b registered for Br-based perovskite samples at that polarization times. Interesting, the transient response of MAPbI₃-MC is different for bias lower than -10 V: a second current increase appears, which tends to a larger saturation value J_2 at longer times.

Then, the magnitude of the electronic current J , both for the first and second current increase, can be described as a function of the time constant τ of the ion migration process (see below) as

$$J = J_i(1 - e^{-t/\tau_i}) \quad (1)$$

being J_i and τ_i ($i = 1, 2$) the corresponding saturation current and response time for each current increase step. Fitting of Equation 1 to the current rise is plot in each transient as a solid line in Figure 1. As noted previously, the time constants reveal the dynamics of the ionic transport within the device,⁴⁴ and can be assimilated to an drift-induced ionic time-of flight that effectively controls the time scale of the electronic current transient toward saturation, while the amplitude of the current response is determined by the electronic carriers (electrons and holes).¹⁰ It is also noticeable that inverted hysteretic responses are observed in Fig. S6,⁴⁵⁻⁴⁷ which correlate to the increment of the current over time reported here and inductive behaviors in the frequency domain.⁴⁷

Following the insights from our recent paper,¹⁰ we are able to rationalize the current phenomenology by assuming that the measured current is always an *electronic* current. However, a *coupling* between ionic and electronic currents exists in such a way that the slower species (ions) condition the value of the measured current, which actually monitors the faster carriers (electrons/holes). As ions move by effect of the electrical field (and eventually accumulate in the vicinity of the contacts), the kinetics of the electronic response follows the slow ion rearrangement. Whatever the ionic/electronic interplay mechanism is behind the current transients, it is evident that initial homogeneous distribution of ions at zero bias hinders the charge extraction at short times, while the applied bias favors the electronic current flowing at longer times. The latter effect can be possibly due to (i) an increment of the effective electronic doping in the bulk perovskite via field ionization, (ii) a local increment of effective doping caused by ion redistribution (dynamic doping).⁴⁸ These two mechanisms would imply an increment in electronic conductivity (and consequently current) over time after bias application.⁴⁹⁻⁵⁰ Finally, (iii) a reduction of contact electronic barriers via electrode polarization caused by ion accumulation, fostering as a consequence carrier injection or (iv) a combination of all these effects may also occur. Elucidation of the effective

mechanism occurring in perovskite-based devices needs of an exhaustive analysis of different structures (electrodes, active material, buffer layers...) aimed at creating a coherent picture.

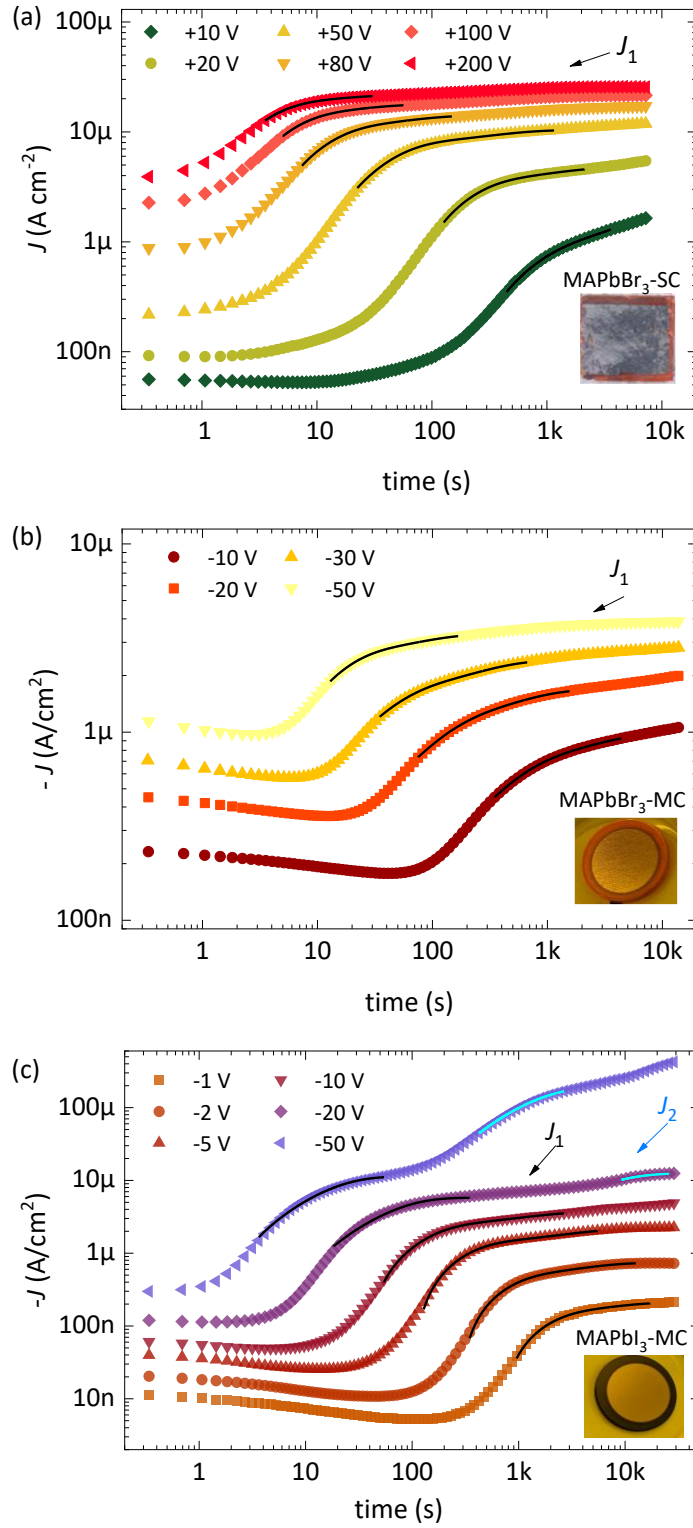


Figure 1. Long-term current response upon a biasing protocol for a) ~ 2 mm-thick MAPbBr₃-SC b) ~ 1.5 mm-thick MAPbBr₃-MC c) ~ 1 mm-thick MAPbI₃-MC. Note the experimental current transient with the corresponding fittings (black solid lines) for each curve following Equation 1. The parameters J_1 and J_2 correspond to the steady-state current during the first and second exponential rise respectively. After each bias, the device is kept under short-circuit (0-V bias) conditions to observe the relaxation current. See the long-term current response of each sample for the other two cycles in Figures S3, S4 and S5 respectively. In the inset is shown the top-view image of each sample. Data in a) reproduced from ref.¹⁰ (under Creative Commons public use license, CC-BY).

Now let us consider the behavior of the steady-state electronic current. From the long-current transients of Figure 1, one can obtain the J_1 - V curve in Figure 2 using the steady-state values of the first current step. The current value J_1 has been marked in Figure 1 for the three samples presented. From an allometric fit with a power law of the type $J_1 \propto V^\beta$, the extracted power β attains values between 0.98 and 1.05 with an average variability of ± 0.07 , which suggests an apparent ohmic conductivity regime for electronic charge carriers within the explored bias range after current saturation (long time). Note that steady-state current is plotted as a function of the applied electrical field $\xi = V/L$, being L the sample thickness, for a better comparison among different structures. The steady-state values in Figure 2 are higher than those encountered with fast cyclic-voltammetry ($J - V$ curve) (Figure S6). One example is observed in Figure S6b with lower electronic current because of a much faster speed of electrons/holes compared to that of ions using a scan rate of 500 mV/s. That observation signals the necessity of full ion relaxation before concluding about of electronic transport regimes in halide perovskite devices.⁴²

We express the total characteristic time from the time constant τ of the current transient increase as $t_t = 4\tau$, which relates to the 98% of the transition to the steady state (instead of the 63 % when only τ is used). For the sake of simplicity, one can assume a homogeneous ionic charge transport across the device. Under these conditions, the ionic time-of-flight mobility can be estimated through the simple form

$$\mu_i = \frac{L^2}{t_t V} \quad (2)$$

In Figure 3a, the ion mobility has been obtained by using the total time t_t obtained from the first current step (closed dots) for polycrystalline samples of different

thickness of MAPbI₃. Also plotted in Figure 3a is the μ_i estimated for the second current step (open dots). Remarkably, ionic mobility exhibits a rather constant behavior with the increasing bias independently for the iodide samples.

On the contrary, Figure 3b shows μ_i to increase with the electric field $\xi = V/L$ for MAPbBr₃ with different crystallinity. From the analysis of Figure 3b, using an allometric fitting, one can calculate a power $m \sim 1.2 \pm 0.05$ for the relationship $\mu_i \propto \xi^m$. See below for more comments about this last point. We also notice that the use of Equation 2 assumes ion drift occurring along the whole sample thickness. Notably, the ion transport would take place in narrow zones $L_{eff} < L$ (either internal bulk regions or in the vicinity of the external contacts related to the ionic Debye length), meaning that the mobility values represented in Figure 3 could be overestimated.

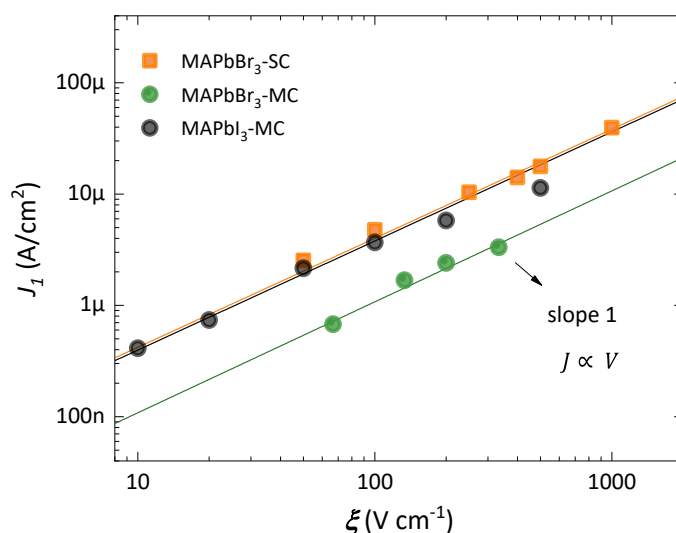


Figure 2. Steady state current as a function of the electric field ξ during the first current increase step for times $t > 100$ s for three different perovskite samples is shown with the corresponding linear fitting (solid lines). The ohmic behavior is highlighted.

On mixed conductors as HPs, one must be cautious about whether the measured signals are due to ionic or electronic defects, otherwise mistaken conclusions may be drawn.⁵¹ Identifying the type of mobile defect is not easy and a number of reports predicts the facile migration of halide-related defects, under biasing conditions, rather than MA and Pb vacancies, with calculated activation barriers of ~ 0.5 eV and 0.8 eV, respectively.^{6, 52} Correlations between specific ionic defects and electronic doping mechanisms have been made based on how the doping concentration is modified

during the application and switching-off of an external bias.^{10, 48} Recalling now Figure 1, one can speculate about the halide vacancies V_X^+ as the ones that dominate and establish the general time response of the first current step, with typical migration times in the range of $10\text{--}10^4$ s. Only in the case of MAPbI₃-MC samples (Figure 1c), the second exponential rise can be possibly originated by (i) imperfections on the perovskite surface or at the grain boundaries introducing alternative, and much slower, ion migration paths (ii) further enhancement in the ion drift of slower-migrating defects at higher electric fields, for instance V_{MA} and V_{Pb} , or (iii) a combination of these effects. Nevertheless, the J_1 values in Figure 2 followed an ohmic regime irrespective of the sample crystallinity or composition, which may indicate that the electronic drift regime is proportional to the electrical field in most of the cases. Hence, our findings confirmed that the electronic-ionic coupling mechanism behind the current transients rely in how the ionic movement establishes the kinetics of the electronic carrier response in HPs materials.

Ionic mobility have been determined by many techniques such as: impedance spectroscopy (IS),^{48-49, 52-53} nuclear magnetic resonance (NMR) spectroscopy,⁵⁴⁻⁵⁵ photocurrent transient,^{9, 55-56} PL quenching method (PLQ),⁵⁰ temperature-dependent conductivity (TDC) measurement,⁵⁷⁻⁵⁸ and chronoamperometry measurements.^{10, 49} Previous works shown values between $\mu_i \sim 1\text{--}3 \times 10^{-6}$ cm² V⁻¹ s⁻¹ for MAPbBr₃ perovskite single crystals by analyzing the resistance response during a diffusion-relaxation mechanism.⁴⁸ The same methodology has been applied for MAPbI₃ thick-pellets⁴⁹ obtaining self-consistent patterns by registering both, current transients and impedance spectra, with values encountered also in the range of $\sim 10^{-6}$ cm² V⁻¹ s⁻¹.

The behavior of μ_i as a function of the electric field in Figure 3a exhibits values within the range of 5×10^{-7} to 3×10^{-6} cm² V⁻¹ s⁻¹ for various micro-crystalline samples of MAPbI₃, which agrees with those reported for the iodine-related defect ionic mobilities. Remarkably, a ξ -independent ion mobility indicates a bulk origin, rather than interfacial, for the mechanism behind the observed electrical response. The μ_i calculated for the second exponential rise is found to be in the order of $\sim 10^{-8}$ cm² V⁻¹ s⁻¹, with a similar, ξ -independent behavior. Therefore, it makes sense to assume, for this second step, that the electronic response relates to other possible moving ions, such as MA⁺ and Pb²⁺ with much lower mobility.⁵⁹⁻⁶⁰ This is in accordance with the

suppression of MA^+ migration in MAPbBr_3 , while it is actually observed for MAPbI_3 .⁶¹ An alternative explanation for the second step in the transient response could be related to the role of grain boundaries. However, bromide-based devices, either of single- or micro-crystalline structure, do not exhibit such a feature at longer times, so as to move us to disregard it as structurally-originated.

By examining Figure 3b, a different trend occurs for bromide samples as $\mu_i \propto \xi^m$, compared to iodine ones. Several models have suggested to rationalize for a field-dependent mobility behavior in different materials with $\partial\mu/\partial\xi > 0$. For instance, surface-charge decay in insulators were described to exhibit nonconstant carrier mobility.⁶²⁻⁶³ In the specific case of ion migration in electrolytes of different ionic strength, molecular dynamics simulations recently revealed that ionic conductivity is constant for strong electrolytes. On the contrary, weaker electrolytes or molten salts exhibit applied-field enhancement of the ion mobility.⁶⁴ Considering a perovskite sample at room temperature, the field-dependent mobility observed for MAPbBr_3 would indicate a weaker character for the bromide-related defect formation in opposition to a more favorable defect formation of iodide-related. Several theoretical predictions for MAPbBr_3 suggest a stronger Pb–Br bond⁶⁵ and considerable lattice contraction by stronger hydrogen bonding to the surrounding Pb–Br₆ octahedra.⁶¹ These effects could, presumably, increase the bromide-related defect formation energy reducing the observed concentration of bromide mobile ions in MAPbBr_3 compared to iodide concentration in MAPbI_3 ,⁶¹ which also explains the superior ambient stability of the bromide compound.

Finally, it is worth mentioned the existence of clear similitudes between our findings and the dynamic response of thin-film perovskite devices as memristors and solar cells. The current increment in the time domain relates to the low-frequency inductive behavior observed in memristors,⁶⁶ and also the change in the conduction regime reported here for MAPbBr_3 -MC (initial current reduction followed by current growth) resembles the observation of transient spikes recently reported.⁶⁷

3. Conclusions

In summary, long-term dark current has been explored for a set of lead-halide perovskite thick samples of different crystallinity and composition. As a general trend, dark current exhibits an exponential-like rise that reaches steady-state values

depending on the applied electrical field. Our findings reveal the coupling between ionic drift and the time-scale of the electronic current. MAPbBr₃ and MAPbI₃ exhibit different response: iodide compounds present double current rise related to the migration of much slower defects such as MA⁺ and Pb²⁺, with much lower values of ion mobility, that are instead suppressed in the case of MAPbBr₃. Also, the dependence of the effective ionic mobility on the electrical field presents dissimilar trends: constant, ξ -independent for MAPbI₃, but clearly ξ -dependent in the case of MAPbBr₃. Such a different behavior may be connected to differences in the chemistry of the defect formation between both compounds.

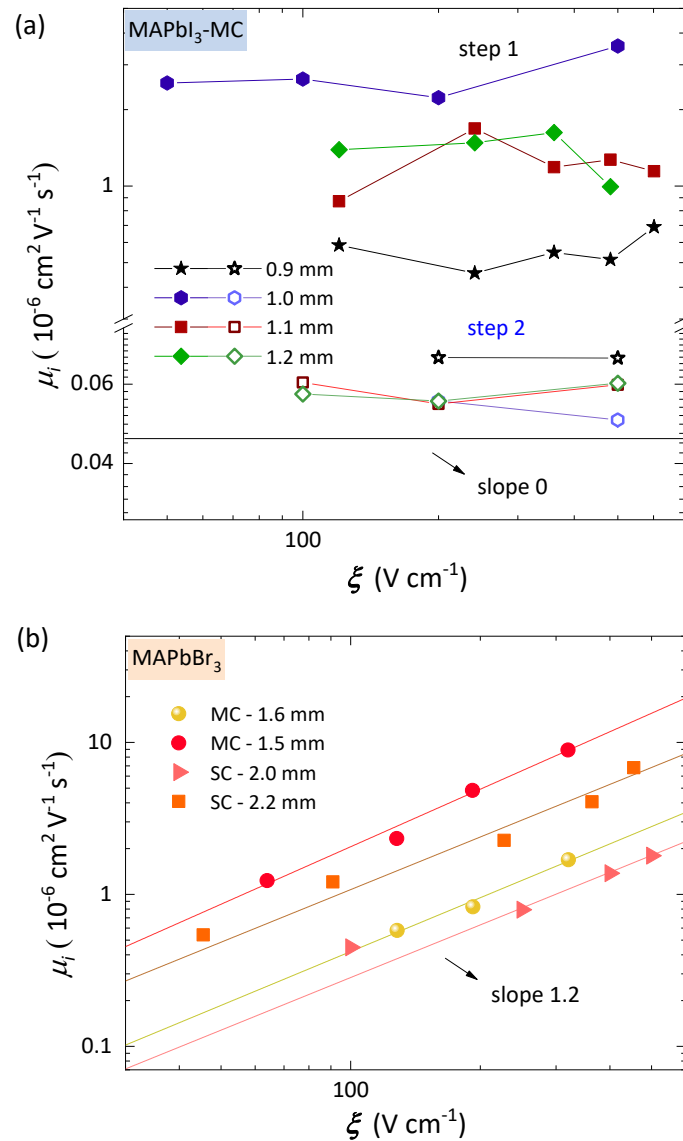


Figure 3. Ion mobility as a function of the electric field ξ for a) various MAPbI₃-MC perovskite samples and b) two MAPbBr₃-SC and two MC perovskite samples. While a linear trend is clearly observed for bromide compounds, no correlation appears for iodide perovskites.

4. Experimental section

Sample preparation: Perovskite samples of two compositions, MAPbBr₃ and MAPbI₃, were analyzed. Firstly, single crystals (SC) of MAPbBr₃ symmetrically contacted with Cr electrodes (see Figure 1a, inset) were prepared following the inverse temperature crystallization (ITC) growth method previously reported.⁶⁸ MAPbBr₃-SC

were grown by ITC method in DMF. In here, the perovskite precursors, $\text{CH}_3\text{NH}_3\text{Br}$, PbBr_2 are dissolved (1:1 mol. %) in DMF to obtain 1 M solutions of MAPbBr_3 . All the solutions were stirred at room temperature and filtered using PTFE filters to remove insoluble particles. An aliquot of the filtered perovskite solutions is placed in a glass flask and the temperature is raised from room to 80–85 °C leading to the spontaneous nucleation and growth of the cubic shape single crystals of MAPbBr_3 . After the mechanically polished of the SC with sandpaper of different roughness, 100 nm of Cr metal is evaporated at two opposite faces (see Table S1). An XRD-2D rotation spectrum along the α cell axis was performed to probe the monocrystalline nature of the SC (Fig S7) and Scanning Electrons Microscopy (Fig S9b) was conducted to observe the smooth surface area of the SC after the polishing process. SC were also characterized by UV-Vis spectrophotometry obtaining the corresponding absorption edge at for MAPbBr_3 with a bandgap of 2.18 eV (see Tauc plot, Fig. S9d).

Secondly, MAPbX_3 ($X = \text{Br}, \text{I}$) micro-crystalline pellets (MC) of ~ 1 mm-thick asymmetrically contacted with evaporated Pt and Cr electrodes of 1 cm^2 area (see Figure 1b and c, inset) were made by a soft-sintering process, which is described in detail in ref.⁶⁹ The MC-pellets with a diameter of ~ 15 mm were made by a soft-sintering process. The microcrystalline MAPbI_3 and MAPbBr_3 powder (Xi'an Polymer Light Technology Corp) were filled into an adjustable height powder container with a polished cylinder placed above it. A constant pressure of 55 MPa (1t) for 30 min at 70 °C results in thick pellets with a thickness of around 1000 μm . Then, Pt and Cr electrodes were deposited via sputtering and vapor deposition respectively. MAPbI_3 and MAPbBr_3 microcrystalline samples were characterized by UV-Vis spectra, SEM analysis and XRD patterns (See Fig S8, Supporting Information). Table S1 in the Supplemental Information summarizes the general characteristics of the samples studied. More information about the structural characterization and optoelectronics properties can be found in references ^{48, 68, 70} for MAPbBr_3 -SC and ^{49, 69} for MAPbI_3 -MC samples.

Electrical Measurements: Chronoamperometry measurements were carried out with a Source Measure Unit Model 2612B from Keithley Instruments, Inc. Current measurements were conducted following the long-term direct-current mode (DC) bias protocol in the ranges of ± 200 to 0 V as previously reported.¹⁰ The samples were kept

in the dark at ambient temperature and with N₂ circulation to avoid humidity- and oxygen-induced degradations.

Data available on request from the authors.

Supporting Information.

Additional information about structural properties and reproducibility tests of the long-term current response.

Acknowledgments

This work has received funding from the European Union's Horizon 2020 research and innovation program under the Photonics Public Private Partnership (www.photonics21.org) with the project PEROXIS under the grant agreement N° 871336.

References

1. Monama, G. R.; Ramohlola, K. E.; Iwuoha, E. I.; Modibane, K. D., Progress on Perovskite Materials for Energy Application. *Results Chem.* **2022**, *4*, 100321.
2. Snaith, H. J., Present Status and Future Prospects of Perovskite Photovoltaics. *Nat Mater* **2018**, *17*, 372-376.
3. Almora, O., et al., Ionic Dipolar Switching Hinders Charge Collection in Perovskite Solar Cells with Normal and Inverted Hysteresis. *Sol. Energy Mater. Sol. Cells* **2019**, *195*, 291-298.
4. Moia, D., et al., Ionic-to-Electronic Current Amplification in Hybrid Perovskite Solar Cells: Ionically Gated Transistor-Interface Circuit Model Explains Hysteresis and Impedance of Mixed Conducting Devices. *Energy Environm. Sci.* **2019**, *12*, 1296-1308.
5. Bisquert, J.; Guerrero, A.; Gonzales, C., Theory of Hysteresis in Halide Perovskites by Integration of the Equivalent Circuit. *ACS Phys. Chem. Au* **2021**, *1*, 25-44.
6. Azpiroz, J. M.; Mosconi, E.; Bisquert, J.; De Angelis, F., Defects Migration in Methylammonium Lead Iodide and Their Role in Perovskite Solar Cells Operation. *Energy Environ. Sci.* **2015**, *8*, 2118-2127

7. Futscher, M. H.; Gangishetty, M. K.; Congreve, D. N.; Ehrler, B., Quantifying Mobile Ions and Electronic Defects in Perovskite-Based Devices with Temperature-Dependent Capacitance Measurements: Frequency Vs Time Domain. *J. Chem. Phys.* **2020**, *152*, 044202.
8. Shi, D., et al., Low Trap-State Density and Long Carrier Diffusion in Organolead Trihalide Perovskite Single Crystals. *Science* **2015**, *347*, 519-522.
9. Bertoluzzi, L.; Boyd, C. C.; Rolston, N.; Xu, J.; Prasanna, R.; O'Regan, B. C.; McGehee, M. D., Mobile Ion Concentration Measurement and Open-Access Band Diagram Simulation Platform for Halide Perovskite Solar Cells. *Joule* **2020**, *4*, 109-127.
10. García-Batlle, M.; Mayén Guillén, J.; Chapran, M.; Baussens, O.; Zaccaro, J.; Gros Daillon, E.; Verilhac, J. M.; Guerrero, A.; Almora, O.; Garcia Belmonte, G., Coupling between Ion Drift and Kinetics of Electronic Current Transients in Mapbbr3 Single Crystals. *ACS Energy Lett.* **2022**, *7*, 946–951.
11. Senocrate, A.; Maier, J., Solid-State Ionics of Hybrid Halide Perovskites. *J. Am. Chem. Soc.* **2019**, *141*, 8382-8396.
12. Kim, J. Y.; Lee, J.-W.; Jung, H. S.; Shin, H.; Park, N.-G., High-Efficiency Perovskite Solar Cells. *Chem. Rev.* **2020**, *120*, 7867-7918.
13. Dong, H.; Yu, H.; Wang, X.; Zhou, Q.; Sun, J., Carbon-Supported Perovskite Oxides as Oxygen Reduction Reaction Catalyst in Single Chambered Microbial Fuel Cells. *J. Chem. Technol. Biotechnol.* **2013**, *88*, 774-778.
14. Cheng, X.; Fabbri, E.; Nachtegaal, M.; Castelli, I. E.; El Kazzi, M.; Haumont, R.; Marzari, N.; Schmidt, T. J., Oxygen Evolution Reaction on La_{1-x}Sr_xCoO₃ Perovskites: A Combined Experimental and Theoretical Study of Their Structural, Electronic, and Electrochemical Properties. *Chem. Mater* **2015**, *27*, 7662-7672.
15. Colsmann, A.; Röhm, H., Ferroelectricity and Stability Measurements in Perovskite Solar Cells. *J. Phys.: Energy* **2019**, *2*, 011003.
16. Fu, L.; Li, B.; Li, S.; Yin, L., Magnetic, Electronic, and Optical Properties of Perovskite Materials. In *Revolution of Perovskite: Synthesis, Properties and Applications*, Arul, N. S.; Nithya, V. D., Eds. Springer Singapore: Singapore, 2020; pp 43-59.
17. Yang, L.; Li, Y.; Sun, Y.; Wang, W.; Shao, Z., Perovskite Oxides in Catalytic Combustion of Volatile Organic Compounds: Recent Advances and Future Prospects. *Energy Environ. Mater.* **2021**, *0*, 1-26.
18. Akkerman, Q. A.; Manna, L., What Defines a Halide Perovskite? *ACS Energy Lett.* **2020**, *5*, 604-610.

19. Zhu, L.; Ran, R.; Tadé, M.; Wang, W.; Shao, Z., Perovskite Materials in Energy Storage and Conversion. *Asia-Pac. J. Chem. Eng.* **2016**, *11*, 338-369.
20. Wolszczak, W. W.; Carroll, D. L.; Williams, R. T., Toward Perovskite-Related Scintillators with Necessary Stokes Shift and Thickness for Hard X-Ray Radiography and Gamma Spectroscopy. In *Advanced X-Ray Detector Technologies: Design and Applications*, Iniewski, K., Ed. Springer International Publishing: Cham, 2022; pp 1-34.
21. Tan, R.; Dryzhakov, B.; Charest, J.; Hu, B.; Ahmadi, M.; Lukosi, E., Improved Radiation Sensing with Methylammonium Lead Tribromide Perovskite Semiconductors. *Nucl. Instrum. Methods Phys. Res., Sect. A* **2021**, *986*, 164710.
22. He, Y., et al., High Spectral Resolution of Gamma-Rays at Room Temperature by Perovskite CsPbBr₃ Single Crystals. *Nat. Commun.* **2018**, *9*, 1609.
23. Tsai, H.; Tisdale, J.; Shrestha, S.; Liu, F.; Nie, W., Emerging Lead-Halide Perovskite Semiconductor for Solid-State Detectors. In *Advanced X-Ray Detector Technologies: Design and Applications*, Iniewski, K., Ed. Springer International Publishing: Cham, 2022; pp 35-58.
24. Wei, H.; Huang, J., Halide Lead Perovskites for Ionizing Radiation Detection. *Nat. Commun.* **2019**, *10*, 1066.
25. Wei, H., et al., Sensitive X-Ray Detectors Made of Methylammonium Lead Tribromide Perovskite Single Crystals. *Nat. Photonics* **2016**, *10*, 333.
26. Saidaminov, M. I., et al., High-Quality Bulk Hybrid Perovskite Single Crystals within Minutes by Inverse Temperature Crystallization. *Nat. Commun.* **2015**, *6*, 7586.
27. Liu, F.; Wu, R.; Wei, J.; Nie, W.; Mohite, A. D.; Brovelli, S.; Manna, L.; Li, H., Recent Progress in Halide Perovskite Radiation Detectors for Gamma-Ray Spectroscopy. *ACS Energy Lett.* **2022**, *7*, 1066-1085.
28. Wang, J.-X., et al., Nearly 100% Energy Transfer at the Interface of Metal-Organic Frameworks for X-Ray Imaging Scintillators. *Matter* **2022**, *5*, 253-265.
29. Rowlands, J. A.; Hunter, D. M.; Araj, N., X-Ray Imaging Using Amorphous Selenium: A Photoinduced Discharge Readout Method for Digital Mammography. *Med. Phys.* **1991**, *18*, 421-431.
30. Kasap, S. O., X-Ray Sensitivity of Photoconductors: Application to Stabilized a-Se. *J. Phys. D: Appl. Phys.* **2000**, *33*, 2853-2865.
31. Liu, Y., et al., Inch-Size 0d-Structured Lead-Free Perovskite Single Crystals for Highly Sensitive Stable X-Ray Imaging. *Matter* **2020**, *3*, 180-196.

32. Zhuang, R., et al., Highly Sensitive X-Ray Detector Made of Layered Perovskite-Like (NH₄)₃Bi₂I₉ Single Crystal with Anisotropic Response. *Nat. Photon.* **2019**, *13*, 602-608.
33. Zheng, X.; Zhao, W.; Wang, P.; Tan, H.; Saidaminov, M. I.; Tie, S.; Chen, L.; Peng, Y.; Long, J.; Zhang, W.-H., Ultrasensitive and Stable X-Ray Detection Using Zero-Dimensional Lead-Free Perovskites. *J. Energy Chem.* **2020**, *49*, 299-306.
34. Song, Y., et al., Elimination of Interfacial-Electrochemical-Reaction-Induced Polarization in Perovskite Single Crystals for Ultrasensitive and Stable X-Ray Detector Arrays. *Adv. Mater.* **2021**, *33*, 2103078.
35. Zhou, T.; Zhang, T., Recent Progress of Nanostructured Sensing Materials from 0d to 3d: Overview of Structure–Property–Application Relationship for Gas Sensors. *Small Methods* **2021**, *5*, 2100515.
36. Karmaoui, M.; Leonardi, S. G.; Latino, M.; Tobaldi, D. M.; Donato, N.; Pullar, R. C.; Seabra, M. P.; Labrincha, J. A.; Neri, G., Pt-Decorated In₂O₃ Nanoparticles and Their Ability as a Highly Sensitive (<10ppb) Acetone Sensor for Biomedical Applications. *Sens. Actuators, B* **2016**, *230*, 697-705.
37. Zhou, D.; Liu, D.; Pan, G.; Chen, X.; Li, D.; Xu, W.; Bai, X.; Song, H., Cerium and Ytterbium Codoped Halide Perovskite Quantum Dots: A Novel and Efficient Downconverter for Improving the Performance of Silicon Solar Cells. *Adv. Mater.* **2017**, *29*, 1704149.
38. Sun, R., et al., Samarium-Doped Metal Halide Perovskite Nanocrystals for Single-Component Electroluminescent White Light-Emitting Diodes. *ACS Energy Lett.* **2020**, *5*, 2131-2139.
39. Wang, C.; Ecker, B. R.; Wei, H.; Huang, J.; Gao, Y., Environmental Surface Stability of the MAPbBr₃ Single Crystal. *J. Phys. Chem. C* **2018**, *122*, 3513-3522.
40. Song, Y., et al., Atomistic Surface Passivation of CH₃NH₃PbI₃ Perovskite Single Crystals for Highly Sensitive Coplanar-Structure X-Ray Detectors. *Research* **2020**, *2020*, 5958243.
41. Pan, Z.; Wu, L.; Jiang, J.; Shen, L.; Yao, K., Searching for High-Quality Halide Perovskite Single Crystals toward X-Ray Detection. *J. Phys. Chem. Lett.* **2022**, *13*, 2851-2861.
42. Duijnste, E. A.; Le Corre, V. M.; Johnston, M. B.; Koster, L. J. A.; Lim, J.; Snaith, H. J., Understanding Dark Current-Voltage Characteristics in Metal-Halide Perovskite Single Crystals. *Phys. Rev. Appl.* **2021**, *15*, 014006.

43. Murali, B.; Kolli, H. K.; Yin, J.; Ketavath, R.; Bakr, O. M.; Mohammed, O. F., Single Crystals: The Next Big Wave of Perovskite Optoelectronics. *ACS Mater. Lett.* **2020**, *2*, 184-214.
44. Li, D.; Wu, H.; Cheng, H.-C.; Wang, G.; Huang, Y.; Duan, X., Electronic and Ionic Transport Dynamics in Organolead Halide Perovskites. *ACS Nano* **2016**, *10*, 6933-6941.
45. Almora, O.; Aranda, C.; Zarazua, I.; Guerrero, A.; Garcia-Belmonte, G., Noncapacitive Hysteresis in Perovskite Solar Cells at Room Temperature. *ACS Energy Lett.* **2016**, *1*, 209–215.
46. Garcia-Belmonte, G.; Bisquert, J., Distinction between Capacitive and Noncapacitive Hysteretic Currents in Operation and Degradation of Perovskite Solar Cells. *ACS Energy Letters* **2016**, *1*, 683-688.
47. Bisquert, J.; Guerrero, A., Chemical Inductor. *J. Am. Chem. Soc.* **2022**, *144*, 5996-6009.
48. García-Batlle, M.; Baussens, O.; Amari, S.; Zaccaro, J.; Gros-Daillon, E.; Verilhac, J. M.; Guerrero, A.; Garcia-Belmonte, G., Moving Ions Vary Electronic Conductivity in Lead Bromide Perovskite Single Crystals through Dynamic Doping. *Adv. Electron. Mater.* **2020**, *6*, 2000485.
49. García-Batlle, M.; Deumel, S.; Huerdler, J. E.; Tedde, S. F.; Guerrero, A.; Almora, O.; Garcia-Belmonte, G., Mobile Ion-Driven Modulation of Electronic Conductivity Explains Long-Timescale Electrical Response in Lead Iodide Perovskite Thick Pellets. *ACS Appl. Mater. Interfaces* **2021**, *13*, 35617-35624.
50. Li, C.; Guerrero, A.; Huettner, S.; Bisquert, J., Unravelling the Role of Vacancies in Lead Halide Perovskite through Electrical Switching of Photoluminescence. *Nat. Commun.* **2018**, *9*, 5113.
51. Futscher, M. H.; Deibel, C., Defect Spectroscopy in Halide Perovskites Is Dominated by Ionic Rather Than Electronic Defects. *ACS Energy Lett.* **2022**, *7*, 140-144.
52. Peng, W.; Aranda, C.; Bakr, O. M.; Garcia-Belmonte, G.; Bisquert, J.; Guerrero, A., Quantification of Ionic Diffusion in Lead Halide Perovskite Single Crystals. *ACS Energy Lett.* **2018**, *3*, 1477-1481.
53. Kim, S.-G.; Li, C.; Guerrero, A.; Yang, J.-M.; Zhong, Y.; Bisquert, J.; Huettner, S.; Park, N.-G., Potassium Ions as a Kinetic Controller in Ionic Double Layers for Hysteresis-Free Perovskite Solar Cells. *J. Mater. Chem. A* **2019**, *7*, 18807-18815.
54. Senocrate, A.; Moudrakovski, I. L.; Kim, G. Y.; Yang, T.-Y.; Gregori, G.; Grätzel, M.; Maier, J., The Nature of Ion Conduction in Methylammonium Lead Iodide: A Multimethod Approach. *Angew. Chem., Int. Ed.* **2017**, *56* 7755 - 7759.

55. Senocrate, A.; Moudrakovski, I. L.; Acartürk, T.; Merkle, R.; Kim, G. Y.; Starke, U.; Grätzel, M.; Maier, J., Slow CH_3NH_3^+ Diffusion in $\text{CH}_3\text{NH}_3\text{PbI}_3$ under Light Measured by Solid-State Nmr and Tracer Diffusion. *J. Phys. Chem. C* **2018**, *122*, 21803-21806.
56. Belisle, R. A.; Nguyen, W. H.; Bowring, A. R.; Calado, P.; Li, X.; Irvine, S. J. C.; McGehee, M. D.; Barnes, P. R. F.; O'Regan, B. C., Interpretation of Inverted Photocurrent Transients in Organic Lead Halide Perovskite Solar Cells: Proof of the Field Screening by Mobile Ions and Determination of the Space Charge Layer Widths. *Energy Environ. Sci.* **2017**, *10*, 192-204.
57. Lin, Y., et al., Excess Charge-Carrier Induced Instability of Hybrid Perovskites. *Nat. Commun.* **2018**, *9*, 4981.
58. Yuan, Y.; Chae, J.; Shao, Y.; Wang, Q.; Xiao, Z.; Centrone, A.; Huang, J., Photovoltaic Switching Mechanism in Lateral Structure Hybrid Perovskite Solar Cells. *Adv. Energy Mater.* **2015**, *5*, 1500615.
59. Yang, T.-Y.; Gregori, G.; Pellet, N.; Grätzel, M.; Maier, J., The Significance of Ion Conduction in a Hybrid Organic-Inorganic Lead-Iodide-Based Perovskite Photosensitizer. *Angew. Chem., Int. Ed.* **2015**, *54*, 7905-7910.
60. Weber, S. A. L.; Hermes, I. M.; Turren-Cruz, S.-H.; Gort, C.; Bergmann, V. W.; Gilson, L.; Hagfeldt, A.; Graetzel, M.; Tress, W.; Berger, R., How the Formation of Interfacial Charge Causes Hysteresis in Perovskite Solar Cells. *Energy Environ. Sci.* **2018**, *11*, 2404-2413.
61. McGovern, L.; Futscher, M. H.; Muscarella, L. A.; Ehrler, B., Understanding the Stability of MAPbBr_3 Versus MAPbI_3 : Suppression of Methylammonium Migration and Reduction of Halide Migration. *J. Phys. Chem. Lett.* **2020**, *11*, 7127-7132.
62. Wintle, H. J., Surface-Charge Decay in Insulators with Nonconstant Mobility and with Deep Trapping. *J. Appl. Phys.* **1972**, *43*, 2927-2930.
63. Sonnonstine, T. J.; Perlman, M. M., Surface-Potential Decay in Insulators with Field-Dependent Mobility and Injection Efficiency. *J. Appl. Phys.* **1975**, *46*, 3975-3981.
64. Lesnicki, D.; Gao, C. Y.; Rotenberg, B.; Limmer, D. T., Field-Dependent Ionic Conductivities from Generalized Fluctuation-Dissipation Relations. *Phys. Rev. Lett.* **2020**, *124*, 206001.
65. Yoon, S. J.; Stamplecoskie, K. G.; Kamat, P. V., How Lead Halide Complex Chemistry Dictates the Composition of Mixed Halide Perovskites. *J. Phys. Chem. Lett.* **2016**, *7*, 1368-1373.

66. Muñoz-Díaz, L.; Rosa, A. J.; Bou, A.; Sánchez, R. S.; Romero, B.; John, R. A.; Kovalenko, M. V.; Guerrero, A.; Bisquert, J., Inductive and Capacitive Hysteresis of Halide Perovskite Solar Cells and Memristors under Illumination. *Front. Energy Res.* **2022**, *10*, 914115.
67. Hernández-Balaguera, E.; Bisquert, J., Negative Transient Spikes in Halide Perovskites. *ACS Energy Letters* **2022**, *7*, 2602–2610.
68. Amari, S.; Verilhac, J.-M.; Gros D'Aillon, E.; Ibanez, A.; Zaccaro, J., Optimization of the Growth Conditions for High Quality $\text{CH}_3\text{NH}_3\text{PbBr}_3$ Hybrid Perovskite Single Crystals. *Cryst. Growth Des.* **2020**, *20*, 1665-1672.
69. Deumel, S., et al., High-Sensitivity High-Resolution X-Ray Imaging with Soft-Sintered Metal Halide Perovskites. *Nat. Electron.* **2021**, *4*, 681-688.
70. Baussens, O.; Maturana, L.; Amari, S.; Zaccaro, J.; Verilhac, J.-M.; Hirsch, L.; Gros-Daillon, E., An Insight into the Charge Carriers Transport Properties and Electric Field Distribution of $\text{CH}_3\text{NH}_3\text{PbBr}_3$ Thick Single Crystals. *Appl. Phys. Lett.* **2020**, *117*, 041904.

8.4 Supplemental Information

Effective Ion Mobility and Long-Term Dark Current of Metal-Halide Perovskites of Different Crystallinity and Composition

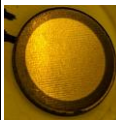
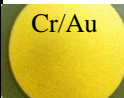
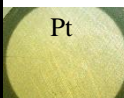



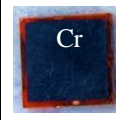


Marisé García-Battle¹, Sarah Deumel², Judith E. Huerdler², Sandro F. Tedde², Osbel Almora¹ and Germà Garcia-Belmonte^{1*}

¹ *Institute of Advanced Materials (INAM), Universitat Jaume I, 12006 Castelló, Spain*

² *Siemens Healthineers AG, Technology Excellence, Guenther-Scharowsky-Strasse 1, 91058 Erlangen, Germany*

*Email: garciag@uji.es

5 October 2022

Table S1. Characteristics of the samples studied							
Sample Composition	Number of samples	Cristallinity	Dimensions	Sample thickness (μm)	Electrode configuration and area	Picture of the sample	Picture of the electrodes
MAPbI ₃	6	MC	diameter ~15 mm	~1000	Pt/Cr ~ 1cm ²		 
MAPbBr ₃	2	MC	diameter ~15 mm	~1560	Pt/Cr ~ 1cm ²		 
MAPbBr ₃	2	SC	3.93 mm × 3.87 mm	~2000	Cr/Cr ~ 0.12 cm ²		 

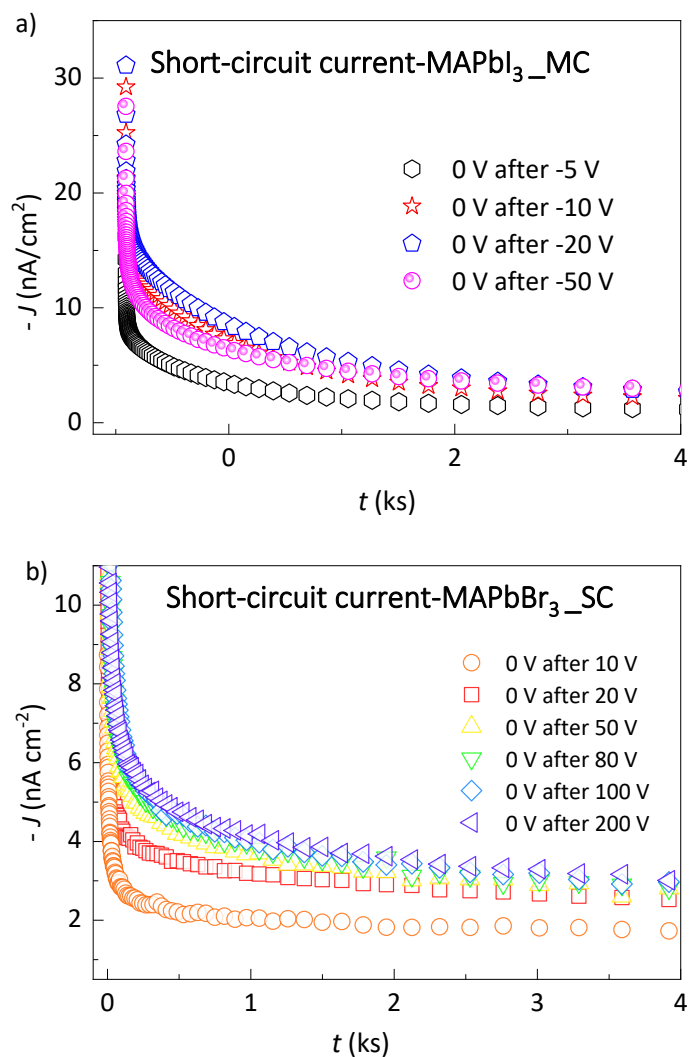


Figure S1 Example on current transient response to short-circuit condition (0 V-bias voltage) of a a) MAPbI₃ MC sample contacted with Pt/Cr electrodes b) a MAPbBr₃ SC symmetrically contacted with evaporated Cr electrodes. Short circuit current

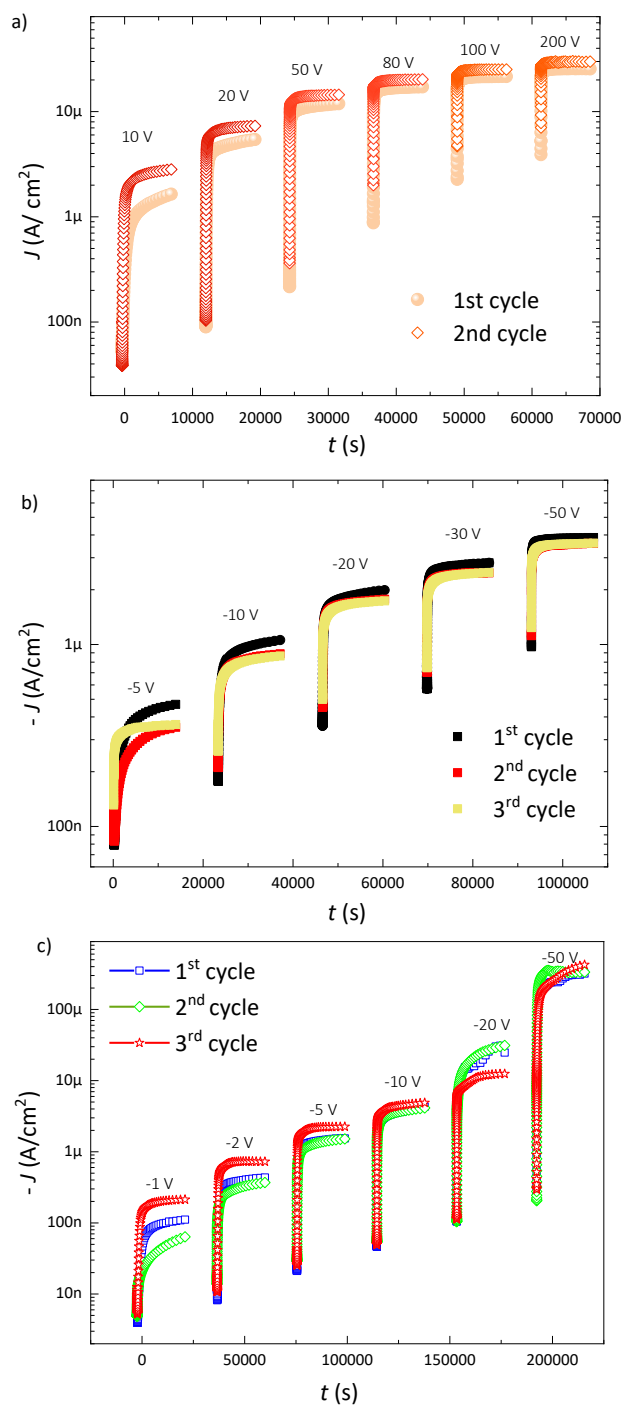


Figure S2. Protocol of measurement based on long-time current transient's response to different voltage steps of a) a 2.2 mm MAPbBr_3 SC- symmetrically contacted with evaporated Cr electrodes and two samples of b) MAPbBr_3 MC and c) MAPbI_3 MC contacted with Pt/Cr electrodes. Note the reproducibility between cycles.

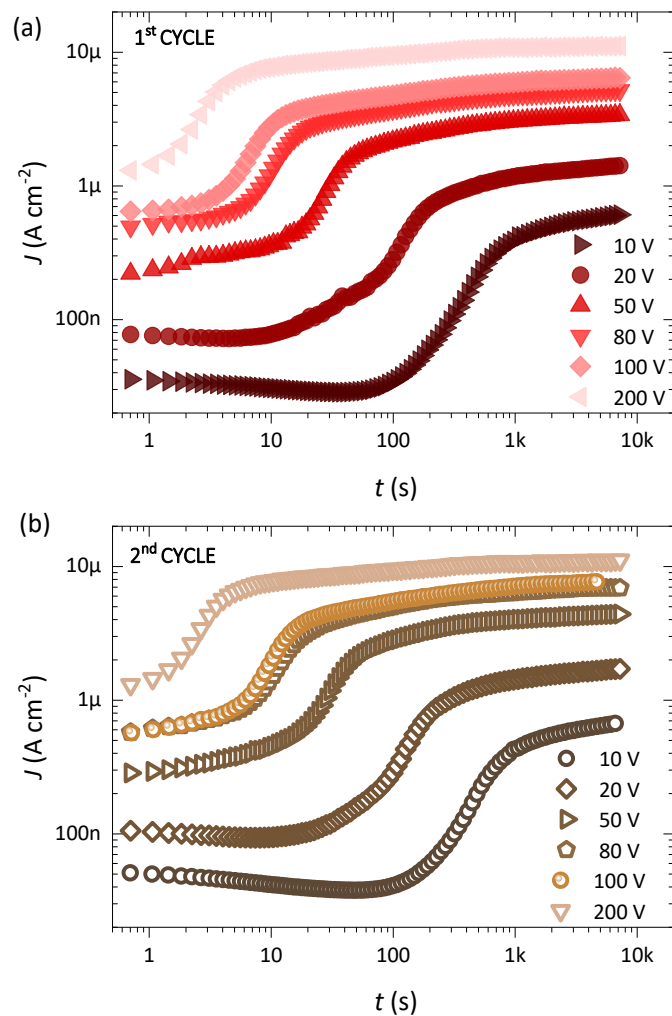


Figure S3. Long-time current transient response to different voltage steps during the 1st and b) 2nd cycle of measurement of a 2 mm-thick MAPbBr₃ SC.

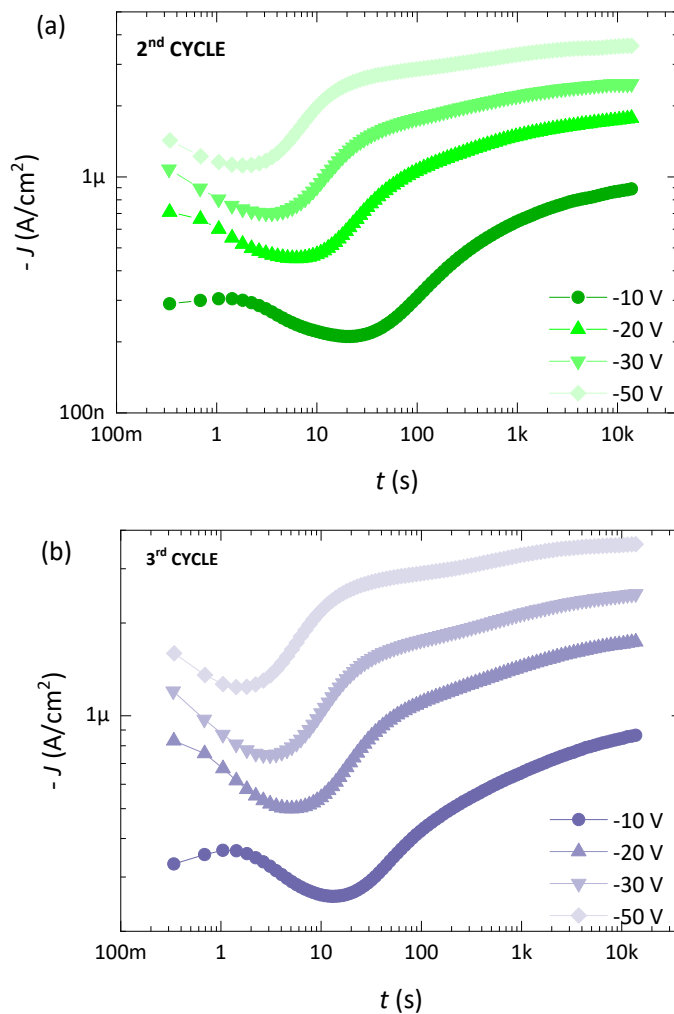


Figure S4. Long-time current transient response to different voltage steps during the 2nd and b) 3rd cycle of measurement of a 1.5 mm-thick MAPbBr₃ MC.

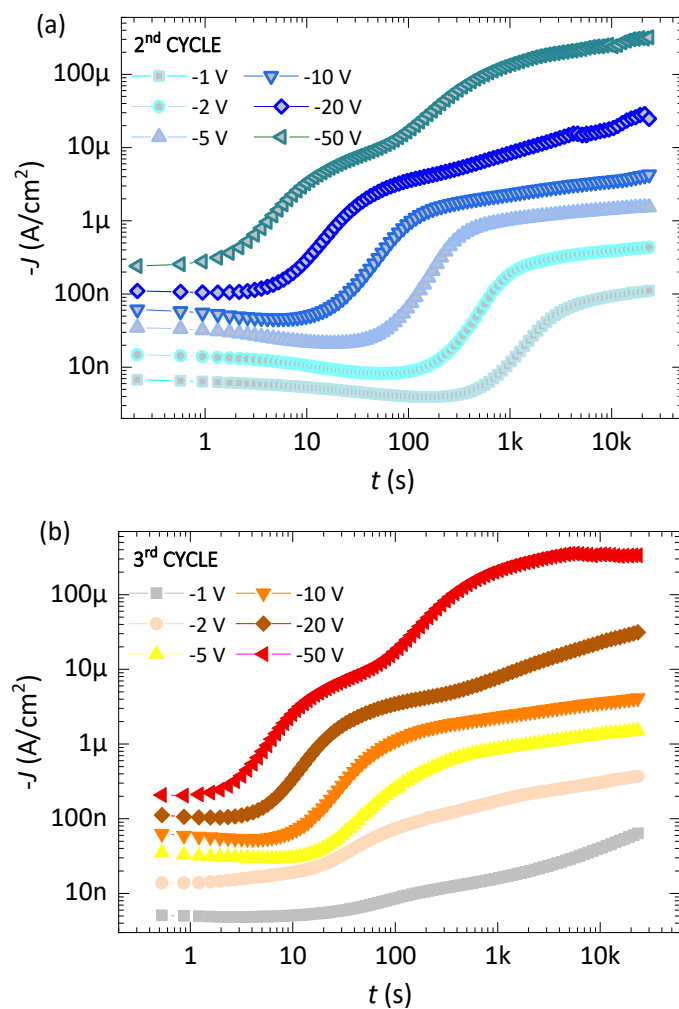


Figure S5. Long-time current transient response to different voltage steps during the 2nd and b) 3rd cycle of measurement of a 1 mm-thick MAPbI₃ MC.

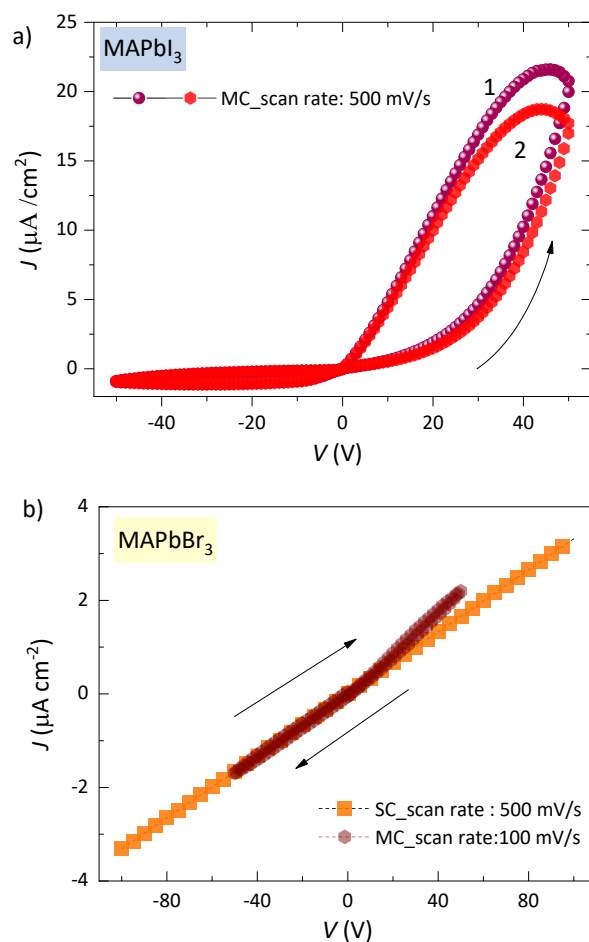


Figure S6. Current–voltage characteristics (j - V) with scan rate of a) 500 mV/s and step of 1 V of 1 mm-thick MAPbI_3 MC sample b) 500 mV/s and 100 mV/s and step of 1 V of firstly, a 2 mm-thick MAPbBr_3 SC and secondly a 1.5 mm-thick MAPbBr_3 MC. In Fig b it is remarkable the ohmic character of the characteristics j - V curve, in agreement with previous analysis on Cr-contacted perovskite device¹

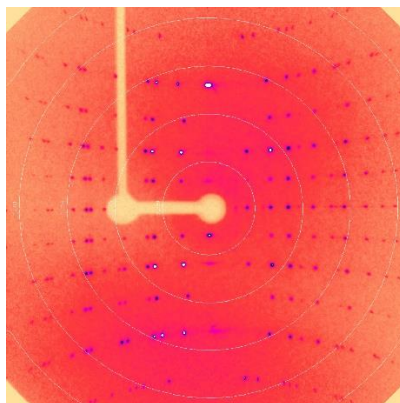


Figure S7. Rotation XRD spectra along α cell axis of a crystal measured with Cu radiation. In here only dots appear and the absence of concentric circles supports the

monocrystalline nature of the crystal. However, is evident the high symmetry observed in the material around one axis

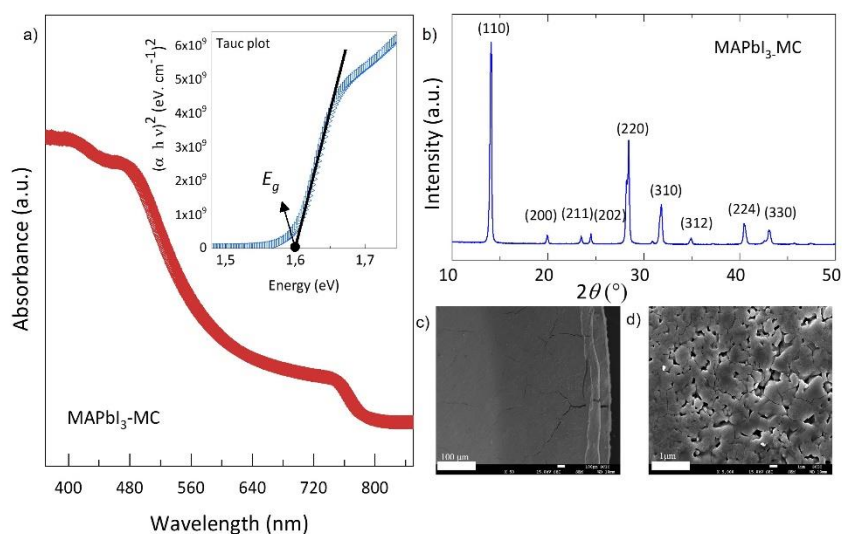


Figure S8. a) Absorbance spectra of MAPbI₃ MC sample Inset: Tauc-plot of the pellet (thickness ~1000 μm), showing the typical absorption edge of MAPbI₃ in 1.60 eV b) PXRD pattern of MAPbI₃-MC sample confirming a single-phase sample with tetragonal symmetry at room temperature. The film show the (110), (220), and (310) peaks at 14.1°, 28.4°, and 32.1°, respectively. These values are in good agreement with the reported values²⁻³ c) and d) SEM images of the top view of a MAPbI₃ thick pellets showing the microcrystalline nature of the sample at different magnified areas.

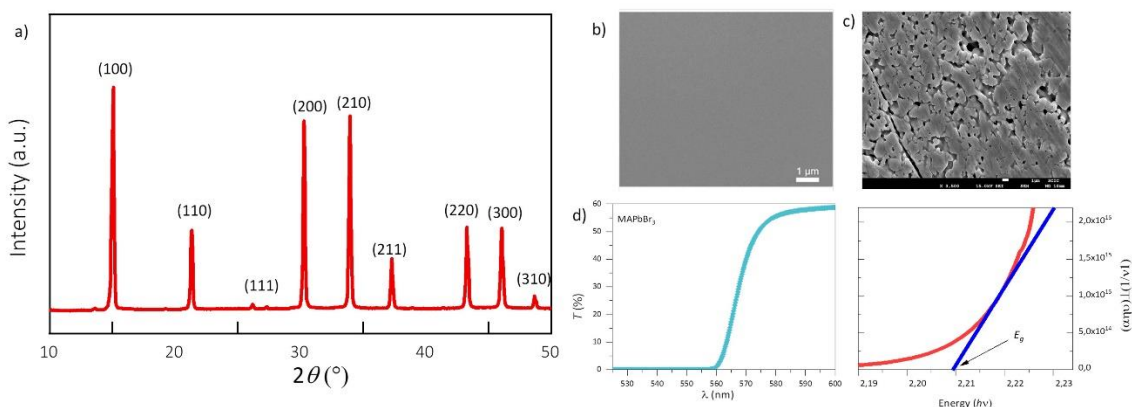


Figure S9. a) Image of the PXRD diffractogram of MAPbBr₃-MC sample showing cubic crystal lattice (Pm3m space group). The diffractogram show the (100), (110), and (200) (210) peaks at 15.0°, 21.21°, and 30.12 ° and 33.78 ° respectively. These values agree with those found in the literature.⁴⁻⁶ SEM images of the top view of b) of MAPbBr₃-SC sample after a polishing procedure and a c) of MAPbBr₃-MC sample showing a different surface morphology d) Transmittance spectra of MAPbBr₃-SC via UV-visible spectroscopy

(SC thickness = 2.0 mm) In the inset: Tauc plot of MAPbBr₃-SC for band gap determination ($E_g = 2.18$ eV)

References

1. García-Batlle, M.; Baussens, O.; Amari, S.; Zaccaro, J.; Gros-Daillon, E.; Verilhac, J. M.; Guerrero, A.; Garcia-Belmonte, G., Moving Ions Vary Electronic Conductivity in Lead Bromide Perovskite Single Crystals through Dynamic Doping. *Adv. Electron. Mater.* **2020**, *6*, 2000485.
2. Aranda, C.; Cristobal, C.; Shooshtari, L.; Li, C.; Huettner, S.; Guerrero, A., Formation Criteria of High Efficiency Perovskite Solar Cells under Ambient Conditions. *Sustainable Energy Fuels* **2017**, *1*, 540-547.
3. Alias, M. S.; Dursun, I.; Saidaminov, M. I.; Diallo, E. M.; Mishra, P.; Ng, T. K.; Bakr, O. M.; Ooi, B. S., Optical Constants of Ch₃nh₃pbbr₃ Perovskite Thin Films Measured by Spectroscopic Ellipsometry. *Opt. Express* **2016**, *24*, 16586-16594.
4. Amari, S.; Verilhac, J.-M.; Gros D'Aillon, E.; Ibanez, A.; Zaccaro, J., Optimization of the Growth Conditions for High Quality Ch₃nh₃pbbr₃ Hybrid Perovskite Single Crystals. *Cryst. Growth Des.* **2020**, *20*, 1665-1672.
5. Murali, B.; Kolli, H. K.; Yin, J.; Ketavath, R.; Bakr, O. M.; Mohammed, O. F., Single Crystals: The Next Big Wave of Perovskite Optoelectronics. *ACS Mater. Lett.* **2020**, *2*, 184-214.
6. Saidaminov, M. I., et al., High-Quality Bulk Hybrid Perovskite Single Crystals within Minutes by Inverse Temperature Crystallization. *Nat. Commun.* **2015**, *6*, 7586.

General Conclusions

In this section we present the conclusions obtained through the work developed during the course of this thesis. In line with the initial goals of this dissertation several materials were synthesized with the aim to improve the long-term operation stability of these perovskite devices for X-ray detection. Moreover, the working mechanisms of the ionic movements in SCs and MCs perovskites devices were investigated in order to address some of the remaining concerns about detrimental effects mobile ions provoke in these devices.

Firstly, a well-controlled seeded growth method based on the ITC procedure was developed and optimized by exploring different growth rates of the seed crystals of MAPbBr₃ perovskite. In addition, the structural and optical characterizations techniques of the micro and single crystalline perovskite devices of MAPbI₃ and MAPbBr₃ respectively proved the pure phase perovskite in both compounds.

Furthermore, we have analyzed the long-time impedance recovery involving ion diffusion, current transient responses at 0V-bias (ion diffusion mechanism), and ion drift under an increasing electric field. Our findings shown that the accumulation and relaxation dynamics of the mobile ionic species is bias- and time-dependent. A dynamic doping effect was proposed caused by moving ions that act as dopants and locally vary the carrier density. Thus, revealing the interplay between ionic and electronic properties in perovskite materials. Hence, we proposed a connection between the ionic species and the electronic conductivity within the device in terms of an electronic-ionic coupling effect.

Ion migration was confirmed in perovskite devices of MAPbI₃-MCs and MAPbBr₃-SCs by examining the electrical performance and dark current stability of the device. The recorded long-term negative current undershoots at zero bias revealing the ion displacement that follows a $J \propto \sqrt{t}$ dependence which is a fingerprint of diffusive transport. The use of a robust and reliable dark current transient protocol showed an exponential increment until saturation to steady-state at longtime under bias. Nonetheless, different responses were observed for MAPbBr₃-SCs compared to MAPbI₃-MCs and this different behavior was connected to the chemistry of the defect formation between both compounds.

The current phenomenology has been understood by assuming that the measured current is always an electronic current. However, a coupling between ionic and electronic currents exists in such a way that the slower species (ions) condition the value of the measured current. The kinetics of the electronic response follows the slow ion rearrangement.

The mechanism behind the dark current transients can be explained as *(i)* an increment of the effective electronic doping in the bulk perovskite via field ionization, *(ii)* a local increment of effective doping caused by ion redistribution (dynamic doping). These two mechanisms would imply an increment in electronic conductivity (and consequently current) over time after bias application. Finally, *(iii)* a reduction of contact electronic barriers via electrode polarization caused by ion accumulation, fostering as a consequence carrier injection or *(iv)* a combination of all these effects may also occur.

Our findings provide insights into the halide perovskite device physics and operating modes highlighting the mechanism through which such connection occurs. The robust electrical model developed accounts for contact mechanisms in addition to bulk conduction and can be used as a guide avoiding inconsistencies of the measured electrical protocol selected. This study reveals several features to be included into a simulation of the long-term operation of the perovskite devices for X-ray detection. Technological realizations would benefit from this fundamental information as being the dark current a persistent technical issue in these facilities. At the end, discerning the transport mechanisms of mobile species under variable electrical fields at the bulk together with the extraction of surface carrier kinetics parameters, helps to create a coherent picture in terms of high sensitivity and high efficiency of the next generation of X-ray detectors based on perovskite compounds.

Conclusiones Generales

En esta sección presentamos las conclusiones generales obtenidas a lo largo de este trabajo de tesis. Dos muestras de diferente composición y cristalinidad fueron analizadas tomando en cuenta la influencia de factores extrínsecos e intrínsecos que afectan la estabilidad operativa a largo plazo de dispositivos basados en materiales de perovskitas para la detección de rayos X.

Si resumimos nuestro trabajo partiendo de los objetivos establecidos: Un método de crecimiento fue optimizado basado en el principio de retro-solubilidad para materiales de perovskita de MAPbBr_3 . El estudio de las diferentes tasas de crecimiento de las semillas de perovskita de MAPbBr_3 , permitió obtener cristales de superficie homogénea y alto grado de cristalinidad. Mientras que las técnicas de caracterización óptica y estructural para las perovskitas monocristalinas (SCs) y microcristalinas (MCs) de MAPbI_3 y MAPbBr_3 respectivamente, probaron la fase pura perovskita en en ambos compuestos.

Se profundizó en los mecanismos de transporte del movimiento iónico en los dispositivos de SCs y MCs de perovskitas mediante el uso de dos métodos diferentes. En primer lugar, se analizó el cambio de resistencias en el tiempo a cortocircuito (polarización a 0 V) de un monocristal de MAPbBr_3 permitiendo así calcular el coeficiente de difusión de iones. En segundo lugar, se exploró transitorios de corriente a polarización de 0 V (mecanismo de difusión de iones) y bajo un campo eléctrico creciente (mecanismo de deriva de iones) en ambos tipos de dispositivos (SCs y MCs). Aquí se observó la existencia de una conexión entre las especies iónicas y la conductividad electrónica dentro de los dispositivos de perovskita en términos de un efecto de acoplamiento electrónico-iónico. Estos hallazgos mostraron que la dinámica de acumulación y relajación de las especies iónicas móviles depende del sesgo y el tiempo. Así como que el mecanismo de dopaje dinámico es causado por iones en movimiento que actúan como dopantes y varían localmente la conductividad electrónica.

La estabilidad de los transitorios de corriente negativos (corriente de cortocircuito) en oscuridad dentro del dispositivo por largos períodos de tiempo en el que se encontró que el desplazamiento de iones mostraba una dependencia de $J \propto \sqrt{t}$, que es una huella de transporte difusivo. Estos transitorios en oscuridad mostraron respuesta reproducibles y confiables en los diferentes dispositivos estudiados.

En los transitorios de corriente bajo campos eléctricos variables se observó un incremento exponencial de la corriente hasta saturación a estado estacionario. No obstante, diferentes respuestas se encontraron para MAPbBr₃-SCs en comparación con las muestras de MAPbI₃-MCs fueron encontradas. Este diferente comportamiento se relacionó a la química de la formación del defecto en ambos compuestos, así como las distancias de enlace entre el halógeno y el átomo de plomo en la estructura.

Aunque la fenomenología de la corriente medida se asume siempre como una corriente electrónica, la existencia del acoplamiento entre las corrientes iónica y electrónica hace que las especies más lentas (iones) condicionen el valor de esta última. En efecto, la cinética de la respuesta electrónica sigue el reordenamiento lento de los iones.

El mecanismo detrás de los transitorios de corriente en oscuridad se puede explicar como (i) un incremento del dopaje electrónico efectivo en la perovskita a través de mecanismos de ionización, (ii) un incremento local del dopaje efectivo causado por la redistribución de iones (dopaje dinámico) (iii) una reducción de las barreras electrónicas de los contactos a través de la polarización de los electrodos producto de la acumulación de iones que favorece así la inyección de portadores o (iv) una combinación de todos estos efectos.

Nuestros hallazgos intentan proporcionar algunas ideas sobre la física y los modos de funcionamiento de los dispositivos de perovskita de haluro. El modelo eléctrico desarrollado aquí es robusto y confiable y toma en cuenta los mecanismos de contacto y la conducción a través del material. Esto podría usarse como guía para evitar inconsistencias en las medidas eléctricas en este tipo de dispositivos.

Este estudio revela además resultados experimentales que se deben incluir en una simulación computacional que permitan verificar nuestras conclusiones. Las instalaciones tecnológicas se podrían beneficiar de esta información, ya que la corriente en oscuridad es un problema técnico persistente en estos dispositivos. El descifrar y extraer los mecanismos de transporte y parámetros cinéticos de las especies móviles bajo campos eléctricos variables ayuda a crear una imagen coherente de como debería diseñarse la próxima generación de detectores de rayos X basados en compuestos de perovskita.

Future Outlooks

Still, large hysteresis is often obtained when measuring the current-voltage sweeps in metal halide perovskite materials, even in those based on single crystalline compounds.¹⁻² Indeed, hysteresis effect has been associated with the slow time dynamics due to ionic motion inside the perovskite layer.² Therefore, it is obvious that mobile ionic species drift under an electric field and may diffuse at short circuit condition even for the purest materials without any grain boundary effects or surface defects.³ Moreover, unveiling the nature of halide ion drift under an electric field should be prioritized, because this can alter the device structure over time making more difficult a stable operation and further commercialization.⁴⁻⁵

Consequently, further improvements are necessary to reach superior environmental stability and optoelectronic properties of metal halide perovskite devices for X-ray detection. In the case of SCs, reports have shown that single crystalline compounds are a suitable alternative to microcrystalline thin films in terms of device performance and long-term stability.⁶⁻⁷ Nonetheless, crystal engineering approaches in MHPs are still a rising field and also new growth techniques have been reported accounting for high quality SCs with less surface roughness, large areas (over 10 cm²) and passivated surfaces. It is also proposed that a fully encapsulated devices may limit some detrimental factors such as external air/moisture exposure avoiding the formation of defective crystal surfaces.⁸⁻⁹ **Figure 9.1** summarizes some of the main problems found during the course of this thesis and several solution strategies developed to solve them.

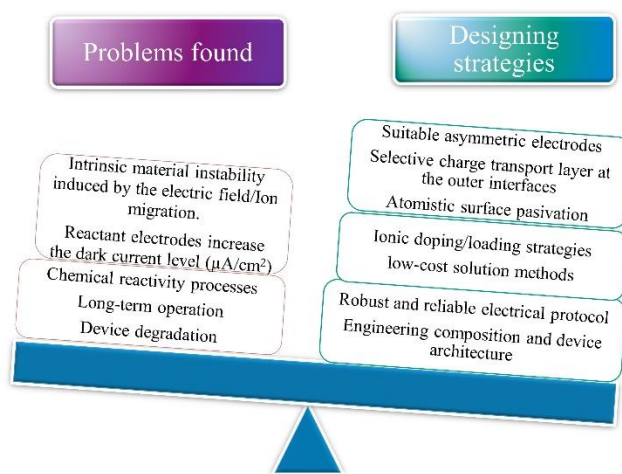


Figure 9.1. Schematic representation of current questions and the problem-solving strategies in the field of perovskites based-X-ray detectors

Table 9.1 reviews various opportunities and environmentally friendly alternatives rising in the field. In the case of 2D perovskite materials which can inherently be quantum well (QW), a system in which the electron motion is restricted in one direction thus producing quantum confinement,¹⁰ novel unforeseen opportunities have been described and SCs with two-dimensional layered structures can be a suitable solution to hinder ion migration.

Table 9.1 Challenges and Outlooks for perovskites-based X ray detectors

Challenges	Outlooks
Reproducible growth of high-quality perovskites.	Optimization of fabrication method and structural design.
	Use of high-quality materials such as Br-perovskite single crystals.
Improving long-term stability of perovskite materials	Use of low-dimension perovskite materials with 2D material.
	Use of additives, interlayer or bulky organic cations
	Development of novel lead-free perovskite materials.

Another strategy relies on an accurate doping of the perovskite compound with other inorganic cations such as Cs, designing in the extreme case a fully inorganic perovskite. Additionally, the use of additives and interlayers will help to reduce defect densities. Furthermore, the use of bulky organic cations has been reported as surface passivation agents to tune the dimensionality of MHPs allowing to tailor their optoelectronic properties while enhancing their stability.¹¹ Finally, novel lead-free perovskite materials for radiation detection which has been successfully tested as solar cells, are a suitable choice that can be explored in the near future by using the experimental methodologies described in our dissertation with the aim of a more stable lead-free halide perovskites-based X ray detectors.

All the strategies for controlling the nature and evolution of defects in perovskite devices are usually related to the improvement of both the X-ray detector efficiency and the sensitivity. In **Figure 9.2** is shown how overtaking the detector efficiency of indirect convertors and its combination with the spatial resolution of direct detectors, the next generation of MHPs devices for X-ray detection can be devised. That increase in signal-to-noise ratio would enable a precise and early diagnosis in radiological

imaging by reducing the minimum X-ray dose required for patients and allowing the detection of small and low-contrast structures.

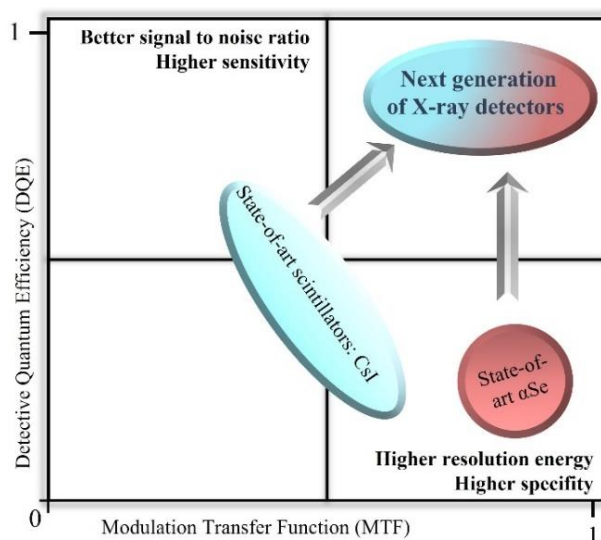


Figure 9.2. Schematic diagram showing how to design the next generation of metal halide perovskite-based devices for X-ray detection. Overtake the detector efficiency of CsI indirect converters (high DQE) with a great spatial resolution (high MFT) of a-Se direct converters.

References

1. Duijnste, E. A.; Le Corre, V. M.; Johnston, M. B.; Koster, L. J. A.; Lim, J.; Snaith, H. J., Understanding Dark Current-Voltage Characteristics in Metal-Halide Perovskite Single Crystals. *Phys. Rev. Appl.* **2021**, *15*, 014006.
2. Bisquert, J.; Guerrero, A.; Gonzales, C., Theory of Hysteresis in Halide Perovskites by Integration of the Equivalent Circuit. *ACS Phys. Chem. Au* **2021**, *1*, 25-44.
3. Azpiroz, J. M.; Mosconi, E.; Bisquert, J.; De Angelis, F., Defect Migration in Methylammonium Lead Iodide and Its Role in Perovskite Solar Cell Operation. *Energy Environ. Sci.* **2015**, *8*, 2118-2127.
4. Kakavelakis, G.; Gedda, M.; Panagiotopoulos, A.; Kymakis, E.; Anthopoulos, T. D.; Petridis, K., Metal Halide Perovskites for High-Energy Radiation Detection. *Adv. Sci.* **2020**, *7*, 2002098.
5. Bisquert, J.; Garcia-Belmonte, G.; Guerrero, A., Ionic/Electronic Conduction and Capacitance of Halide Perovskite Materials. In *Perovskite Photovoltaics and Optoelectronics*, 2022; pp 173-213.
6. Afroz, M. A.; Aranda, C. A.; Tailor, N. K.; Yukta; Yadav, P.; Tavakoli, M. M.; Saliba, M.; Satapathi, S., Impedance Spectroscopy for Metal Halide Perovskite Single Crystals: Recent Advances, Challenges, and Solutions. *ACS Energy Lett.* **2021**, 3275-3286.
7. Cheng, X.; Yang, S.; Cao, B.; Tao, X.; Chen, Z., Single Crystal Perovskite Solar Cells: Development and Perspectives. *Adv. Funct. Mater.* **2020**, *30*, 1905021.
8. La Ferrara, V.; De Maria, A.; Rametta, G.; Delli Veneri, P., The Effect of Storage Cycle on Improvement in the Photovoltaic Parameters of Planar Triple Cation Perovskite Solar Cells. *Mater. Adv.* **2021**, *2*, 5396-5405.
9. Leijtens, T.; Bush, K.; Cheacharoen, R.; Beal, R.; Bowring, A.; McGehee, M. D., Towards Enabling Stable Lead Halide Perovskite Solar Cells; Interplay between Structural, Environmental, and Thermal Stability. *J. Mater. Chem. A* **2017**, *5*, 11483-11500.
10. Wang, K.; Park, J. Y.; Akriti; Dou, L., Two-Dimensional Halide Perovskite Quantum-Well Emitters: A Critical Review. *EcoMat* **2021**, *3*, e12104.
11. Lee, H. B.; Kumar, N.; Tyagi, B.; He, S.; Sahani, R.; Kang, J. W., Bulky Organic Cations Engineered Lead-Halide Perovskites: A Review on Dimensionality and Optoelectronic Applications. *Materials Today Energy* **2021**, *21*, 100759.

**High Quality Perovskite Materials for X-Ray Detection:
Effect of Mobile Ions on Dark Current Stability**

Marisé García-Batlle | 2022